Nonpolar Resistive Switching Based on Quantized Conductance in Transition Metal Oxides

Yusuke NISHI

Abstract

A resistive switching (RS) phenomenon offers various opportunities such as nonvolatile memories and neuromorphic logics. Resistive random access memory (ReRAM) is one of the emerging nonvolatile memory, which has a metal-oxide-metal (MOM) structure. The RS phenomenon in transition metal oxide (TMO)-based ReRAM cells is often explained as nonvolatile transitions in the cell resistance between high-resistance state (HRS) and low-resistance state (LRS) by formation and rupture of localized conductive filaments, after the initial voltage application called forming. However, cell-to-cell and cycle-to-cycle variabilities such as transition voltages hinder the understanding of an universal RS mechanism.

In this thesis, as an approach to elucidate the RS mechanism, distributions of forming voltage and the origin of conductive filaments by forming were investigated in binary TMO-based RS cells. In particular, the formation of a conductive filament with a quantum point contact (QPC) by forming in nickel oxide (NiO)-based RS cells was described. Moreover, the appearance and disappearance of nonpolar RS characteristics based on quantized conductance were discussed.

In Chapter 1, the background of the present work was given, together with the focal point and the originality of this thesis.

In Chapter 2, deposition methods of NiO and titanium dioxide (TiO_2) layers as the TMO and platinum (Pt) electrodes were outlined. The TMO layers were deposited by reactive sputtering, which enabled the control of oxygen composition by means of varying the oxygen (O_2) flow rate. Not only the fabrication procedure of the TMO-based RS cells but also the deposition systems and their modifications for various layers were also described. In addition, dependences of the deposition rate and oxygen composition in the NiO layers on O_2 flow rate during reactive sputtering were analyzed based on Berg's model. As well as the appearance conditions of the RS phenomenon in TMO-based cells, the RS condition based on quantized conductance in NiO-based RS cells was investigated.

In Chapter 3, admittance spectroscopy was performed on NiO layers with various oxygen compositions deposited on *n*-silicon (Si) substrates. In addition, current-voltage (I–V) measurements of Pt/NiO/Pt structures on *p*-Si substrates were also conducted. The correlation between the oxygen composition and these electrical properties was investigated. Based on these results, characterization of localized trap levels and uncertainties of the technique for the NiO layers were discussed. Moreover, potential for high-temperature operation of the NiO-based RS cells was described.

In Chapter 4, effects of crystallinity of the TMO layers and deposition condition on RS characteristics, especially forming characteristics, in TMO-based RS cells were discussed. At first, the annealing contributing to oxygen diffusion toward the NiO surface resulted in changes of the crystalline orientation, strain, and oxygen composition in the NiO layer. Next, crystallinity and time-dependent forming characteristics in as-deposited Pt/NiO/Pt and Pt/TiO_2/Pt RS cells were investigated. While the NiO layers exhibited a granular structure on Pt bottom electrodes (BEs) deposited by electron beam (EB) evaporation, NiO columns preferentially stood <111> orientation on the Pt BE deposited by sputtering. Conversely, whereas both the TiO_2 layers exhibited a granular structure in the two types of samples, the concentration of oxygen vacancies (V_Os) differed between these samples. In addition, Weibull distributions of time to forming in various cells indicated that the formation of conductive filaments at forming followed a weakest-link theory, and that the weakest spots such as V_Os were distributed in the TMO layers according to Poisson statistics. The difference of Weibull distributions between the TMO-based RS cells reflected differences in both grain boundary (GB) density (crystallinity) and the V_O concentration (oxygen composition) in the TMO layers. Furthermore, both a possible reason for the difference of correlation between variations of initial resistance and distributions of time to forming, and where conductive filaments created in the TMO layers by forming were also discussed.

In Chapter 5, the appearance condition of conductance quantization in the Pt/NiO/Pt cells was discussed. Dependence of forming characteristics on the number of V_Os at GB triple points was revealed by transmission electron microscopy (TEM)-energy-dispersive X-ray spectrometry (EDX) mapping. Moreover, cell size dependence of "semi-forming," characteristics was also explained by the area scaling law, which indicated analogy of semi-forming with "second forming," corresponding to the conventional forming. In addition, an RS model based on quantized conductance was proposed as follows. A voltage sweep resulted in a conductive filament with a QPC created by semi-forming at the weakest V_O-rich GB. Upon the voltage sweep after semi-forming, the conductive filament with a QPC began to be fat according to conductance quantization. If the voltage sweep stopped just after semi-forming, RS behavior was observed due to the rupture and formation of the filament by re-applications of voltage.

In Chapter 6, the physical origin of conductance fluctuation accompanied by conductance quantization in the Pt/NiO/Pt cells was described. The voltage-driven conductance fluctuation before and after semi-forming resulted in the cell conductance being a non-integer multiple of the quantized conductance G_0 and originated from the modification of V_O concentration at GBs in the NiO layer. In addition, conductance fluctuation as well as conductance quantization possibly disappeared upon heating the RS cells to 470−570 K or Joule heating conducted from another fat filament in the NiO layer created by second forming. From the viewpoint of voltage- and heat-driven disappearance of the conductive filament with a QPC and the modification of V_Os, driving force behind the reset after semi-forming based on how Joule heating affected conductance quantization and conductance fluctuation was also discussed.

In Chapter 7, the summary of this thesis was presented, together with the remaining challenges and suggestions for future studies.

Acknowledgments

First of all, I would like to express my sincere gratitude to Professor Tsunenobu Kimoto for his supervision, continuous guidance, kind encouragement, and provision of opportunity for fundamental research on alluring phenomena. Without his incredible understanding and generosity throughout the research, this thesis could never have been accomplished and my life would have remained inactivated.

I wish to thank Professor Shizuo Fujita and Professor Hirofumi Yamada for their valuable suggestions and stimulating comments on this dissertation. In addition, I acknowledge Associate Professor Itsuhiro Kakeya and Associate Professor Kazuhiko Sugiyama for their useful advice and heartfelt encouragement.

I would like to show my appreciation for Emeritus Professor Hiroyuki Matsunami for his profound and effective advice on a mental attitude and indispensable preparedness especially for this fundamental research on an unmatured topic in the laboratory. I am sincerely indebted to Professor Jun Suda from Nagoya University for his powerful instruction on advanced experiments, valuable comments based on his remarkable knowledge, and constructive guidance since I was an undergraduate student in the laboratory.

I am grateful to Assistant Professor Mitsuaki Kaneko for his blessed sharing of a number of insane tasks and unpreventable troubleshooting in the laboratory. I also thank Associate Professor Mitsuru Funato for his thoughtful management of the shared equipment we use.

I express my respect for Assistant Professor Tatsuya Iwata from Toyohashi University of Technology for his sharing of initial hardship to explore direction of the research and his strong willingness to execute hosts of experiments originated from his thorough investigation on associated references. I am extraordinarily deferential to Mr. Hiroki Sasakura for his evocative consciousness of the original phenomena and his verification experiments, which greatly contributed to this thesis. I would like to extend my cordial gratitude to Mr. Yutaka Kuriyama for his assiduous efforts of intriguing phenomena he found in a new material owing to his fertile imagination and ability, which have been expanded upon by the next generation of researchers in other materials.

I am very much obliged to Mr. Naoki Okimoto, Mr. Syunsuke Kamata, and Mr. Masaya Arahata for their memorable accomplishment of their troublesome topics, to Mr. Toshiki Miyatani, Mr. Naoki Kanegami, Mr. Kazutaka Yamada, and Mr. Yuto Tsuchiya for their spontaneous and creative attitudes toward a new phase of research on resistive switching, and to Mr. Daisuke Horie and Mr. Ryosuke Matsui for their temporal assistance.

I express my gratitude to Ms. Yoriko Ohnaka who kindly supports my work by providing a comprehensible explanation of mystically complicated jobs and wonderful bureaucratic paperwork. Without her dedicated helps, I would have inevitably wasted more time and energy on intrinsically unnecessary tasks.

I show my sincere appreciation to Associate Professor Kentaro Kinoshita from Tokyo University of Science for useful advice and a number of fruitful discussions about resistive switching. I am also indebted to Dr. Tohru Tsuruoka from the National Institute for Materials Science and Dr. Takumi Moriyama in Sandisk for their helpful and stimulating comments during academic conferences.

I am much obliged to Dr. Hajime Tanaka from Osaka University and Dr. Takuma Kobayashi from Tokyo Institute of Technology for their fruitful comments about resistive switching based on their insatiable curiosity.

I would like to thank Associate Professor Masahiro Horita from Nagoya University for his initial building of the research environment in the laboratory, which followed by voluntary and greatly improvements of the environment by Assistant Professor Takafumi Okuda, Dr. Naoya Morioka, Mr. Taro Enokizono, Mr. Kazutaka Kanegae, and so forth.

I also thank all the members of the laboratory for their continued maintenance of a number of pieces of experimental equipment and contributions to their comfortable daily lives in the laboratory (unfortunate omission of name of the persons concerned due to a page limit).

I am very thankful to administrative staff of the faculty of electrical and electronic engineering for supporting my research and educational activities in various forms. I am specially grateful to Dr. Mitsuaki Takeuchi at Rhesca Co., LTD. for his self-sacrificing cooperation in patient experimental preparations in undergraduate education.

In addition, I need to make my cordial acknowledgment to members at the Occupational Health, Safety and Environmental Management Center for their quick reactions. I wish to raise my hat to traffic control persons and cleaning staff for their stalwart performances early and late in spite of bad weather conditions.

Many of the analyses in this thesis were carried out by external institutions, such as the Foundation for Promotion of Material Science and Technology of Japan, EAG laboratories, Toray Research Center, and Kobelco Research Institute, Inc.

This work was financially supported by several private financial groups, and the Ministry of Education, Culture, Sports, Science and Technology of Japan.

Finally, I really thank my wife and children for their support and inevasible patience despite my insufficient household tasks and spending less time with them especially during the last few months. I renew my appreciation to my parents, brother and sister, and friends for their understanding and touching encouragement.

February, Heisei 31
Yusuke NISHI

Contents

Abstract i

Acknowledgments iii

Contents v

Chapter 1. Introduction 1
1.1 Background . . . 1
1.2 Resistive Switching Phenomenon . . . 3
1.2.1 Concept of RS . . . 3
1.2.2 Memory application . . . 7
1.3 Outline of Thesis . . . 8
References . . . 10

Chapter 2. Fabrication of Resistive Switching Cells 15
2.1 Introduction . . . 15
2.2 Metal Deposition for Electrodes . . . 16
2.3 Reactive Sputtering for Transition Metal Oxides . . . 17
2.3.1 RS material . . . 17
2.3.2 Sputtering system . . . 19
2.3.3 RS cell fabrication . . . 22
2.3.4 Theory of reactive sputtering . . . 24
2.4 Summary . . . 28
References . . . 28

Chapter 3. Characterization of Defects in NiO Layers 31
3.1 Introduction . . . 31
3.2 Sample Fabrication . . . 32
3.2.1 Device structure . . . 32
3.2.2 Admittance spectroscopy . . . 34
3.2.3 Experimental procedure . . . 34

3.3 Defect Levels in NiO Layers and Resistive Switching Characteristics 36
3.3.1 *p*-NiO/*n*-Si heterojunction 36
3.3.2 Dependence of defect levels on oxygen composition in NiO layers 38
3.3.3 Dependence of RS characteristics on oxygen composition in NiO layers . 38
3.4 Discussion 42
3.5 Summary 47
References 47

Chapter 4. Effects of Crystallinity of Transition Metal Oxides on Resistive Switching Characteristics 49
4.1 Introduction 49
4.2 Changes of Crystalline Structures by Thermal Annealing 50
4.2.1 Purpose of thermal annealing 50
4.2.2 Effects of thermal annealing 50
4.2.3 Discussion 57
4.3 Crystallinity of Transition Metal Oxides 59
4.3.1 RS cell fabrication 59
4.3.2 Crystalline Structure 63
4.3.3 Discussion 70
4.4 Weibull Distribution of Forming Characteristics 76
4.4.1 Weibull distribution 76
4.4.2 Cell size dependence of Weibits 78
4.4.3 Constant voltage and oxide thickness dependence of Weibits 80
4.4.4 Initial resistance dependence of Weibits 82
4.4.5 Discussion 84
4.5 Summary 87
References 87

Chapter 5. Formation of Conductive Filaments with a Quantum Point Contact 89
5.1 Introduction 89
5.2 Resistive Switching based on Quantized Conductance 90
5.2.1 RS cell fabrication 90
5.2.2 Two types of forming 92
5.2.3 Temperature dependence of cell conductance 95
5.2.4 Discussion 98
5.3 Dependence of Forming Characteristics on Oxygen Composition and Cell Size . 102
5.3.1 Oxygen composition dependence 102
5.3.2 Cell size dependence 106

5.4 Appearance Condition of Conductive Filaments with a Quantum Point Contact . 109
5.4.1 RS model based on quantized conductance 109
5.4.2 Appearance or disappearance of QPC 111
5.4.3 Discussion 114
5.5 Summary 116
References 117

Chapter 6. Conductance Quantization and Conductance Fluctuation 119
6.1 Introduction 119
6.2 Conductance Fluctuation 121
6.2.1 Sample preparation 121
6.2.2 Equivalent circuit model of conductance quantization 123
6.2.3 Dependence of dominant cell conductance on O_2 flow rate 123
6.2.4 Dependence of dominant cell conductance on cell size 128
6.3 Effect of Voltage Mode and Heating on Conductance Fluctuation 132
6.3.1 Step-by-step voltage sweep 132
6.3.2 Pulse voltage 134
6.3.3 Heat to the cell 140
6.4 Driving Force behind Reset 142
6.4.1 Two types of reset 142
6.4.2 Joule heating by reset 144
6.5 Discussion 147
6.6 Summary 155
References 156

Chapter 7. Conclusions 159
7.1 Conclusions 159
7.2 Future Outlook 161
References 162

Appendix A. Reactive Sputtering Model 163
A.1 Equations in Berg's model 163
A.2 O_2 Flow Rate Dependence 164
References 164

Appendix B. Coupled Simulation 165
B.1 Heat Conduction Simulation 165
B.2 Coupled Simulation for Reset 166
References 170

List of Publications 171

Chapter 1

Introduction

1.1 Background

Every time the author hears his children sing “it’s a small world,” he becomes more aware of this busy and hurried world, being brought back to consciousness from a temporal respite. Because people can find everything they want on the internet conveniently by the recent expansion of mobile communication equipment, such as smart phones and tablets, they are always busy with nerve-fraying e-mail correspondence from social networking services (SNSs) and are eager to acquire “good” reactions from someone they never actually meet, even during lectures and meetings.

In the actual world, people can make high-speed and large-capacity communication anytime and anywhere owing to remarkable advancement in memory devices, especially nonvolatile memory (NVM). Flash memory, one of the dominant nonvolatile solid-state storage devices invented in the 1980s [1], has rapidly enhanced its performance with the development of fabrication technique according to Moore’s law [2]. However, the memory is approaching its scaling limit and facing the problem of limited further dramatic improvement due to its intrinsic operating principle. In addition, another problem is the latency gap between very-fast-operating volatile memory, such as dynamic random access memory (DRAM) and flash memory, as shown in Fig. 1.1 [3]. Therefore, storage class memory (SCM) is the most promising candidate for replacing traditional NVM, such as hard disk drives (HDDs), not only in mobile terminals but also as external storage memory for supercomputers.

One solution to these problems is multiplication of the number of bits per cell in flash memory [4]. While a conventional single-level cell distinguishes between a “0” and “1” depending on the charge of the floating gate of the cell, giving each cell 2−4 bits by increasing the number of threshold levels possesses larger benefit for increasing storage capacity drastically without an increase in process complexity. In fact, NAND flash memory continues to advance toward higher density and lower power, resulting in low-cost storage solutions according to this trend over the past 15 years, as shown in Fig. 1.2 [5]. However, the increase cell bit capacity requires additional circuitry and programming algorithms to compensate for the degradation of performance and endurance.

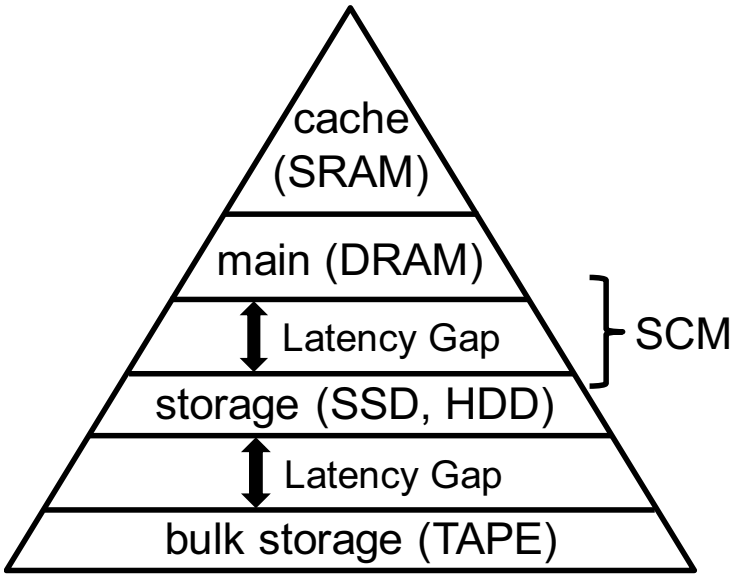

Figure 1.1: Layered structure of the current memories [3].

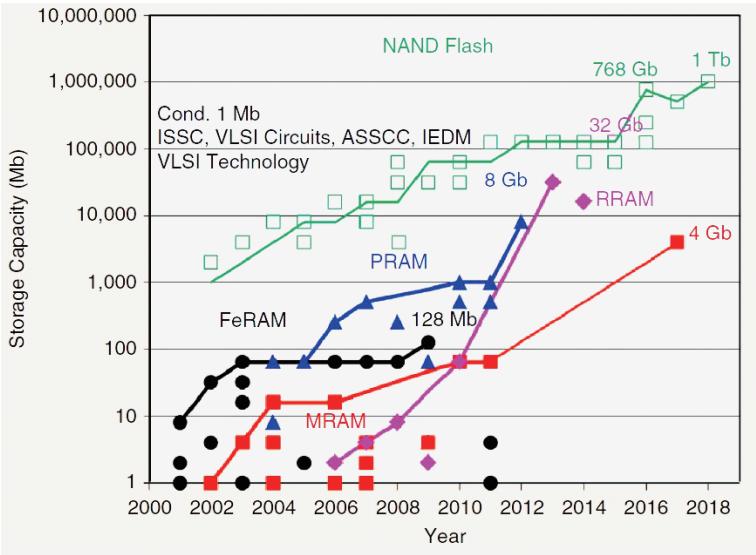

Figure 1.2: Storage capacity trends for emerging NVMs [5].

Another reasonable solution to the problems is the development of the emerging NVM, which avoids the scaling limit to find an alternative to flash memory. In particular, the replacement of volatile memories, including static RAM (SRAM) and DRAM, with the emerging NVM is crucial for obtaining "normally-off computing", in which operating power can be dramatically reduced [6]. Therefore, various next-generation nonvolatile memories, such as magnetic RAM (MRAM) [7, 8], phase change RAM (PRAM) [9–11], and resistive RAM (ReRAM), have been developed. MRAM seems difficult to pursue toward further high density because of its complicated structure and relatively large operating current, although the current of spin-torque-transfer MRAM has drastically decreased. Thus, MRAM may be suitable for cache memory (post-SRAM) and main memory (post-DRAM) owing to its high endurance. Nevertheless, PRAM and ReRAM are appropriate for a large-capacity applications (such as SCM) because of its simple stack structure. From the storage capacity trend shown in Fig. 1.2, ReRAM is the most promising candidate for emerging NVM to overcome the problems described above.

1.2 Resistive Switching Phenomenon

1.2.1 Concept of RS

First, as classifications based on a resistive switching (RS) operation, two different types of RS in ReRAM are well known. Figure 1.3 shows two different types of current-voltage (I–V) characteristics by a voltage sweep. Basically, the resistance states in ReRAM are called high-resistance state (HRS) and low-resistance state (LRS). In the initial state, ReRAM generally exhibits high resistance, which is not necessary the same as HRS. Most ReRAM cells reported in the literature exhibit bipolar RS, as shown in Fig. 1.3(a). When a voltage is increased, current abruptly increases at a certain threshold voltage, which leads to LRS. This initial transition to the LRS is normally called "forming" or electroforming. An increase in voltage of opposite polarity to set voltage results in a transition from LRS to HRS. When the following voltage is swept to the opposite direction, a transition from HRS to LRS occurs. In general, forming voltage magnitude is the same as or greater than the following set ones, the case of forming voltage same as set voltage is called forming-free. The transitions from the HRS to the LRS and from the LRS to the HRS are called "set" and "reset," respectively. Conversely, Fig. 1.3(b) represents unipolar RS, which exhibits both set and reset in only one bias polarity. Reset voltage magnitude is generally smaller than set one, and thus a voltage sweep should be stopped after reset to avoid unintentional occurrence of set. Both in the LRS and the HRS, set and reset take place alternately in the similar manner by the following voltage sweep. Here, the current limit as compliance current (I_{comp}) is adopted during forming and set by measurement system and/or an external circuit to avoid damage to the cell and to optimize the RS operation. It is important that the I_{comp} is inactive (or quite large) in the voltage sweep because reset current is often larger than I_{comp} at forming and set. A read operation is performed at a smaller voltage magnitude than the transition voltage magnitude to detect the current while avoiding a detectable change of the state. Furthermore, an RS operation

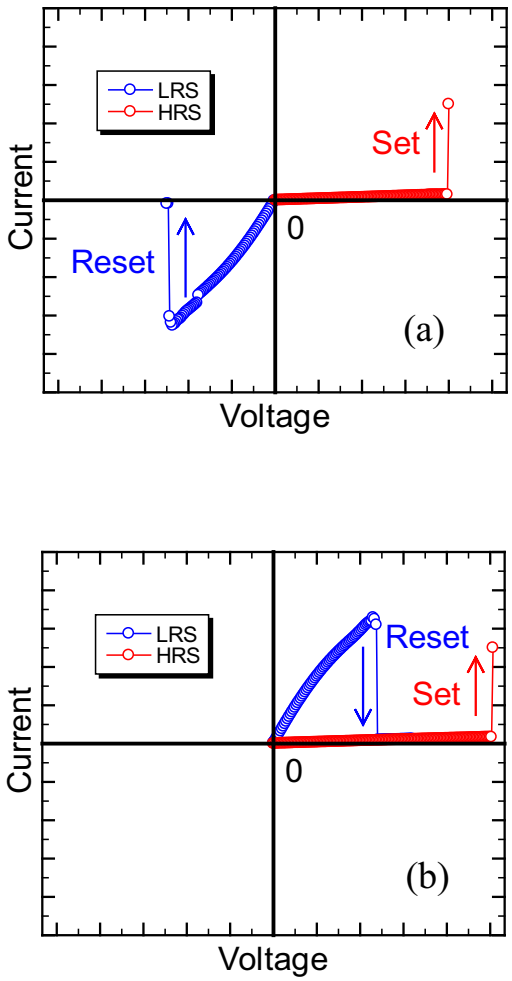

Figure 1.3: *I*–*V* characteristics of (a) bipolar and (b) unipolar RS. The opposite polarity for set and reset is required in bipolar RS, while set and reset occur by the same polarity in unipolar RS.

in which reset can occur by a voltage bias of both positive and negative bias polarities is often referred as nonpolar. Note that the actual device applications will use the pulse application instead of the voltage sweep.

ReRAMs can be classified by their switching mechanism basically depending on the combination of an insulator and electrodes. The three main types of ReRAMs are electrochemical memory (ECM), valence change memory (VCM), and thermochemical memory (TCM). ECM and VCM exhibit bipolar RS, while TCM typically displays unipolar or nonpolar RS.

In ECM cells, the metal-insulator-metal (MIM) stack structure consists of one electrochemically active electrode, such as silver (Ag) or copper (Cu), and generally the counter inert electrode including platinum (Pt) or titanium nitride (TiN). When a positive voltage is applied to the active electrode, cations (Ag^+ or Cu^{2+}) generate at the electrode by oxidation and migrate to the counter inert electrode in the insulator. The reduction of cations takes place at negatively biased electrode, and active atoms grow from the inert electrode toward active electrode in sequence, finally resulting in the formation of conductive bridge corresponding to set. Under a negative voltage applied to the active electrode, the bridge is dissolved as in the opposite manner, corresponding to reset. In the literature, ECM is known as conductive bridge RAM (CBRAM). The insulator in ECM works as a solid ion conductor, which includes binary oxides such as silicon dioxide (SiO_2) [12, 13], chalcogenides such as Ag_2S [14, 15], and superionic electrolyte such as AgI [16].

In contrast, VCM and TCM cells with metal-oxide-metal (MOM) stack structures require forming before emergence of RS, which is believed to be the formation of conductive filaments with reduced chemical composition of metal-rich or oxygen-deficient. The difference between VCM and TCM is reset operation. In VCM cells, disruption of the conductive filament with a valence change in the cations occurs by ionic defect migration upon applied voltage [17]. Conversely, in TCM cells, dissolution of the conductive filament by local oxidation occurs by Joule heating (thermochemical effect) [18, 19], which can be independent of voltage polarity.

From the viewpoint of the locations of the RS event in a MIM stack structure, RS behaviors can be categorized into two types, filamentary RS and interfacial RS. The RS types of most of cells described above are based on the filamentary RS, which occurs at a localized area and is independent of a cell size in LRS. The filamentary RS is schematically illustrated in Fig. 1.4. In the initial state, a conductive filament is created by forming, trigger process to appearance of RS. After forming, reset and set occurs alternately because of rupture and reformation of the filament. In contrast, the interfacial RS is cross-sectional area proportional, and seems to occur close to one electrode. Approximately half of VCM cells with asymmetric stack structure exhibit the interfacial RS because of two electrodes with different oxygen affinity and/or work function, which is suitable for the investigation where RS occurs. The interfacial RS is schematically illustrated in Fig. 1.5 [20]. The RS mechanism without forming possibly originates from charge-induced change in the insulator formed at the one metal/oxide interface. In the interfacial VCMs, the modulation of a Schottky barrier at the interface between an electrode and an oxide probably dominates RS [21].

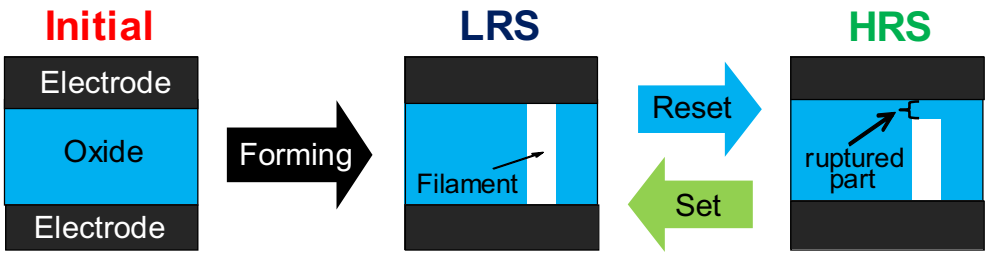

Figure 1.4: A schematic illustration of filamentary RS.

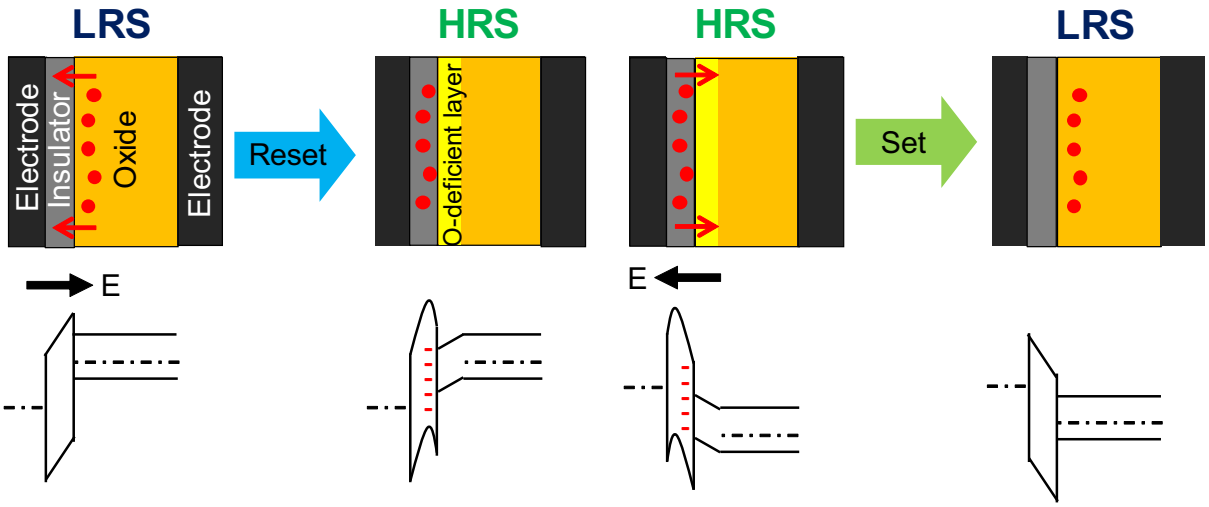

Figure 1.5: A schematic illustration of interfacial RS. Red circles represent oxygen ions (O^{2-}).

1.2.2 Memory application

RS has been studied in various materials for more than 50 years. The negative resistance effect in MIM stack structures was reported as the first RS phenomenon in 1960s [22]. Bistable RS was reported in binary transition metal oxides (TMO), such as nickel oxide (NiO) [23], tantalum pentoxide (Ta_2O_5) [24], titanium dioxide (TiO_2) [25], and hafnium dioxide (HfO_2) [26]. Through a stagnation period for RS in a quarter-century due to insufficient analytical tools, applications based on RS gradually enter the spotlight.

Atomic switch is known as one of ECMs, which enables a control of conductive bridge on a nano scale [14]. While the initial structure of atomic switch consists of active metal electrode (Ag, Cu) and ionic conductor (mainly sulfides) [27, 28], oxide-based atomic switch has been proposed for neuromorphic devices owing to a synaptic behavior [29]. In contrast, the first report on the interfacial VCMs is RS characteristics in PrCaMnO (PCMO) [30], and the PCMO-based RS memory was presented later [31]. In recent years, the PCMO-based RS has been investigated for neuromorphic system [32, 33]. Thus, nonvolatile RS is a promising candidate for neuromorphic computing, thanks to its fast operation, low-power consumption, and multibit storage.

As a binary TMO-based TCM, the first demonstration of ReRAM was presented in Pt/NiO/Pt stack structures [34]. From then on, the performance of ReRAM cells has remarkably enhanced owing to development of fabrication process. However, TCMs were replaced with ECMs and VCMs as ReRAM trend due to mainly large required current in the mA range especially for reset, while ECM and VCM cells can be turned to switch at less than 10 μA. In fact, an ECM 16 GB ReRAM chip was proposed by Micron and Sony, and a VCM 32 GB ReRAM chip was introduced by Sandisk and Toshiba.

A basic-cell structure of ReRAM is a capacitor, where a RS material is sandwiched between a top electrode (TE) and a bottom electrode (BE). Every memory element is connected to a selector such as a transistor. Such cells in active arrays are called 1 transistor - 1 resistor cells (1T1R), in which cell area is approximately $6F^2$ (F is the lithographically defined minimum feature size). The selector should be required to avoid a sneak-path problem and an interconnect effect [35–37]. The merit of 1T1R is regulation of series resistance by selecting gate bias to suppress overcurrent at set. However, a passive array with a cross-point architecture with $4F^2$ area is preferred for further high-density integration. The selector can be a bidirectional device such as a varistor for bipolar RS, or a diode (1D1R) for unipolar RS. As a selector diode, oxide-based *pn* diode such as NiO/TiO_2 junction or Schottky diode with $Pt/TiO_2/Ti/Pt$ has been proposed [38]. Moreover, vertical-type ReRAMs sandwiched between the pillar electrodes and multilayer plane electrodes were also demonstrated [39, 40], as in three-dimensional Flash memory.

In summary, an RS phenomenon is promising for a number of applications, such as memristive devices consisting of TiO_2 [41], logic gates [42], and compact FPGA (ON/OFF switching circuits) [14]. However, ReRAM face a challenge with respect to not only cell-to-cell but also cycle-to-cycle variabilities. The large variabilities should originate from the filamentary nature of the active region in the cells and the stochasticity of the filament states on the nanoscale in filamentary RS

cells. Although the origin of filaments probably related to defects in oxides as resistance change materials [43, 44]. The detailed properties of the filaments including sizes, chemical composition, and electrical properties are still not fully clarified. In addition, the physical mechanism of RS operation has not been completely understood. Of course, the facing problem strongly depends on the type of RS cells, combination of materials, and the featured resistance ranges. Therefore, no one provides guiding principle to reduce the variation.

1.3 Outline of Thesis

A variety of oxides have been reported as a resistance change material. Most of them are metal oxides [3, 17, 45], such as NiO [46–49], TiO_2 [50–52], Ta_2O_5 [53, 54], and $Pr_{1-x}Ca_xTiO_3$ (PCMO) [33, 55]. In addition, double-layer oxides with different oxygen compositions are often adopted as a combination of an RS layer and a reservoir layer of defects [41, 53, 56]. In general, such a double-layer oxide-based ReRAM sandwiched with the same inert electrodes tends to exhibit bipolar RS, as observed in VCMs, while single-binary TMO-based ReRAM sandwiched by the same inert electrodes is a TCM. However, only bipolar RS was reported by a few groups in Pt/NiO/Pt RS cells, which should be known as a typical TCM. As a result, whether RS cells can be categorized as VCM or TCM never depends on the combination of materials.

The author's group has focused on NiO and TiO_2, well-known resistance change materials, since the beginning of RS fundamental research. How the different types of conductivity affect RS characteristics should be clarified to investigate the carrier transportation mechanism during RS. In general, NiO exhibits *p*-type conductivity because of lithium substitutions or nickel (Ni) vacancies [57]. Conversely, TiO_2 exhibits *n*-type conductivity originated from oxygen vacancies (V_Os) or even excess titanium (Ti) atoms [58].

The main adversity for this research probably refers to the RS cells without structural characterization. Almost all of real oxide samples are never single crystals containing only point defects. Grain boundaries (GBs) as planar defects in the polycrystalline oxides seem reasonable candidates for the weakest spots to create conductive filaments at forming and set processes, because GB diffusion of physical origins of the filaments can be normally dominant rather than bulk diffusion. Despite the importance of GB, many reports have not considered GBs in theoretical calculations. In addition, even the structural characterizations of experimental samples, such as crystallinity and oxygen composition in oxides, have not been given sufficiently for validation as appropriate references in most studies. Although several analyses, such as cross-sectional transmission electron microscopy (TEM) [59–61] or conductive-atomic force microscopy (C-AFM) [50, 62–64], have been conducted in several studies, the drawbacks of each analysis produce uncertainties and often hinder the direct and intrinsic characterization of the filaments.

From a practical point of view, atomic-scale filaments have been observed. When a atomic switch is used as a trigger [14], observation of quantized conductance steps has been reported in oxide-based RS cells [29, 65–71]. More details are provided in Section 5.1. Although the specific

characteristics can provide multilevel storage as the basis for analog computing and neuromorphic computing, the appearance condition of quantized conductance in each cell is not given, and hence, remains unclear. Furthermore, the author's group reported the RS operation based on quantized conductance even in TCMs through accumulated studies [72].

Moreover, RS seems to be a result of the combined effect of the electric field and Joule heat [73]. The thermally enhanced diffusion of ions or vacancies is thought to be dominant, especially in nonpolar RS, based on thermal simulations under various assumptions [74–76] and the detection of Joule heat by a temperature mapping microscope [77, 78]. However, these studies are intended for reset with large current, not reset based on quantized conductance described above.

Therefore, in this thesis, the author focuses on nonpolar RS based on quantized conductance to obtain the clue for elucidating the universal RS mechanism in binary TMO-based ReRAM cells. The importance of crystallinity and oxygen composition in resistance change materials is revealed. In addition, appearance and disappearance conditions of the original nonpolar RS characteristics are discussed. From the results involving the disappearance of conductance quantization and conductance fluctuation by heat, the author verifies whether driving force behind reset after semi-forming is Joule heating.

In Chapter 2, the deposition methods of NiO and TiO_2 layers used as the TMO and Pt electrode are outlined. The TMO layers are deposited by reactive sputtering at various oxygen (O_2) flow rate. The fabrication procedure of the TMO-based RS cells and the deposition systems are also described. In addition, dependence of deposition rate and oxygen composition in the TMO layers on O_2 flow rate during reactive sputtering is analyzed based on Berg's model.

In Chapter 3, admittance spectroscopy in Pt/NiO/*n*-silicon (Si) stack structures and electrical measurements in Pt/NiO/Pt stack structures are performed. The correlation between the oxygen composition in the NiO layer and these electrical properties is investigated. Characterization of localized trap levels and uncertainties of the technique for the NiO layers are discussed.

In Chapter 4, effects of crystallinity of the TMO layers and deposition condition on RS characteristics, especially forming characteristics, in TMO-based RS cells are discussed. The annealing contributing to oxygen diffusion toward the NiO surface causes changes of the crystalline orientation, strain, and oxygen composition in the NiO layer. In addition, crystallinity and time-dependent forming characteristics on NiO and TiO_2-based RS cells are investigated. The correlation between Weibull distributions of time to forming between the TMO-based RS cells and GB density (crystallinity) or the V_O concentration (oxygen composition) in the TMO layers is discussed. Moreover, both a possible reason for the difference of correlation between variations of initial resistance and distributions of time to forming, and where conductive filaments create in the TMO layers by forming are also discussed.

In Chapter 5, the appearance condition of conductance quantization in the Pt/NiO/Pt cells is discussed. Dependence of forming characteristics on the number of V_Os at GB triple points is investigated by TEM-energy-dispersive X-ray spectrometry (EDX) mapping. In addition, cell size dependence of forming characteristics is also revealed. In summary, an RS model based on quantized conductance is proposed.

In Chapter 6, the physical origin of conductance fluctuation accompanied by conductance quantization in the Pt/NiO/Pt cells is described. The voltage-driven conductance fluctuation before and after semi-forming is confirmed, which indicates the cell conductance being a non-integer multiple of the quantized conductance. In addition, disappearance of conductance fluctuation as well as conductance quantization by heating to the cells or Joule heating in the NiO layer is also described. From the viewpoint of voltage- and heat-driven disappearance of the conductive filament with a QPC and the modification of V_Os, driving force behind reset after semi-forming is discussed.

In Chapter 7, the summary of this thesis and the suggestions for future studies are given.

References

[1] F. Masuoka, M. Momodomi, Y. Iwata, and R. Shirota, *Tech. Dig. of IEEE Int. Electron Devices Meet.* (1987) p. 552.

[2] G. E. Moore, Electronics Magazine 19 April **38**, (1965).

[3] H. Akinaga and H. Shima, Proc. IEEE **98**, 2237 (2010).

[4] *Advances in Non-volatile Memory and Storage Technology* edited by Y. Nishi (Woodhead Publishing, 2014).

[5] ISSCC 2018 Trend `http://isscc.org/trends/`

[6] *Normally-Off Computing* edited by T. Nakada and H. Nakamura (Springer, 2018).

[7] T. Kawahara, J. Appl. Phys. **109**, 07D325 (2011).

[8] T. Ohsawa, H. Koike, S. Miura, H. Honjo, K. Tokutome, S. Ikeda, T. Hanyu, H. Ohno, and T. Endoh, *2012 Symp. on VLSI Circuits* (2012) p. 46.

[9] G. De Sandre, L. Bettini, A. Pirola, L. Marmonier, M. Pasotti, M. Borghi, P. Mattavelli, P. Zuliani, L. Scotti, G. Mastracchio, F. Bedeschi, R. Gastaldi, and R. Bez, IEEE J. Solid-State Circuits **46**, 52 (2011).

[10] Y. Sasago, M. Kinoshita, H. Minemura, Y. Anzai, M. Tai, K. Kurotsuchi, S. Morita, T. Takahashi, T. Takahama, T. Morimoto, T. Mine, A. Shima, and T. Kobayashi, *2011 Symp. on VLSI Technol.* (2011) p. 96.

[11] M. Kinoshita, Y. Sasago, H. Minemura, Y. Anzai, M. Tai, Y. Fujisaki, S. Kusaba, T. Morimoto, T. Takahama, T. Mine, A. Shima, Y. Yonamoto, and T. Kobayashi, *2012 Symp. on VLSI Technol.* (2012) p. 35.

[12] S. Tappertzhofen, S. Menzel, I. Valov, and R. Waser, Appl. Phys. Lett. **99**, 203103 (2011).

[13] M. Buckwell, L. Montesi, A. Mehonic, O. Reza, L. Garnett, M. Munde, S. Hudziak, and A. J. Kenyon, Phys. Status Solidi C **12**, 211 (2015).

[14] K. Terabe, T. Hasegawa, T. Nakayama, and M. Aono, Nature **433**, 47 (2005).

[15] Z. Xu, Y. Bando, W. Wang, X. Bai, and D. Golberg, ACS Nano **4**, 2512 (2010).

[16] S. Tappertzhofen, I. Valov, and R. Waser, Nanotechnology **23**, 145703 (2012).

[17] R. Waser, R. Dittmann, G. Staikov, and K. Szot, Adv. Mater. **21**, 2632 (2009).

[18] U. Russo, D. Ielmini, C. Cagli, and A. L. Lacaita, IEEE Trans. Electron Devices **56**, 186 (2009).

[19] D. Ielmini, R. Bruchhaus, and R. Waser, Phase Transitions **84**, 570 (2011).

[20] R. Meyer, *2014 European Materials Research Society Spring Meet.* (2014).

[21] A. Sawa, Materials Today **11**, 28 (2008).

[22] T. W. Hickmott, J. Appl. Phys. **33**, 2669 (1962).

[23] J. F. Gibbons and W. E. Beadle, Solid-State Electron. **7**, 785 (1964).

[24] K. L. Chopra, J. Appl. Phys. **36**, 184 (1965).

[25] E. Argall, Solid-State Electron. **11**, 535 (1968).

[26] T. W. Hickmott, J. Vac. Sci. Technol. **6**, 828 (1969).

[27] R. Waser and M. Aono, Nat. Mater. **6**, 83 (2007).

[28] A. Nayak, T. Tsuruoka, K. Terabe, T. Hasegawa, and M. Aono, Appl. Phys. Lett.. **98**, 233501 (2011).

[29] T. Tsuruoka, H. Hasegawa, K. Terabe, and M. Aono, Nanotechnology **23**, 435705 (2012).

[30] A. Asamitsu, Y. Tomioka, H. Kuwahara, and Y. Tokura, Nature **388**, 50 (1997).

[31] W. W. Zhuang,, W. Pan, B. D. Ulrich, J. J. Lee, L. Stecker, A. Burmaster, D. R. Evans, S. T. Hsu, M. Tajiri, A. Shimaoka, K. Inoue, T. Naka, N. Awaya, K. Sakiyama, Y. Wang, S. Q. Liu, N. J. Wu, and A. Ignatiev, *Tech. Dig. of IEEE Int. Electron Devices Meet.* (2002) p.193.

[32] J.-W. Jang, S. Park, G. W. Burr, and H. Hwang, IEEE Electron Device. Lett. **36**, 457 (2015).

[33] K. Moon, E. Cha, J. Park, S. Gi, M. Chu, K. Baek, B. Lee, S. H. Oh, and H. Hwang, IEEE Electron Device. Lett. **37**, 1067 (2016).

[34] I. G. Baek, M. S. M. J. J. S. Lee, S. Seo, D. H. H. Seo, D.-S. Suh, J. C. C. Park, S. O. O. Park, H. S. S. Kim, I. K. K. Yoo, S. Sco, U.-I. Chung, and J. T. Moon, *Tech. Dig. of IEEE Int. Electron Devices Meet.* (2004) p. 587.

[35] A. Flocke and T.G. Noll, *Proceedings of the 33rd European Solid-State Circuits Conference* (2007) p. 328.

[36] E. Linn, R. Rosezin, C. Kügeler, and R. Waser, Nature Materials **9**, 403 (2010).

[37] J. L. Liang, S. Yeh, S. S. Wong, and H. S. P. Wong, ACM J. Emerging Technol. Comput. Syst.**9**, 9 (2013).

[38] G. H. Kim, J. H. Lee, Y. Ahm, W. Jeon, S. J. Song, J. Y. Seok, J. H. Yoon, K. J. Yoon, T. J. Park, and C. S. Hwang, Adv. Funct. Mater. **23**, 1440 (2013).

[39] I. G. Baek, C. J. Park, H. Ju, D. J. Seong, H. S. Ahn, J. H. Kim, M. K. Yang, S. H. Song, E. M. Kim, S. O. Park, C. H. Park, C. W. Song, G. T. Jeong, S. Choi, H. K. Kang, and C. Chung, *Tech. Dig. of IEEE Int. Electron Devices Meet.* (2011) p. 31.8.1.

[40] S. Yu, H.-Y. Chen, B. Gao, J. Kang, and H.-S. P. Wong, ACS Nano **7**, 2320 (2013).

[41] D. B. Strukov, G. S. Snider, D. R. Stewart, and R. S. Williams, Nature **453**, 80 (2008).

[42] J. Borghetti, G. S. Snider, P. J. Kuekes, J. J. Yang, D. R. Steward, and R. S. Williams, Nature **464**, 873 (2010).

[43] D. Ielmini, F. Nardi, and C. Cagli, Appl. Phys. Lett. **96**, 053503 (2010).

[44] S. Yu, X. Guan, and H.-S. P. Wong, Appl. Phys. Lett. **99**, 063507 (2011).

[45] H.-S. P. Wong, H.-Y. Lee, S. Yu, Y.-S. Chen, Y. Wu, P.-S. Chen, B. Lee, F. T. Chen, and M.-J. Tsai, Proc. IEEE **100**, 1951 (2012).

[46] S. Seo, M. J. Lee, D. H. Seo, E. J. Jeoung, D.-S. Suh, Y. S. Joung, I. K. Yoo, I. R. Hwang, S. H. Kim, I. S. Byun, J.-S. Kim, J. S. Choi, and B. H. Park, Appl. Phys. Lett. **85**, 5655 (2004).

[47] J.-W. Park, J.-W. Park, K. Jung, M. K. Yang, and J.-K. Lee, J. Vac. Sci. Technol. B **24**, 2205 (2006).

[48] H. Shima, F. Takano, H. Akinaga, Y. Tamai, I. H. Inoue, and H. Takagi, Appl. Phys. Lett. **91**, 012901 (2007).

[49] C. Kügeler, R. Weng, H. Schroeder, R. Symanczyk, P. Majewski, K.-D. Ufert, R. Waser, and M. Kund, Thin Solid Films **518**, 2258 (2010).

[50] B. J. Choi, D. S. Jeong, S. K. Kim, C. Rohde, S. Choi, J. H. Oh, H. J. Kim, C. S. Hwang, K. Szot, R. Waser, B. Reichenberg, and S. Tiedke, J. Appl. Phys. **98**, 033715 (2005).

[51] K. Tsunoda, Y. Fukuzumi, J. R. Jameson, Z. Wang, P. B. Griffin, and Y. Nishi, Appl. Phys. Lett. **90**, 113501 (2007).

[52] W. Wang, S. Fujita, and S. S. Wong, IEEE Electron Device Lett. **30**, 763 (2009).

[53] Z. Wei, Y. Kanzawa, K. Arita, Y. Katoh, K. Kawai, S. Muraoka, S. Mitani, S. Fujii, K. Katayama, M. Iijima, T. Mikawa, T. Ninomiya, R. Miyanaga, Y. Kawashima, K. Tsuji, A. Himeno, T. Okada, R. Azuma, K. Shimakawa, H. Sugaya, T. Takagi, R. Yasuhara, K. Horiba, H. Kumigashira, and M. Oshima, *Tech. Dig. of IEEE Int. Electron Devices Meet.* (2008) p. 293.

[54] J. J. Yang, M.-X. Zhang, J. P. Strachan, F. Miao, M. D. Pickett, R. D. Kelley, G. Medeiros-Ribeiro, and R. S. Williams, Appl. Phys. Lett. **97**, 232102 (2010).

[55] S. Q. Liu, N. J. Wu, and A. Ignatiev, Appl. Phys. Lett. **76**, 2749 (2000).

[56] T. Ninomiya, S. Muraoka, Z. Wei, R. Yasuhara, K. Katayama, and T. Takagi, IEEE Electron Dev. Lett. **34**, 762 (2013).

[57] H. J. Van Daal and A. J. Bosman, Phys. Rev. **158**, 736 (1967).

[58] *Thin Film Technology, 2nd ed.* edited by S. Yoshida and T. Kondo (Maruzen, Tokyo, 2001).

[59] G.-S. Park, X.-S. Li, D.-C. Kim, R.-J. Jung, M.-J. Lee, and S. Seo, Appl. Phys. Lett. **91**, 222103 (2007).

[60] J. P. Strachan, M. D. Pickett, J. J. Yang, S. Aloni, A. L. D. Kilcoyne, G. Medeiros-Ribeiro, and R. S. Williams, Adv. Mater. **22**, 3573 (2010).

[61] F. Miao, J. P. Strachan, J. J. Yang, M. Zhang, I. Goldfarb, A. C. Torrezan, P. Eschbach, R. D. Kelley, G. Medeiros-Ribeiro, and R. S. Williams, Adv. Mater. **23**, 5633 (2011).

[62] J.-B. Yun, S. Kim, S. Seo, M.-J. Lee, D.-C. Kim, S.-E. Ahn, Y. Park, J. Kim, and H. Shin, Phys. Status Solidi (RRL) **1**, 280 (2007).

[63] D. Deleruyelle, C. Dumas, M. Carmona, C. Muller, S. Spiga, and M. Fanciulli, Appl. Phys. Express **4**, 051101 (2011).

[64] F. Nardi, D. Deleruyelle, S. Spiga, C. Muller, B. Bouteille, and D. Ielmini, J. Appl. Phys. **112**, 064310 (2012).

[65] J. R. Jameson, N. Gilbert, F. Koushan, J. Saenz, J. Wang, S. Hollmer, M. Kozicki, and N. Derhacobian, IEEE Electron Device. Lett. **33**, 257 (2012).

[66] X. Zhu, W. Su, Y. Liu, B. Hu, L. Pan, W. Lu, J. Zhang, and R.-W. Li, Adv. Mater. **24**, 3941 (2012).

[67] E. Miranda, S. Kano, C. Dou, K. Kakushima, J. Suñé, and H. Iwai, Appl. Phys. Lett. **101**, 012910 (2012).

[68] A. Mehonic, A. Vrajitoarea, S. Cueff, S. Hudziak, H. Howe, C. Labbe, R. Rizk, M. Pepper, and A. J. Kenyon, Sci. Rep. **3**, 2708 (2013).

[69] S. Long, X. Lian, C. Cagli, X. Cartoixà, R. Rurali, E. Miranda, D. Jimenez, L. Perniola, M. Liu, and J. Suñé, Appl. Phys. Lett. **102**, 183505 (2013).

[70] H. Lu, X. Xu, P. Sun, H. Liu, Q. Luo, Q. Liu, W. Banerjee, H. Sun, S. Long, L. Li, and M. Liu, Sci. Rep. **5**, 13311 (2015).

[71] S. Tappertzhofen, E. Linn, S. Menzel, A. J. Kenyon, R. Waser, and I. Valov, Nanotechnology **14**, 505 (2015).

[72] H. Sasakura, Y. Nishi, and T. Kimoto, Appl. Phys. Lett. **107**, 233510 (2015).

[73] J. J. Yang, D. B. Strukov, and D. R. Stewart, Nat. Nanotechnol. **8**, 13 (2013).

[74] D. C. Kim, S. Seo, S. E. Ahn, D.-S. Suh, M. J. Lee, B.-H. Park, I. K. Yoo, I. G. Baek, H.-J. Kim, E. K. Yim, J. E. Lee, S. O. Park, H. S. Kim, U.-I. Chung, J. T. Moon, and B. I. Ryu, Appl. Phys. Lett. **88**, 202102 (2006).

[75] U. Russo, D. Ielmini, C. Cagli, and A. L. Lacaita, IEEE Trans. Electron Devices **56**, 193 (2009).

[76] K. Kinoshita, S.-H. Koh, T. Moriyama, and S. Kishida, Sci. Rep. **5**, 18442 (2015).

[77] K. Kado, K. Sharma, H. Yamazaki, S. Urakawa, M. Uenuma, Y. Ishikawa, and Y. Uraoka, Appl. Phys. Lett. **105**, 123506 (2014).

[78] M. Uenuma, Y. Ishikawa, and Y. Uraoka, Appl. Phys. Lett. **107**, 073503 (2015).

Chapter 2

Fabrication of Resistive Switching Cells

2.1 Introduction

Resistive random access memory (ReRAM) can be described as a simple two-terminal device, such as a resistor and a diode. The description of resistive switching (RS) characteristics is quite difficult despite its simple device structure. Although an equivalent circuit model of ReRAM may be given in the strictest sense, including stray capacitance and unignorable leak paths (conductance), RS cells are assumed to be variable resistors, which depend on applied voltage and each resistance state, such as the initial state, high-resistance state (HRS), and low-resistance state (LRS). Therefore, overcurrent through the cells at the transition of resistance states is neglected in experimental cells larger than a practical RS cell size, although the overcurrent can cause serious problems [1].

As described in Chapter 1, RS cells are composed of oxides sandwiched by metal electrodes. A variety of combinations of resistance change materials and electrode materials have been proposed to exhibit an RS operation. Several studies were introduced in Chapter 1, and an endless number of examples can be given. In addition, these materials with various crystalline structures have been deposited by numerous methods. In any case, the specific combination of materials and deposition methods that are most promising is still shrouded in mystery.

In this chapter, the properties of nickel oxide (NiO) and titanium dioxide (TiO_2) used as binary transition metal oxide (TMO) layers in the present study and metal electrode are described. Moreover, their deposition methods are outlined and the deposition systems are explained, as well as the modifications the author made to accomplish specific purposes. The TMO layers are deposited by reactive sputtering using a metallic nickel (Ni) or titanium (Ti) target and oxygen (O_2) as a reactive gas together with argon (Ar), which is often used in reactive sputtering. Platinum (Pt) electrodes are deposited by electron beam (EB) evaporation or sputtering. Furthermore, dependences of deposition rate and oxygen composition in the NiO layers on O_2 flow rate during reactive sputtering are analyzed based on Berg's model [2, 3].

2.2 Metal Deposition for Electrodes

Electrode materials for RS cells affect the RS characteristics, especially a voltage bias polarity for transitions of resistance states. When an inert electrode is needed, Pt has been most frequently adopted [4–12]. However, titanium nitride (TiN) is often used [12–15], and other materials used according to each needed resistance change, including the same materials as a composed element in the oxide [16, 17]. Silver (Ag) and copper (Cu) are electrochemically active noble metal in electrolytes and used for ECMs, but they are outside the scope of this thesis.

The selection of an electrode material should take into account that electrode materials can be oxidized during NiO deposition [18]. RS characteristics may be affected by the oxidation of the electrode material. Pt is a noble metal, and it is most frequently used as electrodes for TMO-based RS cells, because stable RS characteristics have been reported in cells with Pt electrodes. The crystalline structure of Pt is a face-centered cubic (fcc) with a lattice constant of 3.923Å [19]. Pt has a high work function and is insensitive to oxygen. As a result, Pt is often adopted as an electrode material.

The author used EB evaporation or sputtering as a deposition method for bottom electrodes (BEs) and top electrodes (TEs). Although these methods are forms of physical vapor deposition that uses a metal source, the deposition mechanism is different as explained below.

In EB evaporation, a source is bombarded with an EB given off by a tungsten (W) filament, which results in atoms from the solid phase to transform into the gaseous phase. These atoms from the source are deposited on the surface of samples in the vacuum chamber. The EB deposition system (ANELVA: L-043E) that the author used enables not only EB evaporation but also resistance heating deposition. The author tried to use only EB evaporation because the melting point of Pt is relatively high. The wire-cut Pt source with a purity of 99.99% (4N) is evaporated by an EB irradiated from the W filament, which is kept out of the deposition area. The accelerating voltage and background pressure are approximately 4 kV and less than 2.0×10^{-4} Pa, respectively. Moreover, the deposition rate of Pt is kept to be under 1.0 Å/s because a larger rate causes unintentional abrasion from the silicon dioxide (SiO_2)/Si substrate. The author adopted adhesion Ti layers deposited also by EB evaporation to avoid abrasion, as discussed in Section 4.3.

In sputtering, a source is bombarded with energetic particles, particularly ionized inert gas excited by glow discharge. The incident particles that have a kinetic energy greater than that of the surface binding energy cause collision cascades and ejection of atoms or molecules from the source, finally reaching the surface of samples in the vacuum chamber. Sputtering is done using either AC or DC voltage, depending on the equipment. A radio-frequency (RF) sputtering system (EIKO: ES-250L) is described in detail in Section 2.3.2. A DC sputtering system (SANYU: SVC-700TMSG) is compact and has a "desktop" size. The purity of Pt and the Ti target with a diameter of approximately 49 cm is 99.99% (4N). The target-substrate (T-S) distance and background pressure of the chamber are 40 mm and less than 1.0×10^{-3} Pa, respectively. The Ar gas is introduced through valve regulation to keep pressure and current during depositions of the desired values.

2.3 Reactive Sputtering for Transition Metal Oxides

2.3.1 RS material

The author adopted NiO and TiO_2 as resistance change materials from the viewpoint of different types of conductivity, as described in Section 1.3. These materials are well known as promising resistance change materials because of satisfactory RS characteristics. Moreover, Ni and Ti are practically used in the back-end of complementary metal-oxide-semiconductor (CMOS) processes and possess high compatibility with conventional production lines.

NiO is an anti-ferromagnetic material [20] and a charge-transfer-type insulator [21, 22]. The crystalline structure of NiO is shown in Fig. 2.1, and it exhibits a sodium chloride (NaCl) type structure with a lattice constant of 4.177Å [19]. A number of studies on the electrical properties of NiO have been made [23–27]. The RS characteristics of NiO have been also extensively studied since its RS phenomenon was first reported in 1967 [28].

TiO_2 has been examined extensively because it has many applications, such as in photocatalysts, powder pigments, and antibacterial agents [29]. The crystalline structure of TiO_2 is shown in Fig. 2.2. Among its three main metastable polymorphs, including anatase, rutile, and brookite, the anatase type and rutile type are relatively stable. The anatase phase is stable near room temperature (RT) despite its non-equilibrium phase at RT. At temperatures more than 550°C, the anatase phase converts to the rutile phase. The temperature of this transformation tends to strongly depend on the impurities or dopants in TiO_2 [30]. As a result, rutile crystal is thermodynamically the most stable at all temperatures [31].

NiO layers have been deposited by various methods, as described in Section 3.1. In the present study, sputtering was employed for the deposition of NiO and TiO_2 layers because it is the most simple and widely-used commercial method. Moreover, a TMO layer is deposited using a metallic target and O_2 as a reactive gas together with Ar. This deposition method is known as reactive sputtering, which is defined by the reaction between atoms sputtered from a metal target and reactive gas (oxygen molecules) diffused from a discharge gas on the substrate to produce compound (oxide) layers. When the reaction occurs on the substrate, the deposited layer becomes a mixture of a metal or oxide, as determined by the deposition rate and O_2 gas pressure.

A DC reactive sputtering system is composed of a pair of planar electrodes. When a DC voltage is applied between a substrate anode and a cathode, a glow discharge occurs and generated Ar ions are accelerated toward the cathode, which results in sputtering in the cathode target and deposition of oxides on the substrate. However, in DC reactive sputtering, it is impossible to sustain the glow discharge if the target surface is covered with an insulating oxide. Nevertheless, RF reactive sputtering, in which the DC power is replaced by an RF power with a blocking capacitor and an impedance-matching circuit, enables the sputtering of an insulator.

As a result, RF reactive sputtering enables a control of the amount of O_2 process gas during sputtering [5, 32], and therefore, is suitable for the investigation of the influences of the oxygen compositions on the RS characteristics.

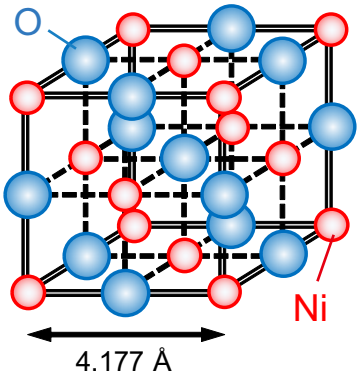

Figure 2.1: Crystalline structure of NiO.

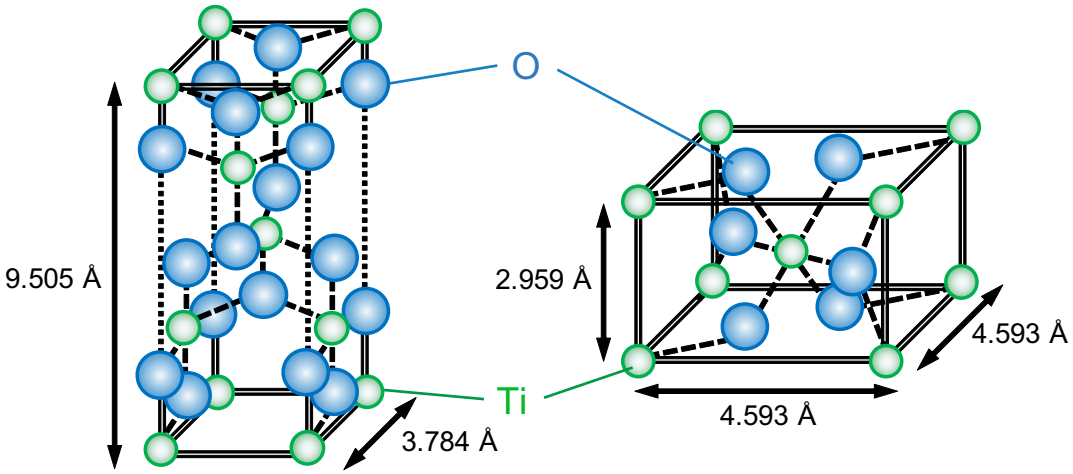

Figure 2.2: Crystalline structure of TiO_2.

2.3.2 Sputtering system

The sputtering system used for NiO deposition (ANELVA L-250-FHL) is composed of sputtering features on not only the cathode side but also on the anode side. Three planar targets (cathodes) with a diameter of 2 inches can be set on each magnet electrode on a sputtering gun opposite each anode (substrate holder). An RF power supply (frequency: 13.56 MHz) under the sputtering guns is used for glow discharge. The vacuum chambers consist of a sputtering chamber and a load-lock (LL) chamber so that sample holders can be exchanged without exposing the sputtering chamber to the air. The sputtering chamber is evacuated by a turbo molecular pump (TMP) with an auxiliary rotary pump (RP), while the LL chamber is evacuated by another RP. The background pressure of the sputtering chamber can reach 5×10^{-5} Pa without substrate heating, by which the substrate holder can be heated up to 600°C. Three kinds of gases, such as Ar, O_2, and hydrogen (H_2) can be introduced to the sputtering chamber with a flow rate controlled by three separate mass-flow controllers (MFCs). The schematic illustration of the system is given in Fig. 2.3.

During NiO deposition, a Ni target with a purity of 99.99% (4N) and a mixture of Ar and O_2 as a process gas were used. At the early stage of fabrication of NiO-based RS cells, the RS characteristics exhibit large dispersion and poor reproducibility. Therefore, the author added purifiers to the Ar and O_2 gas lines, resulting in improved reproducibility. In addition, the most effective modification of this RF sputtering system is replacement of the MFC for the O_2 gas line. For the appearance of quantum point contact (QPC), the O_2 flow rate during the deposition should be controlled within the extremely narrow window of no more than 0.04 sccm, as described in Section 5.2.1. However, the conventional maximum flow rate and resolution of the flow rate of the MFC is 30 sccm and approximately 0.1 sccm, respectively. Therefore, the author replaced the conventional MFC with new MFC with a maximum flow rate of 3.0 sccm, which means that the resolution of O_2 flow rate was 0.01 sccm.

The author designed and introduced another sputtering system (EIKO: ES-250L), as schematically shown in Fig. 2.4, to add new targets, such as Ti for TiO_2 deposition. The sputtering system includes at most five planar targets with a diameter of 60 cm. Not only a RF power supply but also a DC power supply is provided. A substrate holder can be set to manipulator (anode), including a halogen lamp for heating a substrate in diagonally opposite from a sputtering gun under the cathode. A main chamber and a LL chamber with a transfer rod (TR) are continuously evacuated by each TMP with each auxiliary scroll pump (SP). The background pressure of the main chamber can be less than 1×10^{-5} Pa. The substrate holder can be heated up to 500°C and rotated to obtain uniformly thick deposition layers over the sample holder in plane. The shutter for pre-deposition is placed under the sample holder, which enables a minimal change in the main chamber state from pre-deposition to deposition. Three kinds of gases, such as Ar, O_2, and nitrogen (N_2) can be introduced to the main chamber through each indispensable purifier with a controlled flow rate using each MFC. The sputtering system can deposit NiO by introducing a Ni target in addition to TiO_2. However, in the present study mainly TiO_2 and Pt/Ti BEs were deposited by RF sputtering in this system.

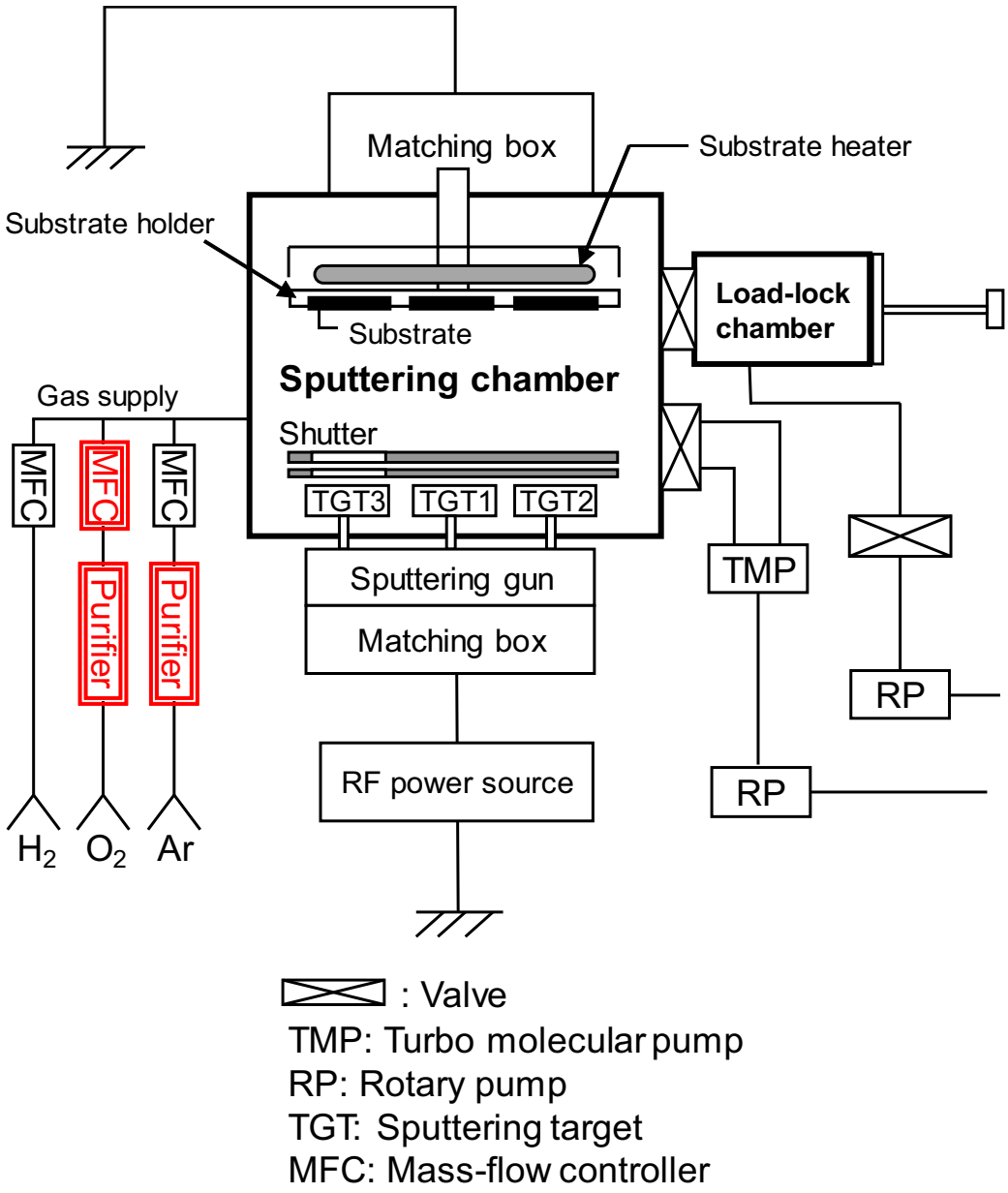

Figure 2.3: A schematic illustration of the sputtering system for NiO deposition.

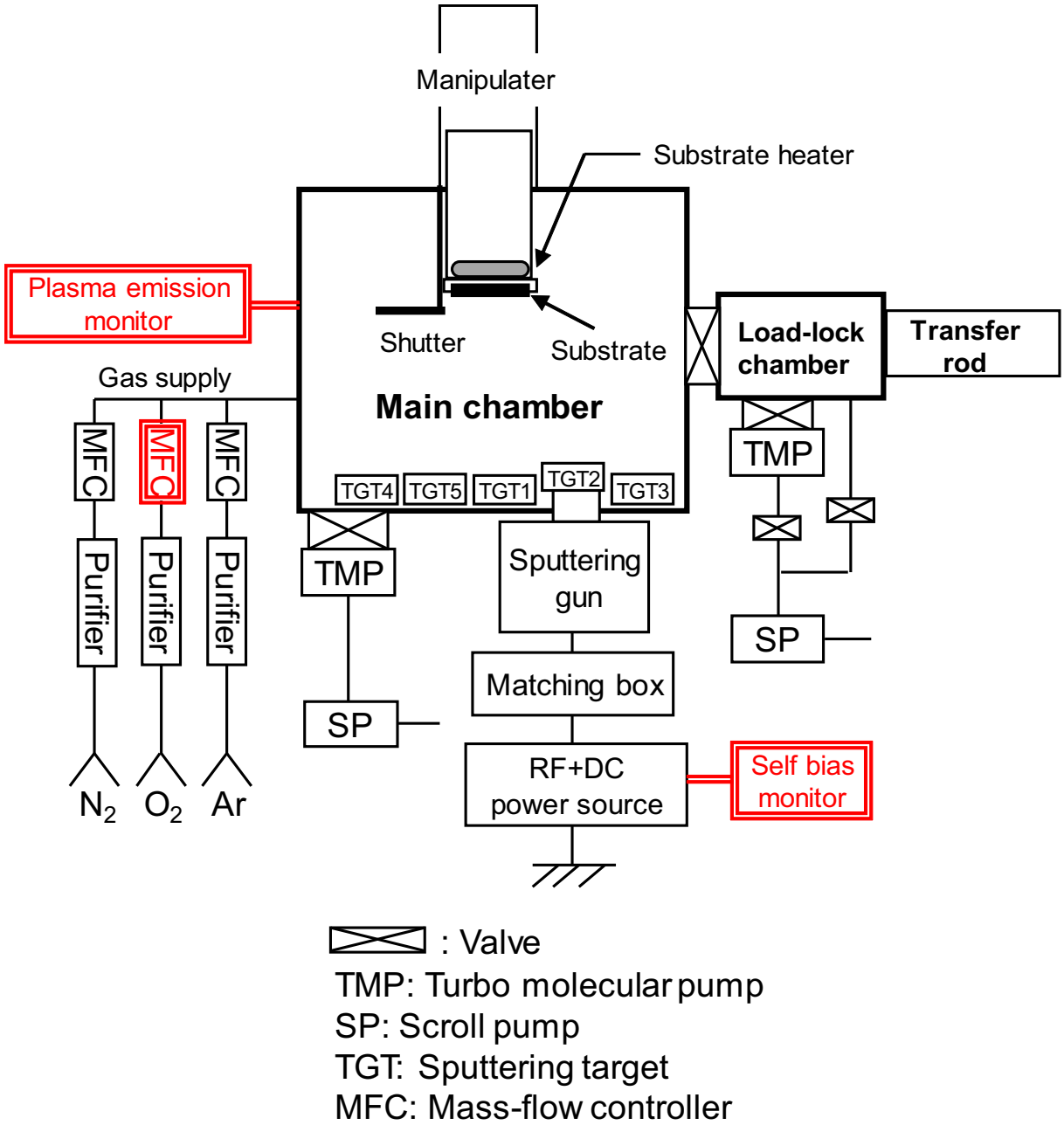

Figure 2.4: A schematic illustration of the sputtering system for TiO_2 deposition.

During TiO_2 deposition, a Ti target with the purity of 99.99% (4N) and a mixture of Ar and O_2 as a process gas were used. The author introduced a plasma emission monitor (PEM) to confirm stable plasma emissions during the pre-sputtering and sputtering. In the similar manner, a logger software can monitor the self-bias voltage during sputtering by the modification of a connector line from DC voltage measuring equipment. In addition, the author replaced the conventional MFC for O_2 with a maximum flow rate of 10 sccm, with a new MFC having a maximum flow rate of 2.0 sccm. Moreover, the author replaced a blank flange and a shutter for target changeout with two transparent windows to observe the entire target surface, which provides a way to see whether extraneous particles have fallen on the target surfaces without breaking the vacuum in the main chamber.

2.3.3 RS cell fabrication

The structure of an RS cell is composed of a TE/TMO/BE stack structure. The typical example of the cross section of the RS cell is schematically illustrated in Fig. 2.5. In this thesis, the author prepared two kinds of TE/TMO/BE RS samples. One is capacitor-type RS samples, which is easy to fabricate and a basic type throughout the study. The other is crossbar-type RS samples, which is used in Chapter 5 and Chapter 6 for obtaining smaller cell sizes than those in the capacitor-type samples. The author used Pt as BEs and TEs as described in Section 2.2.

Capacitor-type Pt/TMO/Pt RS samples were fabricated as follows. A Pt BE was deposited by RF or DC sputtering on a SiO_2/*p*-Si(100) substrate. A TMO layer as a resistance change material was subsequently deposited in Ar and O_2 gas mixture by using reactive RF sputtering. The details of the parameters for TMO deposition are explained in every chapter. Pt TEs with a diameter of 50−500 μm were deposited on the TMO layer by EB evaporation through a metal shadow mask. However, the diameter of less than 100 μm has low precision because of processing dimension of the metal mask with a thickness of 100 μm. The Pt/TMO/Pt RS cell size is determined by the area of the Pt TE. An optical microscopy image of a capacitor-type sample is given in Fig. 2.6, where a number of Pt TEs with different diameters are formed all over a TMO layer. The inner squared region with round corners is a TMO layer. A Pt BE is on the entire area of the substrate, and is exposed to the air near the edges of the sample.

Crossbar-type Pt/TMO/Pt RS samples were fabricated as follows. The Pt/TMO/Pt RS cells were directly sandwiched between bar-shape top and bottom electrodes with pad regions selectively formed by ultra-violet (UV) photolithography. The details of the parameters for Pt BEs and a TMO layer are explained in every chapter. Pt TEs were deposited on the TMO layer by RF or DC sputtering. The TEs of cells were separated from each other to avoid a sneak-path problem [33, 34]. The cell size is equivalent to the cross-point area between both electrodes, which falls in the range from 4×4 μm^2 to 88×88 μm^2. In addition, several tens of RS cells with a structure of the capacitor-type cells are fabricated on planar-BE areas. An optical microscopy image of a crossbar-type sample is shown in Fig. 2.7. The bar-shape BEs have two pad regions on the left and right outside the NiO region to contact BE in all cells.

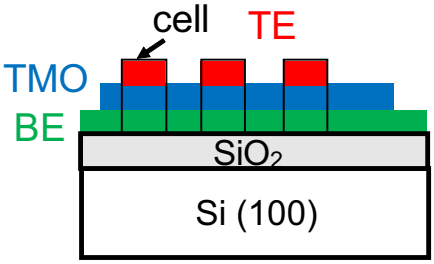

Figure 2.5: A schematic illustration of the cross section of a sample.

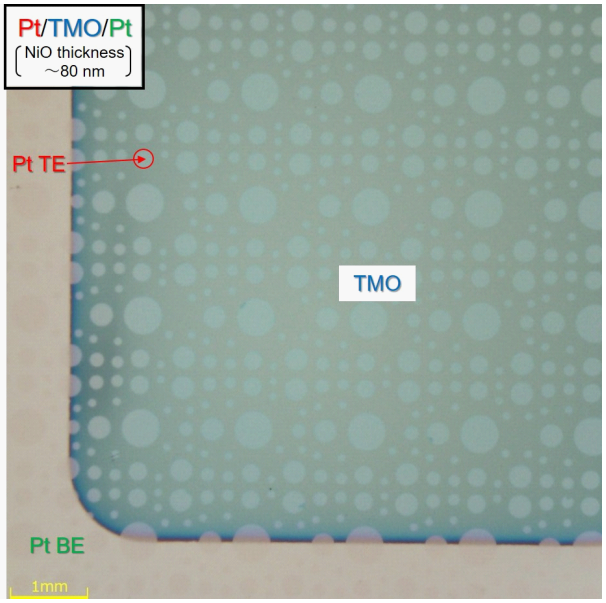

Figure 2.6: An optical microscopy image of a capacitor-type sample.

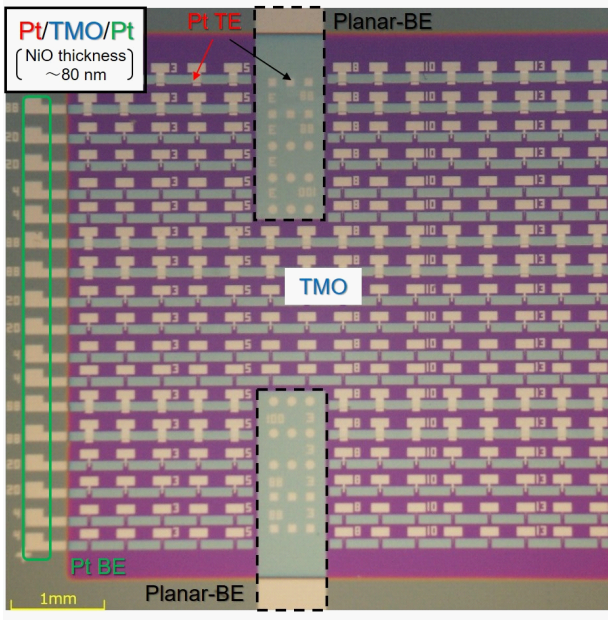

Figure 2.7: An optical microscopy image of a crossbar-type sample.

2.3.4 Theory of reactive sputtering

In this subsection, the O_2-flow-rate dependences of deposition rate and oxygen composition in the NiO layers during reactive sputtering were analyzed based on Berg's model [2, 3]. The details of the model are described in Appendix A.

The author determined the parameter required for the calculation according to Berg's model based on the O_2-flow-rate dependence of the experimental O_2 partial pressure. The deposition condition of the NiO layer is for the appearance of QPC, as described in Section 5.2.1. The dependence exhibits a hysteresis in the O_2-flow-rate range of 1.0−1.3 sccm, as shown in Fig. 2.8(a), which is a typical characteristic of reactive sputtering. The sputtering modes in region below 1.0 sccm and that above 1.3 sccm are called a metallic mode and an oxide mode, respectively. The values of the parameters are shown in Table 2.1. By using these parameters, the O_2-flow-rate dependences of the deposition rate and oxygen composition x in NiO_x are calculated as shown in Fig. 2.8(b) and (c). Although the gaps between the experimental and calculated values are relatively large for the deposition rate in an oxide mode and for the oxygen composition in a metallic mode, the experimental values almost agree with the theory.

For the appearance of QPC, the O_2 flow rate during the deposition should be controlled within the extremely narrow window of no more than 0.04 sccm. One of the window is 0.94−0.98 sccm, as described in Section 5.2.1. Nevertheless, these values should be tuned depending on changes in deposition parameters, such as the erosion depth (equivalent to effective target size A_t) of the metallic Ni target. In fact, the O_2 flow rate for the appearance of QPC was 1.1 sccm in the previous study of the author's group [35]. Therefore, the deposition condition for the appearance of QPC is very difficult to control.

Since the effective target size A_t can not be measured, how to search for the best value of O_2 flow rate for the appearance of QPC is to vary an RF power every 1 W. It seems not to be the best approach to vary O_2 flow rate by a potentiometer, because the resolution of 0.01 sccm is large to control yet. Figure 2.9 exhibits the calculated dependences with different RF powers. The various RF powers can correspond to the difference of the ion current density J. The correlation between J and the RF power turned out to be 0.072 A/cm^2 for 90 W, 0.076 A/cm^2 for 100 W, and 0.081 A/cm^2 for 110 W, respectively, through many experiments during the specific period. The deposition rate and oxygen composition in a NiO layer are very sensitive to the RF power in the O_2-flow-rate range of 0.9−1.1 sccm. Moreover, another parameter with a relatively large unintentional variation is the collector size A_c, which corresponds to effective sputtered area including a substrate, not the actual surface area inside the chamber. The effective area A_c may change due to a memory effect (previous deposition conditions) and discontinuation of the chamber evacuation. As a result, the difference between 0.96 sccm and 1.1 sccm as the best value for the appearance of QPC can be within the expected range, as discussed in Section 5.4.3.

In contrast, the deposition condition in an oxide mode can be more stable, such as TiO_2 deposition. From the viewpoint of reproducibility, the deposition in an oxide mode should be desirable.

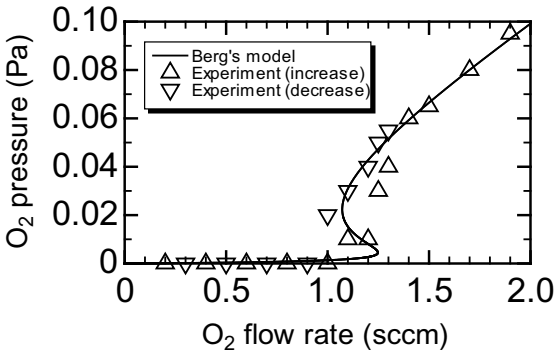

(a) O_2 partial pressure

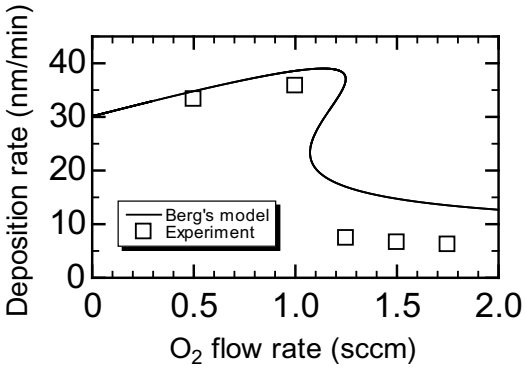

(b) deposition rate

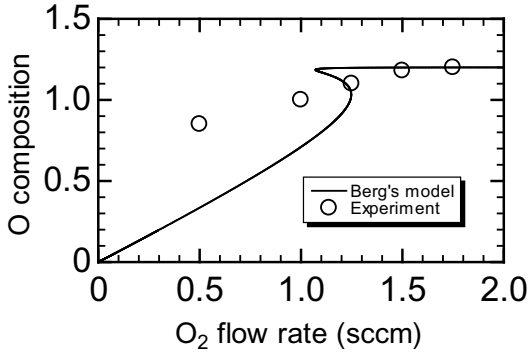

(c) oxygen composition x in NiO_x

Figure 2.8: O_2-flow-rate dependences of (a) O_2 partial pressure, (b) deposition rate, and (c) oxygen composition x in NiO_x by experiments and calculation according to Berg's model.

Table 2.1: Values of parameters used in a calculation according to Berg's model.

target size A_t	4.7 cm^2
collector size A_c	320 cm^2
sticking coefficient for target α_t	0.8
sticking coefficient for collector α_c	0.8
sputtering yield of compound Y_c	0.1
sputtering yield of metal Y_m	0.65
exhausting speed S	0.03 m^3/s
ion current density J	0.076 A/cm^2

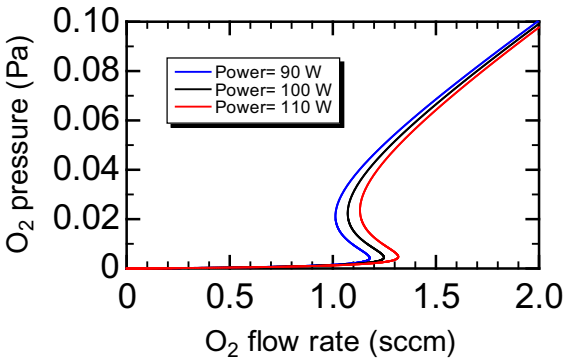

(a) O_2 partial pressure

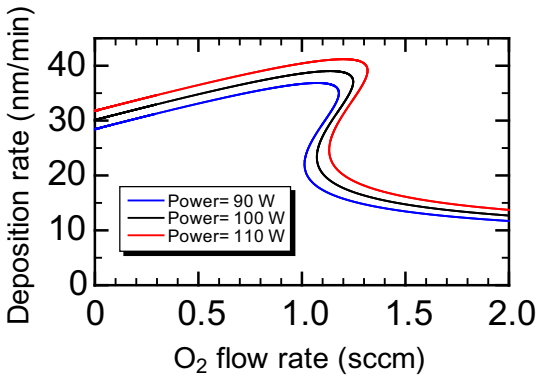

(b) deposition rate

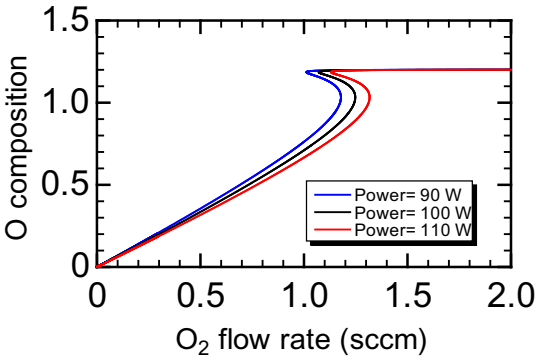

(c) oxygen composition x in NiO_x

Figure 2.9: The calculated O_2-flow-rate dependences with different RF powers of (a) O_2 partial pressure, (b) deposition rate, and (c) oxygen composition x in NiO_x.

2.4 Summary

The properties of NiO and TiO_2 as binary transition metal oxide (TMO) layers in the present study and a Pt metal electrode were described. The TMO layers were deposited by reactive sputtering by using a metallic Ni or Ti target and an O_2 as a reactive gas together with Ar. In contrast, Pt electrodes were deposited by EB evaporation or sputtering. Moreover, the outline of deposition methods of them and the deposition systems were explained, as well as the modifications the author performed for improvements of reproducibility of the RS cells and controllability of O_2 flow rate. Furthermore, dependences of deposition rate and oxygen composition in the NiO layers on O_2 flow rate during reactive sputtering were analyzed based on Berg's model.

References

[1] K. Kinoshita, K. Tsunoda, Y. Sato, H. Noshiro, S. Yagaki, M. Aoki, and Y. Sugiyama, Appl. Phys. Lett. **93**, 033506 (2008).

[2] S. Berg, J. Vac. Sci. Technol. A **5**, 202 (1987).

[3] S. Berg and T. Nyberg, Thin Solid Films **476**, 215 (2005).

[4] S. Seo, M. J. Lee, D. H. Seo, E. J. Jeoung, D.-S. Suh, Y. S. Joung, I. K. Yoo, I. R. Hwang, S. H. Kim, I. S. Byun, J.-S. Kim, J. S. Choi, and B. H. Park, Appl. Phys. Lett. **85**, 5655 (2004).

[5] J.-W. Park, J.-W. Park, K. Jung, M. K. Yang, and J.-K. Lee, J. Vac. Sci. Technol. B **24**, 2205 (2006).

[6] K. Tsunoda, K. Kinoshita, Y. Yamazaki, T. Izuka, Y. Ito, A. Takahashi, A. Okano, Y. Sato, T. Fukano, M. Aoki, and Y. Sugiyama, *Tech. Dig. of IEEE Int. Electron Devices Meet.* (2007) p. 767.

[7] B. J. Choi, D. S. Jeong, S. K. Kim, C. Rohde, S. Choi, J. H. Oh, H. J. Kim, C. S. Hwang, K. Szot, R. Waser, B. Reichenberg, and S. Tiedke, J. Appl. Phys. **98**, 033715 (2005).

[8] H. Shima, F. Takano, H. Akinaga, Y. Tamai, I. H. Inoue, and H. Takagi, Appl. Phys. Lett. **91**, 012901 (2007).

[9] U. Russo, D. Ielmini, C. Cagli, and A. L. Lacaita, IEEE Trans. Electron Devices **56**, 186 (2009).

[10] H. D. Lee and Y. Nishi, Appl. Phys. Lett. **97**, 252107 (2010).

[11] W. Wang, S. Fujita, and S. S. Wong, IEEE Electron Device Lett. **30**, 763 (2009).

[12] L. Goux, X. P. Wang, Y. Y. Chen, L. Pantisano, N. Jossart, B. Govoreanu, J. A. Kittl, M. Jurczak, L. Altimime, and D. J. Wouters, Electrochem. Solid-State Lett. **14**, H244 (2011).

[13] G. Bersuker, D. C. Gilmer, D. Veksler, P. Kirsch, L. Vandelli, A. Padovani, L. Larcher, K. McKenna, A. Shluger, V. Iglesias, M. Porti, and M. Nafria, J. Appl. Phys. **110**, 124518 (2011).

[14] C. Walczyk, D. Walczyk, T. Schroeder, T. Bertaud, M. Sowinska, M. Lukosius, M. Fraschke, D. Wolansky, B. Tillack, E. Miranda, and C. Wenger, IEEE Trans. Electron Devices **58**, 3124 (2011).

[15] S. Yu, X. Guan, and H.-S. P. Wong, Appl. Phys. Lett. **99**, 063507 (2011).

[16] L. Goux, J. G. Lisoni, X. P. Wang, M. Jurczak, and D. J. Wouters, IEEE Trans. Electron Devices **56**, 2363 (2009).

[17] C. Kügeler, R. Weng, H. Schroeder, R. Symanczyk, P. Majewski, K.-D. Ufert, R. Waser, and M. Kund, Thin Solid Films **518**, 2258 (2010).

[18] H. Shima, F. Takano, H. Muramatsu, H. Akinaga, Y. Tamai, I. H. Inque, and H. Takagi, Appl. Phys. Lett. **93**, 113504 (2008).

[19] I. Wakabayashi, H. Kobayashi, H. Nagasaki, and S. Minomura, J. Phys. Soc. Jpn. **25**, 227 (1968).

[20] G. A. Slack, J. Appl. Phys. **31**, 1571 (1960).

[21] G. A. Sawatzky and J. W. Allen, Phys. Rev. Lett. **53**, 2339 (1984).

[22] J. Zaanen, G. A. Sawatzky, and J. W. Allen, Phys. Rev. Lett. **55**, 418 (1985).

[23] S. Koide, J. Phys. Soc. Jpn. **20**, 123 (1965).

[24] A. J. Springthorpe, I. G. Austin, and B. A. Austin, Solid State Commun. **3**, 143 (1965).

[25] H. J. Van Daal and A. J. Bosman, Phys. Rev. **158**, 736 (1967).

[26] I. G. Austin, A. J. Springthorpe, B. A. Smith, and C. E. Tuner, Proc. Phys. Soc. **90**, 157 (1967).

[27] A. J. Bosman and C. Crevecoeur, Phys. Rev. **144**, 763 (1966).

[28] J. F. Gibbons and W. E. Beadle, Solid-State Electron. **7**, 785 (1964).

[29] A. Fujishima and K. Honda, Nature **238**, 37 (1972).

[30] D. A. H. Hanaor and C. C. Sorell, J. Mater. Sci. **46**, 855 (2011).

[31] D. A. H. Hanaor, W. Xu, M. Ferry, and C. C. Sorell, J. Cryst. Growth **359**, 83 (2012).

[32] I. Hotový, D. Búc, Š. Haščík, and O. Nennewitz, Vacuum **50**, 41 (1998).

[33] A. Flocke and T.G. Noll, *Proceedings of the 33rd European Solid-State Circuits Conference* (2007) p. 328.

[34] E. Linn, R. Rosezin, C. Kügeler, and R. Waser, Nature Materials **9**, 403 (2010).

[35] T. Iwata, Dr. Thesis, Faculty of Engineering, Kyoto University, Kyoto, 2014.

Chapter 3

Characterization of Defects in NiO Layers

3.1 Introduction

Nickel oxide (NiO)-based resistive random access memory (ReRAM) cells have been reported to exhibit a resistive switching (RS) phenomenon. Various NiO deposition methods are adopted, such as not only reactive sputtering using oxygen (O_2) and a metallic nickel (Ni) target [1–5], but also sputtering using a NiO target, electron beam (EB) evaporation [6], thermal oxidation [7, 8], pulsed-laser deposition [9], and atomic-layer deposition [10]. However, the common factor among these methods is that only NiO is used as a resistance change material, and the physical origins of the RS behavior in the NiO layer have not been clarified.

In the case of single crystalline NiO, most defects under thermal equilibrium are Ni vacancies (V_{Ni}s) that act as acceptors, which leads to *p*-type conduction [11–14]. However, the crystalline structure of NiO layers deposited by various methods is not actually a single crystal. Moreover, a non-stoichiometric oxide includes defects, such as oxygen vacancies (V_Os) in the matrix. Normally, point defects (vacancies or interstitials) in ideal oxide matrix act as dopants, which transforms the material from an insulator to semiconductor [11]. Furthermore, the degree of non-stoichiometry of NiO layers was rarely determined, and macroscopic oxygen compositions in resistance change material were not investigated in most studies on RS characteristics. Therefore, characterization of defects in NiO with various oxygen compositions is one of the reasonable approaches to elucidate the physical origins and the mechanism of an RS operation.

In this chapter, admittance spectroscopy measurements are performed on NiO layers with various oxygen compositions deposited on *n*-silicon (Si) substrates. The oxygen composition x in NiO_x was intentionally changed over the wide range of approximately 1.0 to 1.2, as confirmed by Rutherford backscattering spectrometry (RBS). Current-voltage (I–V) measurements of platinum (Pt)/NiO_x/Pt structures on *p*-Si substrates are also conducted. The correlation between the oxygen composition and these electrical properties is discussed.

3.2 Sample Fabrication

3.2.1 Device structure

To characterize defect levels in a semiconductor material by admittance spectroscopy, a depletion region in the material is required. The author assumes a Schottky barrier junction between a metal and a *p*-type material with a single hole trap level shown in Fig. 3.1. A diffusion potential and a reverse bias is V_d and V_r, respectively. The deep trap level E_t crosses the Fermi level E_f at point x_t less than depletion width w, while the level of shallow acceptor does not cross it. Within the depletion region, the positive and negative charge increments for a change in bias are spatially separated.

As described above, NiO is normally considered as a metal deficient oxide, and thus, a *p*-type semiconductor [14]. However, the ideal Schottky barrier junction was difficult to obtain in spite of utilizing many electrodes as a metal with low work function. One of the reasons seems poor crystallinity of bottom electrode (BE), which may lead to an insufficient clear interface for the characterization of defects near the interface. Therefore, the author prepared highly-doped *n*-type Si substrates (approximately $2 \times 10^{19}\mathrm{cm}^{-3}$) instead of metallic BE on substrates. The admittance of a *pn* junction is determined by the changes of the total charge in the junction bias [15]. When an acceptor concentration N_a in the *p*-type NiO is smaller than a donor concentration N_d in the *n*-Si, a space charge region assumingly exists only in the NiO side, as shown in Fig. 3.2, and the *n*-Si can be regarded as a metal for a Schottky barrier junction. A reverse bias V_r is zero, and bandgaps of NiO and Si are approximately 4 eV and 1.1 eV at room temperature (RT), respectively. As a result, the author attempted to perform the characterization of defect levels in the NiO layers using the *p*-NiO/*n*-Si heterojunction.

The stack structure for admittance spectroscopy is Pt/NiO/*n*-Si/aluminum (Al), as shown in Fig. 3.3. After the chemical treatment of the *n*-Si substrate, NiO layers were deposited on the substrates by using reactive radio-frequency (RF) sputtering system (ANELVA: L-250-FHL). The purity of a Ni target was 99.99% (4N). The proportion of O_2 in the argon (Ar) + O_2 gas mixture was varied in the range from 3% to 10% to change the oxygen composition in NiO (hereinafter, referred to as NiO_x). The total pressure, substrate temperature (T_{sub}) and RF power during sputtering were kept at 1.0 Pa, 300°C and 100 W, respectively. The thickness of NiO_x layers was 200 to 300 nm. The cross-sectional high-resolution transmission electron microscopy (HRTEM) showed the deposited NiO_x layers to be a mixture of both polycrystalline regions with grain sizes of less than 50 nm and amorphous regions. The oxygen composition x of NiO_x films was determined as 1.0 to 1.2 by RBS and energy-dispersive X-ray spectrometry (EDX). Pt electrodes with a diameter of 300 μm were deposited by using an EB-evaporation system (ANELVA: L-043E) through a shadow mask. Finally, Al layers was deposited on a backside of the *n*-Si substrates for obtaining an ohmic contact.

The device structure for RS cell is composed of a typical Pt/NiO_x/Pt stack. Pt was deposited as a BE on the entire area of a *p*-Si substrate by EB evaporation. The thickness of BEs was

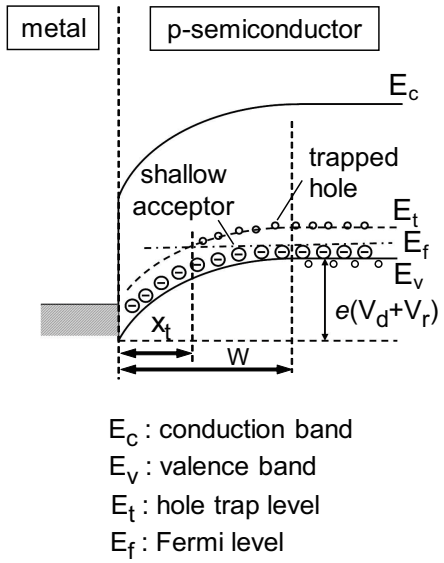

Figure 3.1: The band diagram of a reverse biased Schottky barrier junction between a metal and a *p*-type semiconductor with a single hole trap level.

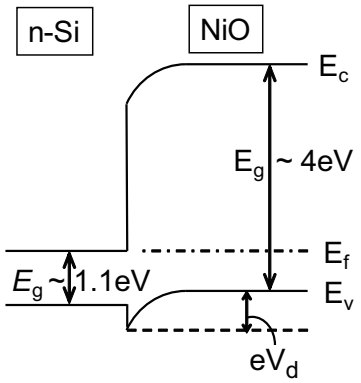

Figure 3.2: The band diagram of *pn* junction between *p*-type NiO and *n*-type Si.

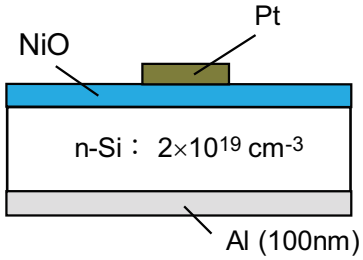

Figure 3.3: A Pt/NiO/*n*-Si/Al stack structure for admittance spectroscopy.

approximately 100 nm. Over 100 nm-thick NiO_x layer was deposited by the method described above. Approximately 100 nm-thick Pt top electrodes (TEs) was deposited by EB evaporation. The diameter of TEs was 200, 300, and 500 μm.

3.2.2 Admittance spectroscopy

Admittance spectroscopy is useful for characterization of localized defect levels in semiconductor bulk or films [16]. Although several defect levels in the materials and their effects on the admittance should be taken into account [17], only a single deep levels in a *p*-type semiconductor is assumed in this subsection.

Admittance spectroscopy can be explained as follows. Admittance Y is divided into conductance component G and capacitance component $j\omega C$;

$$\frac{G}{\omega} = \frac{\omega\tau}{1+(\omega\tau)^2}\Delta C, \tag{3.1}$$

$$C = C_{\mathrm{HF}} + \frac{1}{1+(\omega\tau)^2}\Delta C. \tag{3.2}$$

Here, ω and τ represent angular frequency of a small AC bias and emission time constant of hole, respectively. Figure 3.4 shows ideal frequency dependence of these parameters in the films with a single carrier trap level. C_{HF} and $C_{\mathrm{LF}} = C_{\mathrm{HF}} + \Delta C$ are the high and low frequency limits of the capacitance, respectively. C_{HF} reflects the change of the charge due to shallow acceptor, while C_{LF} reflects that due to shallow acceptor and hole trap because hole emission/capture from/to the trap can occur only at much lower frequency than $1/\tau$ near the point x_{t} in Fig. 3.1.

τ can be estimated from the peak position of G/ω curve because the maximum of G/ω equals with $\Delta C/2$ at $\omega = 1/\tau$ in Eq. (3.1). The temperature dependence of τ is given by

$$\tau = \frac{1}{N_{\mathrm{v}}\langle v_{\mathrm{th}}\rangle\sigma_{\mathrm{p}}}\exp\left(\frac{E_{\mathrm{t}}-E_{\mathrm{v}}}{k_{\mathrm{B}}T}\right). \tag{3.3}$$

Here, N_{v} is the effective density of states in the valence band, $\langle v_{\mathrm{th}}\rangle$ the mean thermal velocity of holes, σ_{p} the hole capture cross section; k_{B} and T are the Boltzmann constant and the absolute temperature, respectively. When N_{v} and $\langle v_{\mathrm{th}}\rangle$ are assumed to be proportional to $T^{3/2}$ and $T^{1/2}$, respectively, the activation energy of the hole trap $E_{\mathrm{t}} - E_{\mathrm{v}}$ can be estimated from the Arrhenius plot of $\log(\tau T^2)$.

3.2.3 Experimental procedure

Admittance spectroscopy involves both frequency and temperature dependence of conductance G and capacitance C. There are two methods to obtain the dependence. One is the plot of parameters (G and C) as a function of temperature at several frequencies [18], the other is the plot as a function of frequency at several temperatures [19]. In this study, the author adopted the latter method because temperature response and stability of the samples during measurements seem to be insufficient by using prober system below.

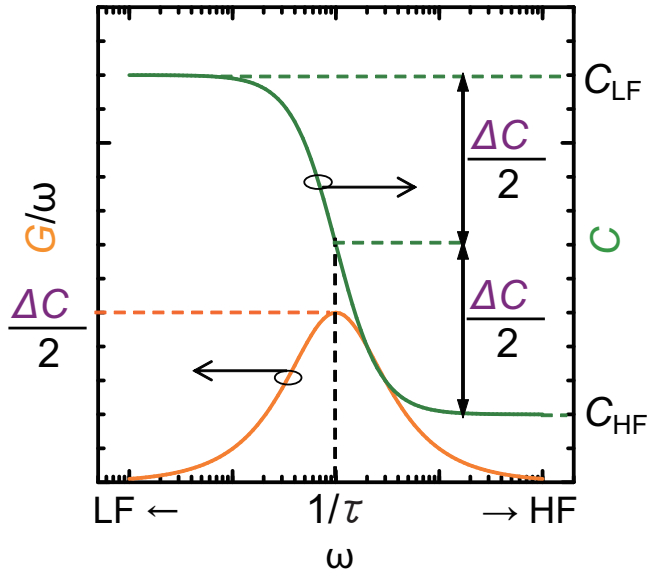

Figure 3.4: Ideal angular frequency dependence of G/ω and C.

The measurements were carried out by using prober system (Nagase Sangyo: BCT-20MDCHT). Frequency dependence of G and C was measured using a Yokogawa Hewlett Packard 4192A LF impedance analyzer. Several times of frequency sweep were required in every frequency range because the frequency step should be linear (impossible to sweep by the logarithmic step) in the analyzer. The author tried to check G and C measured at zero bias of ceramic capacitors, capacitance values of which are 1.0 nF and 0.22 nF. Figure 3.5 shows the plots of $(G - G_{\mathrm{dc}})/\omega$ and C of the ceramic capacitors as a pre-measurement. Here, G_{dc} is the DC component of the conductance of the investigated samples, which can be approximated to be the conductance at 10 Hz (the minimum frequency of the impedance analyzer). In the range of sub nF, $(G - G_{\mathrm{dc}})/\omega$ and C increase abruptly over 3 MHz. The increase originates from LC resonance because C transfers from positive to negative values at the point of resonance frequency ($= 1/2\pi\sqrt{LC}$). From the LC resonance frequency, parasitic inductance L of the electric line in the prober system can be estimated to be approximately 0.8 μH. The temperature range for the measurements was from 150 K to 400 K in vacuum (< 1 mTorr).

I–V measurement of Pt/NiO_x/Pt structures on p-Si substrates were also conducted using a Keithley 4200-SCS semiconductor parameter analyzer. During I–V and RS measurement, the bottom electrode was grounded and the bias voltage was applied to the top electrode. The temperature dependence of I–V characteristics was carried out in the temperature range from 300 K to 550 K.

3.3 Defect Levels in NiO Layers and Resistive Switching Characteristics

3.3.1 *p*-NiO/*n*-Si heterojunction

The author prepared not only Pt/NiO_x/n-Si/Al stack cells but a Pt/n-Si/Al cell to check the intentionally correct operation of the p-NiO/n-Si heterojunction. Figure 3.6 shows the plots of $(G - G_{\mathrm{dc}})/\omega$ and C measured at zero bias and at RT of both cells, the oxygen composition x in the NiO_x is 1.07. $(G - G_{\mathrm{dc}})/\omega$ of Pt/$NiO_{1.07}$/n-Si/Al has a single peak, while $(G - G_{\mathrm{dc}})/\omega$ of Pt/n-Si/Al has no peak. Moreover, capacitance-voltage (C–V) characteristics of Pt/NiO_x/Pt RS cells indicate almost constant capacitance values irrespective of applied voltage less than forming voltage. Therefore, Pt/NiO_x junction can be regarded as ohmic instead of at least Schottky-like. As a result, origin of the peaks in various NiO_x layers is confirmed to be NiO_x/n-Si heterojunction.

The author performed the C–V measurement of a typical NiO_x/n-Si heterojunction at RT. Figure 3.7 shows the result of the cell with oxygen composition x in NiO_x of 1.07. The diffusion potential V_{d} and the net acceptor concentration N_{s} of NiO_x layers were confirmed to be approximately 0.8 eV and in the 10^{18} cm^{-3} range, respectively. The depletion layer width of the heterojunction was about 10 nm at zero bias, which is much thinner than the thickness of NiO_x layers within x of 1.0−1.2. Furthermore, I–V measurements of the heterojunction were

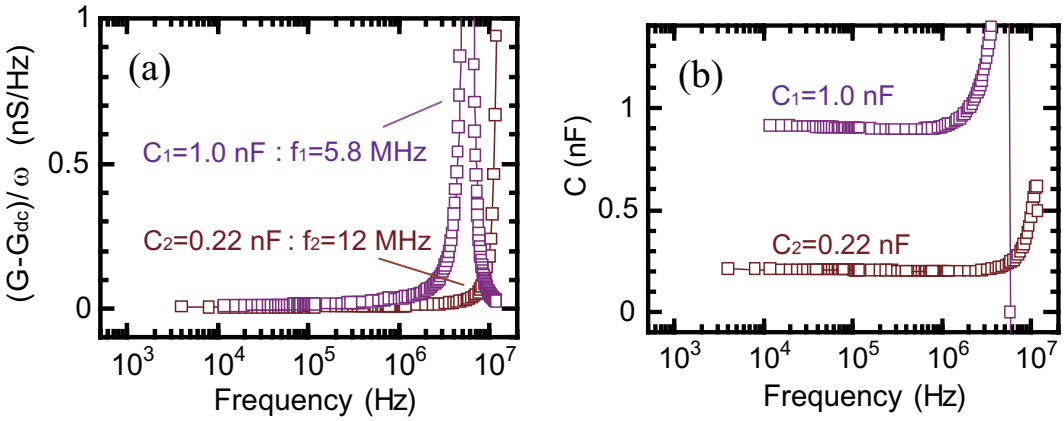

Figure 3.5: Frequency dependence of $(G - G_{dc})/\omega$ and C of ceramic capacitors with $C_1 = 1.0$ nF and $C_2 = 0.22$ nF. LC resonance frequencies are $f_1 = 5.8$ MHz and $f_2 = 12$ MHz, respectively.

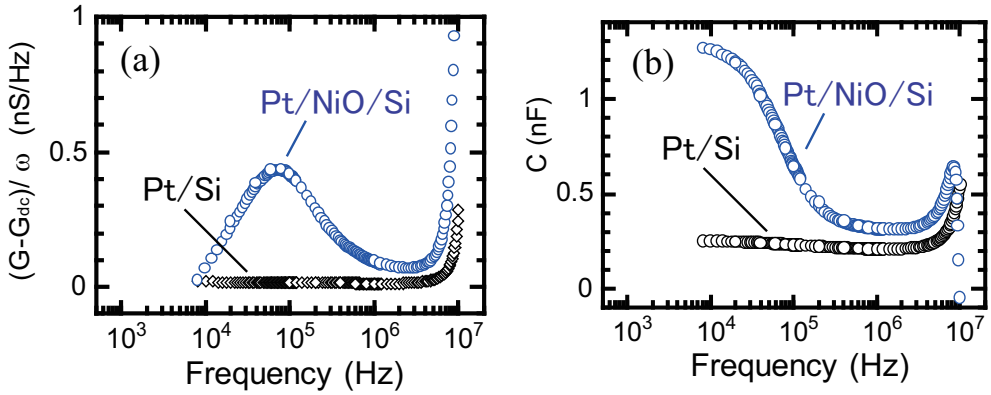

Figure 3.6: Frequency dependence of $(G - G_{dc})/\omega$ and C for Pt/n-Si and Pt/$NiO_{1.07}$/n-Si stack structures.

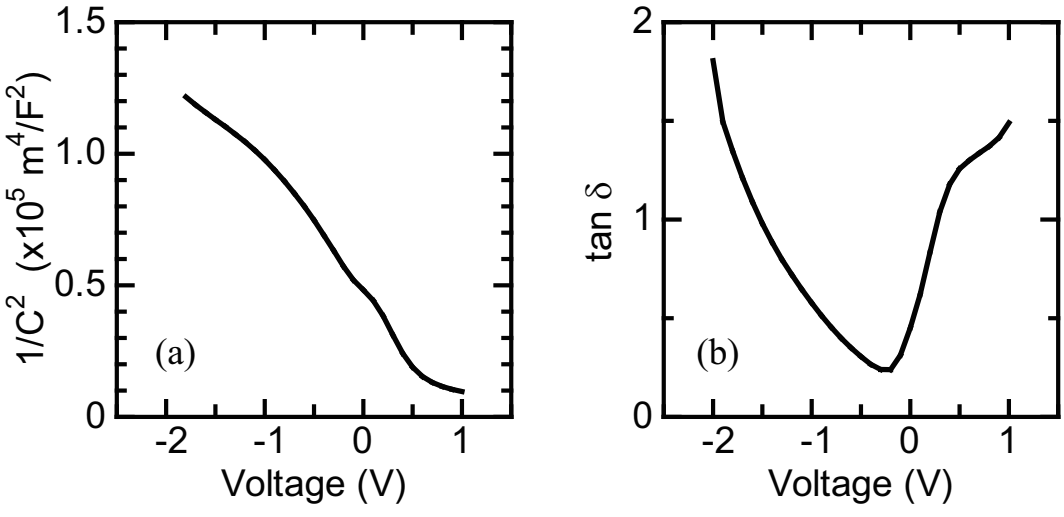

Figure 3.7: Voltage dependence of (a) $1/C^2$ and (b) $\tan\delta$ in $NiO_{1.07}$/n-Si heterojunction.

also performed. Figure 3.8 shows I–V characteristics of a Pt/$NiO_{1.07}$/n-Si/Al stack. Although leak current and $\tan\delta$ in Fig. 3.7(b) at reverse bias (especially over 1 V) are relatively larger, the heterojunctions were confirmed to show good rectification at the voltage range of −1 to 0.2 V. Therefore, the author selected zero DC bias during admittance measurements below.

3.3.2 Dependence of defect levels on oxygen composition in NiO layers

Figure 3.9 shows the plots of $(G - G_{dc})/\omega$ and C measured at zero DC bias for three p-NiO_x/n-Si heterojunctions as a function of frequency at different temperature. As described in Section 3.2.3, the sharp rise of $(G - G_{dc})/\omega$ at more than 3 MHz was confirmed to originate from the resonance caused by the measured capacitance and parasitic inductance (approximately 0.8 μH) of the measurement system. The result reveals that the NiO_x layer has a single defect level, of which emission time constant decreases with elevated temperature.

Figure 3.10 shows the plots of $(G - G_{dc})/\omega$ and C measured at RT for the NiO_x/n-Si heterojunctions with various oxygen composition x as a function of frequency. The localized levels in NiO_x layers strongly depend on the oxygen composition. For the NiO_x layers with low oxygen compositions ($x \leqq 1.07$), only a single peak is observed in the $(G - G_{dc})/\omega$ curve, whereas two peaks (or one peak and a shoulder) exist for the NiO_x films with higher oxygen composition ($x \geqq 1.15$). For the layers with high oxygen compositions, the capacitance values exhibit a steady rise toward the low-frequency region, indicating an additional defect level. All of the peak frequencies decrease with elevated temperature. Moreover, the emission time constant at RT (τ_{RT}) increase with an increase in oxygen composition in the NiO_x layer. τ_{RT} is 1.8 μs for $NiO_{1.05}$, and 8.8 μs for $NiO_{1.15}$. Note that the emission time constant which originates from the additional defect level is much smaller (0.24 μs) for the $NiO_{1.15}$.

The energy levels of observed defects located above the valence band edge (equivalent to $E_t - E_v$) in each NiO_x layer are obtained from the Arrhenius plots of $\log(\tau T^2)$, as described in Section 3.2.2. Figure 3.11 shows the Arrhenius plots of $\log(\tau T^2)$ in various NiO_x/n-Si heterojunctions. The value of $E_t - E_v$ in NiO_x layers with low oxygen compositions ($x \leqq 1.07$) is relatively large, 120−170 meV, while that in layers with higher oxygen compositions ($x \geqq 1.10$) is smaller than 100 meV.

3.3.3 Dependence of RS characteristics on oxygen composition in NiO layers

The author investigated RS characteristics of the Pt/NiO_x/Pt stack cells with a TE-diameter of 300 μm at RT. Values of resistance, such as resistance in the initial state R_{ini}, that in high-resistance state (HRS) R_{HRS}, and that in low-resistance state (LRS), were measured at 0.3 V in this chapter. Figure 3.12 shows the oxygen composition dependence of R_{ini} in the Pt/NiO_x/Pt stack structures. R_{ini} exhibits remarkable decrease with an increase in the oxygen composition of NiO_x layers. Samples with higher oxygen compositions ($x \geqq 1.10$) do not show RS operation because R_{ini} is

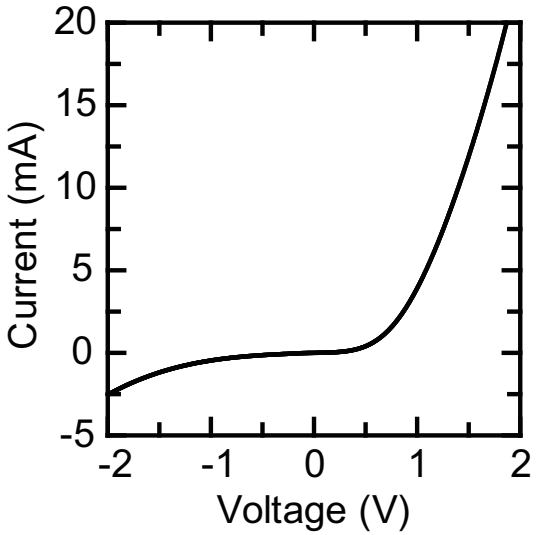

Figure 3.8: Current-voltage characteristics of $NiO_{1.07}$/*n*-Si heterojunction.

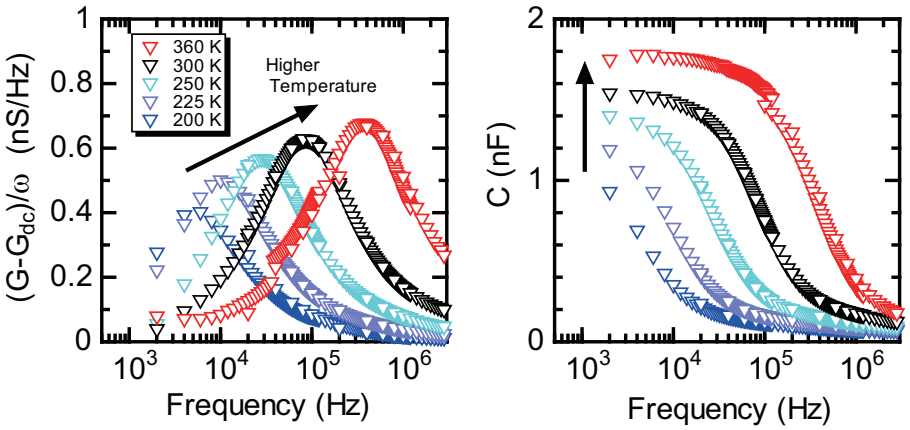

(a) p-$NiO_{1.05}$ / n-Si

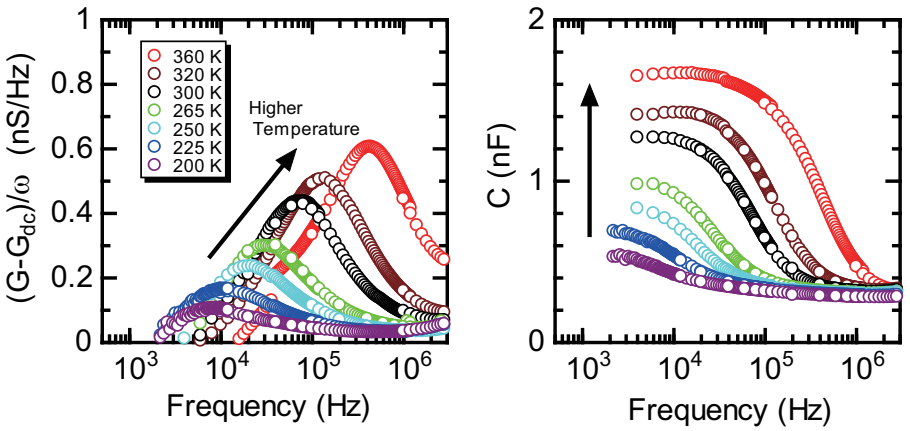

(b) p-$NiO_{1.07}$ / n-Si

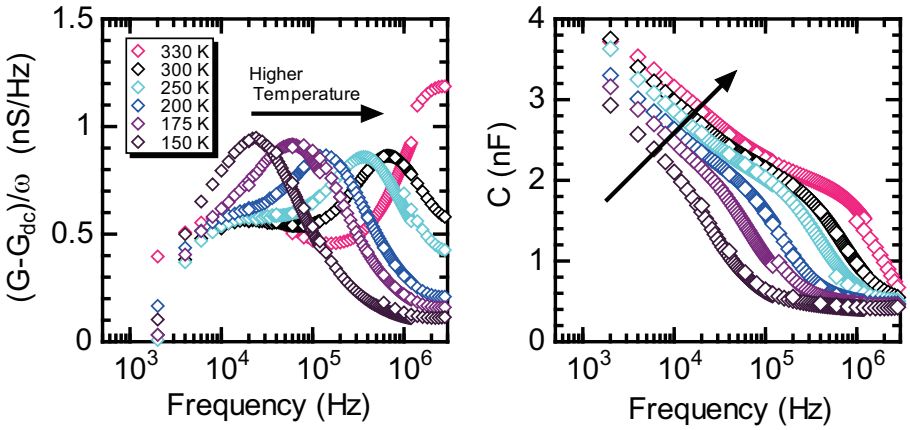

(c) p-$NiO_{1.15}$ / n-Si

Figure 3.9: Frequency dependence of $(G - G_{dc})/\omega$ and C for three NiO_x/n-Si heterojunctions at different temperatures.

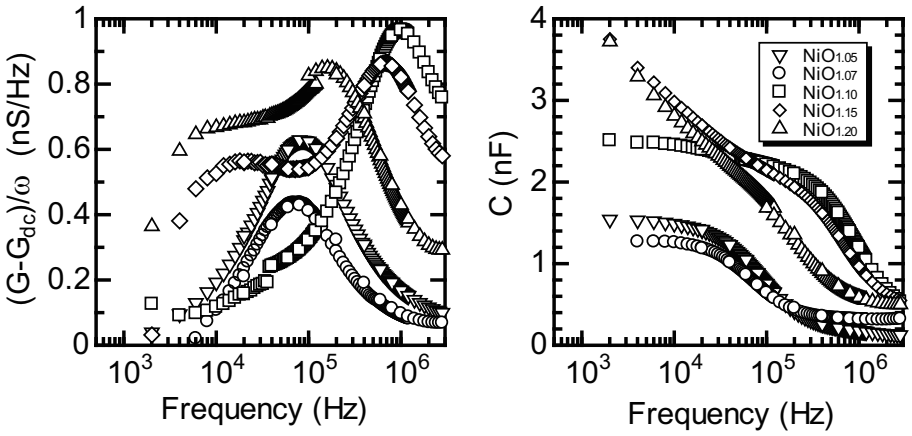

Figure 3.10: Frequency dependence of $(G - G_{\mathrm{dc}})/\omega$ and C for NiO_x/n-Si heterojunction at RT.

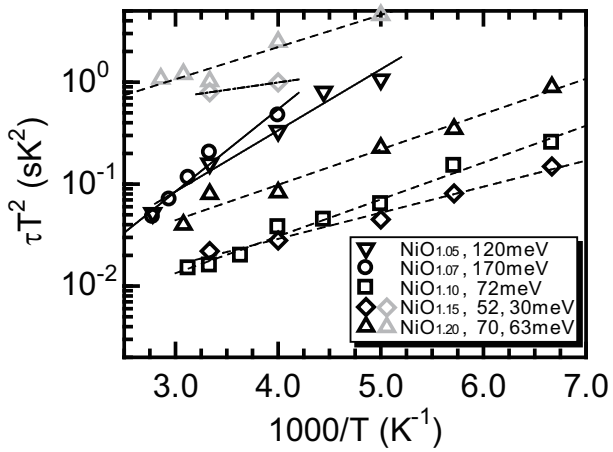

Figure 3.11: Arrhenius plots of τT^2 in various NiO_x/n-Si heterojunctions.

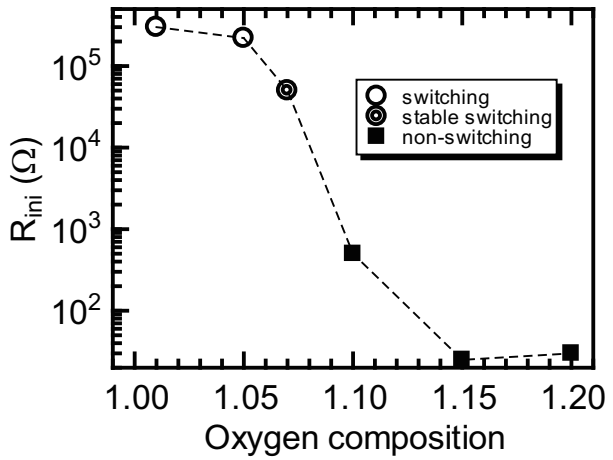

Figure 3.12: Oxygen composition dependence of R_{ini} in Pt/NiO_x/Pt stack structures with a TE-diameter of 300 μm at RT.

too low. The current reaches the compliance level (I_{comp}) of more than 10 mA before the forming process occur. The NiO_x layers with oxygen compositions of 1.15 and 1.20 were deposited by reactive sputtering in an oxide mode, which tended to result in low resistance of several tens of Ω. Conversely, samples with lower oxygen compositions ($x \leqq 1.07$) exhibit RS operation. The NiO_x layers in these samples were deposited by reactive sputtering in a metallic mode. R_{ini} in a sample with an oxygen composition of 1.10 indicates 300 Ω, which may be involved in the NiO_x layer deposited in the mixture of the metallic mode and the oxide mode because O_2 flow rate corresponds to a transition region during reactive sputtering.

Note that RS operation was repeatable and stable especially in the Pt/$NiO_{1.07}$/Pt stack structures. The author focuses on the RS characteristics of the Pt/$NiO_{1.07}$/Pt stack structure in the temperature range of 300 – 550 K. Temperature dependences of R_{ini} and R_{HRS} in Pt/$NiO_{1.07}$/Pt stack structures with a TE-diameter of 200, 300, and 500 μm are shown in Fig. 3.13. I_{comp} was set to 10 mA to avoid damage at forming. R_{ini} and R_{HRS} of the Pt/$NiO_{1.07}$/Pt stack structure exhibit very similar temperature dependence. The cell size dependence reveals almost constant resistivity of the $NiO_{1.07}$ layer, indicating that R_{ini} and R_{HRS} are proportional to cell size. Moreover, resistivity of NiO is thermally activated [12, 13, 20], and R_{ini} can be described by:

$$R_{ini} = R_0 \exp\left(\frac{E_a}{k_B T}\right), \tag{3.4}$$

where R_0 is a constant and E_a is the activation energy. Therefore, using the R_{ini} values near RT, the activation energy was estimated. The Arrhenius plots of R_{ini} and R_{HRS} result in the activation energy E_a of 170 meV.

Figure 3.14 shows the typical RS characteristics of the Pt/$NiO_{1.07}$/Pt stack structure at 300, 400 and 550 K. The set voltage V_{set} was confirmed to be independent of current level before set and measured temperature, whereas the reset voltage V_{reset} increased with increased current level before reset. Typical R_{HRS} and R_{LRS} values at 300 K were approximately 40 kΩ and 50 Ω, and those at 550 K were approximately 2 kΩ and 50 Ω, respectively. Therefore, the approximate on-off ratio of cell resistance (R_{HRS}/R_{LRS}) is 800 at 300 K and 40 at 550 K.

3.4 Discussion

The concentration of shallow acceptors N_s is obtained from the C–V measurement at high frequency where the holes trapped at defect levels can not follow. In contrast, the concentration of hole trap levels N_t can be estimated from the equation as [16]

$$\Delta C = \frac{\varepsilon}{w}\frac{N_t}{N_s}\frac{1-\frac{x_t}{w}}{1+\frac{x_t}{w}\frac{N_t}{N_s}}. \tag{3.5}$$

When x_t at which the deep trap level E_t crosses the Fermi level E_f is much less than depletion width w,

$$\Delta C \simeq \frac{\varepsilon}{w}\frac{N_t}{N_s}, \tag{3.6}$$

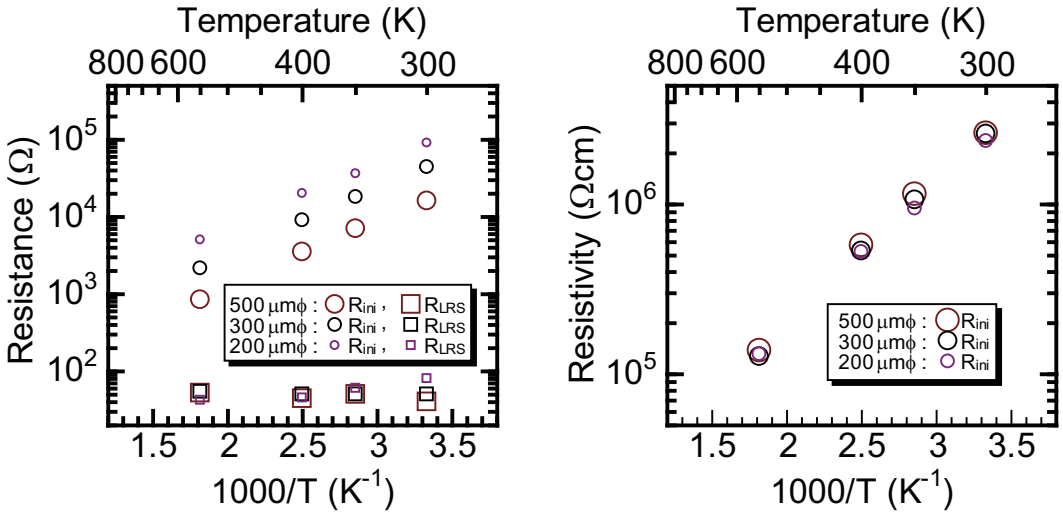

Figure 3.13: Arrhenius plots of R_{ini} and R_{LRS} in Pt/$NiO_{1.07}$/Pt stack structures with a TE-diameter of 200, 300, and 500 μm.

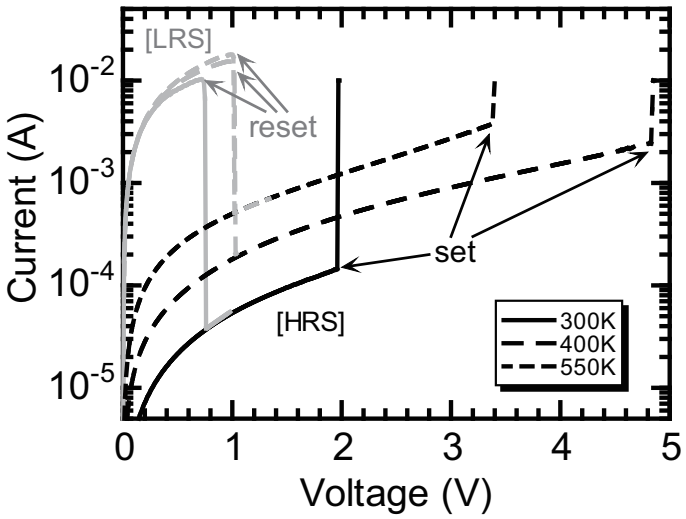

Figure 3.14: Typical RS characteristics of Pt/$NiO_{1.07}$/Pt stack structures with a TE-diameter of 300 μm at 300, 400, and 550 K.

is established. Here, ΔC can be obtained from the frequency dependence of $(G - G_{dc})/\omega$ and C as Eqs.(3.1) and (3.2), respectively, and ε is dielectric constant of NiO_x layer. Since ΔC can be obtained from $(G - G_{dc})/\omega$ and C values at $\omega\tau = 1$ by admittance spectroscopy, N_t can be estimated from the equation as

$$N_t \simeq 2\left(\frac{C}{G/\omega}\bigg|_{\omega\tau=1} - 1\right)^{-1} N_s. \tag{3.7}$$

The estimated parameters, such as τ_{RT}, $E_t - E_v$, N_s, and N_t with various oxygen compositions, are summarized in Table 3.1. Note that the faster defect level can not be observed for $NiO_{1.10}$ layers, and the slower defect level can be observed for only NiO_x layers with higher oxygen compositions ($x \geqq 1.15$). τ_{RT} of each peak tends to increase with increased oxygen composition in NiO_x layers. Although N_s increases with increased oxygen composition, N_t remains unchanged by varying the oxygen composition.

The concentration of hole trap levels is higher than or equivalent to that of shallow acceptors, which suggests that most holes in NiO_x layers are trapped. NiO_x layers with lower oxygen compositions ($x \leqq 1.07$) have a relatively high concentration of hole trap levels and high activation energy. This is why most holes are trapped by the defect levels at RT and R_{ini} is sufficiently high. Conversely, in the case of NiO_x layers with higher oxygen compositions ($x \geqq 1.10$), the concentration of shallow acceptors and hole trap levels are high and the activation energy is low, which suggests that most holes are thermally excited from shallow acceptor even at RT and R_{ini} is low.

From the viewpoint of RS operation, these different properties of RS originate from the difference of the energy level of the hole trap located above the valence band edge. The desirable range of oxygen composition of NiO_x layers may be narrow for obtaining repeatable and stable RS operation. Note that in the p-$NiO_{1.07}$/n-Si heterojunction, the activation energy of 170 meV is similar to $E_t - E_v$ estimated above from the emission time constant. Carrier conduction in NiO has been reported according to small polaron hopping [12] or band conduction [21]. The activation energy of 170 meV reflects most likely the temperature dependence of the carrier concentration in NiO bulk. Thus, thermal excitation of holes from the defect level at 170 meV above the valence band edge dominates the electrical conduction, at least, above 300 K.

However, these experimental results include several uncertainties. One is whether a NiO_x/n-Si heterojunction as a Schottky barrier is completely valid or not. In addition, N_s and N_t may not be neglected compared to donor concentration of approximately $2 \times 10^{19}\mathrm{cm}^{-3}$ in n-Si substrates. A reverse leak current and the index of $\tan\delta$ of several samples were relatively large despite sufficiently small reverse voltages, especially for NiO_x layers with higher oxygen compositions deposited in the oxide mode. Therefore, the author was forced to perform admittance spectroscopy at only zero DC bias. DC bias dependence of $(G - G_{dc})/\omega$ and C is necessary to confirm the validity as a Schottky barrier. Moreover, the author should perform other experiments to characterize defect levels in the NiO_x layers. Deep-level transient spectroscopy (DLTS) is a powerful candidate for

Table 3.1: Emission time constant at RT, activation energy, and concentration of defect levels obtained by admittance spectroscopy on NiO_x layers with various oxygen compositions.

x in NiO_x	τ_{RT} (μs)	$E_t - E_v$ (meV)	N_s (cm^{-3})	N_t (cm^{-3})
1.05	1.8	120	2×10^{-18}	1×10^{-19}
1.07	2.3	170	5×10^{-18}	1×10^{-19}
1.10	0.18	72	8×10^{-18}	5×10^{-19}
1.15	0.24	52	1×10^{-19}	5×10^{-19}
	8.8	30		8×10^{-18}
1.20	0.88	70	1×10^{-19}	5×10^{-19}
	11	3		1×10^{-19}

the characterization. The signal $C(t)$ is as follows,

$$C(t) = C_{\mathrm{st}} \left\{ 1 - \frac{N_{\mathrm{t}}}{N_{\mathrm{s}}} \exp\left(-\frac{t}{\tau}\right) \right\}^{1/2} \tag{3.8}$$

$$\simeq C_{\mathrm{st}} \left\{ 1 - \frac{1}{2}\frac{N_{\mathrm{t}}}{N_{\mathrm{s}}} \exp\left(-\frac{t}{\tau}\right) \right\}. \tag{3.9}$$

Note that the approximation is effective when N_{t} is much smaller than N_{s}, which is not established from the results of admittance spectroscopy. Therefore, isothermal capacitance transient spectroscopy (ICTS) is more appropriate characterization of defect levels in NiO_x layers on *n*-Si substrates, because the signal $S(t)$ is given by the following equation [22],

$$S(t) = t\frac{dC_{\mathrm{st}}}{dt} = C_{\mathrm{st}}^2 \frac{t}{\tau}\frac{N_{\mathrm{t}}}{N_{\mathrm{s}}} \exp\left(-\frac{t}{\tau}\right). \tag{3.10}$$

Second, the crystalline structure of NiO_x layers on *n*-Si substrates for admittance spectroscopy may be different from that of NiO_x layers on a Pt BE, as discussed in Chapter 4. The crystallinity of a NiO_x layer strongly depends on a lower BE, and thus, RS characteristics have clear difference between NiO_x layers on different BEs, or NiO_x layers even on the same material deposited by different methods. Accordingly, the author intended to avoid the uncertainty of different NiO_x crystallinities. However, the author did not confirm the reset process in the Pt/NiO_x/*n*-Si/Al stack structure, although another study reported that Pt/NiO/*n*-Si stack structures exhibited an RS operation [23]. Therefore, a comparison of depth of the trap level $E_{\mathrm{t}} - E_{\mathrm{v}}$ estimated from the emission time constant by admittance spectroscopy and the activation energy E_{a} derived from temperature dependence of R_{ini} and R_{HRS} in the Pt/$NiO_{1.07}$/Pt RS cells may be invalid because these $NiO_{1.07}$ layers are not identical.

In addition, the activation energy E_{a} exhibits unignorable gaps from the results of the author's group. It was estimated from the temperature dependence of R_{ini} of the other Pt/NiO_x/Pt RS cells that E_{a} was approximately 330 meV above 170 K [24]. Although oxygen composition in the NiO_x layer (x was 1.11±0.1 [25]) differs from that in the $NiO_{1.07}$ layers, the value is twice as large as 170 meV in the Pt/$NiO_{1.07}$/Pt RS cells. The gap may originate from the difference of NiO layers because of difference of Pt BEs.

Nevertheless, the on-off ratio of cell resistance is approximately 800 at 300 K and approximately 40 at 550 K. These ratios are sufficiently large to provide a dynamic margin for practical switching operation. Regarding the rupture of conducting filament paths by Joule heating [26–29], the present result indicates that the critical temperature of the inner paths at which reset occurs is at least higher than 550 K. Other emerging nonvolatile memories, such as magnetic RAM (MRAM), will face severe difficulty in high-temperature operation due to the relatively low Curie temperature, while the NiO-based RS cells exhibit the potential for many applications at extremely high temperatures.

3.5 Summary

Admittance spectroscopy measurements were performed on NiO_x layers with various oxygen compositions (x =1.0−1.2). The samples for the measurements were Pt/p-NiO_x/n-Si/Al stack structures as pn heterojunctions. Several properties of the hole trap levels in NiO_x layers were characterized. The activation energy of localized states in NiO_x films with low oxygen compositions ($x \leqq 1.07$) deposited by reactive sputtering in a metallic mode was relatively large, 120−170 meV, while that with higher oxygen compositions ($x \geqq 1.10$) deposited in the oxide mode was smaller than 100 meV. The results indicated that most holes were trapped by the defect levels at RT and R_{ini} was sufficiently high for the low oxygen composition.

The best oxygen composition of NiO_x layers turned out to be about 1.07 for obtaining repeatable and stable RS operation in Pt/NiO_x/Pt stack structures. The NiO-based ReRAM cells showed promise for high-temperature applications in the future, because the present Pt/$NiO_{1.07}$/Pt stack structure exhibited repeatable RS operation even at temperature as high as 550 K.

References

[1] S. Seo, M. J. Lee, D. H. Seo, E. J. Jeoung, D.-S. Suh, Y. S. Joung, I. K. Yoo, I. R. Hwang, S. H. Kim, I. S. Byun, J.-S. Kim, J. S. Choi, and B. H. Park, Appl. Phys. Lett. **85**, 5655 (2004).

[2] H. D. Lee and Y. Nishi, Appl. Phys. Lett. **97**, 252107 (2010).

[3] J.-W. Park, J.-W. Park, K. Jung, M. K. Yang, and J.-K. Lee, J. Vac. Sci. Technol. B **24**, 2205 (2006).

[4] K. Tsunoda, K. Kinoshita, Y. Yamazaki, T. Izuka, Y. Ito, A. Takahashi, A. Okano, Y. Sato, T. Fukano, M. Aoki, and Y. Sugiyama, *Tech. Dig. of IEEE Int. Electron Devices Meet.* (2007) p. 767.

[5] H. Shima, F. Takano, H. Akinaga, Y. Tamai, I. H. Inoue, and H. Takagi, Appl. Phys. Lett. **91**, 012901 (2007).

[6] C. Dumas, D. Deleruyelle, A. Demolliens, C. Muller, S. Spiga, E. Cianci, M. Fanciulli, I. Tortorelli, and R. Bez, Thin Solid Films **519**, 3798 (2011).

[7] L. Goux, J. G. Lisoni, X. P. Wang, M. Jurczak, and D. J. Wouters, IEEE Trans. Electron Devices **56**, 2363 (2009).

[8] H. Kondo, M. Arita, T. Fujii, H. Kaji, M. Moniwa, T. Yamaguchi, I. Fujiwara, M. Yoshimaru, and Y. Takahashi, Jpn. J. Appl. Phys. **50**, 081101 (2011).

[9] M. Kawai, K. Ito, and Y. Shimakawa, Appl. Phys. Lett. **95**, 012109 (2009).

[10] D. Ielmini, S. Spiga, F. Nardi, C. Cagli, A. Lamperti, E. Cianci, and M. Fanciulli, J. Appl. Phys. **109**, 034506 (2011).

[11] P. A. Cox, *Transition Metal Oxides —An introduction to their electronic structure and properties* (Oxford University Press, New York, 2010).

[12] S. Koide, J. Phys. Soc. Jpn. **20**, 123 (1965).

[13] I. G. Austin, A. J. Springthorpe, B. A. Smith, and C. E. Tuner, Proc. Phys. Soc. **90**, 157 (1967).

[14] H. J. Van Daal and A. J. Bosman, Phys. Rev. **158**, 736 (1967).

[15] W. G. Oldham and S. S. Naik, Solid-State Electron. **15**, 1085 (1972).

[16] J. L. Pautrat, B. Katircioglu, N. Magnea, D. Bensahel, J. C. Pfister, and L. Revoil: Solid State Electron. **23**, 1159 (1980).

[17] M. Begwala and C. R. Crowell, Solid-State Electron. **17**, 203 (1974).

[18] T. Kimoto, A. Itoh, H. Matsunami, S. Sridhara, L. L. Clemen, R. P. Devaty, W. J. Choyke, T. Dalibor, C. Peppermüller, and G. Pensl, Appl. Phys. Lett. **67**, 2833 (1995).

[19] S. E. Debebe, W. Mammo, T. Yohannes, F. Tinti, A. Zanelli, and N. Camaioni, Appl. Phys. Lett. **96**, 082109 (2010).

[20] D. Adler and J. Feinleib, Phys. Rev. B **2**, 3112 (1970).

[21] A. J. Bosman and C. Crevecoeur, Phys. Rev. **144**, 763 (1966).

[22] H. Okushi, and Y. Tokumaru, Jpn. J. Appl. Phys. **20**, 261 (1980).

[23] S. Spiga, A. Lamperti, C. Wiemer, M. Perego, E. Cianci, G. Tallarida, H. L. Lu, M. Alia, F. G. Volpe, M. Fanciullin, Microelectron. Eng. **85**, 2414 (2008).

[24] T. Iwata, Y. Nishi, and T. Kimoto, J. Appl. Phys. **117**, 225701 (2015).

[25] T. Iwata, Dr. Thesis, Faculty of Engineering, Kyoto University, Kyoto, 2014.

[26] D. C. Kim, S. Seo, S. E. Ahn, D.-S. Suh, M. J. Lee, B.-H. Park, I. K. Yoo, I. G. Baek, H.-J. Kim, E. K. Yim, J. E. Lee, S. O. Park, H. S. Kim, U.-I. Chung, J. T. Moon, and B. I. Ryu, Appl. Phys. Lett. **88**, 202102 (2006).

[27] Y. Sato, K. Kinoshita, M. Aoki, and Y. Sugiyama, Appl. Phys. Lett. **90**, 033503 (2007).

[28] U. Russo, D. Ielmini, C. Cagli, and A. L. Lacaita, IEEE Trans. Electron Devices **56**, 186 (2009).

[29] U. Russo, D. Ielmini, C. Cagli, and A. L. Lacaita, IEEE Trans. Electron Devices **56**, 193 (2009).

Chapter 4

Effects of Crystallinity of Transition Metal Oxides on Resistive Switching Characteristics

4.1 Introduction

As a resistive switching (RS) mechanism in transition metal oxide (TMO)-based RS cells, the formation and rupture of conductive filaments composed of oxygen vacancies (V_Os) or cation atoms have been widely accepted [1, 2]. The cell shows reversible transitions by applying repeated electrical stress between the low-resistance state (LRS) and the high-resistance state (HRS). Although many efforts have been made to find the conductive filament structures, understanding of the RS phenomenon is still not satisfactory. Forming by the application of electrical stress to a pristine cell is generally required to create conductive filaments in TMO layers between top electrodes (TEs) and bottom electrodes (BEs). Therefore, forming is a key for elucidating the RS phenomenon, especially in binary TMO-based resistive random access memory (ReRAM).

Forming in the cell to create the conductive filament exhibits some analogies with dielectric breakdown of silicon dioxide (SiO_2) thin films in metal-oxide-semiconductor (MOS) structures [2]. Time-dependent dielectric breakdown (TDDB) is a useful method for the analysis of failure mechanism and reliability of insulators in MOS structure. This analysis is based on a percolation model, where percolation paths are formed by defects due to electrical stress [3–5]. The distribution of time to forming in ReRAM cells under constant voltage stress can be similar to that of the time for SiO_2 breakdown. Despite the analogy with breakdown, there are few studies with statistical analyses of time-dependent forming (TDF) characteristics in nickel oxide (NiO)-based ReRAM cells [6]. In addition, the formation of a conductive filament that includes V_Os or is composed of Ti_nO_{2n-1} (Magneli phase) seems to be required to induce the RS phenomenon in titanium dioxide (TiO_2)-based ReRAM cells [7]. Although a few papers have reported on the electrical properties of resistive switching cells with some TiO_2 crystallinities [7, 8], it remains unclear how conductive filaments are formed at grain boundaries (GBs) in a TiO_2 layer.

In this chapter, the author assumes a conductive filament model in the forming process in pristine TMO-based RS cells. Dependencies of the electrical properties, especially forming characteristics, of the cells on TMO deposition conditions using a common BEs are investigated. Effects of TMO crystallinity and deposition condition on TDF characteristics are discussed.

4.2 Changes of Crystalline Structures by Thermal Annealing

4.2.1 Purpose of thermal annealing

Thermal annealing is a most simple method to make an alloyed material or enhance solid-phase growth in the material, which results in a possible change in a crystal structure and chemical composition of the material. In a previous study by the author's group, oxygen desorption from NiO layers as a resistance change material was observed by thermal annealing with specific conditions [9]. In addition, thermal annealing without oxygen desorption invoked an increase in the initial resistance and the activation energy of the resistance, which originates from a change of formation properties of conductive filaments in the NiO layers [9]. Moreover, another group reported that forming voltage of hafnium dioxide (HfO_2)-based RS cells could be reduced by high-temperature and high-pressure hydrogen (H_2) annealing [10].

For an investigation of the thermal annealing effect, NiO/platinum (Pt) BE stack structures were fabricated as follows. First, 50-nm-thick Pt BEs were deposited directly on *p*-silicon (Si) by electron beam (EB) evaporation. NiO layers were deposited by reactive sputtering in a mixture of argon (Ar) and oxygen (O_2), of which the proportion of O_2/(Ar + O_2) was 5%. The substrate temperature and total gas pressure were kept at 300°C and 1.5 Pa, respectively. The thickness of the NiO layers was 270 nm for investigation of crystalline structure by X-ray diffraction (XRD) or approximately 45 nm for other characterizations.

Thermal annealing was carried out without deposition of metallic TEs to avoid a chemical reaction at the TE/NiO interface, and only the effect at the NiO/BE interface was investigated for simplicity. Annealing temperature was 400−1000°C in an O_2 or Ar atmosphere. Annealing time was 5 min, 10 min (only 800°C and 1000°C) and 30 min. After the thermal annealing, effects of various kinds of thermal annealing were investigated.

4.2.2 Effects of thermal annealing

Surface morphologies of NiO layers were characterized by atomic force microscopy (AFM). Figure 4.1 shows typical AFM images of the NiO before and after thermal annealing. When root mean square (RMS) roughness with a scan size of 2.0 μm × 2.0 μm is adopted, the values of NiO layers are 0.8−1.4 nm before thermal annealing. Figure 4.1(a) indicates that the grain size of as-deposited NiO layers is approximately 50 nm. After the thermal annealing at less than 600°C, the morphology remained unchanged. In contrast, the roughness and grain size after the thermal annealing at more than 800°C increased with increased annealing time and temperature, as shown

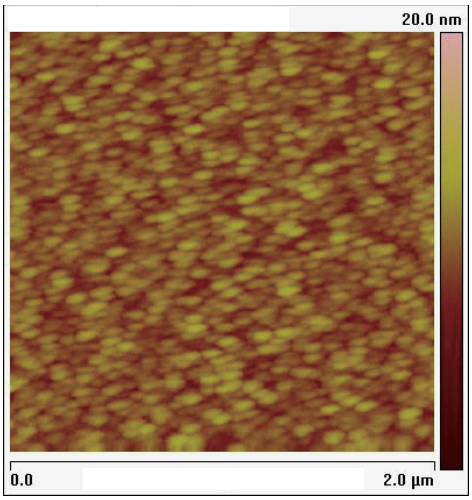

(a) as-deposited

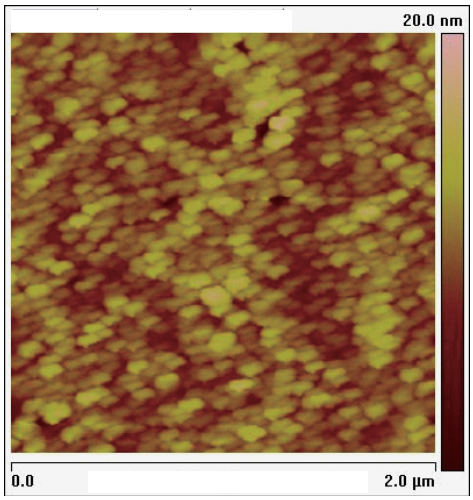

(b) annealed 800°C,10 min

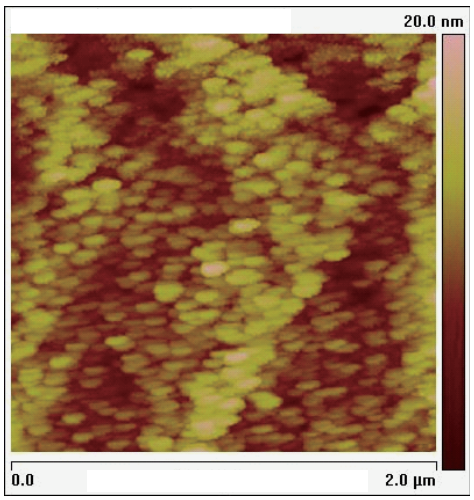

(c) annealed 1000°C,10 min

Figure 4.1: AFM images of (a) as-deposited NiO layers. The morphology changed to (b) after thermal annealing at 800°C during 10 min in Ar atmosphere, or (c) after thermal annealing at 1000°C during 10 min in Ar atmosphere.

in Fig. 4.1(b) and (c). The annealing temperature dependence of the roughness of NiO layers are exhibited in Fig. 4.2. The increase in the roughness by O_2 annealing was confirmed to be larger than that by Ar annealing. Moreover, the cross-sectional transmission electron microscopy (TEM) images in Fig. 4.3 revealed a change in the crystalline structure of NiO layers by thermal annealing at 700°C for 30 min in an Ar atmosphere. Although the as-deposited NiO layer indicates a mixture of both polycrystalline regions with grain sizes of approximately 50 nm, the annealing at 700°C can enhance a solid-phase growth in the NiO layers, resulting in the expansion of grain size to approximately 100 nm.

A NiO crystal has a face-centered cubic crystal lattice, and the lattice constant is 4.17Å at room temperature (RT). XRD curves of NiO/Pt/Si samples before and after the thermal annealing in an O_2 atmosphere are shown in Fig. 4.4. The thickness of NiO layers are approximately 270 nm. NiO (200) and (111) diffraction peaks are detected respectively at $2\theta = 37.2°$ and 43.3° because the X-ray wavelength is 1.5406 Å (CuKα_1). Although the Si (200) forbidden diffraction peak is detected in several samples, the peak is confirmed to depend on whether the thermal annealing was carried out. The diffraction peaks at 2θ of 37−47° revealed a polycrystalline structure in the NiO and Pt BE layers before the thermal annealing. The thermal annealing at 600°C can relax a compressive strain in plane of NiO layers from the shift of the peak position of NiO (200) diffraction, which agrees with experimental results of a strain relaxation by annealing at 500°C in vacuum or air [11]. Moreover, the relative intensity of the NiO (200) diffraction peak tends to increase with increased annealing time and temperature, indicating the acceleration of crystallization and solid-phase growth in NiO layers.

XRD curves of NiO/Pt/Si samples before and after thermal annealing in an Ar atmosphere are shown in Fig. 4.5. As a reference, the result for a NiO/Si sample after thermal annealing at 1000°C for 30 min is added on the top of the curves. The relaxation of the compressive strain and crystallization in NiO layers can be also confirmed by the thermal annealing at 600°C. In addition, separation of the nickel (Ni) phase begins to be observed as a Ni (200) diffraction peak due to the Ar annealing at more than 600°C. In addition to the Ni phase, the thermal annealing at 1000°C induces an additional shoulder peak on the higher-angle side of the Si diffraction peak. The appearance of the additional peak may originate from formation of the platinum silicide because the annealed NiO/Si reference sample does not indicate the peak.

To determine whether thermal annealing changes the oxygen composition in a NiO layer, scanning electron microscopy (SEM)-energy-dispersive X-ray spectrometry (EDX) and X-ray photoelectron spectroscopy (XPS) were performed. The oxygen composition represents x in NiO_x as described in Chapter 3. Note that an x value of approximately 1.07 was confirmed in as-deposited NiO_x layers by Rutherford backscattering spectrometry (RBS) because the quantified x values from EDX results have a large margin of error based on whether the ZAF method or $\phi(\rho z)$ method is adopted for correction. Thus, x values of annealed NiO_x layers in Fig. 4.6 are only relative compared with the value of the as-deposited $NiO_{1.07}$ layer. Figure 4.6 reveals a decrease of the oxygen composition with elevated annealing temperature. In O_2 annealing, however, the decrease is gradually saturated to the minimum of x=0.9, which indicates an oxygen desorption

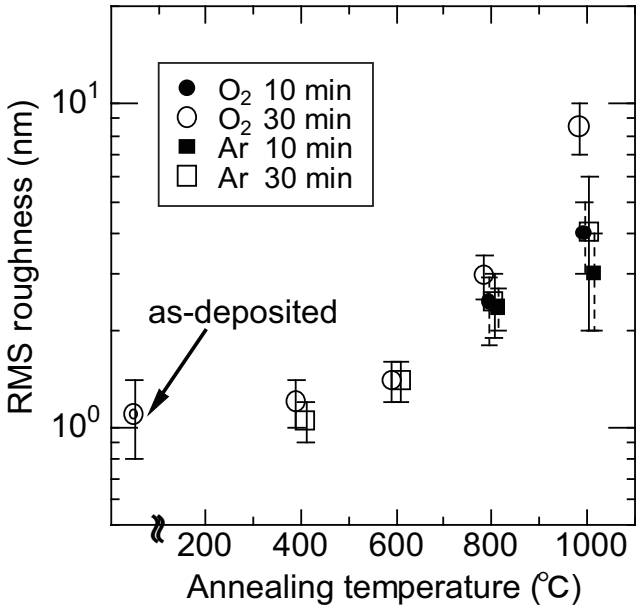

Figure 4.2: Annealing temperature dependence of the roughness of NiO layer during 10 and 30 min in O_2 or Ar atmosphere.

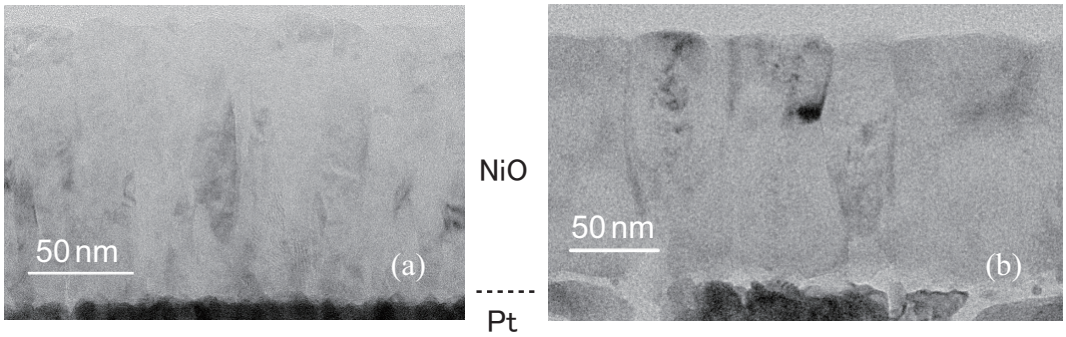

Figure 4.3: Cross-sectional TEM images of (a) as-deposited NiO/Pt sample and (b) annealed NiO/Pt sample at 700°C during 30 min in Ar atmosphere.

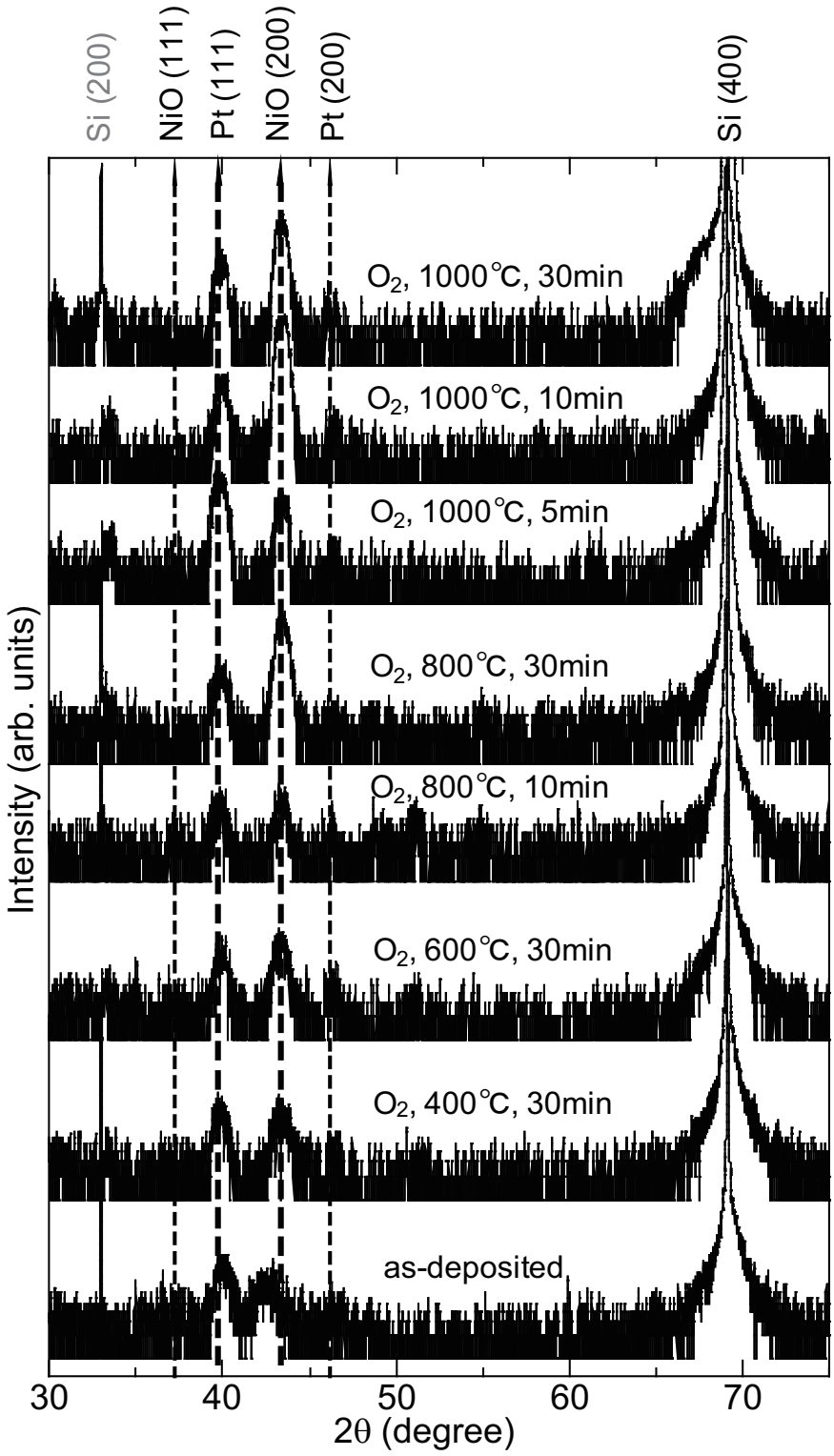

Figure 4.4: XRD curves of NiO/Pt/Si samples before and after thermal annealing in O_2 atmosphere.

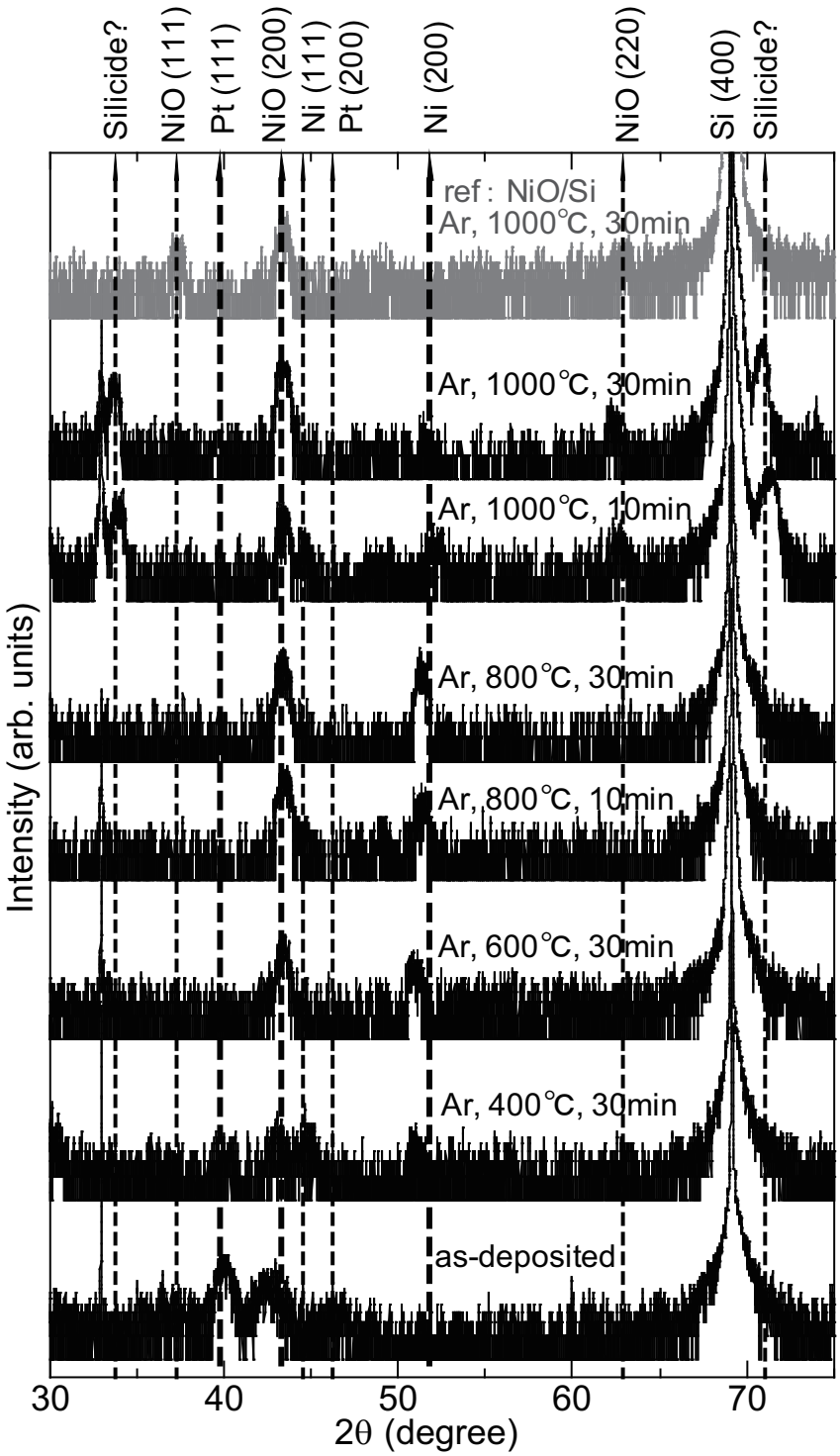

Figure 4.5: XRD curves of NiO/Pt/Si samples and a NiO/Si reference sample before and after thermal annealing in Ar atmosphere.

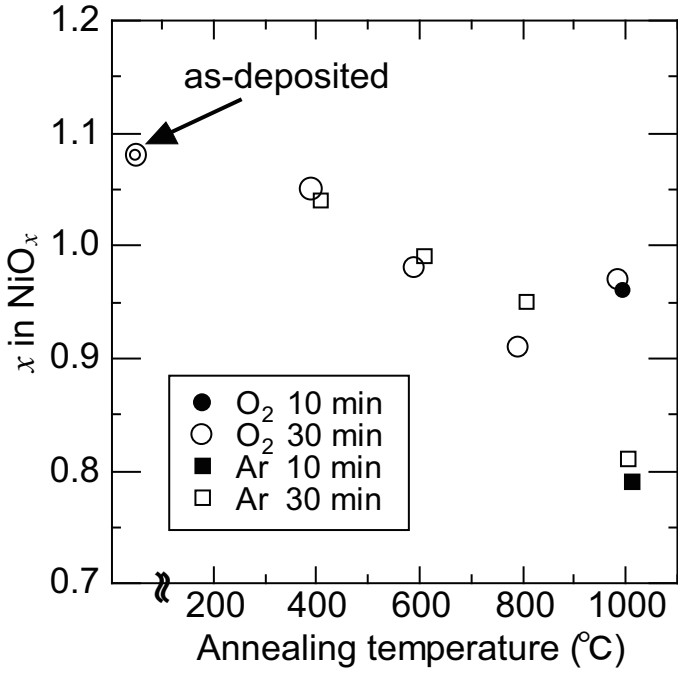

Figure 4.6: Annealing temperature dependence of oxygen composition in NiO layers estimated by SEM-EDX in O_2 and Ar atmosphere.

caused by heating in a reducible gas (Ar). In fact, the author also confirmed the decrease of the oxygen composition by nitrogen (N_2) annealing at 400−700°C. Furthermore, the depth profile of the oxygen composition in the NiO layers was investigated by XPS. Figure 4.7 shows XPS spectra of the surface of the as-deposited sample after Ar ion sputtering every 10 min. The sputtering rate is estimated to be approximately 0.9 nm/min because Pt BE appears after the sputtering during more than 50 nm. Although the depth profile can be estimated by integrating O_{1s} and Ni_{2p} line peak intensities, the ratio of integrated intensities of the O_{1s} line to those of the Ni_{2p} line is just a relative value instead of an absolute oxygen composition in a NiO layer. Thus, the oxygen composition after the sputtering should be normalized to that before the sputtering, as shown in Fig. 4.8. Thermal annealing tends to decrease the oxygen composition in the NiO layer along the depth direction, an example of which is O_2 annealing at 1000°C. The result indicates oxygen diffusion from an inner part near the NiO/Pt interface toward the surface of the NiO layer by the thermal annealing in both O_2 and Ar atmospheres.

4.2.3 Discussion

The thermal annealing changes the crystallinity in NiO layers as described above. The surface roughness and grain size of NiO layers increase with elevated annealing temperature in O_2 and Ar atmospheres. In conjunction with enhancement of the crystallization and the solid-state growth, relaxation of a compressive strain in plane of NiO layers can be observed by thermal annealing at more than 400°C. These experimental results suggest that the solid-state growth of NiO eliminates compressive strain from Pt BE and reconfigures the structure according to the intrinsic crystal lattice of NiO.

In addition, the oxygen composition in NiO layers is also sensitive to thermal annealing at more than 400°C, which decreases the oxygen content during thermal annealing. The author's group reported that no marked change in the chemical composition of NiO layers was observed after thermal annealing at lower than 300°C in an Ar atmosphere [9]. In contrast, the oxygen composition decreased by thermal annealing at 300°C in vacuum. Considering the results, whether thermal annealing is done in an oxidable, reducible gas atmosphere or in vacuum is crucial for varying degrees of oxygen desorption from the NiO layer, even at the same temperature. Moreover, the depth profile of the oxygen compositions of NiO layers in Fig. 4.8 should be further considered. The oxygen composition is regarded as unchanged along the depth direction in the as-deposited NiO layer, which indicates that a selective sputtering of the NiO can be neglected and the decrease in depth profile of the oxygen composition in O_2-annealed samples are essential. Therefore, oxygen atoms near the NiO/Pt interface tended to diffuse toward the surface of the NiO layer by thermal annealing at 400°C at the lowest. Furthermore, the author also focused on Si_{2p} line peaks in XPS spectra before and after Ar ion sputtering. The Si_{2p} line peaks were not observed in most of the samples before and after the thermal annealing. In the case of the Ar sample annealed at 1000°C, however, a peak at 103.3 eV can be confirmed even at the surface of NiO layers (before Ar ion sputtering), and the peak gradually shifts to 99.8 eV as the sputtering proceeds. The former

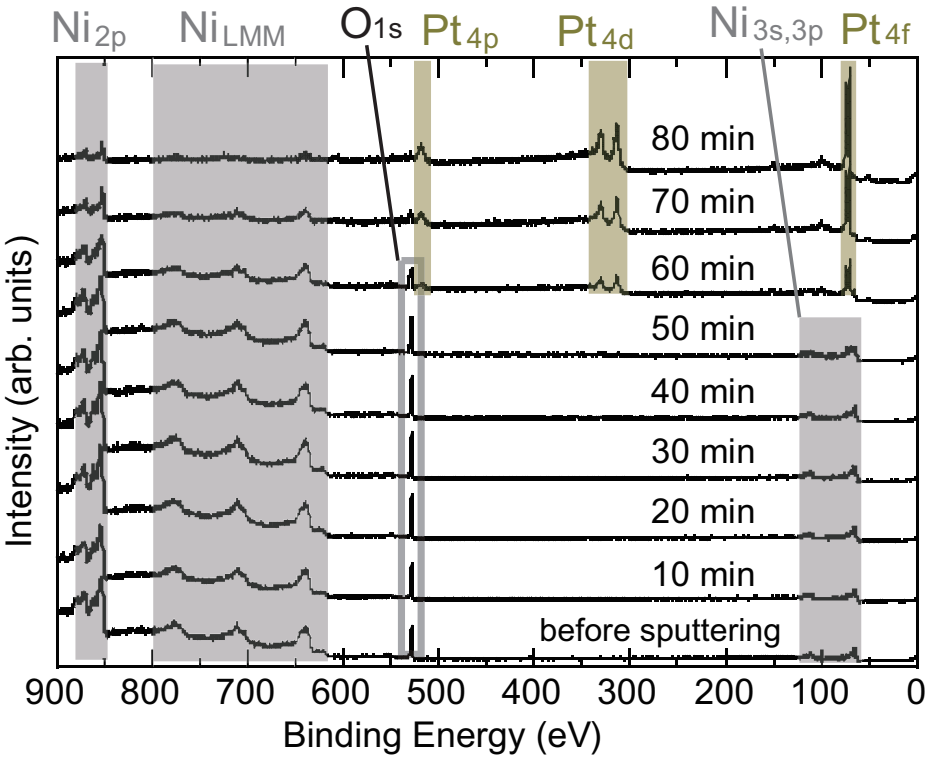

Figure 4.7: XPS spectra of the surface of the as-deposited sample after Ar ion sputtering for each 10 min. The sputtering rate is estimated to be approximately 0.9 nm/min.

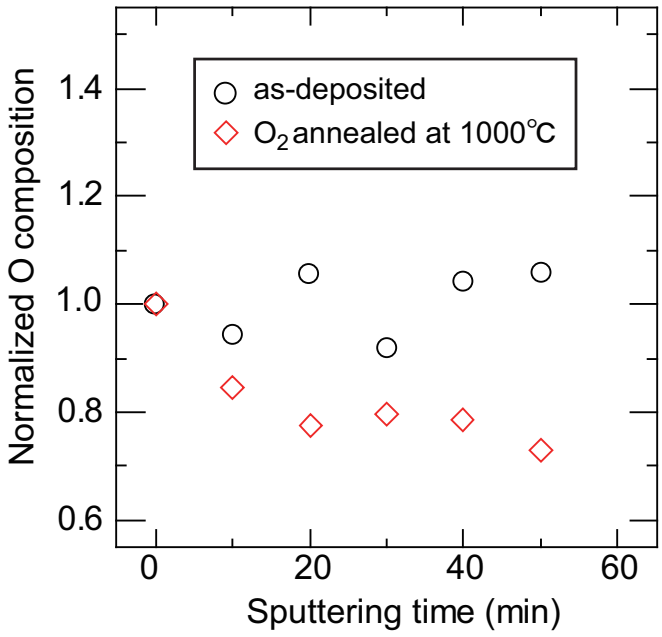

Figure 4.8: Depth profile of oxygen composition in NiO layers before and after O_2 annealing at 1000°C. NiO/Pt interface was observed after Ar ion sputtering during more than 50 min.

and latter peaks are attributed to SiO_2 (Si^{4+}) and Si (Si^0), respectively. The existence of the latter peak seems to reflect the additional shoulder peak of Si diffraction in Fig. 4.5, which may originate from formation of platinum silicide. These results suggest that not only O_2 in NiO but also Pt and Si can diffuse toward the surface during thermal annealing at 1000°C in an Ar atmosphere. As a result, especially in a reducible gas atmosphere, too high of an annealing temperature should be avoided to prevent the diffusion of Pt or Si. The authors will adopt thermal oxide (SiO_2) covered Si substrates instead of Si substrates going forward because a barrier layer between the Pt BE and Si substrate is needed to prevent the formation of platinum silicide.

Next, the author investigated effects of thermal annealing on the electrical and RS characteristics in the NiO/Pt samples. A tungsten (W) probe directly contacts the NiO surface instead of TEs. The cell size nearly corresponds to a contact area of the probe with a tip curvature radius of approximately 25 μm. The BE was grounded and a bias voltage was applied to the W probe. The RS characteristics of W/NiO/Pt stacks were measured in a voltage-sweep mode by using a Keithley 4200-SCS semiconductor parameter analyzer at RT in air. The author confirmed that initial resistance (R_{ini}) at 0.1 V was over the range of 1 to 100 MΩ before the thermal annealing. After forming with a compliance current of 10 mA, RS operation can be observed. Typical resistance in the low resistance state (R_{LRS}) is 50−80 Ω. After the thermal annealing, the R_{LRS} changes as shown in Fig. 4.9, and the RS operation was confirmed. The R_{LRS} values gradually increase with elevated annealing temperature. Here, in the samples annealed at more than 800°C in an Ar atmosphere, R_{ini} values were lower than 3 kΩ (indicated in Fig. 4.9 as R_{LRS}), but RS did not occur. This initial low resistance can originate from the diffusion of Pt and Si into NiO layers. Note that several contact points in the samples annealed at 400°C in an Ar atmosphere and at more than 600°C in an O_2 atmosphere exhibit RS characteristics with multiple ranges of resistance in the high-resistance state (R_{HRS}). An example of the RS characteristics is shown in Fig. 4.10. Although two R_{HRS} values (R_{HRS1} and R_{HRS2}) can be obtained in this case, whether R_{HRS} after reset indicates R_{HRS1} or R_{HRS2} was uncontrollable, nor could the author control reset voltage. However, the specific RS operation holds potentialities for multiple resistance states because thermal annealing changed the properties of NiO.

4.3 Crystallinity of Transition Metal Oxides

4.3.1 RS cell fabrication

As a resistance change material, the author adopted NiO and TiO_2 hereinafter in this chapter. A NiO is normally regarded as a *p*-type semiconductor as described in Chapter 3, while a TiO_2 is well known as a typical *n*-type semiconductor. Materials for both electrodes were Pt for simplicity.

Pt/NiO/Pt stack structures were fabricated as follows. A Pt layer as a BE was deposited with a thickness of 80−100 nm on a SiO_2(200 nm)/*p*-Si substrate as discussed in Section 4.2.3. The authors inserted a titanium (Ti) layer between Pt BE and SiO_2 interface because Pt removes easily without sticking sufficiently to SiO_2 sometimes especially when a Pt layer was deposited

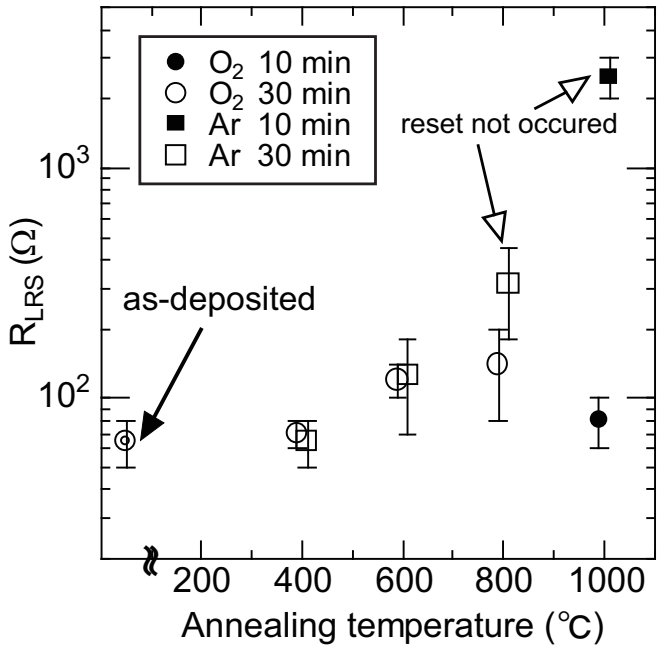

Figure 4.9: Annealing temperature dependence of resistance after forming during 10 and 30 min in O_2 or Ar atmosphere.

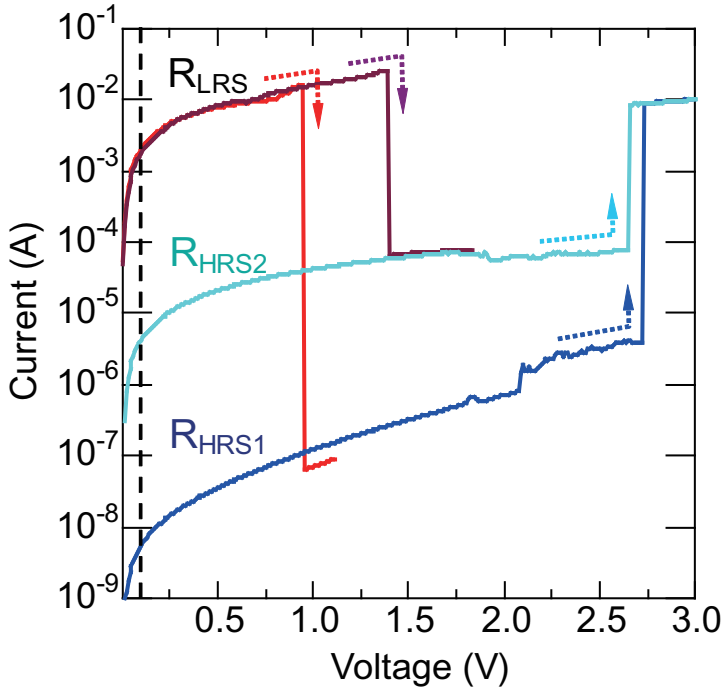

Figure 4.10: RS characteristics with two ranges of resistance in the high resistance state in the samples annealed at 400°C during 30 min in Ar atmosphere.

by EB evaporation with a higher deposition rate than 1.0 Å/s. The thickness of the Ti inserted layers was approximately 5 nm and thereby adhesion force enough. A NiO layer as a resistance change material was deposited on the BE in an Ar and O_2 gas mixture by using reactive radio-frequency (RF) sputtering system (ANELVA: L-250-FHL). The purity of a metallic Ni target was 99.99% (4N). The thickness of NiO layer (d_{NiO}) was varied from 30 nm to 100 nm for RS cells and over 100 nm for structure analyses. Pt TEs with diameters in the range from 50 μm to 500 μm were deposited on the NiO layer by EB evaporation through a metal shadow mask. A cell size is equivalent to a TE area. The above is a common procedure in fabrication of Pt/NiO/Pt stack structures.

Two kinds of BE layers were prepared, deposited either by EB evaporation or RF sputtering (SP). A sample with the Pt/NiO/Pt cells using Pt BE deposited by EB or SP is referred to as the EB-Pt samples or SP-Pt samples, respectively. The deposition of Pt BE in the SP-Pt samples was carried out by using multi-target sputtering system (EIKO: ES-250L). The purity of a metallic Pt target was 99.99% (4N). The deposition conditions of Ti adhesion layers and Pt BEs by RF sputtering are summarized in Table 4.1 and Table 4.2, respectively. The substrate temperature during NiO deposition in one condition (condition A) was RT. Condition A was adopted as the standard deposition condition of NiO layers in the EB-Pt samples. After the author's group introduced Pt BE deposited by RF sputtering, NiO deposition at high substrate temperature was basically adopted from the viewpoint of high reproducibility of the deposition. Here, the authors investigated temperature dependence of a surface morphology of Pt BE on SiO_2(200 nm)/*p*-Si substrate after a thermal treatment in vacuum during 1 hour in the sputtering chamber (ANELVA: L-250-FHL) [12]. This condition of the thermal treatment corresponds to before pre-sputtering for the NiO deposition. The surface morphology and grain size of Pt were confirmed to remain almost unchanged compared with the as-deposited sample when the temperature was less than 450°C. Therefore, the author adopted basically 350°C as a substrate temperature during the NiO deposition. After the optimization of deposition condition, NiO layers in the SP-Pt samples were deposited under condition B, which was different from condition A. The Ar and O_2 flow rates, and substrate temperature in condition A and condition B are summarized in Table 4.3. Unless otherwise specified, the condition A or condition B was adopted in the EB-Pt samples or the SP-Pt samples as the deposition condition of NiO layers, respectively.

In contrast, Pt/TiO_2/Pt stack structures were fabricated as follows. A Pt layer as a BE in the EB-Pt samples was deposited in the same method as described above. The deposition of Pt BE in the SP-Pt samples was carried out by using DC sputtering system (SANYU: SVC-700TMSG). The purity of a metallic Pt target was also 99.99% (4N). The pressure and current during depositions of Ti adhesion layers and Pt BEs by DC sputtering were kept to be approximately 0.8 Pa and 30 mA, respectively. The thickness of the Pt BE layers was 25−70 nm. Next, a TiO_2 layer as a resistance change material was deposited on the BE layer by using reactive RF sputtering system (EIKO: ES-250L). The purity of a metallic Ti target was 99.999% (5N). The deposition condition of TiO_2 layers summarized in Table 4.4. The thickness of the TiO_2 layers was in the range of 30−50 nm for RS and over 100 nm for structural analyses. Pt TEs with a circular shape and diameters of

Table 4.1: Deposition condition of Ti adhesion layers by RF sputtering.

Ar flow rate (sccm)	O_2 flow rate (sccm)	Substrate temperature
5.0	–	RT
Pressure (Pa)	RF power (W)	Deposition rate (nm/min)
0.25–0.3	255	3

Table 4.2: Deposition condition of Pt bottom electrodes by RF sputtering.

Ar flow rate (sccm)	O_2 flow rate (sccm)	Substrate temperature
5.0	–	RT
Pressure (Pa)	RF power (W)	Deposition rate (nm/min)
0.25–0.3	245	8

Table 4.3: Ar and O_2 flow rates, and substrate temperature in condition A and condition B during NiO deposition by RF sputtering.

	Ar flow rate (sccm)	O_2 flow rate (sccm)	Substrate temperature
condition A	9.1	0.8–0.9	RT
condition B	7.8	1.04–1.10	350°C

Table 4.4: Deposition condition of TiO_2 layers by RF sputtering.

Ar flow rate (sccm)	O_2 flow rate (sccm)	Substrate temperature
10.0	1.0	RT
Pressure (Pa)	RF power (W)	Deposition rate (nm/min)
0.675	290	0.4

100−200 μm were deposited on the TiO_2 layer by EB evaporation through a metal shadow mask. The thickness of the Pt TE layers was approximately 25 nm.

If the EB-Pt samples with NiO layers and with TiO_2 layers are potentially confusing, these samples will be designated as "EB-Pt NiO samples" and "EB-Pt TiO_2 samples", respectively. The same is true of the SP-Pt samples.

4.3.2 Crystalline Structure

The authors investigated crystallinity of a resistance change material before performing electrical measurements, because the crystallinity (of NiO layers or TiO_2 layers in this section) naturally affects to the electrical and RS characteristics of the RS cells as discussed in Section 4.2.

First of all, surface morphologies of the samples were characterized. Figure 4.11 shows typical AFM images of Pt BE layers of (a) the EB-Pt sample and (b) the SP-Pt sample deposited by RF sputtering. The thickness of the Pt BE of the SP-Pt sample was 60 nm and that of the EB-Pt samples was either 70 or 25 nm: the latter is designated as the "thinner EB-Pt sample" shown in Fig. 4.11(c). Pt BE layers deposited by RF sputtering are for the SP-Pt NiO samples. A typical AFM image of Pt BE layers deposited by DC sputtering is shown in Fig. 4.11(d). A root-mean-square (RMS) roughness value from a scan area of 0.5 μm × 0.5 μm was used hereinafter as an index for the surface roughness. The typical roughness values of Pt BE layers deposited by RF and DC sputtering are approximately 0.5 nm in common. The value of the Pt BE surface of the EB-Pt sample (0.6−0.8 nm) is greater than that of the SP-Pt sample. Conversely, the Pt BE roughness value of the thinner EB-Pt sample (0.3−0.4 nm) is smaller than that of the SP-Pt sample.

Figure 4.12 shows typical AFM images of NiO layers of the EB-Pt sample and the SP-Pt sample. The typical values of NiO layers with a thickness of 50 nm of the EB-Pt samples and the SP-Pt samples are 0.9−1.1 nm and 0.5−0.7 nm, respectively. Although the surface roughness of NiO layers increases with increased NiO thickness, the NiO surface basically reflects the Pt BE surface. In the case of TiO_2 with a thickness of approximately 30 nm, typical AFM images of TiO_2 of the EB-Pt samples and the SP-Pt samples are shown in Fig. 4.13. Although the thickness of the TiO_2 layers was almost the same, the roughness values of the TiO_2 layers increase as the thickness of the Pt BE layer increases. Note that the typical value of the TiO_2 layers of the SP-Pt samples (0.9−1.0 nm) is smaller than that of the thinner EB-Pt samples (1.0−1.1 nm), although the Pt BE roughness value of the SP-Pt samples is larger than that of the thinner EB-Pt samples. Thus, the TiO_2 surface reflected the Pt BE surface as in the case of NiO surface, and however, the deposition method (EB evaporation or sputtering) for the Pt BE layer induce clear difference on the TiO_2 surface.

Next, the authors investigated the typical depth profile of the microscopic structure of resistance change materials. Figure 4.14 shows typical cross-sectional TEM images of the EB-Pt NiO samples and the SP-Pt NiO samples. Whereas Pt BEs in the EB-Pt samples contain granules, Pt BE layers in the SP-Pt samples exhibit a columnar polycrystalline structure with a grain diameter of tens of nanometers. The NiO/Pt interface in the EB-Pt samples is confirmed to be more rough than that in

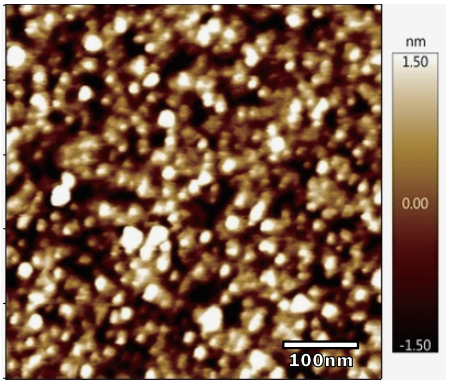

(a) EB-Pt sample

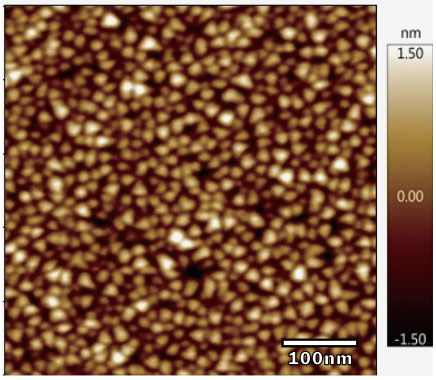

(b) SP-Pt sample (RF)

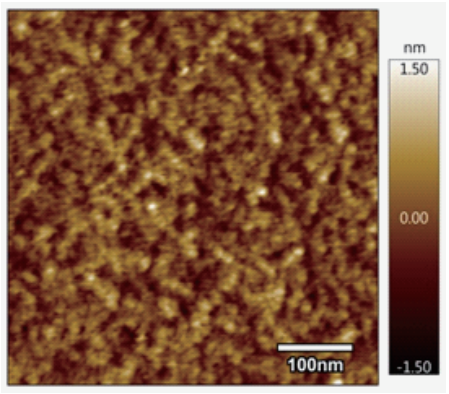

(c) thinner EB-Pt sample

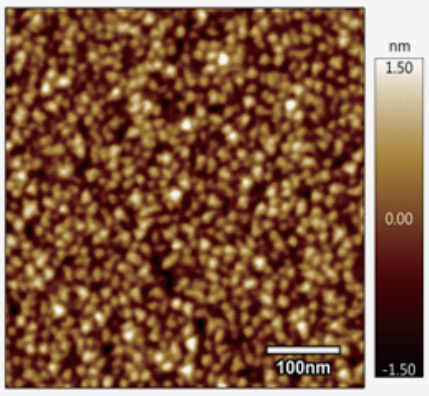

(d) SP-Pt sample (DC)

Figure 4.11: AFM images of Pt BE layers of (a) the EB-Pt samples, (b) the SP-Pt samples deposited by RF sputtering, (c) the thinner EB-Pt samples, and (d) the SP-Pt samples deposited by DC sputtering. A thicknesses of the Pt BE layer is (a) 70 nm and (c) 25 nm.

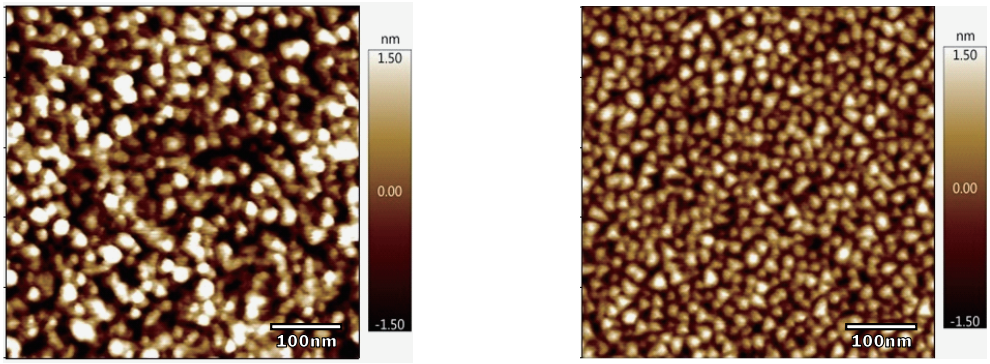

(a) EB-Pt sample (b) SP-Pt sample

Figure 4.12: AFM images of NiO with a thickness of 50 nm of (a) the EB-Pt samples and (b) the SP-Pt samples.

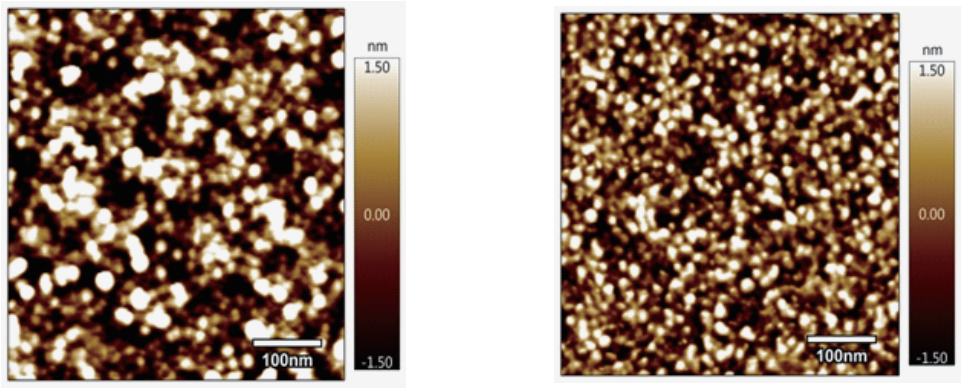

(a) EB-Pt sample (b) SP-Pt sample

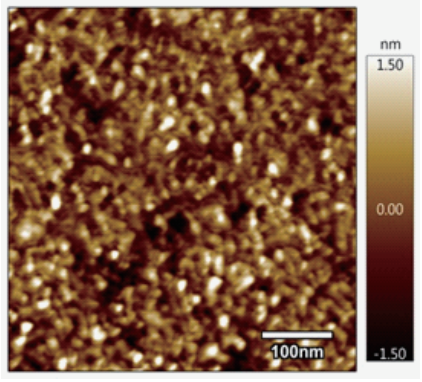

(c) thinner EB-Pt sample

Figure 4.13: AFM images of TiO_2 with a thickness of 30 nm of (a) the EB-Pt samples, (b) the SP-Pt samples, and (c) the thinner EB-Pt samples. A thickness of the Pt BE layer is (a) 70 nm and (c) 25 nm.

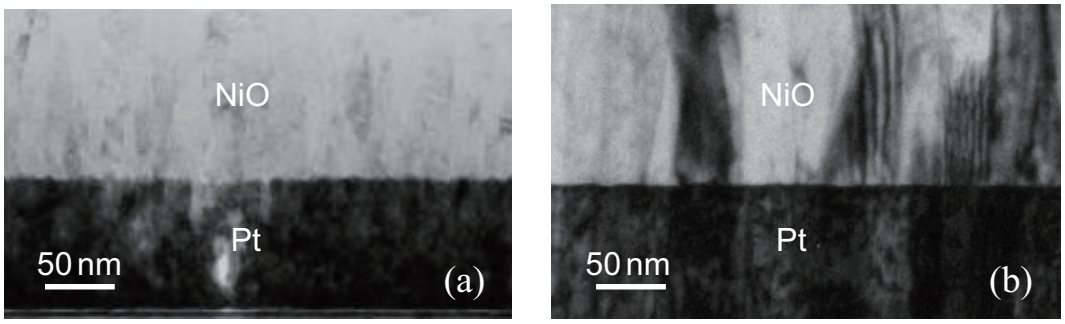

Figure 4.14: Cross-sectional TEM images of (a) the EB-Pt NiO samples and (b) the SP-Pt NiO samples.

the SP-Pt samples. Moreover, the crystallinity of the NiO layers in the EB-Pt samples seems to be granular such as the Pt, and the structure of the NiO layers in the SP-Pt samples indicates columnar polycrystalline as expected. In contrast, typical cross-sectional TEM images of the SP-Pt TiO_2 sample and the EB-Pt TiO_2 sample are shown in Fig. 4.15(a) and (b), respectively. Although the TiO_2 layers of both samples seem to be composed of granules near the TiO_2/Pt BE interface, the crystallinity of the TiO_2 layer in the SP-Pt sample appeared to be better than that in the EB-Pt sample, particularly at the region far from the interface. Selected-area electron diffraction (SAED) images taken from the TiO_2 areas in Fig. 4.15(a) both at a distance of approximately 60 nm from the TiO_2/Pt interface and near the interface in the EB-Pt sample, as shown in Fig. 4.16. Several diffraction spots of d_1, d_2, and d_3 exhibit rutile-type TiO_2 (110), (101), and (310), respectively. Thus, the EB-Pt sample in Fig. 4.16(b) exhibits more diffraction spots based on different crystalline phases than the SP-Pt sample in Fig. 4.16(a). As a result, at greater distances from the TiO_2/Pt interface, the crystallinity of the TiO_2 layer tends to improve. Note that the difference of the crystallinity of the TiO_2 layer along the thickness direction is not an important factor for the Pt/TiO_2/Pt RS cells because the TiO_2 layers are sufficiently thin. Rather the crystallinity depends on the deposition method of the Pt BE layers as described above.

The authors attempted to confirm the crystalline structure and the crystalline orientation by non-destructive method. One of the appropriate characterization methods is XRD. However, if the structure of characterized layers is not single crystal, the thickness of the layer should be relatively large (normally larger than the thickness of resistance change materials in RS cells) because the intensities of the XRD diffraction peaks are too weak.

Figure 4.17 shows out-of-plane XRD curves of both the NiO samples. The thickness of NiO layers is approximately 100 nm. The XRD curves reveal that not only the NiO layer but also the Pt BE in the EB-Pt samples exhibits diffraction peaks by both (111) and (200) planes, which indicates that the crystalline orientation is not so strong. In contrast, columns of the NiO layer and Pt BE in the SP-Pt samples are preferentially oriented to the [111] direction, which agrees the cross-sectional TEM (XTEM) shown in Fig. 4.14(b). In the case of a sample with NiO deposited under condition B on an EB-Pt layer, it was confirmed that the AFM image of NiO resembles the typical NiO surfaces deposited under condition A on the EB-Pt layers (namely of the EB-Pt samples), and that a NiO (200) peak in XRD was observed. In contrast, Fig. 4.18 shows out-of-plane XRD curves of both the TiO_2 samples. The thickness of TiO_2 layers is approximately 500 nm. The Pt (111) and (200) diffraction peaks can be observed in the EB-Pt samples, whereas only (111) diffraction peak from Pt BE exhibits in the SP-Pt samples in analogy with NiO samples. Furthermore, both TiO_2 samples include many diffraction peaks corresponding to anatase-type TiO_2, whereas the EB-Pt samples indicate the existence of rutile-type TiO_2 component. Therefore, the crystalline structure of NiO and TiO_2 layers strongly depends on that of Pt BE. The tendency is confirmed to be true in the sputtering parameters during NiO or TiO_2 deposition,

The authors performed in-plane XRD measurements, irradiating both samples with X-ray at a small incident angle because the diffraction peaks from polycrystalline thin films for RS cells is available. In-plane XRD measurements for NiO samples were not conducted because the thickness

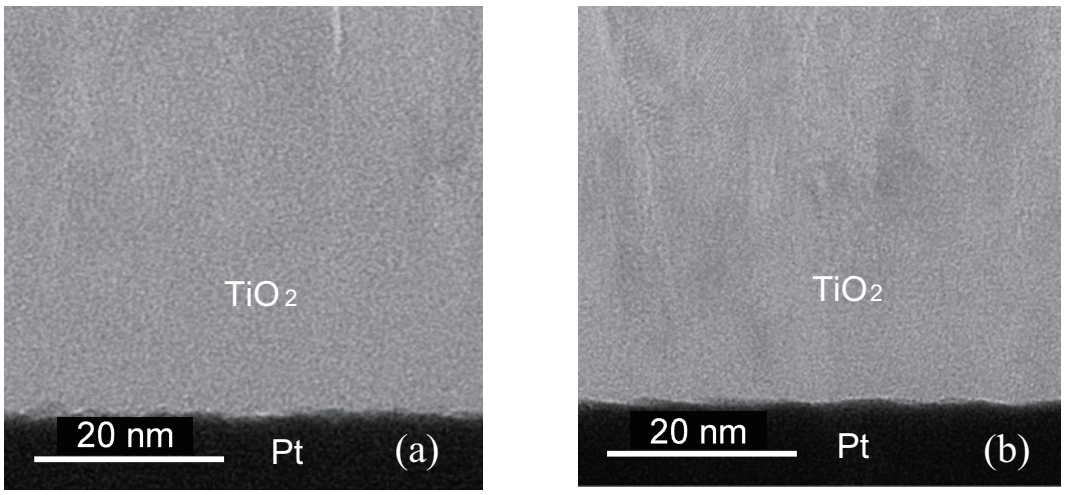

Figure 4.15: Cross-sectional TEM images of (a) the EB-Pt TiO_2 samples and (b) the SP-Pt TiO_2 samples.

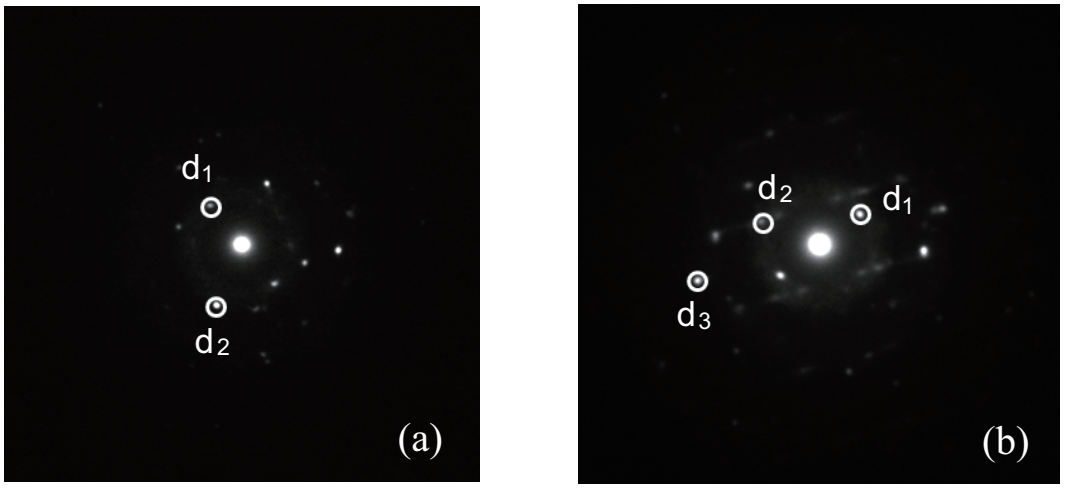

Figure 4.16: Selected area electron diffraction (SAED) patterns of (a) an area of TiO_2 at a distance approximately 60 nm from the TiO_2/Pt interface and (b) an area of TiO_2 near the interface of the EB-Pt sample. Several diffraction spots of d_1, d_2, and d_3 indicates rutile-type TiO_2 (110), (101), and (310), respectively.

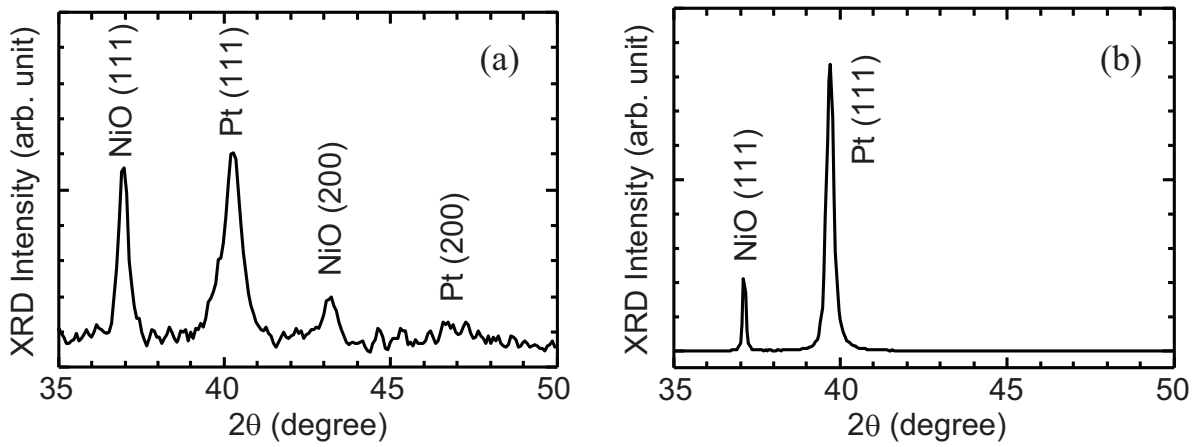

Figure 4.17: Out-of-plane XRD curves of (a) the EB-Pt NiO samples and (b) the SP-Pt NiO samples. The thickness of NiO layers is approximately 100 nm.

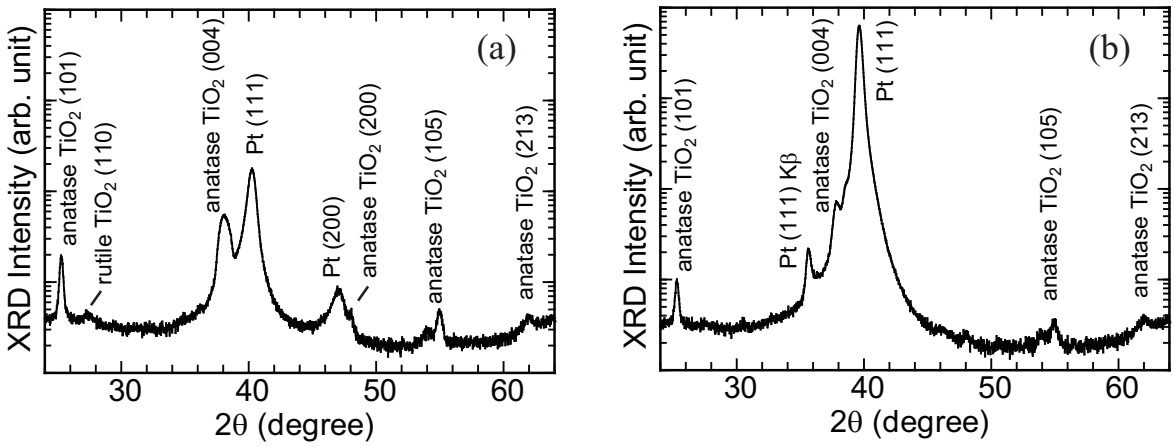

Figure 4.18: Out-of-plane XRD curves of (a) the EB-Pt TiO_2 samples and (b) the SP-Pt TiO_2 samples. The thickness of TiO_2 layers is approximately 500 nm.

of NiO layers is nearly equivalent to that in RS cells and out-of-plane XRD of the samples already done. The XRD patterns of Pt/TiO_2/Pt RS samples were also investigated, as shown in Fig. 4.19. Pt BEs were deposited by EB evaporation (the EB-Pt sample) and sputtering (the SP-Pt sample), and the thickness of TiO_2 was 40 nm. Although the SP-Pt sample is expected to exhibit only a (220) diffraction peak from Pt BEs, corresponding to the $[1\bar{1}0]$ plane perpendicular to the [111] preferential orientation, additional diffraction peaks from (111), (200), and (220) are detected, as shown in Fig. 4.19(b). Thus, the in-plane XRD measurements reveal that the SP-Pt sample contains Pt TEs and additional peaks derived from the polycrystalline Pt TEs with an almost random orientation. Several diffraction peaks from rutile-type TiO_2 (110), (101), and (310) in Fig. 4.19(a) agree with the SAED images shown in Fig. 4.16. Moreover, the diffraction peaks from the TiO_2 layers in both samples reveal that the crystalline structure of the TiO_2 layers in both samples is mainly a rutile-type polycrystal. Here, the integrated intensity ratio of the rutile-type TiO_2 (101) to (310) diffraction peaks in the SP-Pt sample was more than twice as high as that of the EB-Pt sample. The EB-Pt sample peak ratio was very similar to that of powdered TiO_2 with randomly oriented crystallites. Furthermore, the grain size from full width at half maximum (FWHM) of the rutile-type TiO_2 (101) diffraction peaks was estimated by using the Scherrer equation. The FWHM is 1.0 degree in the EB-Pt sample and 1.3 degree in the SP-Pt sample. Although the estimated grain size of TiO_2 in the EB-Pt sample is a bit larger than that in the SP-Pt sample, the EB-Pt sample includes an anatase-type TiO_2 component, as shown in Fig. 4.19(a), and the in-plane crystalline orientation of the rutile-type TiO_2 (101) in the SP-Pt sample is greater, These results indicate that the TiO_2 crystallinity of the SP-Pt sample is better than that of the EB-Pt sample. In addition, compared to Fig. 4.19(a) and (c), Pt BE thickness tends to affect the crystallinity of the TiO_2 layers. The crystalline structure of the TiO_2 layers on the thinner EB-Pt samples is amorphous. Therefore, the crystalline orientation of the TiO_2 layers as well as NiO layers depends on the deposition method of the lower Pt BE layers.

4.3.3 Discussion

The crystallinities of NiO and TiO_2 layers are confirmed to depend on the crystallinity of Pt BE as described in Section 4.3.2. NiO layers on Pt BEs deposited by sputtering are preferentially oriented to the [111] direction, which agrees with the XRD results of the author's group in the same structures with NiO thickness of 640 nm [12]. The author determined that the cause of the strong [111] crystalline orientation of the NiO can be the [111]-oriented columnar polycrystalline structure of Pt BEs, because both NiO and Pt compose a cubic crystalline structure. The difference of crystal lattice constant between them is only approximately 6%, and thus, a NiO layer has a high affinity for a Pt BE. In contrast, TiO_2 composes normally three types of crystal forms. In the author's results, anatase and rutile-type with different crystalline structures each other can be obtained. A TiO_2 layer does not have affinity for Pt BEs because the crystalline structures of anatase and rutile-type TiO_2 differ from cubic one such as Pt. However, the crystalline structure of TiO_2 layers exhibits dependence of the crystalline orientation of Pt BEs. Note that the crystalline

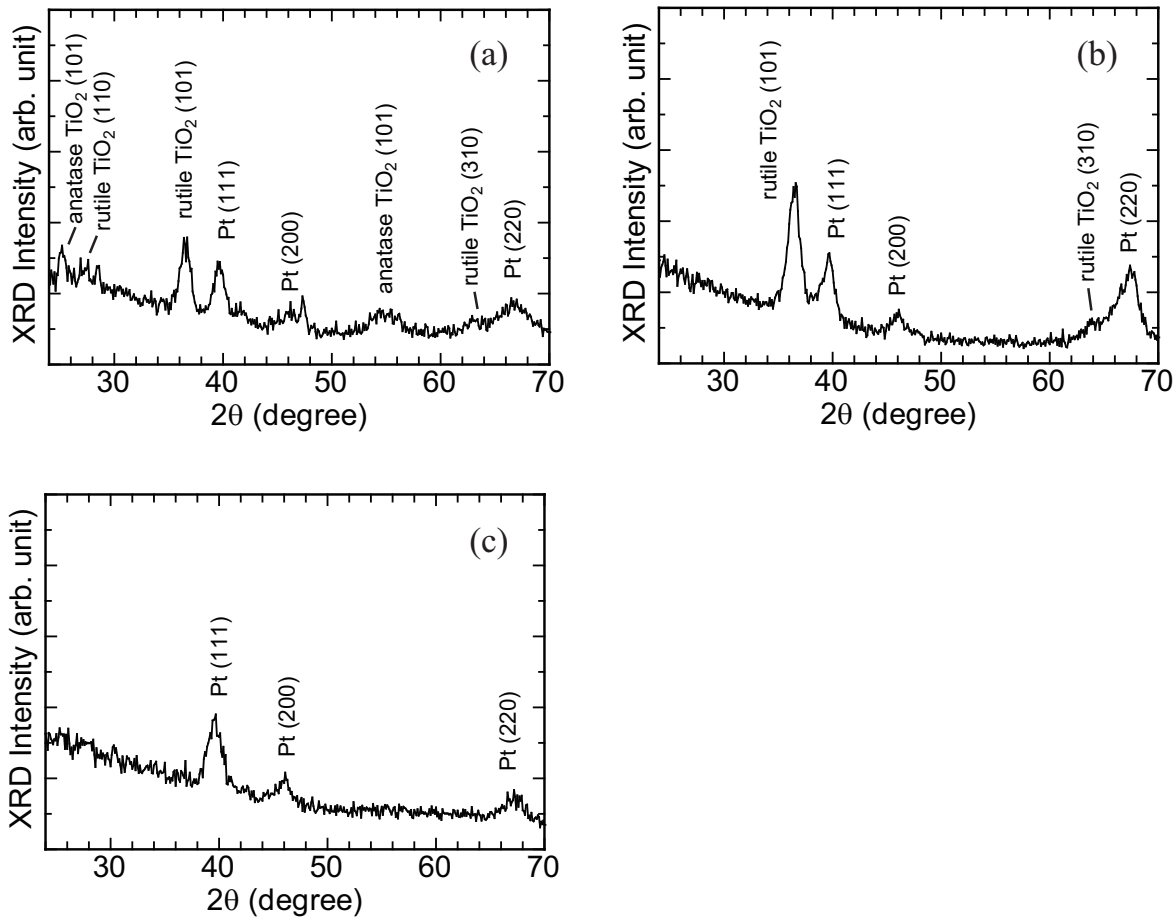

Figure 4.19: In-plane XRD curves of (a) the EB-Pt TiO_2 samples, (b) the SP-Pt TiO_2 samples, and (c) the thinner EB-Pt TiO_2 samples. The thickness of TiO_2 layers is approximately 40 nm.

structure of TiO_2 layers changes as the TiO_2 thickness increases. Figure 4.20 shows typical cross-sectional TEM images of the EB-Pt TiO_2 samples and the SP-Pt TiO_2 samples. Although both samples near the TiO_2/Pt interface exhibit seemingly amorphous regions (irregular vague parts in the figure), the average thickness of the amorphous in the EB-Pt sample is larger than that in the SP-Pt sample. Considering the SAED images shown in Fig. 4.16 taken from the area in the EB-Pt sample, amorphous regions seem to transfer gradually to rutile-type TiO_2 as a TiO_2 thickness increases. Furthermore, the in-plane XRD curves shown in Fig. 4.19 and Fig. 4.21 reveal that the rutile-type TiO_2 transfers finally to anatase-type TiO_2. The fact that the crystallinity of the TiO_2 layer improves as a TiO_2 thickness increases, which suggests that the influence of crystalline orientation of the Pt BE on the crystallinity of the TiO_2 layer decreased gradually during deposition. In addition, comparison between the out-of-plane XRD in Fig. 4.18 and in-plane XRD in Fig. 4.21 reveals the stronger [001] crystalline orientation of the anatase-type TiO_2 in the SP-Pt samples to the thickness direction than in the EB-Pt samples. As a consequence, the influence of crystalline orientation of the Pt BE in the EB-Pt samples is weaker than that in the SP-Pt samples. The results above indicate the possibility of controlling the crystalline structure and the crystalline orientation of TiO_2.

The author should consider the effect of NiO deposition condition on the crystallinity of the NiO layers. In short, the difference of condition A for the EB-Pt samples and condition B for the SP-Pt samples is complicated, and therefore, the author confirmed the effect. The substrate temperature during NiO deposition was 350°C or RT. NiO layers in both samples were deposited under the same condition at each substrate temperature. The Ar and O_2 flow rates were 7.8 sccm and 1.00 sccm at total gas pressure of 0.6 Pa, respectively, in which the reactive sputtering mode was kept as a metallic mode. As a referenced sample, the author prepared a NiO layer deposited in an oxide mode on the SP-Pt BE. The Ar and O_2 flow rates were 7.8 sccm and 2.00 sccm at total gas pressure of 0.64 Pa, respectively. The thickness of NiO layers was approximately 30 nm.

Figure 4.22 exhibits typical cross-sectional TEM images of these NiO samples. These typical characteristics (contrast, Moiré fringe, *etc*.) indicate a granular polycrystalline structure of NiO layers on the EB-Pt BEs and a columnar polycrystalline structure of NiO layers on the SP-Pt BEs irrespective of substrate temperatures during NiO deposition. The NiO/Pt interface roughness on the EB-Pt BEs is larger than that on the SP-Pt BEs. Nevertheless in Fig. 4.22(e), the crystalline structure of the NiO layer deposited in an oxide mode exhibits remarked difference from others. In-plane XRD curves shown in Fig. 4.23 confirms the results from the viewpoint of crystalline orientations. Obvious diffraction peaks from (111), (200), and (220) of both NiO layers and Pt BEs are obtained in the EB-Pt samples, indicating that the crystalline orientation of NiO layers and Pt BEs is almost random. In contrast, Pt (220) and NiO (220) diffraction peaks is much stronger than the other peaks in the SP-Pt samples. The (220) diffraction peaks in in-plane XRD curves correspond to the $[1\bar{1}0]$ plane perpendicular to the [111] preferential orientation along the thickness direction of NiO layers and Pt BEs. The substrate temperature dependence of their crystalline orientation reveals that the preferential degree of [111]-oriented NiO columnar structure becomes stronger as the substrate temperature during NiO deposition enhances on the SP-Pt BEs.

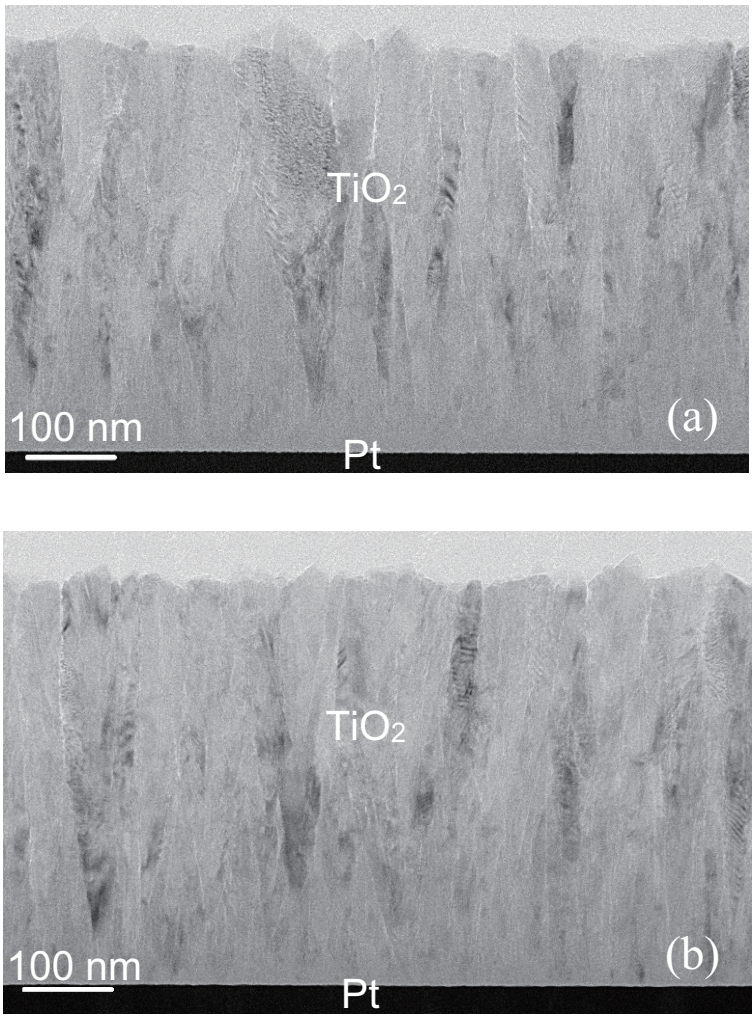

Figure 4.20: Typical cross-sectional TEM images of (a) the EB-Pt TiO_2 samples and (b) the SP-Pt TiO_2 samples. The thickness of TiO_2 layers is approximately 500 nm.

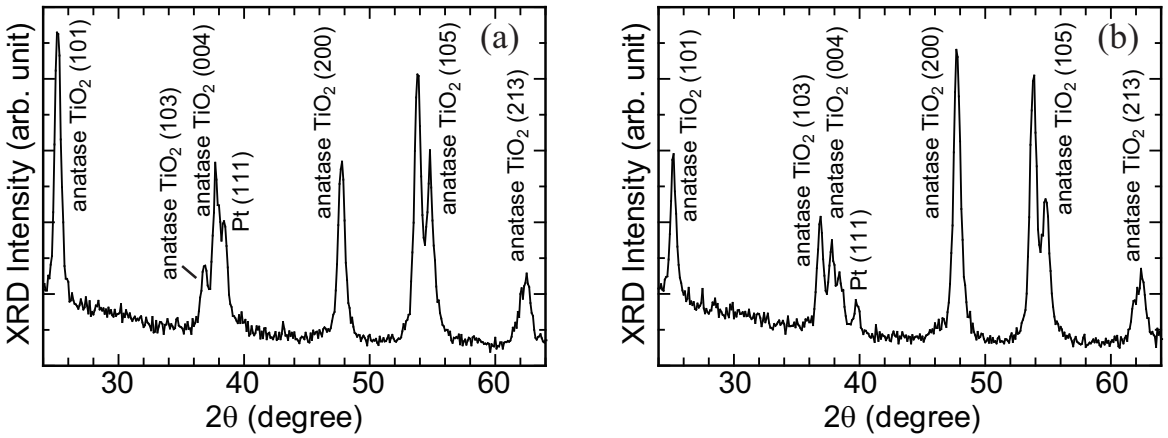

Figure 4.21: In-plane XRD curves of (a) the EB-Pt TiO_2 samples and (b) the SP-Pt TiO_2 samples. The thickness of TiO_2 layers is approximately 500 nm.

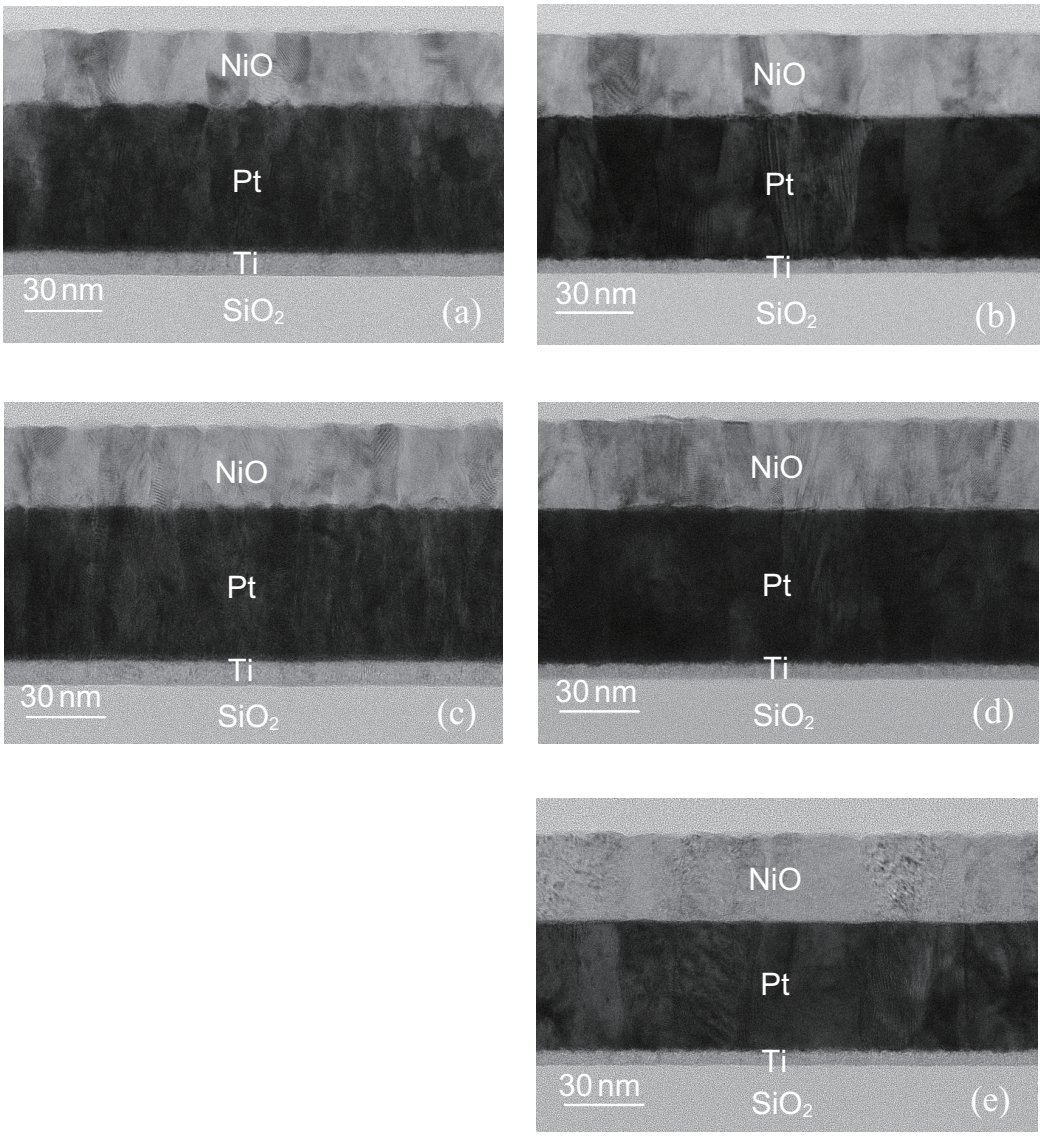

Figure 4.22: Typical cross-sectional TEM images of NiO samples. NiO layers were deposited at 350°C on (a) EB-Pt BEs and (b) SP-Pt BEs, or at RT on (c) EB-Pt BEs (d) SP-Pt BEs, respectively. In addition, NiO layers were deposited at RT on (e) SP-Pt BEs in the oxide mode.

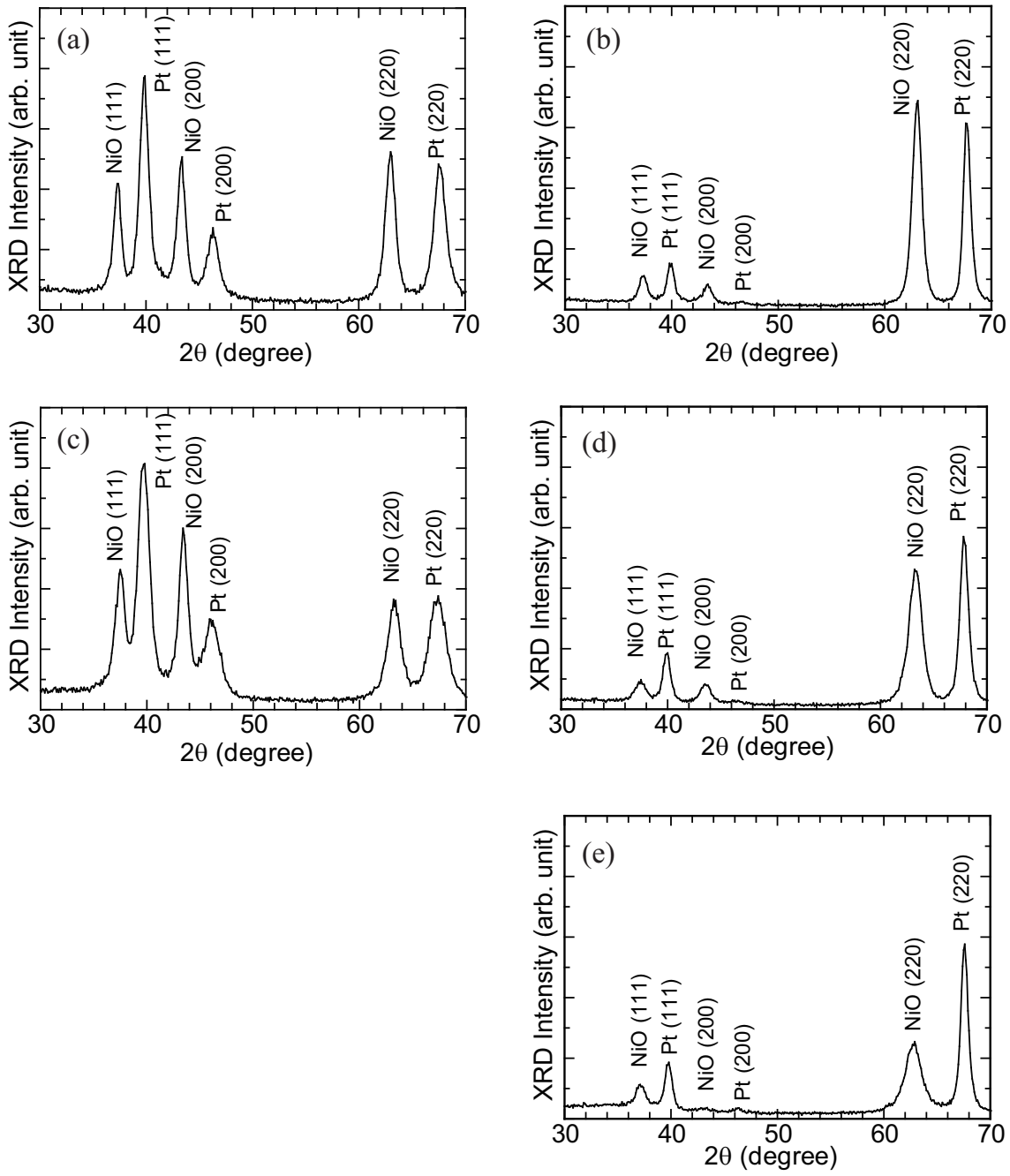

Figure 4.23: In-plane XRD curves of NiO samples. NiO layers were deposited at 350°C on (a) EB-Pt BEs and (b) SP-Pt BEs, or at RT on (c) EB-Pt BEs (d) SP-Pt BEs, respectively. In addition, NiO layers were deposited at RT on (e) SP-Pt BEs in the oxide mode. The thickness of NiO layers is approximately 30 nm.

Intriguingly, the NiO layer deposited in an oxide mode suggests the [111]-oriented NiO component on the SP-Pt BEs, weaker than that in NiO layer deposited in a metallic mode.

4.4 Weibull Distribution of Forming Characteristics

4.4.1 Weibull distribution

TDDB is a widely accepted characterization technique of breakdown in SiO_2 of MOS structures. This analysis is based on a percolation model, where percolation paths are formed by defects due to electrical stress [3–5]. The statistics of the time to breakdown (t_{BD}) can be described by the Weibull distribution:

$$F = 1 - \exp\left(\frac{t_{BD}}{\alpha}\right)^{\beta}, \tag{4.1}$$

$$W = \ln(-\ln(1-F)) = \beta \ln(t_{BD}) - \beta \ln(\alpha), \tag{4.2}$$

where F is the cumulative breakdown probability, W the index of Weibull distribution (Weibit), α a scale factor which means a modal value of 63% of the samples to breakdown, and β a shape factor equivalent to a slope of Weibit.

Forming in RS cells by a conductive filament exhibits some analogies with dielectric breakdown of SiO_2 thin films in MOS structures [2]. The distribution of time to forming in RS cells under constant voltage stress can be similar to that of time to SiO_2 breakdown. Despite the analogy with breakdown, there are few studies on statistical analyses of TDF characteristics in RS cells using NiO, which is known as one of the most promising TMOs [6]. In this section, the authors investigated TDF characteristics in Pt/NiO/Pt and Pt/TiO_2/Pt cells in the EB-Pt samples and the SP-Pt samples. The characteristic parameters in constant voltage TDF of time to forming (t_{form}) can replace t_{BD} described above.

In electrical measurements, a Pt BE was grounded and the positive or negative bias voltage was applied to a Pt TE. Current-voltage (I–V) characteristics of the cells were measured in a voltage-sweep mode using a Keithley 4200-SCS semiconductor parameter analyzer at RT. The current compliance (I_{comp}) was set to be 10 mA to prevent catastrophic breakdown of the cells at forming. Note that most of the cells in both samples were confirmed to exhibit unipolar and bipolar type RS characteristics after forming. Forming voltage (V_{form}) in cells in NiO samples exhibits a large variation, as shown in Fig. 4.24. For example, V_{form} values in the EB-Pt NiO samples are 4.0−6.0 V, and the values in the SP-Pt NiO samples are 3.5−7.5 V. Values of initial resistance (R_{ini}) at 0.1 V in the EB-Pt NiO samples with a NiO thickness of 50 nm and a TE diameter of 100 μm are in the range of 10−200 kΩ, whereas the values in the SP-Pt NiO samples with a NiO thickness of 60 nm and a TE diameter of 200 μm are approximately 70 kΩ.

Figure 4.25 shows typical I–V characteristics in the initial state obtained by a voltage sweep of the Pt/TiO_2/Pt resistive switching cells with a TiO_2 thickness of 30 nm. The range of V_{form} values in the EB-Pt TiO_2 samples is 2.7−5.1 V, whereas that in the SP-Pt TiO_2 samples is 5.0−9.3 V. Similar tendencies for the forming characteristics in samples with the other TiO_2 thickness were

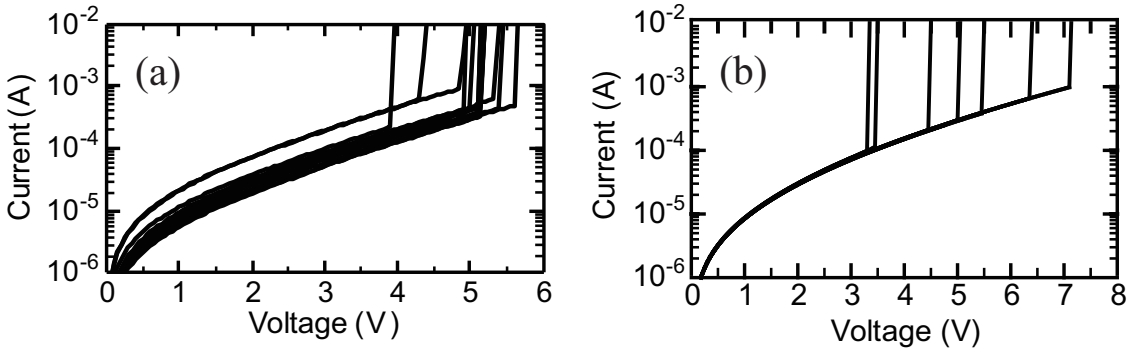

Figure 4.24: Typical current-voltage curves in (a) the EB-Pt NiO samples with a TE-diameter of 100 μm and a NiO thickness of 50 nm, and in (b) the SP-Pt NiO samples with a TE-diameter of 200 μm and a NiO thickness of 60 nm.

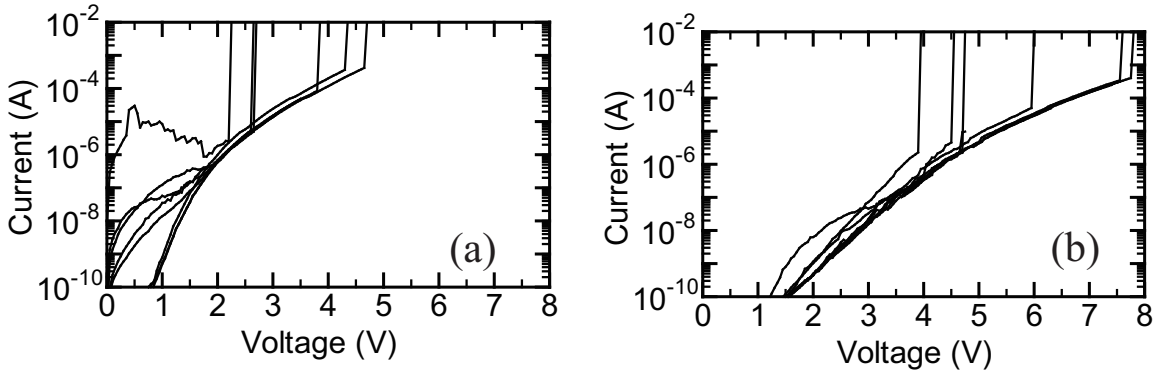

Figure 4.25: Typical current-voltage curves in (a) the EB-Pt TiO_2 samples and (b) the SP-Pt TiO_2 samples. A TE-diameter and TiO_2 thickness are 100 μm and 30 nm, respectively.

confirmed. The distributions of R_{ini} for the EB-Pt TiO_2 samples and the SP-Pt TiO_2 samples with different TiO_2 thickness was also investigated. Here, R_{ini} denotes cell resistance at 1 V, because the resistivity of TiO_2 layers are much larger than that of NiO layers. In the case of a TiO_2 thickness of 30 nm, the ranges of R_{ini} in the EB-Pt TiO_2 samples and the SP-Pt TiO_2 samples are from 0.1 MΩ to 2 GΩ and from 40 GΩ to 350 GΩ, respectively. This result indicates that the R_{ini} values in the EB-Pt TiO_2 samples are smaller than those in the SP-Pt TiO_2 samples. Furthermore, the variation of R_{ini} in the EB-Pt TiO_2 samples is much larger than that in the SP-Pt TiO_2 samples. As a result, variation of R_{ini} does not affect that of V_{form} although V_{form} tends to increase with an increase in R_{ini}.

Values of t_{form} in the cells were measured while keeping a constant applied voltage, value of which (setting voltage: V_{S}) was 50−95% of the typical V_{form} in each sample. Typical current-time (I–t) characteristics during constant voltage stress are shown in Fig. 4.26. Here, I_{comp} was selected as 10 mA to prevent sudden breakdown of the cells at forming. Figure 4.26(a) shows several $I-t$ curves of the EB-Pt NiO samples with a TE-diameter of 50 μm and a NiO thickness of 50 nm under V_{S} of 3.25 V. The range of current levels at even the same voltage reflects a large distribution of initial cell resistance. Figure 4.26(b) shows several $I-t$ curves of the SP-Pt NiO samples with a TE-diameter of 200 μm and a NiO thickness of 80 nm under V_{S} of 7.0 V. These figures demonstrate that cell resistance remains almost unchanged before abrupt resistance degradation (forming). After forming, all of the cells in both samples were confirmed to exhibit sufficiently low resistance in the range of 20−200 Ω and to show repeatable RS characteristics.

Figure 4.27 shows the typical $I-t$ characteristics in the EB-Pt and SP-Pt TiO_2 samples with a TiO_2 thickness of 35 nm under V_{S} of 6.6 V and 4.2 V, respectively. Here, the authors regard t_{form} as the time to reach I_{comp} despite a gradual increase in current before forming. The range of t_{form} in the EB-Pt TiO_2 samples was larger than that in the SP-Pt TiO_2 samples although the current levels before forming were very similar to each other. The similarity of the current levels under different values of V_{S} indicates that the differences in the voltage were a few tens of μA for both samples, as shown in Fig. 4.25. Moreover, current before forming gradually increases in the EB-Pt TiO_2 samples, whereas it slightly decreases in the SP-Pt TiO_2 samples. Note that the small range of the current level (approximately 0.01−1 mA) before forming in both samples is not linked with the initial cell resistance at voltages less than approximately 2 V (including R_{ini}), as can be seen from Fig. 4.25.

4.4.2 Cell size dependence of Weibits

Figure 4.28(a) shows Weibits of t_{form} for five cell sizes under V_{S} of 3.25 V in the EB-Pt NiO sample with a NiO thickness of 50 nm. The cell size dependence of Weibits of t_{form} in SP-Pt NiO sample with a NiO thickness of 80 nm is shown in Fig. 4.28(b). The V_{S} value was set as 7.0 V, about 80% of the scale factor of Weibits of V_{form} in the cells with a diameter of 100 μm. As the cell size increases, t_{form} tends to decrease. This characteristic reflects the result that the values of V_{form} decrease with increased the cell size. The Weibits in the EB-Pt NiO samples and the SP-Pt

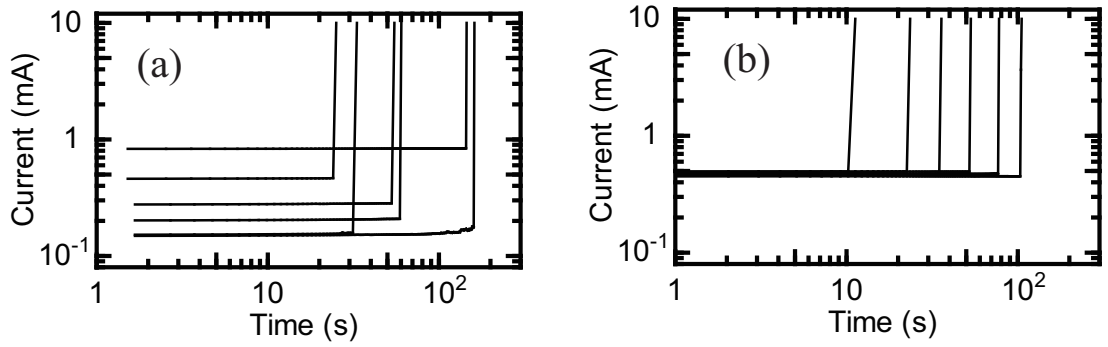

Figure 4.26: Representative current-time curves of (a) the EB-Pt NiO samples with a TE-diameter of 50 μm and a NiO thickness of 50 nm under V_S of 3.25 V, and of (b) the SP-Pt NiO samples with a TE-diameter of 200 μm and a NiO thickness of 80 nm under V_S of 7.0 V.

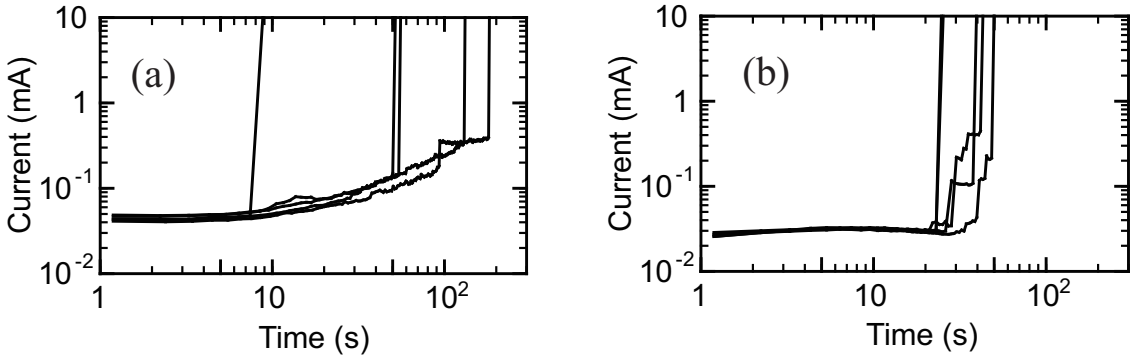

Figure 4.27: Representative current-time curves of (a) the EB-Pt TiO_2 samples under V_S of 4.2 V, and of (b) the SP-Pt TiO_2 samples under V_S of 6.6 V. A TE-diameter and TiO_2 thickness are 100 μm and 35 nm, respectively.

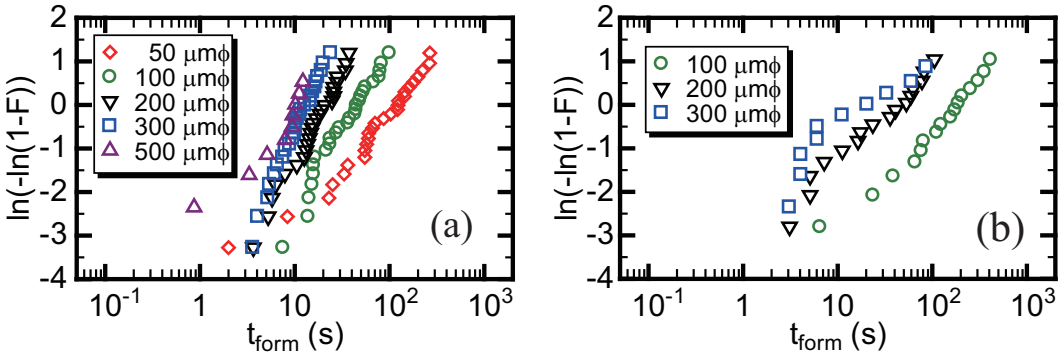

Figure 4.28: Individual Weibits of t_{form} for different cell sizes of (a) the EB-Pt NiO samples with a NiO thickness of 50 nm under V_S of 3.25 V, and of (b) the SP-Pt NiO samples with a NiO thickness of 80 nm under V_S of 7.0 V.

NiO samples with different diameters exhibit different lines with a similar slope of 1.5 and 0.9, respectively. Note that the slope of the EB-Pt NiO samples is clearly larger than that of the SP-Pt NiO samples, indicating that distributions of t_{form} in the EB-Pt NiO samples are smaller than those in the SP-Pt NiO samples.

The forming characteristics above can be quantitatively evaluated due to analogy with SiO_2 breakdown. When defects related to the intrinsic breakdown in SiO_2 thin films are randomly distributed according to Poisson statistics, the cumulative breakdown probability can be described as follow [13]:

$$F = 1 - \exp\left(-DA\right), \tag{4.3}$$

where D is the defect density in a SiO_2 layer and A is a cell area. From Eqs. (4.1) and (4.3), the area scaling law using the reference area A_0 can be expressed by [13, 14]

$$\ln\left(-\frac{\ln(1-F)}{A/A_0}\right) = \beta \ln(t_{\mathrm{BD}}) + \text{const.} \tag{4.4}$$

It is well known that formation of percolation paths, namely breakdown in SiO_2 thin films follows a weakest-link theory as an empirical model and satisfies Eq. (4.4) [3, 13].

Weibits of t_{form} in the EB-Pt NiO sample normalized by reference area A_0 of $\pi(50\ \mu\mathrm{m}/2)^2$ applying to the area-scaling law are shown in Fig. 4.29(a). Although a few plots less than 10 s are unsatisfied, almost all the normalized Weibits can fall in the same line. Weibits of t_{form} in the SP-Pt NiO sample are normalized with reference area A_0 of $\pi(100\ \mu\mathrm{m}/2)^2$ in the same manner, as shown in Fig. 4.29(b). The normalized Weibits including different cell sizes also overlay each other. At the same time, Fig. 4.30(a) and (b) exhibit the Weibits of t_{form} under V_{S} of 6.0 V and 6.6 V in the EB-Pt TiO_2 samples and the SP-Pt TiO_2 samples with a TiO_2 thickness of 50 nm and 35 nm normalized by A_0 of $\pi(100\ \mu\mathrm{m}/2)^2$ applying to the area-scaling law, respectively. Although some data points with Weibits of less than -2 lay outside the lines in both samples, most data points followed the same lines with different Weibull slopes irrespective of the TiO_2 thickness. From the difference between the Weibull slopes of 1.1 in the EB-Pt TiO_2 samples and 2.5 in the SP-Pt TiO_2 samples, the variation of t_{form} under a constant voltage in the EB-Pt TiO_2 samples is larger than that in the SP-Pt TiO_2 samples.

As a consequence, these results indicate that formation of conductive filaments at the forming process by applying voltage follows a weakest-link theory. Furthermore, the weakest spots seem to be almost randomly distributed in NiO layers and TiO_2 layers according to Poisson statistics, each of which can contribute conductive paths locally generated by an external stress.

4.4.3 Constant voltage and oxide thickness dependence of Weibits

The dependencies of Weibits of t_{form} on an applied constant voltage (V_{S}) were investigated. Figure 4.31(a) shows Weibits of t_{form} in EB-Pt NiO sample with a TE-diameter of 50 μm and a NiO thickness (d_{NiO}) of 30 nm. V_{S} values were varied in the range from 2.5 V to 3.0 V. Although t_{form} values tend to decrease with increased V_{S}, the shape factor β is 1.5 and independent of applied

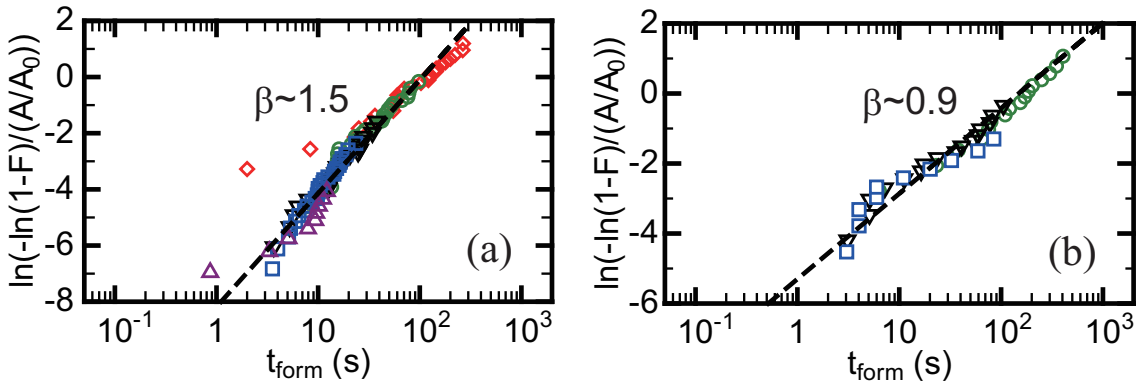

Figure 4.29: Individual Weibits of t_{form} normalized by cell sizes of (a) the EB-Pt NiO samples in Fig. 4.28(a) at A_0 of $\pi(50\ \mu m\ /2)^2$ and of (b) the SP-Pt NiO samples in Fig. 4.28(b) at A_0 of $\pi(100\ \mu m\ /2)^2$.

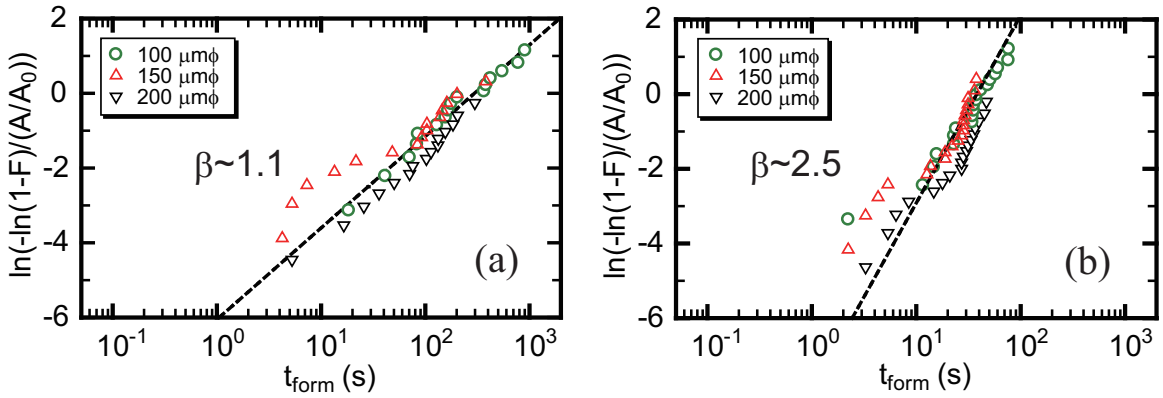

Figure 4.30: Individual Weibits of t_{form} normalized by cell sizes of (a) the EB-Pt TiO_2 samples with a TiO_2 thickness of 50 nm under V_S of 6.0 V and of (b) the SP-Pt TiO_2 samples with a TiO_2 thickness of 35 nm under V_S of 6.6 V at A_0 of $\pi(100\ \mu m\ /2)^2$.

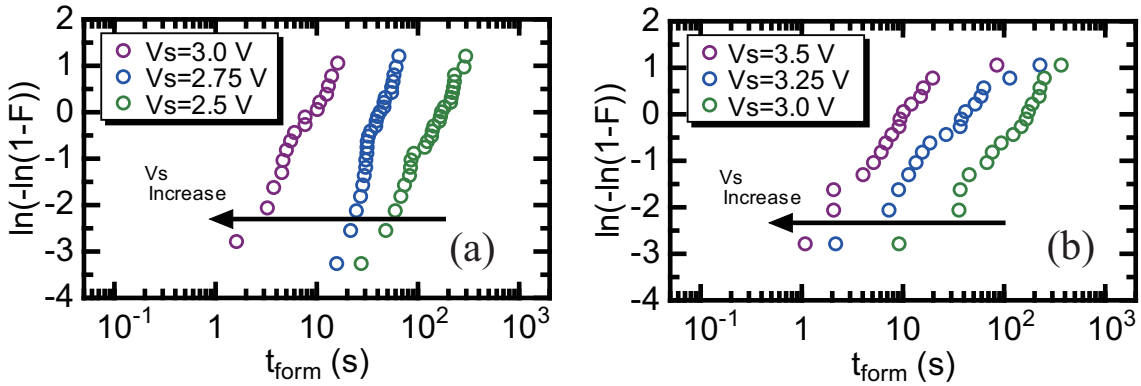

Figure 4.31: Weibits of t_{form} in (a) the EB-Pt samples with a TE-diameter of 50 μm and a NiO thickness of 30 nm and in (b) the SP-Pt samples with a TE-diameter of 200 μm and a NiO thickness of 35 nm.

voltages. Figure 4.31(b) shows Weibits of t_{form} in SP-Pt NiO sample with a TE-diameter of 200 μm and a NiO thickness of 35 nm. V_S values were varied in the range from 3.0 V to 3.5 V. The shape factors of 0.9 are also independent of applied voltages and smaller than the shape factors of 1.5 in EB-Pt NiO samples.

Here, the author assumes uniform distribution of electric field along the thickness of a NiO layer. Figure 4.32(a) shows distributions of t_{form} vs electric field (namely V_S/d_{NiO}) in EB-Pt NiO samples with a TE-diameter of 50 μm and NiO thickness of 30−100 nm. The typical t_{form} decreases almost exponentially with electric field in the cells with the same NiO thickness, tendency of which is the same as the report by Buh [6]. Given the range of t_{form}, larger electric filed is clearly required for thinner NiO layer. Beale *et al.* theoretically analyzed a simple model of dielectric breakdown in a mixture of metal and dielectric layer, by which the average electric field to breakdown decreases logarithmically with thickness (size) of the layer [15]. Although our experimental results are described by t_{form} instead of V_{form}, the NiO thickness dependence of forming electric field (namely V_{form}/d_{NiO}) follow their model. Figure 4.32(b) shows distributions of t_{form} vs electric field in SP-Pt NiO samples with a TE-diameter of 200 μm and NiO thickness of 35−80 nm. Although NiO thickness dependence of forming electric field is less remarkable than that in EB-Pt NiO samples, the above model is satisfied. Note that shape factors of Weibits of t_{form} remain constant (1.5 in EB-Pt NiO samples, 0.9 in SP-Pt NiO samples) and independent of NiO thickness, applied voltages (electric fields), and scale factors of Weibits of t_{form}.

The dependencies of Weibits of t_{form} in TiO_2 samples under V_S of 6−7 V were also investigated. The TiO_2 thickness is 50 nm in the EB-Pt TiO_2 samples and 35 nm in the SP-Pt TiO_2 samples. The value of t_{form} decreased as V_S increased in the both TiO_2 samples, as well as the NiO samples. Note that the β values of 1.1 in the EB-Pt TiO_2 samples were also independent of the applied voltage, and furthermore, these values were smaller than the β values of 2.5 in the SP-Pt TiO_2 samples.

4.4.4 Initial resistance dependence of Weibits

The author investigated correlation between R_{ini} and Weibits of t_{form}. Figure 4.33 shows distributions of R_{ini} vs t_{form} in both (a) EB-Pt NiO sample with a TE-diameter of 50 μm and a NiO thickness of 50 nm and (b) SP-Pt NiO samples with a TE-diameter of 200 μm and NiO thickness of 30−80 nm. In the case of the EB-Pt NiO sample, Fig. 4.32(a) reveals that variation of R_{ini} is large from 10 kΩ to 200 kΩ and that R_{ini} is clearly independent of t_{form}. Moreover, it was confirmed that Weibits of t_{form} of the cells, even when the cells with $R_{ini} < 70$ kΩ were excluded, remained almost unchanged. In contrast, R_{ini} values in the SP-Pt NiO samples with the same NiO thickness are almost constant of 75 kΩ (d_{NiO} =80 nm) and 35 kΩ (d_{NiO} =35 nm). Here, the electric fields of these data are in a range from 0.8 MV/cm to 1.0 MV/cm. Although the variation of R_{ini} is very small, the variation of t_{form} (1−300 s) is larger than that for the EB-Pt NiO sample, which is consistent with the smaller slope of 0.9 as described above. Moreover, the current level before forming in both TiO_2 samples is not linked with the wide range of initial cell resistance at

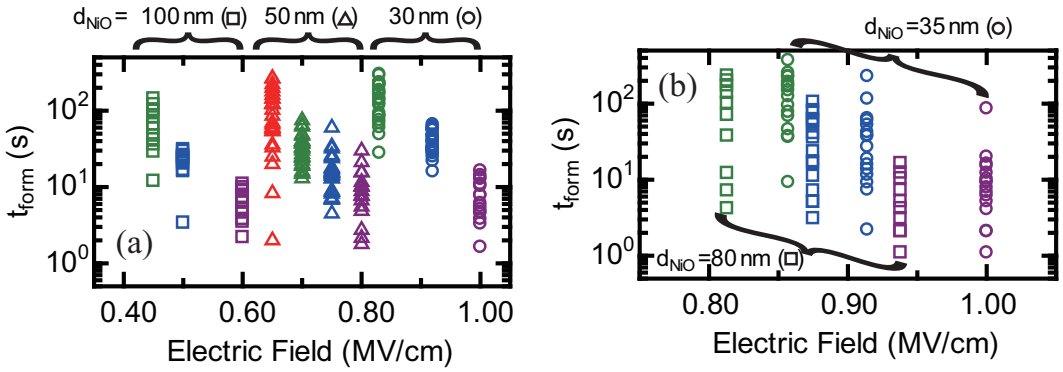

Figure 4.32: Distributions of t_{form} vs electric field in (a) the EB-Pt NiO samples with a TE-diameter of 50 μm and a NiO thickness of 30-100 nm and in (b) the SP-Pt NiO samples with a TE-diameter of 200 μm and a NiO thickness of 35~80 nm.

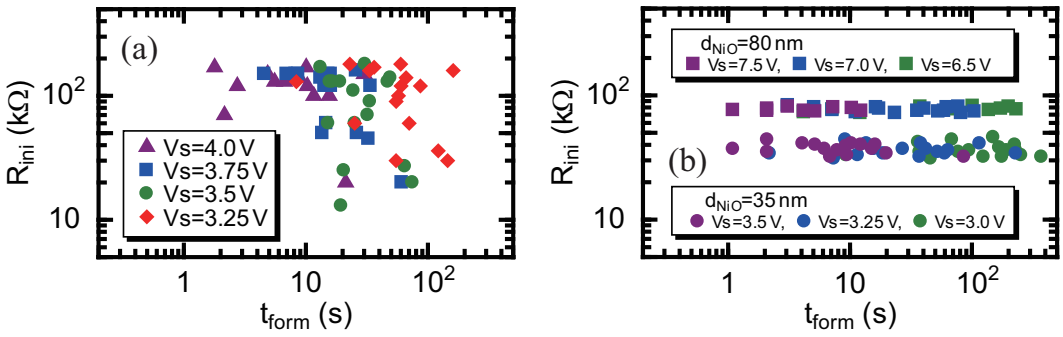

Figure 4.33: Distributions of R_{ini} vs t_{form} in (a) the EB-Pt NiO samples with a TE-diameter of 50 μm and a NiO thickness of 50 nm and in (b) the SP-Pt NiO samples with a TE-diameter of 200 μm and a NiO thickness of 35~80 nm.

voltages less than approximately 2 V, as shown in Fig. 4.25. In cells in the same TiO_2 samples, the distribution of t_{form} is very large, even though the initial resistance values before forming under the same constant voltage are similar, as can be seen from Fig. 4.27. Anyway, these results imply no relation between initial resistance and time to forming.

Meanwhile, the authors estimated the ratio of O to Ti in the TiO_2 layers in both samples by high-resolution RBS. The oxygen composition x in the TiO_x was 1.41 for the EB-Pt TiO_2 samples and 1.57 for the EB-Pt TiO_2 samples. Thus, TiO_2 layers in the EB-Pt TiO_2 samples contained more V_Os than those in the SP-Pt TiO_2 samples, as estimated from the author's previous results of V_O segregation at GB triple points in resistance change oxide layers [16, 17]. Another reason for more V_Os in the EB-Pt TiO_2 samples is that the initial resistance values before forming in the SP-Pt TiO_2 samples were considerably higher than those in the EB-Pt TiO_2 sample. Note that there are considerable differences of the initial cell resistance and forming characteristics of the both TiO_2 samples irrespective of thickness (25−70 nm) as well as the surface roughness of Pt BEs. Thus, the structural and electrical properties of the cells depend on the oxygen composition of the TiO_2 layers and the crystallinity of both the TiO_2 and Pt BEs.

4.4.5 Discussion

First, the surface roughness of Pt BEs and NiO layers is described. The RMS roughness values of Pt BEs increase with increased Pt thickness. For example, in the case of Pt deposited by EB evaporation, the roughness is in a range from 0.3 nm to 0.8 nm as the thickness increases from 25 nm to 70 nm, as described in Section 4.3.1. The typical roughness values of NiO layers tend to increase with increased NiO thickness, in a range of 0.8−1.6 nm for the EB-Pt samples and 0.4−1.0 nm for the SP-Pt samples with NiO thickness of 30−100 nm. Therefore, the shape factors of Weibits of t_{form} were confirmed to be insensitive to roughness (at least in the range of 0.4−1.6 nm).

The author considers that these different properties can originate from a difference of NiO crystallinity. A NiO layer in the EB-Pt NiO samples or the SP-Pt NiO samples is composed of granular or columnar grains of a NiO crystal, respectively. These structures shown in Fig. 4.34(a) can be simplified, as shown in Fig. 4.34(b). A NiO layer in EB-Pt NiO samples is divided into a grid pattern equivalent to GBs (black lines). For simplicity, every grain size is considered to be similar and current can flow either horizontally and vertically through only GB paths. In the case of the SP-Pt NiO samples, GBs exist along only the vertical direction. Assuming that defects which act as the source of conductive paths by forming (white circles) are distributed on several GBs in the initial state, as shown in Fig. 4.34(c). In a random circuit breaker (RCB) model, which can explain not only forming but also unipolar RS behaviors [18], this situation resembles an arrangement of on-state circuit breakers with lower resistivity on several GBs before voltage is applied. The schematic shown in Fig. 4.34(c) reveals that the combination number of conductive paths with a minimum resistivity (arrows) in a NiO layer for the EB-Pt NiO samples can be naturally larger than that for the SP-Pt NiO samples. This result reflects difference of variation

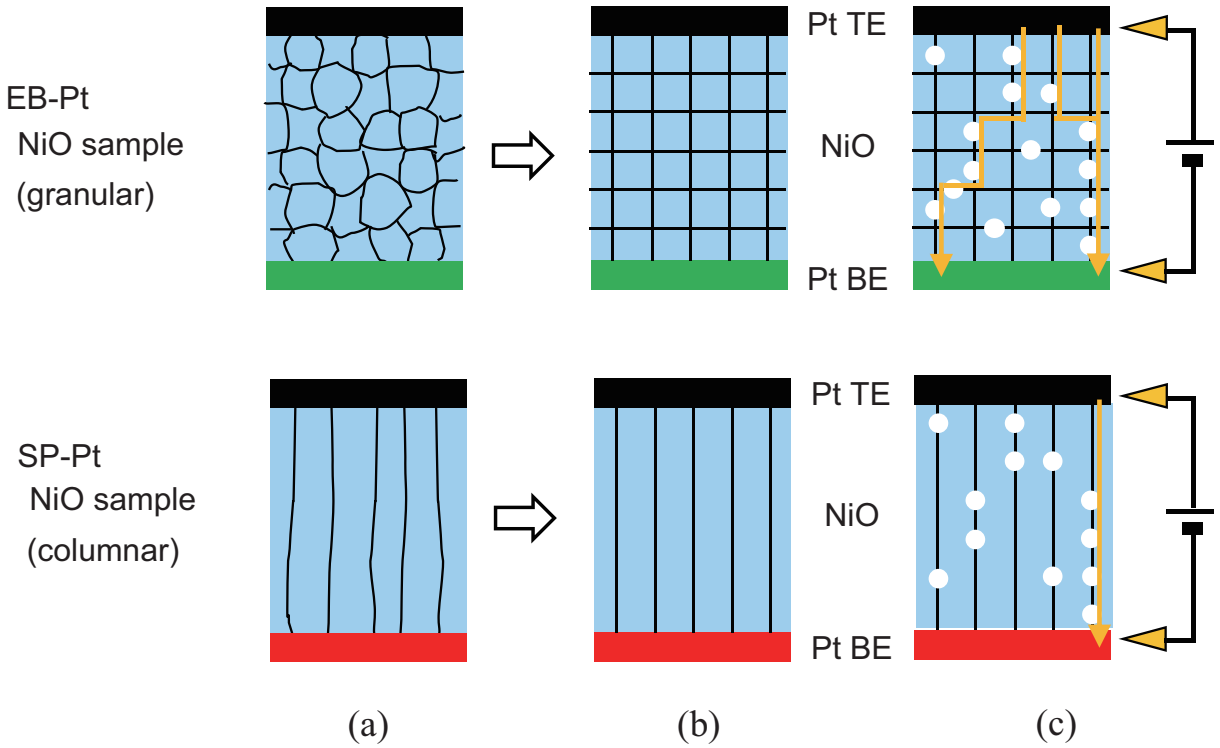

Figure 4.34: (a) Schematics of the cells with granular (in the EB-Pt sample) and columnar (in the SP-Pt sample) structures. (b) The schematics are simplified into grid and stripe pattern, respectively. (c) Randomly distributed defects (white circles) form possible conductive paths (arrows).

of R_{ini}. However, the multiple conductive paths introduce more candidates for weakest defects to forming process by the application of electrical stress. As a result, distribution of t_{form} in the EB-Pt NiO samples becomes more tight than that in the SP-Pt NiO samples. Whereas the driving force for defect generation (switching of on-state circuit breakers from the off-state) is voltage in a RCB model, it is natural to replace it with time to forming in the results for TDF characteristics the author investigated. Although real grain sizes are different from each other and conductive filament networks are complicated, the distribution of TDF characteristics can depend on NiO crystallinity. A small variation in initial resistance tends to result in a large variation of time to forming and vice versa.

Next, the author discusses the difference of the variation of t_{form} between the EB-Pt TiO_2 samples and the SP-Pt TiO_2 samples. The authors can assume that conductive paths with minimum resistivity are created along GBs (mainly at their triple points) with nearly random orientations in the TiO_2 layer. Furthermore, the conductive filaments likely originate from the weakest defects at forming and are created along one of the conductive paths. The multiple conductive paths naturally introduce more candidates for conductive filaments at forming and a larger variation of the forming characteristics, such as t_{form} under a constant voltage stress. In the EB-Pt TiO_2 samples, more V_Os are distributed mainly in GB network in the TiO_2 layer than they are in the similar GB network in the SP-Pt TiO_2 samples; thus, the conductive paths are more pronounced in the EB-Pt TiO_2 samples than in the SP-Pt TiO_2 samples and the variation of t_{form} in the EB-Pt TiO_2 samples became larger than that of the SP-Pt TiO_2 samples.

Finally, the author compared the Weibull distributions of the Pt/TiO_2/Pt cells with the results for Pt/NiO/Pt cells. In the Pt/NiO/Pt cells, the Weibull slope β under a constant voltage was independent of the applied voltage and cell size, which was approximately 1.5 in the EB-Pt NiO samples and approximately 0.9 in the SP-Pt NiO samples. The columnar structure in NiO layers in the SP-Pt samples includes less candidates for weakest defects at forming because of fewer conductive paths along the GBs than the granular structure in NiO layers in the EB-Pt samples, and therefore, the variation of t_{form} in the EB-Pt NiO samples is actually smaller than that in the SP-Pt NiO samples. Conversely, in the Pt/TiO_2/Pt cells, TiO_2 crystalline structures in both samples are commonly composed of granular grains. As a result, the variation of t_{form} decreases as the distribution of R_{ini} decreases in the Pt/TiO_2/Pt cell, while the variation of t_{form} increases as the distribution of R_{ini} decreases in the Pt/NiO/Pt cells as mentioned above.

This clear difference may be partly attributed to different oxide deposition modes during reactive sputtering. In the case of NiO deposition in a metallic mode, the NiO layers react on the sample surface and the NiO crystallinity is affected by the crystallinity of the Pt BEs. Conversely, in the case of TiO_2 deposition in an oxide mode, the effect of crystallinity of the Pt BEs on TiO_2 layers seems to be weaker because of oxide formation at the surface of a Ti sputtering target [19, 20]. Although TiO_2 crystalline structures are commonly composed of granular grains, the differences in crystalline orientations and amounts of V_Os in the TiO_2 layers of the both TiO_2 samples were caused by the crystallinity of the underlying Pt BEs, leading to the different forming characteristics.

4.5 Summary

Thermal annealing affected crystallinity and oxygen composition of NiO layers on Pt BEs. Depth profile of oxygen in the NiO layers was sensitive to thermal annealing conditions, which suggested oxygen diffusion toward the NiO surface. These changes by thermal annealing possibly contributed to obtain multiple resistance states of RS cell.

Moreover, crystallinity and time-dependent forming characteristics on Pt/NiO/Pt and Pt/TiO_2/Pt RS cells were investigated. The NiO layer exhibited a granular or columnar structure in samples on Pt BEs deposited by EB evaporation or sputtering, respectively. Conversely, whereas both the TiO_2 layers exhibited a granular structure in the two types of samples, the concentration of oxygen vacancies and oxygen composition seemed to differ in these sample. In addition, although the Weibull distributions of time to forming (t_{form}) in the samples with different diameters exhibited different lines, almost all the Weibits normalized by cell sizes fell in the same line. This result indicated that the formation of conductive filaments at forming by applying electrical stress followed a weakest-link theory, and that weakest spots and defects such as oxygen vacancies were distributed in NiO and TiO_2 layers according to Poisson statistics. The variation of t_{form} increased as the distribution of initial resistance was reduced in Pt/NiO/Pt cells with different NiO crystallinities. In contrast, the variation of t_{form} decreased as the distribution of the initial resistance was reduced in the case of the Pt/TiO_2/Pt cells. These results reflected differences in both the grain boundary density (crystallinity) and the oxygen-vacancy concentration (oxygen composition) of resistance change materials used in the RS cells. The clear difference of crystallinities and oxygen compositions seemed to originate from differences in the oxide deposition mode during reactive sputtering.

The results in this chapter revealed that where the conductive filament created by forming was at grain boundaries in the TMO layers, and that crystallinities and oxygen compositions of the TMO layers played an important role on forming and RS operation.

References

[1] R. Waser, R. Dittmann, G. Staikov, and K. Szot, Adv. Mater. **21**, 2632 (2009).

[2] H. Akinaga and H. Shima, Proc. IEEE **98**, 2237 (2010).

[3] R. Degraeve, J. L. Ogier, R. Bellens, P. J. Roussel, G. Groeseneken, and H. E. Maes, IEEE Trans. Electron Devices **45**, 472 (1998).

[4] J. Suñé, IEEE Electron Device Lett. **22**, 296 (2001).

[5] E. Y. Wu and J. Suñé, Microelectron. Reliab. **45**, 1809 (2005).

[6] G. Buh, I. Hwang, and B. H. Park, Appl. Phys. Lett. **95**, 142101 (2009).

[7] D.-H. Kwon, K. M. Kim, J. H. Jang, J. M. Jeon, M. H. Lee, G. H. Kim, X.-S. Li, G. Park, B. Lee, S. Han, M. Kim, and C. S. Hwang, Nature Nanotechnology **5**, 148 (2010).

[8] H. Mahne, S. Slesazeck, S. Jakschik, I. Dirnstorfer, and T. Mikolajick, Microelectronic. Eng. **88**, 1148 (2011).

[9] T. Iwata, Y. Nishi, and T. Kimoto, Jap. J. Appl. Phys. **50**, 081102 (2011).

[10] S. Kim, D. Lee, J. Park, S. Jung, W. Lee, J. Shin, J. Woo, G. Choi, and H. Hwang, Nanotechnology **23**, 325702 (2012).

[11] W. Brückner, R. Kaltofen, J. Thomas, M. Hecker, M. Uhlemann, S. Oswald, D. Elefant, and C. M. Schneider, J. Appl. Phys. **94**, 4853 (2003).

[12] T. Iwata, Dr. Thesis, Faculty of Engineering, Kyoto University, Kyoto, 2014.

[13] E. Y. Wu and R.-P. Vollertsen, IEEE Trans. Electron Devices. **49**, 2131 (2002).

[14] R. Degraeve, G. Groeseneken, R. Bellens, J. L. Ogier, M. Depas, P. J. Roussel, and H. E. Maes, IEEE Trans. Electron Devices **45**, 904 (1998).

[15] D. Beale, and B. M. Duxbury, Phys. Rev. B **37**, 2785 (1988).

[16] H. Sasakura, Y. Nishi, and T. Kimoto, Appl. Phys. Lett. **107**, 233510 (2015).

[17] Y. Nishi and T. Kimoto, J. Appl. Phys. **120**, 115308 (2016).

[18] S. C. Chae, J. S. Lee, S. Kim, S. B. Lee, S. H. Chang, C. Liu, B. Kahng, H. Shin, D.-W. Kim, C. U. Jung, S. Seo, M.-J. Lee, and T. W. Noh, Adv. Mater. **20**, 1154 (2008).

[19] S. Berg, J. Vac. Sci. Technol. A **5**, 202 (1987).

[20] S. Berg and T. Nyberg, Thin Solid Films **476**, 215 (2005).

Chapter 5

Formation of Conductive Filaments with a Quantum Point Contact

5.1 Introduction

The resistive switching (RS) mechanism in resistive random access memory (ReRAM), especially using binary transition metal oxide (TMO) layers, has been explained by the formation and rupture of conductive filaments. This reversible resistance transition by applying repeated electrical stress between the low-resistance state (LRS) and the high-resistance state (HRS) can occur after the forming process to create conductive filaments in pristine TMO layers, such as nickel oxide (NiO) and titanium dioxide (TiO_2), between top electrodes (TEs) and bottom electrodes (BEs). The conductive filaments are believed to be composed of oxygen vacancies (V_Os) [1–3] or cation interstitials [4–6], which result in the change of microscopic oxygen stoichiometry and the associated formation of point defects in the TMO layers. The V_Os or cation interstitials typically act as mobile donors because the migration of a negatively charged oxygen ion from the oxygen lattice site creates a positive charge according to the charge neutrality condition.

In particular, RS memories based on the migration of nanoscale ions and a redox reaction are named as valence change memories (VCMs) after this valence change [2]. The voltage polarities between the transition from HRS to LRS (set) and that from LRS to HRS (reset) are opposite in VCMs. In other specific TMO-based RS cells, RS behaviors are, however, not dominated by the migration of oxygen ions but by thermally controlled diffusion and a redox reaction. These RS memories are categorized into thermochemical memories (TCMs) [7]. TCMs exhibit unipolar RS behaviors, which means that the voltage polarities between set and reset are the same, as opposed to bipolar RS behaviors in VCMs. However, RS memories consisting of both one active (oxidizable) electrode, such as silver (Ag) or copper (Cu), and the counter inert electrode, such as platinum (Pt) or titanium nitride (TiN), are widely known as conductive bridging random access memories (CBRAMs) [8]. When a positive voltage is applied to the active electrode, dissolution and ionization of the active metal and bridging of a metallic conductive filament occur to the opposite inert electrode through the TMO layer. The metal ions move toward the

active electrode and the filament is eventually ruptured by application of a negative voltage to the active electrode. This kind of memory is called electrochemical metalization memory (ECM) owing to these electrochemical processes [7]. ECMs show only bipolar RS behaviors. When the scale of the weakest spot in conductive filaments reaches an atomic contact size, conductance quantization is expected to appear. In recent years, the observation of quantized conductance discrete steps, characterized by integer or half integer multiples of $G_0 = 2e^2/h$, has been reported in ECMs [5, 9–15] and VCMs [16–20]. There have only been a few studies on the conductance quantization effect in TCMs [11, 21].

In this chapter, the author investigates the appearance condition of conductance quantization in the Pt/NiO/Pt cells by controlling oxygen (O_2) flow rate during NiO deposition by reactive sputtering. Dependences of both the forming characteristics and oxygen composition ratio at grain boundaries (GBs) in NiO layers on deposition parameters are focused on. Distribution of microscopic oxygen stoichiometry and the source of point defects in the NiO layers are revealed by transmission electron microscopy (TEM) analyses. Moreover, the oxygen composition dependence of semi-forming voltage indicates the correlation between the oxygen stoichiometry of the weakest spot in conductive filaments and the O_2 flow rate. Finally, the RS model based on quantized conductance is also discussed.

5.2 Resistive Switching based on Quantized Conductance

5.2.1 RS cell fabrication

The author prepared two kinds of Pt/NiO/Pt RS samples. One is capacitor-type RS samples, and the other is crossbar-type RS samples. Capacitor-type RS samples can be fabricated by a simple process and therefore is for optimization of NiO deposition to exhibit the specific forming characteristics discussed in later. Crossbar-type RS samples is suitable for a reduction in the accurate RS cell size. The schematic illustration of these samples is shown in Fig. 5.1.

Capacitor-type Pt/NiO/Pt RS samples were fabricated as follows. A Pt BE was deposited by radio-frequency (RF) or DC sputtering on a silicon dioxide (SiO_2)/*p*-Si(100) substrate inserted by a titanium (Ti) adhesion layer. Here, surface roughness, crystalline structures, and crystalline orientations of Pt BEs deposited by RF and DC sputtering can be almost the same, as described in Section 4.3.2. The thickness of the Pt BE was roughly 80 nm. A NiO layer as a resistance change material was subsequently deposited in argon (Ar) and O_2 gas mixture by using reactive RF sputtering system (ANELVA: L-250-FHL). The Ar flow rate was kept at 7.8 sccm. The O_2 flow rate was precisely controlled from 0.90−1.05 sccm in a metallic mode because electrical properties in Pt/NiO/Pt RS cells are sensitive to oxygen composition in a NiO layer. The pressure and the substrate temperature during sputtering were kept at 0.6 Pa and 350°C, respectively. The thickness of the NiO layers was 80 nm. Pt TEs with a diameter of 100 μm and 180 μm (in 50−500 μm) were deposited on the NiO layer by electron beam (EB) evaporation through a metal shadow mask. The Pt/NiO/Pt RS cell size is determined by the area of the TE.

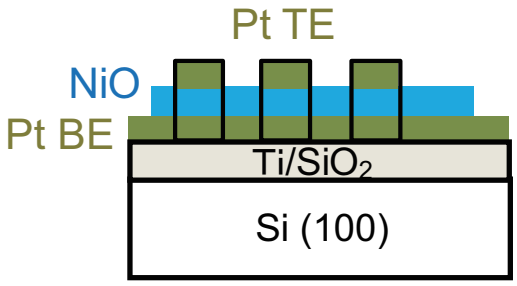

(a) capacitor-type RS sample (cross-sectional)

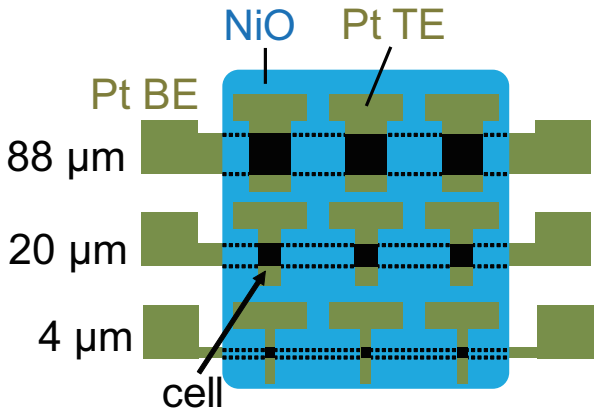

(b) crossbar-type RS sample (top view)

Figure 5.1: Schematic illustration of (a) capacitor-type Pt/NiO/Pt RS samples and (b) crossbar-type Pt/NiO/Pt RS samples.

Crossbar-type Pt/NiO/Pt RS samples were also fabricated to investigate the cell size dependence of the forming characteristics. The Pt/NiO/Pt RS cells were directly sandwiched between bar-shape top and bottom electrodes with pad regions selectively formed by ultra-violet (UV) photolithography. The photolithography process sequence is described in Table 5.1. The Pt TEs of cells were separated from each other to avoid a sneak-path problem [22, 23]. The deposition conditions of Pt BEs and a NiO layer were the same as capacitor-type samples. The thickness of the Pt top and bottom electrodes was approximately 50 nm. Pt TEs were deposited on the NiO layer by DC sputtering. The cell size is equivalent to the cross-point area between both electrodes, which falls under any of 4×4 μm^2, 20×20 μm^2, and 88×88 μm^2.

A Pt BE was grounded and a voltage was applied to a Pt TE. A beryllium-copper (BeCu) probe was contacted to the pad regions without cell areas in the case of the crossbar-type RS samples. Current-voltage (I–V) characteristics, such as the forming characteristics of the cells, were measured in a voltage-sweep mode at room temperature (RT) by using a Keithley 4200-SCS semiconductor parameter analyzer.

5.2.2 Two types of forming

The I–V characteristics in the initial state and RS characteristics of cells in several capacitor-type RS samples were measured. When a NiO layer was deposited by reactive sputtering at a selected O_2 flow rate, the specific characteristics of two types of forming can be observed, as shown in Fig. 5.2.

In the pristine cells, a voltage sweep results in the first abrupt current increase at $V_{\mathrm{s-form}}$. When compliance current (I_{comp}) is relatively low to be approximately 100 μA, cell conductance reaches nearly G_0 corresponding to quantized conductance by the current increase. In the meantime, when I_{comp} is relatively high to be more than 1 mA, a voltage sweep results in a discrete increase of the cell conductance value several times and finally the sudden current jump to I_{comp}. The first abrupt current increase at $V_{\mathrm{s-form}}$ will hereafter be referred to as "semi-forming," and the second one at V_{form2} as "second forming." When a voltage sweep stops just after semi-forming within a relatively low compliance current, an RS behavior can be observed at the cell conductance of below G_0 by the following voltage sweep, as shown in Fig. 5.2(b). After second forming occurs when the compliance current is relatively high, the following applied voltage induces a different RS behavior at the cell conductance of above G_0, as shown in Fig. 5.2(d). Semi-forming and second forming are derived from the following RS characteristics, which involve the initial formation of conductive filaments, nothing but forming process. Moreover, the discrete increase of the cell conductance is based on integer or half-integer multiples of G_0 after semi-forming, as shown in Fig. 5.2(e). Note that $V_{\mathrm{s-form}}$ and V_{form2} of cells exhibited a relatively smaller variation than normal forming voltage.

The author focused on the decrease in forming voltage and reset current at the beginning [24]. The specific characteristics enable the decrease by suppressing a compliance current level. In fact, relatively low forming voltage of 1−2 V can be obtained, which is nearly equivalent to set voltage. However, if I_{comp} is lower than 30 μA before semi-forming, an RS operation occurs with

Table 5.1: Photolithography process sequence.

photoresist formation	
dehydration bake	120°C, 3 min
HMDS vapor coating	140°C, 30 sec
photoresist coating	4000 rpm, 30 sec
pre-bake	100°C, 90 sec
UV exposure	105 mJ/cm^2
development by TMAH(2.38%)	90 sec
post-bake	120°C, 90 sec
SiO_2 etching on Si substrates	150 sec (BHF)
Pt BE deposition	
Lift off	
NiO deposition	
photoresist formation	
photoresist coating	4000 rpm, 30 sec
pre-bake	100°C, 60 sec
UV exposure	105 mJ/cm^2
development by TMAH(2.38%)	90 sec
Pt TE deposition	
Lift off	

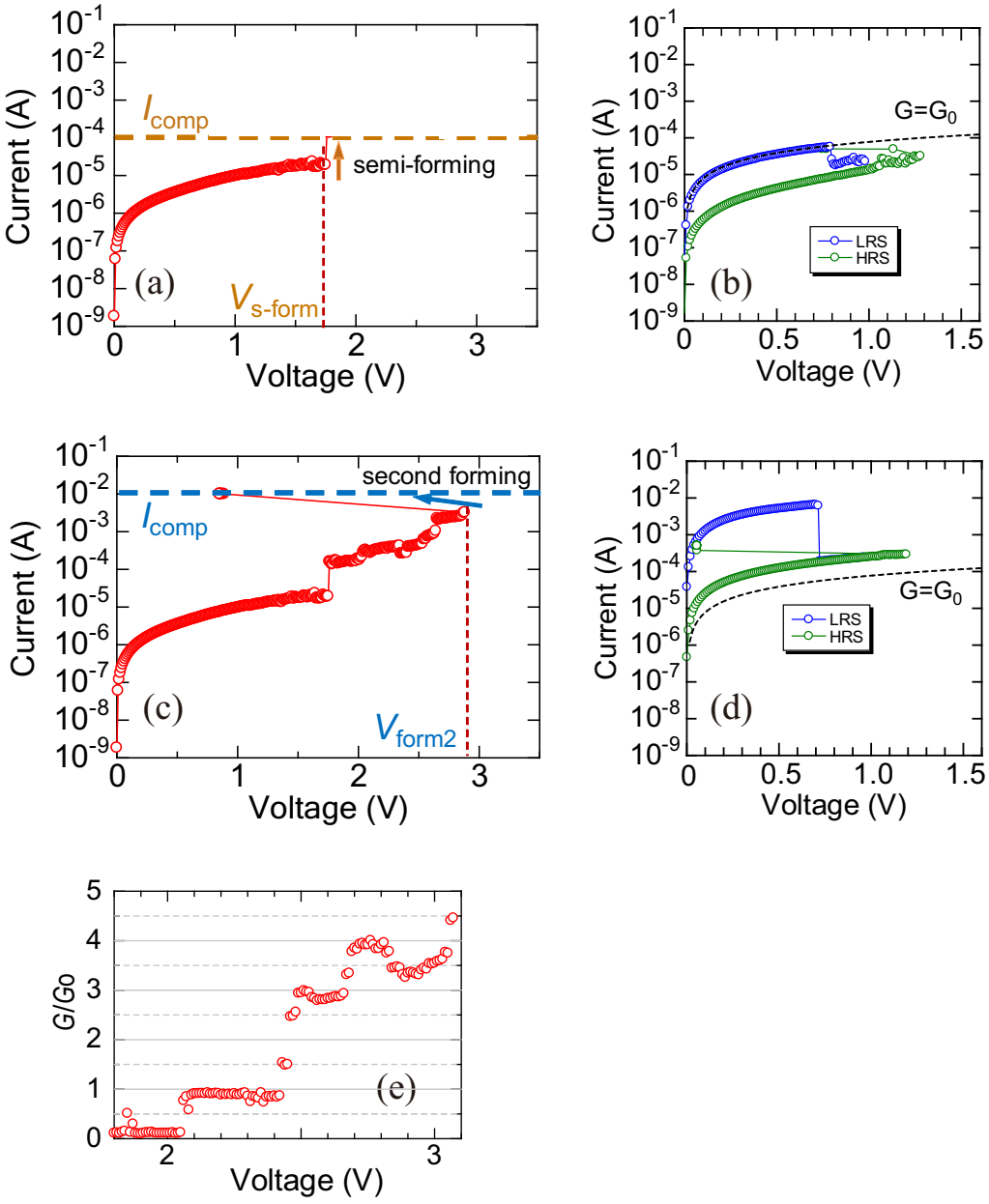

Figure 5.2: Typical $I-V$ characteristics of the forming process showing two modes in Pt/NiO/Pt cells. After (a) semi-forming occurs when compliance current is low, (b) RS operation can be observed at cell conductance of below G_0. After (c) second forming occurs when compliance current is high, (d) RS operation can be observed at cell conductance of above G_0. (e) $G/G_0 - V$ characteristics before second forming.

a cell conductance of lower than even several tens of μS, and therefore an RS behavior based on quantized conductance was hindered by the suppression. Anyway, RS characteristics seem to originate from the formation and rupture of conductive filaments in NiO layers. Hence, the discrete increase of cell conductance in the second mode indicates conductive filaments with a quantum point contact (QPC).

5.2.3 Temperature dependence of cell conductance

In order to clarify the possible source and distributions of conductive filaments with a QPC and to explore the cause of QPCs, the temperature dependence of the conductance was investigated [25]. The temperature range was from 77 K to 400 K by using prober system (TOYO Corporation: CPX-VF). The measured states of cells were in the initial state, just after semi-forming, during the second mode, and in the HRS after second forming.

First, the cell conductance in the initial state G_{ini} at 0.1 V was measured over the wide temperature range from 77 K to 400 K. After only semi-forming was performed under I_{comp} of 100 μA at RT, the cell conductance G just after semi-forming was also measured. G was equivalent to G_0 in most cells regardless of the cell area. Here, repeatable RS was confirmed with the conductance of between G_{ini} and G_0. The typical temperature dependence of G/G_0 is shown in Fig. 5.3(b). Although G/G_0 was unity over the temperature range from 77 K to RT, the value increased with elevated in temperature above RT. In contrast, the value of $(G - G_{\mathrm{ini}})/G_0$ was unity and independent of temperature, as illustrated in Fig. 5.3(c). This result revealed that the conductive and bulk regions were separated in parallel as an equivalent circuit in the cell, as shown in Fig. 5.4, and that a conductive filament with a QPC with a conductance of G_0 formed as a conductive region because the temperature dependence of G can be expressed as $G(T) = G_0 + G_{\mathrm{bulk}}(T)$. Note that G_{bulk} is equal to G_{ini} above RT because the filament area is thought to be negligibly small compared to the bulk area and the bulk conductance increases exponentially with elevated temperature [26].

The cell conductance exhibited two types of temperature dependences in the same sample, as shown in Fig. 5.5(a). In several cells (defined as a Type 1 cell), the G values at RT did not change between before and after heating to 400 K. This result means that the conductive filaments in NiO maintain their states during heating. In contrast, the G values in other cells (defined as a Type 2 cell) differed. G in Type 2 cells decreased at 370 K, while the temperature dependence of G coincided with that in Type 1 cell below 350 K. The conductance gap at 370 K between Type 1 and Type 2 cells was equivalent to G_0 and was kept even while the temperature changed. These results indicate that the conductive filament with a QPC is possibly ruptured by heat at a temperature of merely about 100°C, as shown in Fig. 5.5(b), which is presumably much lower than Joule heating [7, 27, 28]. Note that the author analyzed several tens of cells and have confirmed enough their reproducibility [25] for exhibiting their typical characteristics even by using another prober systems. The ruptured of the conductive filament with a QPC by heating to more than 370 K will be discussed in the next chapter.

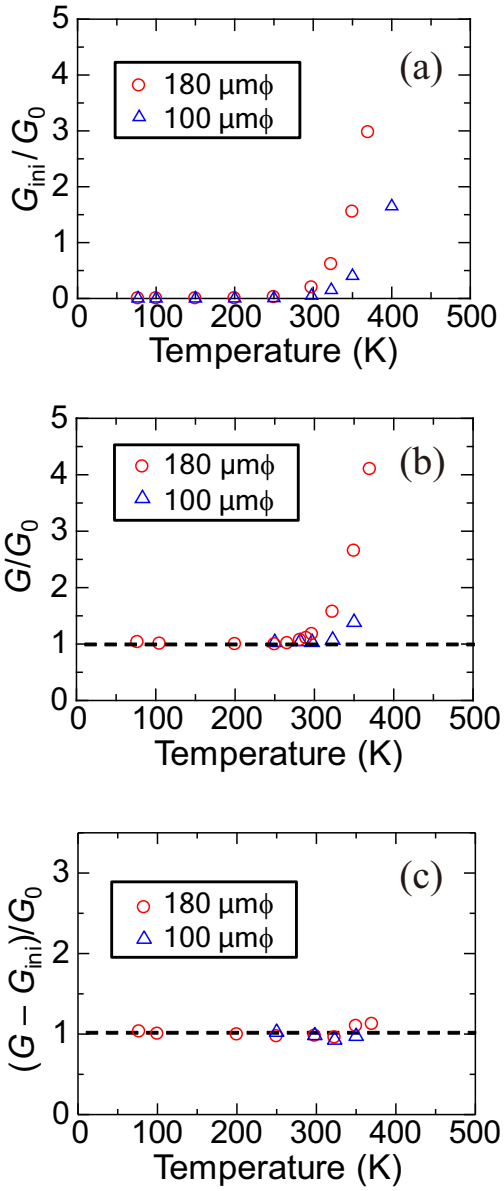

Figure 5.3: Temperature dependence of (a) G_{ini}/G_0, (b) G/G_0, and (c) $(G - G_{ini})/G_0$ just after semi-forming in cells, which were equal to unity at RT for diameters of 100 μm and 180 μm.

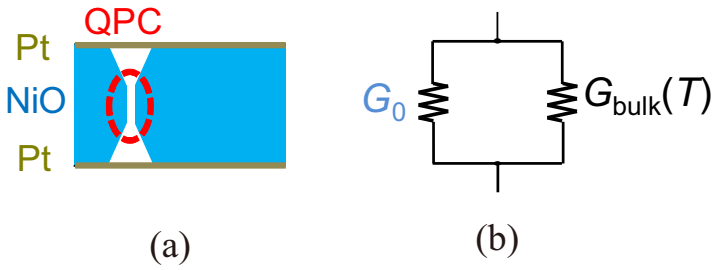

Figure 5.4: Equivalent circuit model of a Pt/NiO/Pt RS cell. (a) schematic illustration of the cell and (b) equivalent circuit of the cell conductance.

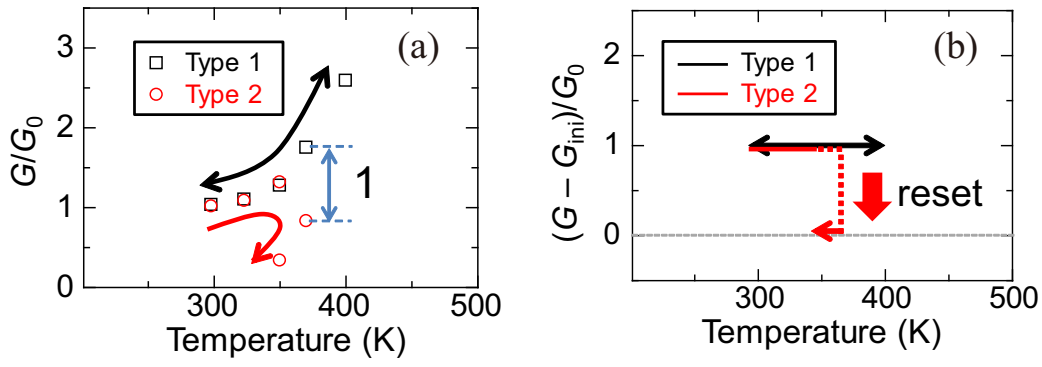

Figure 5.5: Temperature dependence of (a) G/G_0 just after semi-forming in Type 1 cells and Type 2 cells. Conceptual illustration of temperature dependence of (b) $(G - G_{ini})/G_0$ of these RS cell.

Next, voltage sweep under I_{comp} of a few mA was performed in cells with a diameter of 180 μm before second forming so that they would exhibit different quantized conductance after semi-forming. When they exhibited different quantized conductance (nG_0), the voltage sweep was stopped manually to prepare such states in the cells. Figure 5.6(a) shows the typical temperature dependence of $(G - G_{ini})/G_0$, which not only took on the value of 1 just after semi-forming [see Fig. 5.3(c)], but also approximately 2 and 4 at RT before second forming. The temperature dependence of G can be expressed as $G(T) = G_0 + G_{bulk}(T)$ because G is almost constant at each n and almost independent of temperature. The discrete fluctuation of G in Fig. 5.2(e) corresponds to the change in n in this equation. This result points to either a change in width of a conductive filament with a QPC or the formation of conductive filaments with a QPC under an applied voltage.

Finally, second forming was performed under I_{comp} of a few mA, followed by the re-application of a positive voltage to cause each cell to be in the HRS. Repeatable RS phenomenon can be observed after second forming, as shown in Fig. 5.2(d). The typical temperature dependence of $(G - G_{ini})/G_0$ in the HRS after second forming in cells with a diameter of 180 μm is shown in Fig. 5.7. As in the case of the trend before second forming, $(G - G_{ini})/G_0$ was almost independent of temperature and satisfied the equation $G(T) = nG_0 + G_{bulk}(T)$. This suggests that the conductive filament with a QPC retains its states before and after second forming, because the resistance in the HRS after second forming is closer to the resistance just before second forming (at V_{form2}) compared with the initial resistance.

5.2.4 Discussion

The specific forming and RS characteristics based on the various temperature dependencies are discussed. NiO layers on Pt BEs deposited by sputtering exhibit a columnar structure containing GBs almost perpendicular to the thickness direction as confirmed in Chapter 4. Normally, the atomic arrangements within GBs are considered to be more open than in the bulk phase, and GBs seem to exhibit the crystallographic mismatch between adjacent grains. In addition, dielectric breakdown takes place by increasing the applied electric field to SiO_2 in metal-oxide-semiconductor field-effect transistor (MOSFET) according to weakest-link theory, although the universal mechanism of the breakdown has not been fully clarified yet. Therefore, the author presumes that the cells showing two types of forming process include "moderately" defect-rich GBs in the NiO layers. The defects (weakest spots) as possible source of conductive filaments exist presumably along the GBs of the NiO layers in their initial state, suggesting that the conductive filaments are formed along the GBs due to electrical stress.

The author considers an RS behavior model based on conductive filaments. The application of a voltage to the initial cells results in semi-forming and the formation of a conductive filament with a QPC at the weakest GB (with the maximum number of defects) in NiO layers. When a voltage sweep just after semi-forming is stopped manually or under relatively low compliance current, the following voltage leads to reset and set alternately, as shown in Fig. 5.2(b). The RS behavior corresponds to the rupture and reformation of the conductive filament with a QPC.

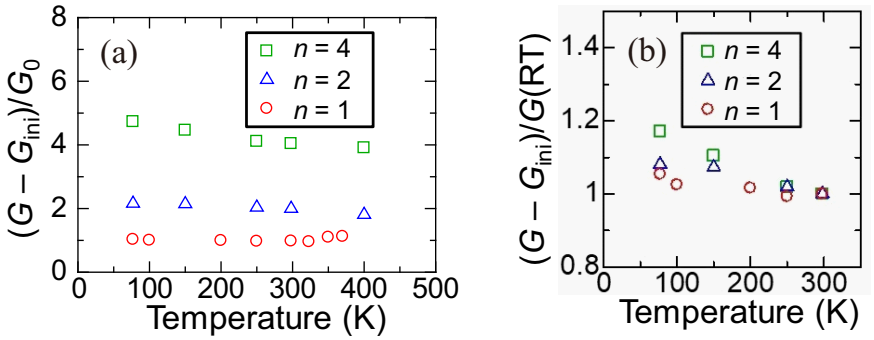

Figure 5.6: Temperature dependence of (a) G/G_0, which equals to 1 just after semi-forming and approximately 2 and 4 at RT in the second mode in cells with a diameter of 180 μm. (b) The temperature dependence of G/G_0 normalized to $(G - G_{\text{ini}})/G_0$ at RT.

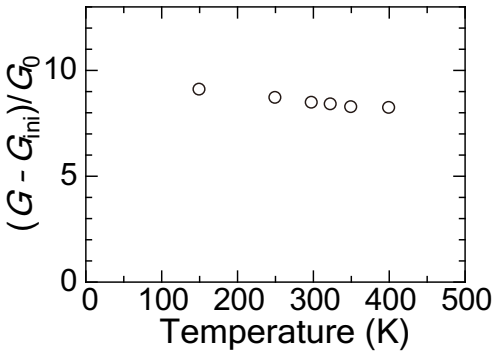

Figure 5.7: Temperature dependence of (a) G/G_0, which equals to approximately 8 at RT in HRS after second forming in cells with a diameter of 180 μm.

In the meantime, a possible reason for cell conductance discrete increase has been discussed whether a change in width of a conductive filament with a QPC or the formation of incremental conductive filaments with a QPC in parallel [25]. The temperature dependence of G/G_0 normalized to $(G - G_{\mathrm{ini}})/G_0$ at RT in the second mode is exhibited in Fig. 5.6(b). Although values of G barely decrease with elevated in temperature, despite the almost temperature independency of G before second forming. Moreover, the rate of decrease was enhanced and G started to take on even non-integer values, as $G(\mathrm{RT})/G_0$ $(= n)$ increased. The case of $n = 4$ in Fig. 5.6(b) should be equivalent to $n = 1$ if four conductive filaments are present, each with a conductance of G_0. It can be inferred that as the quantum wire width increased, the effective length of the wire also increased and the energy interval between subbands in the quantum wire narrowed, making carriers more prone to being affected by inter-subband scattering. The conductance became more sensitive to thermal fluctuations as n increased because the career transport became less ballistic and the interval became as small as a few $k_{\mathrm{B}}T$. Thus, the results imply that n of conductive filaments with a conductance of quantized conductance G_0 are unlikely to be formed before second forming. Nevertheless, additional formation of several conductive filaments with a QPC should not be denied completely. The temperature dependency indicates that at least a single fat filament with a QPC is considered to be formed [29]. As a result, upon the application of a higher voltage after semi-forming, the conductive filament with a QPC gradually begins to be fat according to conductance quantization.

Further voltage application induces second forming and formation of a new fat conductive filament. The resistance in the LRS after second forming varied from 50 Ω to 150 Ω and was comparable to the resistance after the conventional single forming. After second forming occurs, the applied voltage transfers the resistance state of a cell from the LRS to the HRS. The cell conductance in the HRS barely decreases with elevated temperature, as shown in Fig. 5.7, which resembles the temperature dependence of cell conductance before second forming. In addition, values and their temperature dependence exhibit similarity between the conductance just before second forming (at V_{form2}) and that in the HRS after second forming. These results reveal that the formation and rupture of the new fat filament, rather than filaments with a QPC, are observed as an RS phenomenon after second forming.

Moreover, the driving force behind reset is regarded as Joule heating through current because Pt/NiO/Pt cell can be categorized into TCM. The threshold current required for the reset process in RS operation after second forming seems to be much larger than the current after semi-forming, although the conductive filaments with a QPC are possibly sensitive to heat. Therefore, the new conductive filament forms by second forming at one of other defect-rich GBs, instead of a change in the conductive filament with a QPC to much fatter filament. The author confirmed that the maximum number n_{max} was 15, and however, such the large conductance before second forming was easily disappeared by the application of a DC voltage, which preclude stable measurements such as temperature dependence of cell conductance of approximately $n_{\mathrm{max}}G_0$.

In conclusion, Fig. 5.8 exhibits the proposed RS behavior model based on conductive filaments in NiO layers.

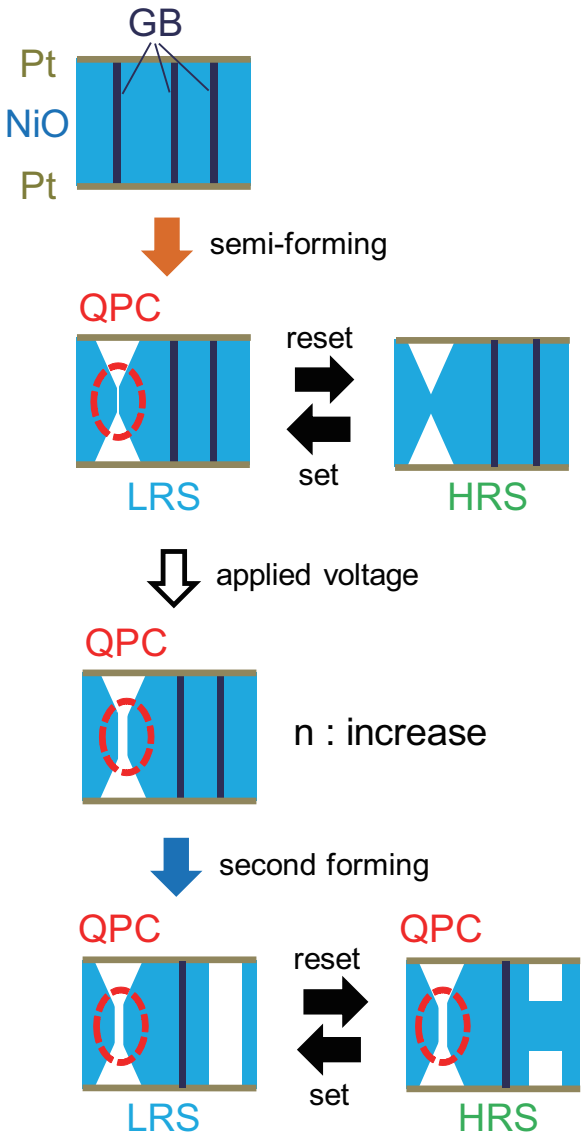

Figure 5.8: Proposed RS behavior model based on conductive filaments in NiO layers of Pt/NiO/Pt RS cells.

5.3 Dependence of Forming Characteristics on Oxygen Composition and Cell Size

5.3.1 Oxygen composition dependence

NiO layers in capacitor-type Pt/NiO/Pt RS samples were deposited on Pt BEs in Ar and O_2 gas mixture by using reactive RF sputtering system (ANELVA: L-250-FHL). Whereas the Ar flow rate was kept at 7.8 sccm, the O_2 flow rate was precisely controlled at approximately 0.96 sccm in a metallic mode to obtain two types of forming characteristics in Pt/NiO/Pt RS cells relied on the rules of thumbs. The pressure and the substrate temperature during sputtering were kept at 0.6 Pa and 350°C, respectively. The thickness of the NiO layers was 80 nm.

Figure 5.9 exhibits dependence of the forming characteristics in capacitor-type RS samples on O_2 flow rate during NiO deposition by reactive sputtering. The varied range of O_2 flow rate was less than 5% of the middle. The values of O_2 flow rate in Fig. 5.9(a), (b), and (c) were 0.94 sccm, 0.96 sccm, and 0.98 sccm, respectively. When the O_2 flow rate is relatively low, forming does not occur below an I_{comp} of 10 mA (non-forming) because cell resistance in the initial state is too low to reach the compliance current, as shown in Fig. 5.9(a). Conversely, the cells fabricated with a higher O_2 flow rate tend to show only single forming, which corresponds to conventional typical forming characteristics in TMO-based RS cells, as shown in Fig. 5.9(c). As a result, when the NiO layer is deposited with a selected O_2 flow rate (0.96 sccm in this case), conductance quantization appears between semi-forming and second forming, as shown in Fig. 5.9(b). Strictly speaking, the selected O_2 flow rate can shift slightly because of erosion depth of the metallic nickel (Ni) target and RF power.

The author confirmed a columnar polycrystalline structure of NiO layers on Pt BEs deposited by DC sputtering, as described in Section 4.3.2. A cross-sectional TEM image of a typical capacitor-type Pt/NiO/Pt stack structure is shown in Fig. 5.10(a). The image reveals that NiO layers and Pt BEs exhibit a columnar structure with a grain diameter of tens of nanometer scale. Note that roughly all of GBs run along the thickness direction, which distribute along mainly [111] orientation from X-ray diffraction (XRD) in Section 4.3.2. The structure of NiO layers in crossbar-type RS samples is columnar polycrystalline as capacitor-type RS samples.

Next, taking advantage of GBs along thickness direction in NiO layers, plane-view high-angle annular dark-field (HAADF) scanning TEM (STEM) images were taken at NiO layers. The samples for HAADF are strictly selected as NiO/Pt BEs stacks, that is, regions without Pt TEs for investigating the forming characteristics and RS operation, because Pt TEs possibly hinder the signal detection from NiO layers. Moreover, the backside materials (Pt BEs and substrate) and protection layers (mainly carbon deposited for TEM observation) on NiO layers should be completely removed by focused ion beam for the TEM observation to acquire the intrinsic signals only from the NiO layers, as shown in Fig. 5.10(b). Figure 5.11 shows plane-view HAADF images taken at NiO layers deposited with different O_2 flow rates. As the O_2 flow rate decreases, more bright spots appear in the images.

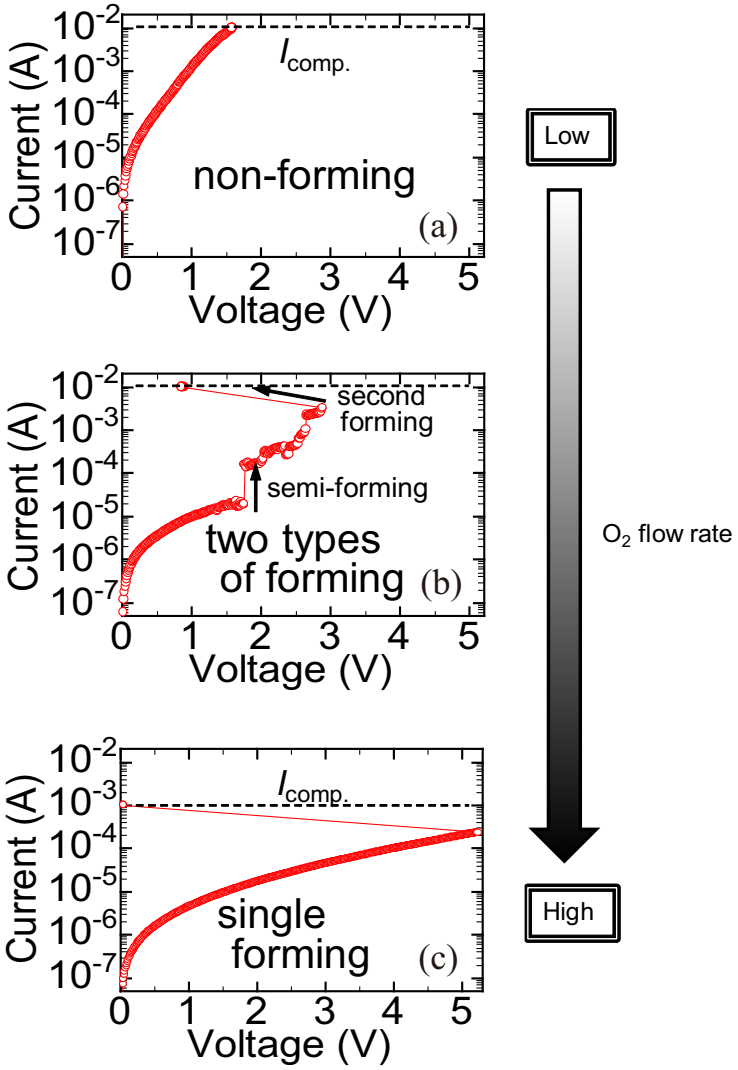

Figure 5.9: O_2 flow rate dependence of forming characteristics in capacitor-type Pt/NiO/Pt cells. The O_2 flow rate gradually increases from (a) to (c).

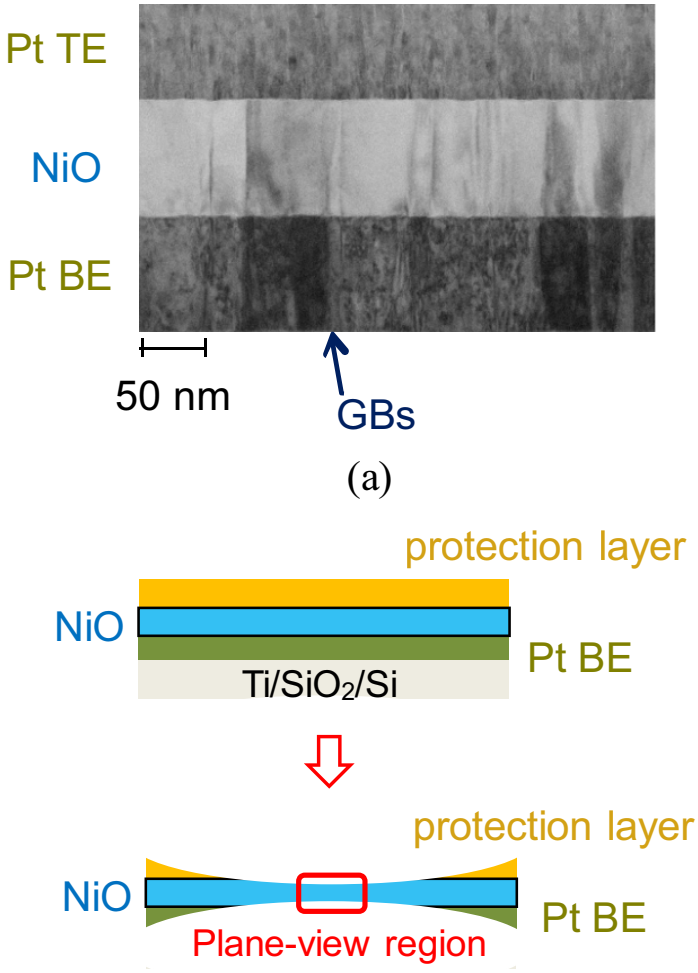

Figure 5.10: (a) A cross-sectional TEM image of a capacitor-type Pt/NiO/Pt RS sample and (b) a plane-view STEM region in the sample.

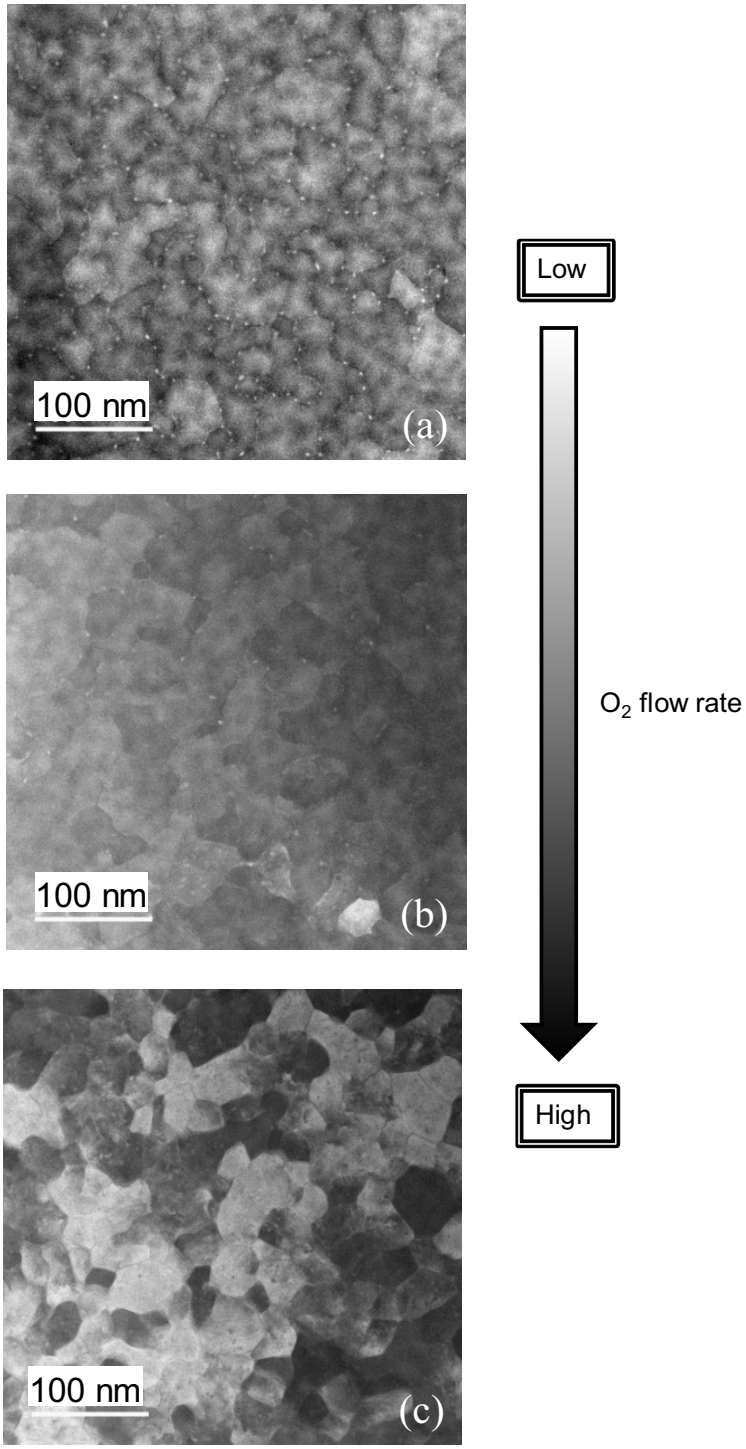

Figure 5.11: Plane-view HAADF STEM images taken at only NiO deposited with different O_2 flow rates in capacitor-type Pt/NiO/Pt samples. The O_2 flow rate gradually increases from (a) to (c).

The magnified image near bright spots shown in Fig. 5.12(a) reveals that the bright spots can be observed at GBs, and more specifically frequently at the GB triple-points. Figure 5.12(b) and (c) are energy-dispersive X-ray spectrometry (EDX) mapping images of O and Ni signals corresponding to the area shown in Fig. 5.12(a), respectively. These maps reveal that the bright spots in HAADF images indicate V_O-rich and Ni-rich GBs. Because the brightness of the spots in Fig. 5.12(a) means the average composition ratio of O to Ni along the thickness direction, the ratio at the triple-points is smaller than the value within grains. These results suggest that O adatoms desorb from the GBs in Pt BEs and deposited NiO layers more easily than from other regions within grains during NiO deposition. This is because formation of stable Ni-O chemical bonds is more difficult at GBs than on the NiO grain surface.

As the O_2 flow rate decreases, V_O-rich GBs generate an extremely low oxygen composition ratio at the GB triple-points, which correspond to bright spots in the HAADF images. However, it is difficult to determine whether the physical origin of bright spots is a row of V_Os or segregated Ni atoms. For simplicity, the author hereafter proceeds discussion in terms of the number of V_Os as a source of the distribution of the oxygen composition ratio rather than excess Ni atoms. As a consequence, V_Os are randomly distributed at GBs, especially the triple points in NiO layers, as a function of brightness in the HAADF images. As the O_2 flow rate decreases, the number of V_O-rich GBs increases, as expected. Therefore, defects (weakest spots) exist as V_Os locally at mainly the GB triple points in the NiO layers.

5.3.2 Cell size dependence

Next, cell size dependence of the forming characteristics in crossbar-type Pt/NiO/Pt RS samples was also investigated. NiO layers in the RS samples were deposited by the same method as the capacitor-type RS samples. Whereas the values of Ar flow rate during NiO deposition was kept at 7.8 sccm, the values of O_2 flow rate was selected to be 0.94 sccm, value of which is a bit lower than the appropriate value (0.96 sccm) for the appearance of conductance quantization after semi-forming in the cell with a TE diameter of 100 μm in the capacitor-type RS samples. Figure 5.13 exhibits the dominant forming characteristics in each cell with a size of (a) 4×4 μm^2, (b) 20×20 μm^2, and (c) 88×88 μm^2. The dominant forming characteristics for a cell size of 88×88 μm^2 in crossbar-type RS samples is very similar to that of the same size (a TE diameter of 100 μm) in capacitor-type RS samples.

Figure 5.13(b) shows two types of forming and conductance quantization between semi-forming and second forming. When the cell size reduces, the cells tend to exhibit single forming, as shown in Fig. 5.13(a), which is similar to the forming characteristics shown in Fig. 5.9(c). Although the cell size and initial resistance are different with those of the cells in Fig. 5.9, this forming characteristic is equivalent to that shown in Fig. 5.9(c). Conversely, forming does not occur because of initial low resistance as the cell size increases, as shown in Fig. 5.13(c). These results suggest that magnitude relationship of Pt/NiO/Pt cell size is the same as that of V_O-rich GBs in NiO layers.

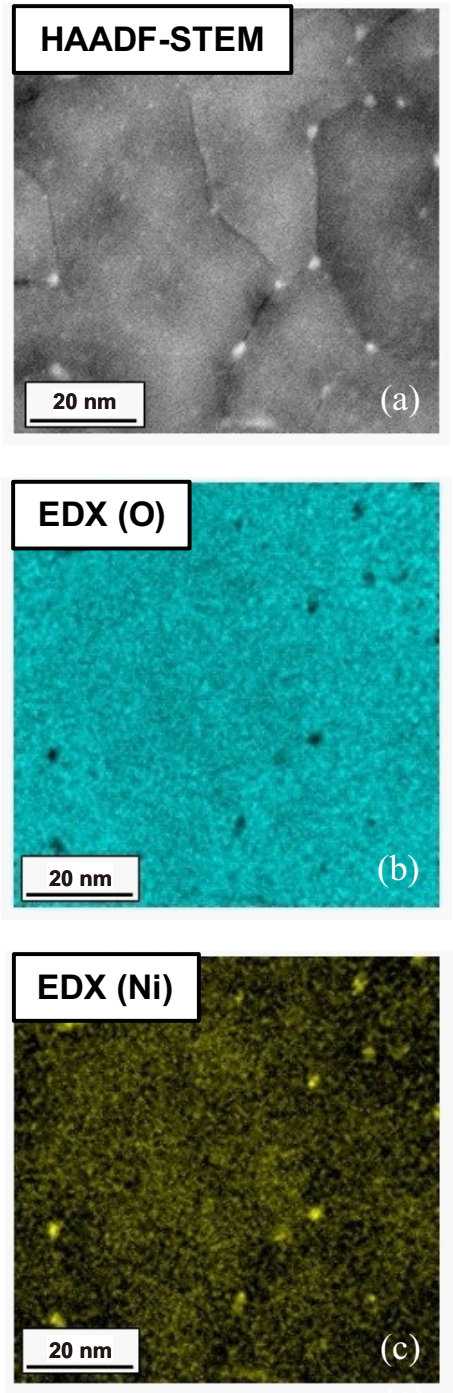

Figure 5.12: Bright spots at grain-boundary, especially triple-points, in (a) a HAADF-STEM image indicated (b) V_O-rich (O-deficient) and (c) Ni-rich regions in EDX maps of oxygen and nickel signals, respectively.

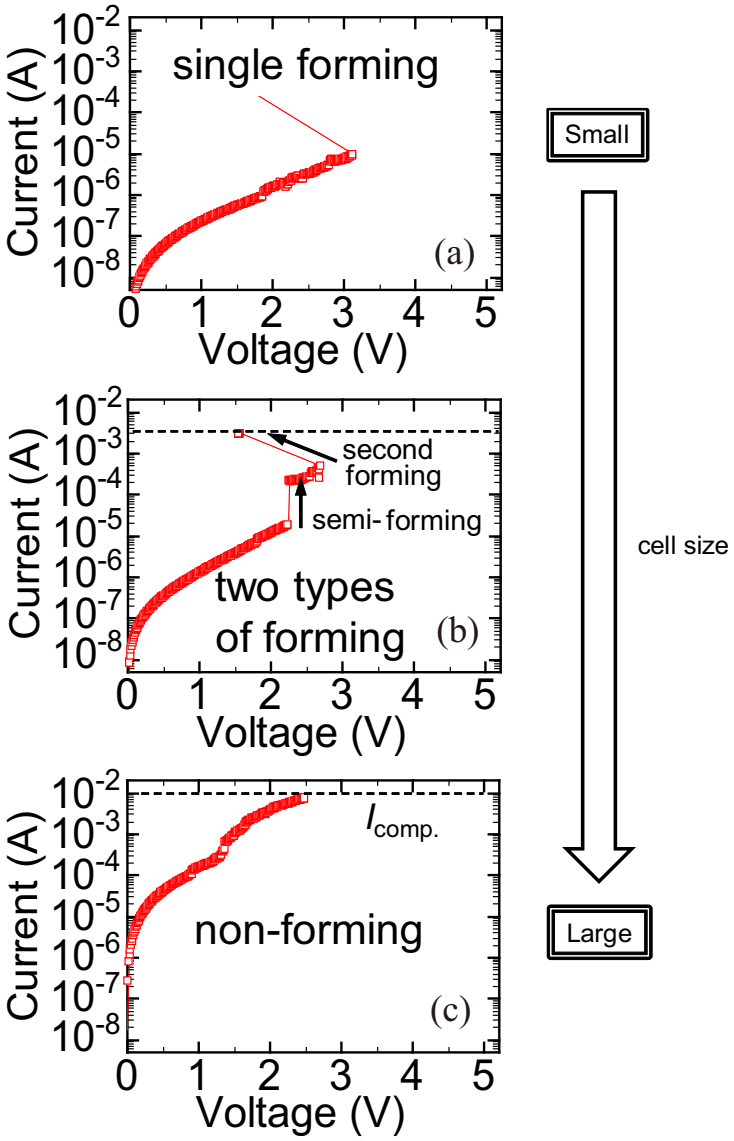

Figure 5.13: Cell size dependence of forming characteristics in crossbar-type Pt/NiO/Pt cells. The cell size is (a) $4 \times 4\ \mu m^2$, (b) $20 \times 20\ \mu m^2$, and (c) $88 \times 88\ \mu m^2$.

5.4 Appearance Condition of Conductive Filaments with a Quantum Point Contact

5.4.1 RS model based on quantized conductance

The appearance condition of conductive filaments with a QPC are discussed based on the experimental tendency of the forming characteristics described in Section 5.3. Figure 5.14 illustrates the schematics of a proposed RS model, which is a revised version of the model discussed in Section 5.2.4 by considering V_Os at GBs. When too many V_Os are present along a GB in a NiO layer, the initial resistance of the cell is low and it is difficult to observe the forming (non-forming). This kind of cell should be excluded to consider the proposed RS model because forming does not occur. The number of V_Os at all GBs in a cell, which exhibits a low initial resistance, is assumed to be larger than 4 in Fig. 5.14.

When a voltage is swept for the pristine cells, semi-forming occurs and a conductive filament with a QPC forms at the weakest V_O-rich GB (with the maximum number of V_Os), in which a "moderate" number of V_Os are included (the number of V_Os is assumed to be 4 in Fig. 5.14). If voltage sweeping is stopped just after semi-forming, re-application of the voltage results in reset and set alternately, as shown in Fig. 5.2(b), which corresponds to the rupture and formation of the conductive filament with a QPC.

Upon the application of a higher voltage after semi-forming, the conductive filament with a QPC gradually begins to be fat according to conductance quantization. Further voltage application causes second forming by creating a new fat conductive filament at one of the other weak GBs (the number of V_Os is assumed to be less than 4 in Fig. 5.14) rather than by changing a conductive filament with a QPC to a much fatter filament. In the case that a "moderately" V_O-rich GB (the number of V_Os is 4) does not exist in the cell, that is to say the maximum number of V_Os at all GBs is less than 4, only single forming occurs in the same manner.

After second forming or single forming, an RS behavior is observed by the rupture and formation of a new fat filament, namely, the alternate occurrence of the reset and set, as shown in Fig. 5.2(d). This is because the resistance in the HRS just after a large current through a higher-conductive filament followed by reset is closer to the resistance just before second forming compared with the initial resistance, although the conductive filaments with a QPC are possibly ruptured by heating to even 370 K, as described in Section 5.2.3.

As a result, the author concludes that the maximum number of V_Os at a GB is a key parameter. Too-many or too-few V_Os result in a non-forming or single forming, respectively. It is necessary to be careful that the number of V_Os at a GB is never actually 4 for a "moderately" V_O-rich GB, because the number of 4 was used in Fig. 5.14 only for the simplicity of schematic illustration. In summary, a key factor for the appearance of conductive filaments with a QPC in a Pt/NiO/Pt RS cell is the existence of a "moderate" V_O-rich GB in a NiO layer.

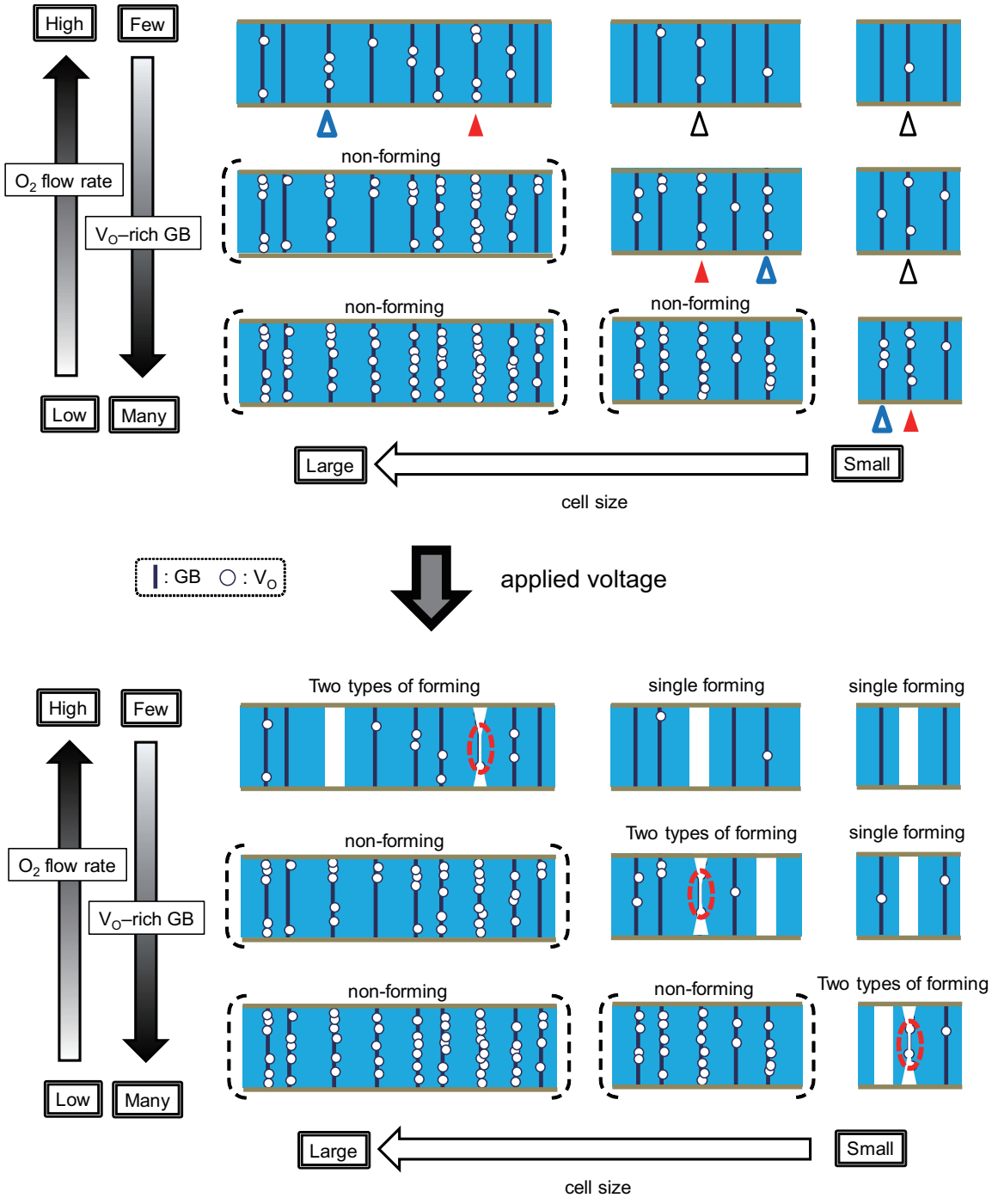

Figure 5.14: Schematics of a proposed RS model. When voltage is swept to the initial cells, semi-forming occurs and a conductive filament with a QPC is formed at the weakest V_O-rich GB (red solid triangle). Further voltage application brings about second forming by creating a new fat conductive filament at one of other weak V_O-rich GBs (blue open triangle). In the case that a "moderate" V_O-rich GB does not exist in the cell, single forming occurs and only a fat conductive filament at the weakest V_O-rich GB is formed (black open triangle).

5.4.2 Appearance or disappearance of QPC

Figure 5.15 shows the typical forming characteristics in capacitor-type RS samples deposited with slightly different O_2 flow rates, which exhibit two types of forming or single forming. Figure 5.15(a) and (c) were previously shown as Fig. 5.9(b) and (c), respectively. The values of the O_2 flow rate in Fig. 5.15(a), (b), and (c) were 0.96 sccm, 0.97 sccm, and 0.98 sccm, respectively, and the Ar flow rate was 7.8 sccm. The physical meaning of semi-forming voltage (V_{s-form}) is of importance for considering the appearance of QPC. As the O_2 flow rate increases, the number of V_O-rich GBs decrease, the average V_{s-form} gradually increases, and finally a cell exhibits only single forming.

From the viewpoint of the appearance of QPC in conductive filaments created by semi-forming, too-few V_Os in the NiO layers is equivalent to the absence of a "moderately" V_O-rich GB, and thus, the number of V_Os at the weakest V_O-rich GB (with the maximum number of V_Os) is less than the "moderate" number of V_Os. Conversely, too-many V_Os in the NiO layers can be regarded as too many V_Os at more than one of the GBs to result in forming because of a low cell resistance. Therefore, the appropriate number of V_Os at the weakest V_O-rich GB should be equal to the "moderate" number of V_Os, and a GB with a "moderate" number of V_Os is designated as a "moderately" V_O-rich GB in Section 5.4.1. As a result, the appearance condition of QPC is not only that "moderately" V_O-rich GBs exist in a NiO layer, but also that the "moderately" V_O-rich GB is identical to the weakest V_O-rich GB in the NiO layer. A conceptual illustration for the appearance of QPC is depicted in Fig. 5.16. Average V_{s-form} decreases as the number of V_O-rich GBs increases; therefore, the density of "moderately" V_O-rich GBs D also increases as long as the GB is the weakest.

As discussed in Chapter 4, forming in RS cells can be often compared with SiO_2 soft breakdown in MOS structures [30–32]. The forming follows the weakest link theory based on a percolation model, where percolation paths thorough SiO_2 thin films are created by defects arising from electrical stress [33–35]. Because the defects are randomly distributed according to Poisson statistics, the cumulative breakdown probability F is described as follows:

$$F = 1 - \exp(-DA), \tag{5.1}$$

where D is the defect density in a SiO_2 layer and A is the cell size. When F and D are replaced by the cumulative semi-forming probability and "moderately" V_O-rich GB density, respectively, Eq. (5.1) supports the cell size dependence of the semi-forming characteristics, as shown in Fig. 5.14. As the "moderately" V_O-rich GB density decreases, the value of F changes from 1 to 0. $F = 0$ means the disappearance of QPC in the conductive filaments created by semi-forming and only single forming is observed.

The relationship of the Pt/NiO/Pt RS cell size and the number of V_Os at GBs in a NiO layer reveals that a decrease in the "moderately" V_O-rich GB density D or cell size A leads to an increase in V_{s-form}, which means less occurrence of semi-forming and the appearance of QPC. Actually, as V_{s-form} increases, second forming voltage (V_{form2}) tends to decrease, and finally not only conductance quantization but also two types of forming disappear. Figure 5.17 exhibits the

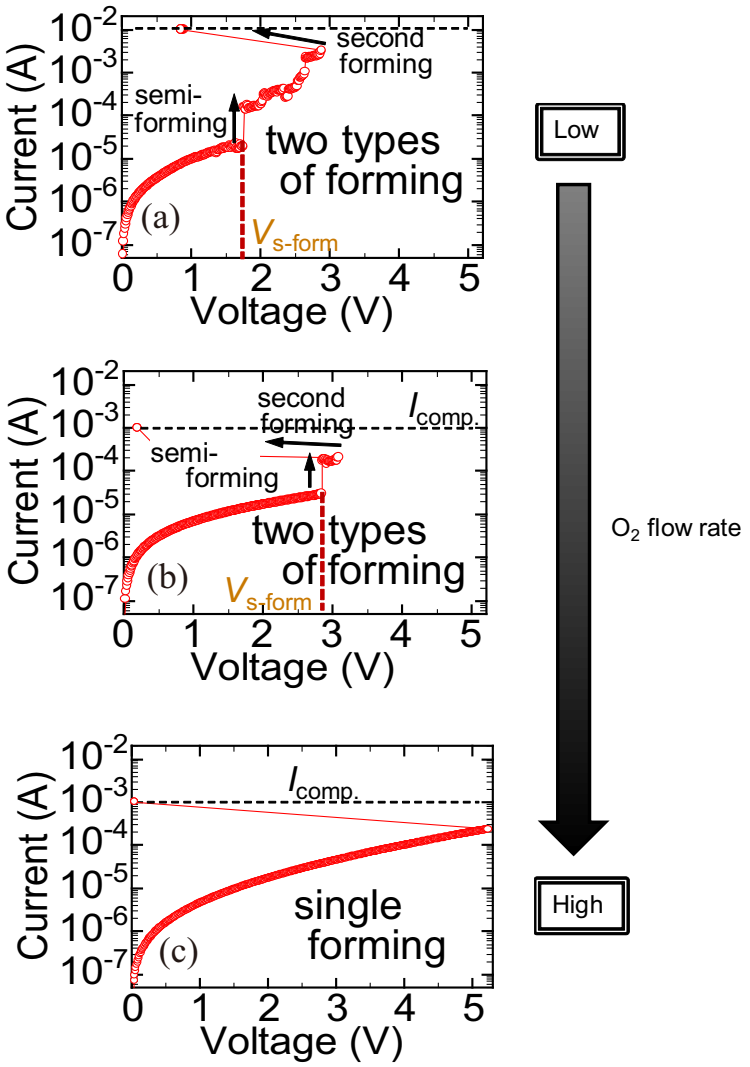

Figure 5.15: Forming characteristics in capacitor-type samples deposited with slightly different O_2 flow rates, which exhibit two types of forming or single forming. The O_2 flow rate gradually increases from (a) to (c).

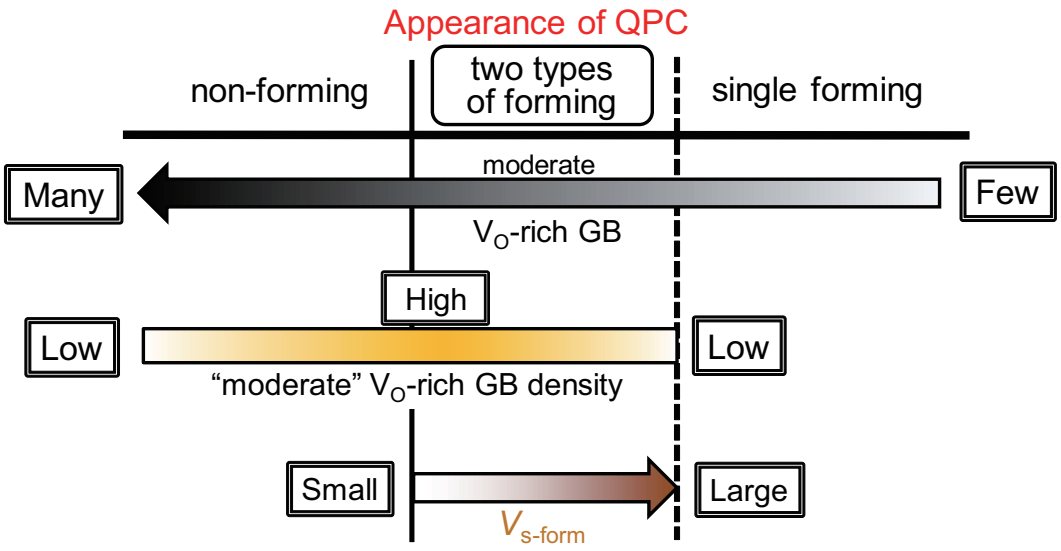

Figure 5.16: Conceptual illustration for appearance of QPC in conductive filaments created by semi-forming.

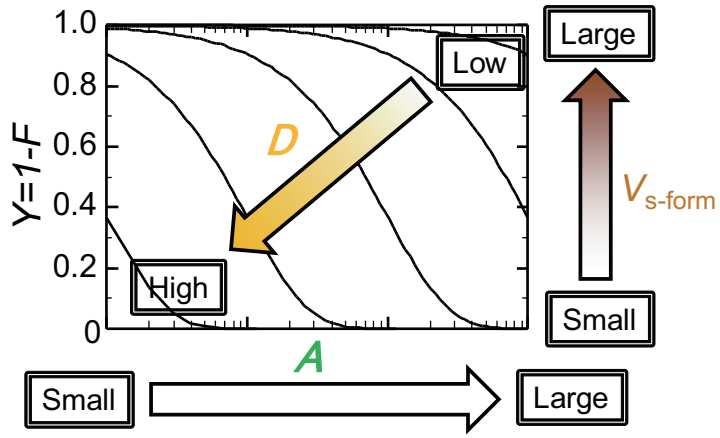

Figure 5.17: Degree of disappearance of QPC in conductive filaments at semi-forming, which indicates that V_{s-form} (Y) increases with decrease in "moderate" V_O-rich GB density D and cell size A. Y can be represented as $\exp(-DA) - 1$.

degree of the disappearance of QPC defined as $Y = 1 - F$ and Eq. (5.1). which is similar to production yield analysis for semiconductor manufacturing. Figure 5.15 and Fig. 5.13 correspond to the dependences of the "moderately" V_O-rich GB density D and cell size A on the probability change of the appearance of QPC. As a consequence, these results indicate that "moderately" V_O-rich GBs, which act as the source of a conductive filament with a QPC by semi-forming, are distributed in a NiO layer according to Poisson statistics.

5.4.3 Discussion

Dependencies of the forming characteristics in Pt/NiO/Pt RS cells on the number of V_O-rich GB and cell size were clarified. The author considered why a V_O-rich GB is preferentially formed in the NiO layers. In reactive sputtering, a reactive gas reacts with sputtered molecules or atoms on the substrate surface [36]. During NiO deposition by reactive sputtering in a metallic mode, the oxygen composition incorporated into the deposited layers is determined by the balance between the mean time for the reaction with sputtered Ni atoms and the mean residence time of O adatoms on the substrate surface. The O adatoms desorb from the GBs, which reflects GBs of Pt BEs, more easily than from stable grain surfaces during NiO deposition.

The author attempted to characterize the oxygen composition ratio (O to Ni) especially at the GB triple points in NiO layers, to estimate the number of V_Os at each triple point for quantification of the "moderately" V_O-rich GB density D. EDX results indicated that the oxygen composition within grains was approximately $1.12-1.23$, which agreed with the previous result of the author's group [24, 25]. Conversely, oxygen compositions at areas near the GB triple points were obviously lower than the value within grains, as long as the brightness of the areas in the HAADF images was stronger than that within grains. However, the calculated absolute values definitely depend on a conversion coefficient (K factor) and how many carbon atoms remain on the characterization area, and thus the values exhibit a large variation. Therefore, these absolute values do not necessarily reflect the intrinsic oxygen composition even within possibly stoichiometric grains in NiO, and accurate quantification of the density D was confirmed to be impossible.

Next, the author challenged to identify the location of a conductive filament with a QPC. A temperature mapping microscope system (Quantum Focus Instruments: InfraScope™) may enable the identification by detecting the local Joule heating at semi-forming. The temperature of the sample stage was kept at 50°C to enhance the capture sensitivity of the infrared camera, where heating to 50°C was confirmed to confer no adverse effect to RS operation after semi-forming. Figure 5.18 shows the temperature maps in one of the Pt/NiO/Pt RS cells, which exhibited two types of forming. Whereas local Joule heating with maximum temperature of approximately 250°C can be observed below the center of the cell when second forming occurred, a slight temperature change was never observed at semi-forming in all cases. The estimated low Joule heating at semi-forming seems to be difficult to detect in a conventional system, even if thermal diffusion to the outer region is restricted by means of a reduction in the thickness of Pt TE and so on. This result indicates the temperature of Joule heating can be estimated to be more than 250°C.

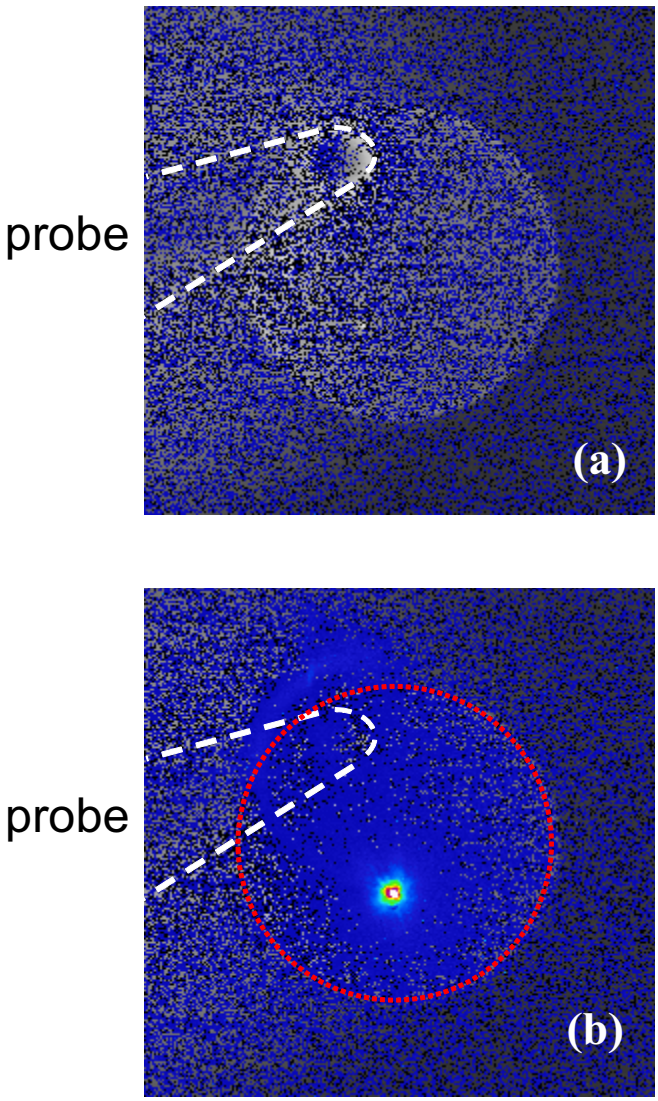

Figure 5.18: Temperature maps overlaid on captured images (a) at semi-forming and (b) at second forming. Pt TE edge is depicted by red dash circle with a diameter of 200 μm.

Moreover, the author also performed conductive-atomic force microscopy (C-AFM) measurements (Asylum: Cypher S). A platinum-iridium (PtIr)-coated conductive probe with a tip radius of 20 nm was used to scan the area without Pt TEs in Pt/NiO/Pt RS samples, where the forming characteristics were investigated. Although a minimal leakage current was detected in several spots near GBs in the RS samples, which exhibited non-forming because of a low resistance like the previous results [24], no current was detected even at a number of GBs in the RS samples which exhibited two types of forming.

Although TEM-EDX observation was carried out in a vacuum after destructive sample modification, V_O-rich GB could be observed and the fact that the number of GBs in the NiO layers tended to decrease with an increase in O_2 flow rate during NiO deposition was confirmed. The appropriate value of O_2 flow rate was 0.96 sccm for the appearance of QPC in the cell with a TE diameter of 100 μm in the capacitor-type RS samples. Nevertheless, these values should be tuned depending on changes of deposition parameters, such as the erosion depth of the metallic Ni target, as described in Section 2.3.4. In fact, the O_2 flow rate for the appearance of QPC was 1.1 sccm in the previous study of the author's group [24]. Although the difference can be within the expected range, the window for the appearance of QPC is very narrow during the deposition of NiO layers.

5.5 Summary

The temperature dependence of conductance was investigated after semi-forming in Pt/NiO/Pt ReRAM cells showing two types of forming. The dependence just after semi-forming indicated that a conductive filament with a QPC was formed in the NiO layer and that the conductive filament could be ruptured by heat at even 100°C. The O_2 flow rate and cell size dependences of the forming characteristics and the composition ratio of O to Ni in NiO layers were also investigated. TEM-EDX maps revealed that the ratio at GBs, especially near the triple points, was either equal to or clearly smaller than the value within grains. Too-many or too-few V_Os in GBs resulted in the disappearance of QPC because of the non-forming or single forming characteristics, respectively. The cell size dependence of the forming characteristics was well explained by the area scaling law, because V_O-rich weak spots seemed to be randomly distributed at the GB triple-points according to Poisson statistics. The appearance condition of QPC in a Pt/NiO/Pt cell was not only that "moderately" V_O-rich GBs existed in a NiO layer, but also that the "moderately" V_O-rich GBs were identical to the weakest V_O-rich GB in the NiO layer.

Furthermore, the author proposed an RS model based on forming characteristics especially obtained from the RS cells with different sizes. When a voltage was swept for the initial cells, semi-forming occurred and a conductive filament with a QPC was formed at the weakest V_O-rich GB. Further voltage application resulted in second forming by creating a new fat conductive filament at one of the other weak V_O-rich GBs. After both semi-forming and second forming, the RS behavior occurred by the rupture and formation of both a conductive filament with a QPC and a new fat filament, respectively.

References

[1] R. Waser and M. Aono, Nat. Mater. **6**, 83 (2007).

[2] R. Waser, R. Dittmann, G. Staikov, and K. Szot, Adv. Mater. **21**, 2632 (2009).

[3] H. Akinaga and H. Shima, Proc. IEEE **98**, 2237 (2010).

[4] I. Valov, R. Waser, J. R. Jameson, and M. N. Kozicki, Nanotechnology **22**, 254003 (2011).

[5] T. Tsuruoka, H. Hasegawa, K. Terabe, and M. Aono, Nanotechnology **23**, 435705 (2012).

[6] W. Lu, D. S. Jeong, M. Kozicki, and R. Waser, MRS Bull. **37**, 124 (2012).

[7] D. Ielmini, R. Bruchhaus, and R. Waser, Phase Transitions **84**, 570 (2011).

[8] C. Gopalan, Y. Ma, T. Gallo, J. Wang, E. Runnion, J. Saenz, F. Koushan, P. Blanchard, and S. Hollmer, Solid-State Electron. **58** 54 (2011).

[9] S. Tappertzhofen, I. Valov, and R. Waser, Nanotechnology **23**, 145703 (2012).

[10] J. R. Jameson, N. Gilbert, F. Koushan, J. Saenz, J. Wang, S. Hollmer, M. Kozicki, and N. Derhacobian, IEEE Electron Device. Lett. **33**, 257 (2012).

[11] X. Zhu, W. Su, Y. Liu, B. Hu, L. Pan, W. Lu, J. Zhang, and R.-W. Li, Adv. Mater. **24**, 3941 (2012).

[12] D. Liu, H. Cheng, X. Zhu, G. Wang, and N. Wang, ACS Appl. Mater. Interfaces **5**, 11258 (2013).

[13] S. Gao, F. Zeng, C. Chen, G. Tang, Y. Lin, Z. Zheng, C. Song, and F. Pan, Nanotechnology **24**, 335201 (2013).

[14] S. Tappertzhofen, E. Linn, S. Menzel, A. J. Kenyon, R. Waser, and I. Valov, Nanotechnology **14**, 505 (2015).

[15] H. Lu, X. Xu, P. Sun, H. Liu, Q. Luo, Q. Liu, W. Banerjee, H. Sun, S. Long, L. Li, and M. Liu, Sci. Rep. **5**, 13311 (2015).

[16] E. Miranda, S. Kano, C. Dou, K. Kakushima, J. Suñé, and H. Iwai, Appl. Phys. Lett. **101**, 012910 (2012).

[17] C. Chen, S. Gao, F. Zeng, G. Y. Wang, S. Z. Li, C. Song, and F. Pan, Appl. Phys. Lett. **103**, 043510 (2013).

[18] A. Mehonic, A. Vrajitoarea, S. Cueff, S. Hudziak, H. Howe, C. Labbe, R. Rizk, M. Pepper, and A. J. Kenyon, Sci. Rep. **3**, 2708 (2013).

[19] C. Hu, M. D. McDaniel, J. G. Ekerdt, and E. T. Yu, IEEE Electron Device Lett. **34**, 1385 (2013).

[20] Y.-E. Syu, T.-C. Chang, J.-H. Lou, T.-M. Tsai, K.-C. Chang, M.-J. Tsai, Y.-L. Wang, M. Liu, and S. M. Sze, Appl. Phys. Lett. **102**, 172903 (2013).

[21] S. Long, X. Lian, C. Cagli, X. Cartoixà, R. Rurali, E. Miranda, D. Jimenez, L. Perniola, M. Liu, and J. Suñé, Appl. Phys. Lett. **102**, 183505 (2013).

[22] A. Flocke and T.G. Noll, *Proceedings of the 33rd European Solid-State Circuits Conference* (2007) p. 328.

[23] E. Linn, R. Rosezin, C. Kügeler, and R. Waser, Nature Materials **9**, 403 (2010).

[24] T. Iwata, Dr. Thesis, Faculty of Engineering, Kyoto University, Kyoto, 2014.

[25] H. Sasakura, Y. Nishi, and T. Kimoto, Appl. Phys. Lett. **107**, 233510 (2015).

[26] H. Shima, F. Takano, H. Akinaga, Y. Tamai, I. H. Inoue, and H. Takagi, Appl. Phys. Lett. **91**, 012901 (2007).

[27] U. Russo, C. Cagli, S. Spiga, E. Cianci, and D. Ielmini, IEEE Electron Device Lett. **30**, 817 (2009).

[28] U. Russo, D. Ielmini, C. Cagli, and A. L. Lacaita, IEEE Trans. Electron Devices **56**, 193 (2009).

[29] C. Hu, M. D. McDaniel, A. Posadas, A. A. Demkov, J. G. Ekerdt, and E. T. Yu, Nano Lett. **14**, 4360 (2014).

[30] W.-C. Luo, J.-C. Liu, H.-T. Feng, Y.-C. Lin, J.-J. Huang, K.-L. Lin,.and T.-H. Hou, *Tech. Dig. of IEEE Int. Electron Devices Meet.* (2012) p. 215.

[31] S. Long, X. Lian, C. Cagli, L. Perniola, E. Miranda, M. Liu, and J. Sune, IEEE Electron Device Lett. **34**, 999 (2013).

[32] Y. Nishi and T. Kimoto, J. Appl. Phys. **120**, 115308 (2016).

[33] R. Degraeve, J. L. Ogier, R. Bellens, P. J. Roussel, G. Groeseneken, and H. E. Maes, IEEE Trans. Electron Devices **45**, 472 (1998).

[34] J. Suñé, IEEE Electron Device Lett. **22**, 296 (2001).

[35] E. Y. Wu and J. Suñé, Microelectron. Reliab. **45**, 1809 (2005).

[36] S. Berg, J. Vac. Sci. Technol. A **5**, 202 (1987).

Chapter 6

Conductance Quantization and Conductance Fluctuation

6.1 Introduction

An essential process for creating conductive filaments between top and bottom metal electrodes is called forming, and is carried out by applying a voltage across a transition metal oxide (TMO), such as nickel oxide (NiO) and titanium dioxide (TiO_2). If the weakest spot of the conductive filaments becomes an atomic-scaled quantum point contact (QPC), quantized conductance, characterized by integer or half-integer multiples of $G_0 = 2e^2/h$, appears. A resistive switching (RS) phenomenon is believed to be dominated by the migration of oxygen ions and a redox reaction in valence change memories (VCMs) [1]. VCMs exhibit only bipolar RS operation, which means that the polarities of their set and reset voltages are opposite [2–6]. Conversely, the driving force for set and reset in thermochemical memories (TCMs) is reported to be thermal diffusion and a redox reaction [7]. TCMs exhibit unipolar RS operation, which means that the polarities of their set and reset voltages are the same [8, 9].

As was described in Chapter 5, two types of forming and RS behaviors exist in specific platinum (Pt)/NiO/Pt RS cells. The first forming and the next forming are referred to as semi-forming and second forming, respectively. Moreover, a unipolar RS operation is observed after semi-forming and second forming. Here, the voltage polarity of two types of RS behaviors is confirmed never to depend on the prior polarity of the set or reset. A nonpolar RS operation like that includes unipolar and bipolar RS operations, which means a random order of voltage polarities. Figure 6.1 shows the nonpolar RS characteristics after semi-forming and second forming in RS cells. The conductance in the low-resistance state (LRS) after semi-forming is approximately equivalent to the quantized conductance G_0. Furthermore, the probability that the conductance quantization occurs after semi-forming depends on the distribution of the oxygen vacancy (V_O)-rich grain boundary (GB) triple points in NiO layers, as suggested by the high-angle annular dark-field (HAADF) scanning transmission electron microscopy (STEM) images and energy-dispersive X-ray spectrometry (EDX) maps provided in Section 5.3.1.

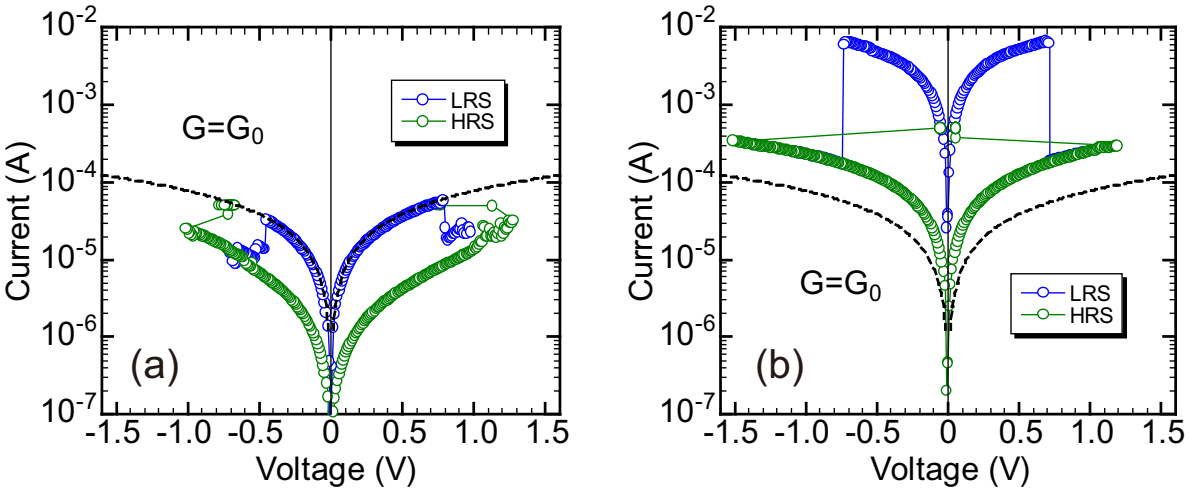

Figure 6.1: Two typical types of nonpolar RS characteristics (a) after semi-forming and (b) after second forming in Pt/NiO/Pt cells. The cell diameter of is 100 μm.

In this chapter, the author observes conductance fluctuations before and after semi-forming of the Pt/NiO/Pt cells, as shown in Fig. 6.2. Note that the conductance fluctuation differs from conductance quantization because the discrete fluctuation step is clearly smaller than half of quantized conductance G_0. These fluctuations imply the existence of multilevel resistances [10, 11], which offers the possibility of multiple discrete weighting of the synapse [12–15]. Moreover, the author discusses the driving force behind reset after semi-forming based on how Joule heating affects the conductance fluctuations.

6.2 Conductance Fluctuation

6.2.1 Sample preparation

Two types of Pt/NiO/Pt RS cells were fabricated on the same samples as in Section 5.2.1. Capacitor-type RS cells consist of a planer Pt bottom electrode (BE) of millimeter-scale size, a common NiO layer as a resistance change material, and a circular Pt top electrode (TE) with a diameter of 100 μm. Crossbar-type RS cells consist of bar-shape bottom and top electrodes with a pad region for probing and the common NiO layer. The Pt TEs of cells were separated from each other to avoid a sneak-leak path [16, 17]. The electrodes with various sizes were formed by using UV photolithography and a lift-off technique. The cell size is equivalent to the cross-point area between top and bottom electrodes, which is 2500π μm^2 for capacitor-type RS cells, and basically 88×88 μm^2, 20×20 μm^2, and 4×4 μm^2 (as needed additionally 50×50 μm^2, 30×30 μm^2, and 10×10 μm^2) for crossbar-type RS cells. The size of crossbar-type RS cells with a bar width of 88 μm is identical to that of capacitor-type RS cells.

Pt BEs were deposited by DC sputtering on a silicon dioxide (SiO_2)/*p*-silicon (Si) substrate inserted by a titanium (Ti) adhesion layer. The common NiO layer with a thickness of basically 80 nm (as needed 30−80 nm) was subsequently deposited on the Pt BEs and the SiO_2 insulator areas by radio-frequency (RF) reactive sputtering in the mixture of argon (Ar) and oxygen (O_2) using a metallic nickel (Ni) target. The total pressure and substrate temperature during sputtering were held at 0.6 Pa and 350°C, respectively. The O_2 flow rate was precisely controlled because the probability of a QPC occurring was extremely sensitive to the number of V_Os at GB triple points in NiO layers, as discussed in Section 5.4.3. Finally, Pt TEs were deposited on the NiO layer by DC sputtering in the same way as done for the BE. The top and bottom Pt electrodes were approximately 50 nm thick.

The current-voltage (*I*–*V*) characteristics of Pt/NiO/Pt cells were measured in a voltage-sweep mode by using a Keithley 4200-SCS or 4200A-SCS semiconductor parameter analyzer. The BE was grounded and the bias voltage was applied to the TE. The samples were heated in air by using the heater stage of a vacuum prober system (Nagase Techno-Engineering: Grail10-Logos01S-4-LV-HT). The temperature was varied from room temperature (RT) to 570 K at the widest. In all samples, most of the cells were confirmed to exhibit nonpolar RS characteristics after any forming processes.

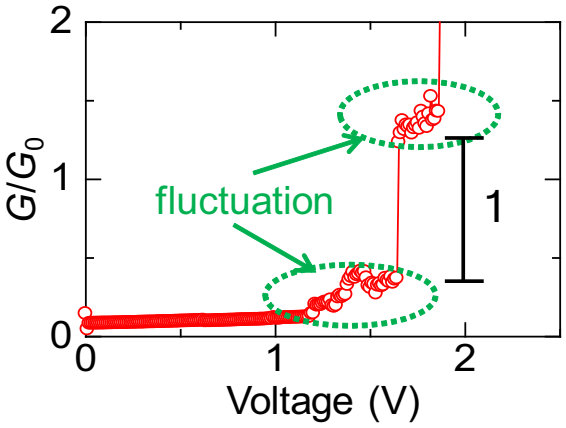

Figure 6.2: Typical conductance fluctuations before and after semi-forming.

6.2.2 Equivalent circuit model of conductance quantization

Capacitor-type RS cells with a NiO layer deposited using a moderate O_2 flow rate exhibit conductance quantization between semi-forming and second forming such as Chapter 5. When voltage sweeping is stopped just after semi-forming, reset and set occur alternately, as shown in Fig. 6.1(a). The cell conductance in the LRS is then equivalent to quantized conductance G_0, which indicates the rupture and reformation of a conductive filament with a QPC by reset and set, respectively. The dominant force behind reset seems to be Joule heating originating from a small current (sub-mA range) because the bias polarity of reset is not restricted by the prior polarity of set. Conversely, when voltage sweeping continues after semi-forming, the conductive filament with a QPC gradually grows according to the increase in conductance quantization. Considering the temperature dependence of cell conductance G after semi-forming as described in Section 5.2.3, G can be expressed as $G = nG_0 + G_{\mathrm{bulk}}$. Note that G_{bulk} represents the conductance component after removing the conductive filament with a QPC, which corresponds to the conductance not only of the bulk but also of the GB regions (except for the conductive filament).

In addition to the conductive filamentary and bulk components (nG_0 and G_{bulk}), conductance fluctuations (G_{f}) can be observed and tend to appear mainly in capacitor-type RS cells with a NiO layer deposited at an O_2 flow rate slightly less than the moderate flow rate mentioned above. Figure 6.2 shows an example of conductance fluctuations from 1.2 to 1.9 V, (i.e., before and after semi-forming at 1.7 V). Although the conductance fluctuation implies a mostly gradual increase in cell conductance as the voltage is swept, sometimes the conductance decrease occurs between 1.4 to 1.5 V, as shown in Fig. 6.2. The discrete fluctuation step is irregular and is clearly smaller than half of the quantized conductance G_0. Therefore, the conductance of the conductive filament should not fluctuate because the incremental step of the cell conductance is G_0 at semi-forming and the conductance fluctuation remains basically unchanged before and after semi-forming. The fluctuation can also be observed in the high-resistance state (HRS) after semi-forming, as shown in Fig. 6.1(a) for voltages greater than 1.0 V. These results indicate that, as the applied voltage increases, a certain alternating phenomenon occurs in the NiO layer in parallel with the formation of the conductive filament with a QPC. Thus, G should be modified to $G = nG_0 + G_{\mathrm{bulk}} + G_{\mathrm{f}}$, as indicated in Fig. 6.3, because such a conductance fluctuation makes the cell conductance G a non-integer multiple of G_0. The alternating component G_{f} in the NiO layer (contributing to the conductance fluctuation) and the properties of the alternation are explained below.

6.2.3 Dependence of dominant cell conductance on O_2 flow rate

The O_2 flow rate during NiO deposition by reactive sputtering should be precisely controlled to obtain cells, in which a conductive filament with a QPC is created by semi-forming. Figure 6.4 shows how the O_2 flow rate affects the RT cell conductance as forming characteristics in capacitor-type RS cells. Here, five samples (denoted sample I–V) were prepared, with the O_2 flow rate gradually increasing from sample I to sample V. Between samples, the O_2 flow rate was changed by less than 5% of the flow rate for sample III.

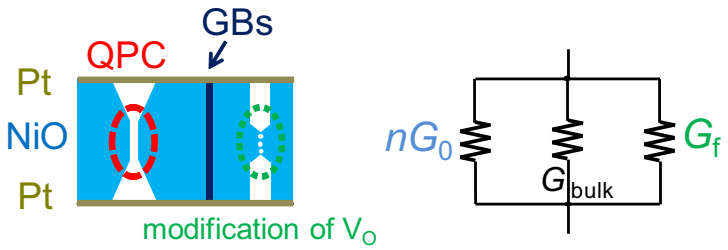

Figure 6.3: Equivalent circuit model of conductance of a Pt/NiO/Pt RS cell. nG_0 and G_f refer to conductance quantization and conductance fluctuation, respectively.

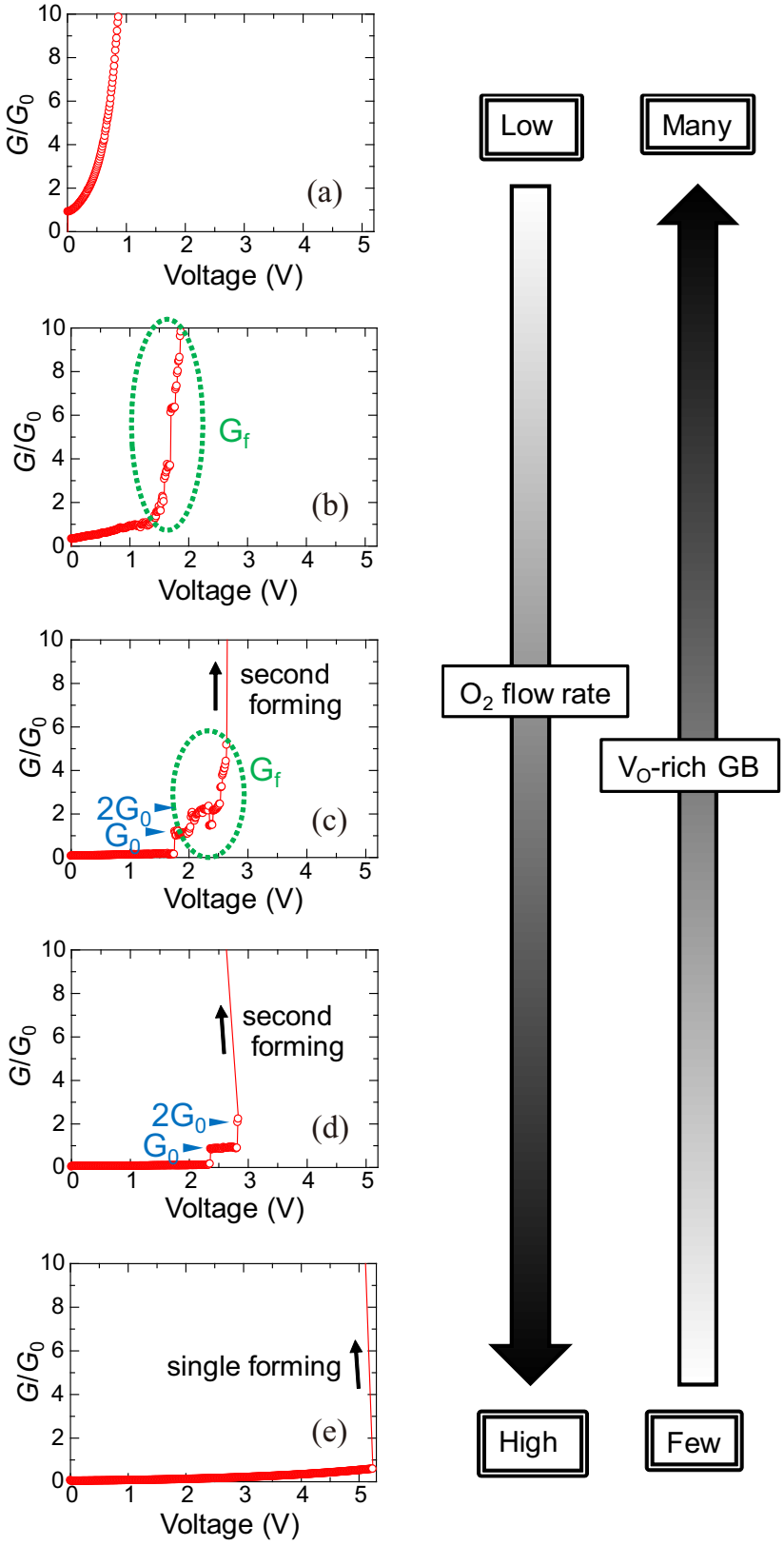

Figure 6.4: Normalized RT cell conductance as a function of applied voltage for several O_2 flow rates to show the forming characteristics in capacitor cells. The O_2 flow rate during NiO deposition gradually increases from sample I to sample V, which exhibits the dominant change shown in panel (a) to panel (e), respectively.

For low O_2 flow rate, as with sample I, the cell conductance G is too large and neither semi-forming nor second forming occurs, as shown in Fig. 6.4(a). This result is explained by too many V_Os in the initial state at the GBs in the NiO layer. In this case, the G_{bulk} component is large. In sample II with a NiO layer deposited at a higher O_2 flow rate, most cells have a smaller G_{bulk} because of fewer V_Os at GBs than for sample I. Figure 6.4(b) shows the increase in conductance accompanied by conductance fluctuations that occurs upon applying a voltage greater than 1 V. Moreover, conventional forming occurs upon further increasing the applied voltage, which corresponds to second forming in the cells, as mainly observed in sample III, which undergoes semi-forming and conductance quantization. Some of the cells in sample III undergo conductance fluctuation during conductance quantization before second forming, as shown in Fig. 6.4(c). Furthermore, the conductance fluctuation disappears around semi-forming in some of the cells in sample IV. For high O_2 flow rate, as with sample V, only single forming occurs, which corresponds to conventional forming characteristics, as shown in Fig. 6.4(e). Surface topographies of NiO layers deposited for three O_2 flow rates were investigated by atomic force microscopy. They exhibit no significant difference, indicating roughness of Pt/NiO interfaces does not affect the appearance probability of conductance quantization and conductance fluctuation.

How the cell conductance depends on the O_2 flow rate should be discussed. The range of cell conductance G at 0.1 V begins to decrease from 1−10 mS to a saturated conductance of less than 10 μS according to the decrease in V_Os at the GBs in the NiO layer. Here, G corresponds to G_{bulk} because of the larger number of V_Os. The component G_f becomes dominant above 1 V in Fig. 6.4(b) and (c) because the number of V_Os at several GBs is more strongly modified upon increasing the voltage. With slightly fewer V_Os, the component nG_0 of a conductive filament with a QPC created at semi-forming appears clearly because the relatively small G_f does not hinder the cell conductance nG_0 after semi-forming. From the viewpoint of the sudden conductance increase by the electrically driven process, the modification of V_Os resembles the formation of the conductive filament with a QPC and may be thought of as a possible precursor of a conductive filament with a QPC created by semi-forming or even as a precursor of a fat filament created by second forming. As the number of V_Os decreases further, (i.e., the density decreases of "moderately" V_O-rich GBs for the appearance of QPC), the average semi-forming voltage gradually increases. This phenomenon results in the disappearance of the conductance fluctuation ($G = nG_0 + G_{bulk}$), as shown in Fig. 6.4(d), and finally the disappearance of semi-forming ($G = G_{bulk}$), as shown in Fig. 6.4(e).

The dependence of the transitions in the dominant cell conductance on O_2 flow rate can be explained using Fig. 6.4 and Fig. 6.5. The cell conductance G is determined solely by G_{bulk} for applied voltages below 1 V because neither conductance fluctuation nor conductance quantization occurs. The schematic diagram of Fig. 6.5(a) shows the dominant cell conductance in a NiO layer at 1.0 V with increasing O_2 flow rate or decreasing number of V_Os at GBs. Conversely, the dominant cell conductance at 2.5 V in Fig. 6.4 evolves according to the number of V_Os, as shown by the solid lines in Fig. 6.5(b). Too few V_Os make the cell conductance G equal to G_{bulk}, which is the same result as too many V_Os, although the forming characteristics and G_{bulk} in both cells

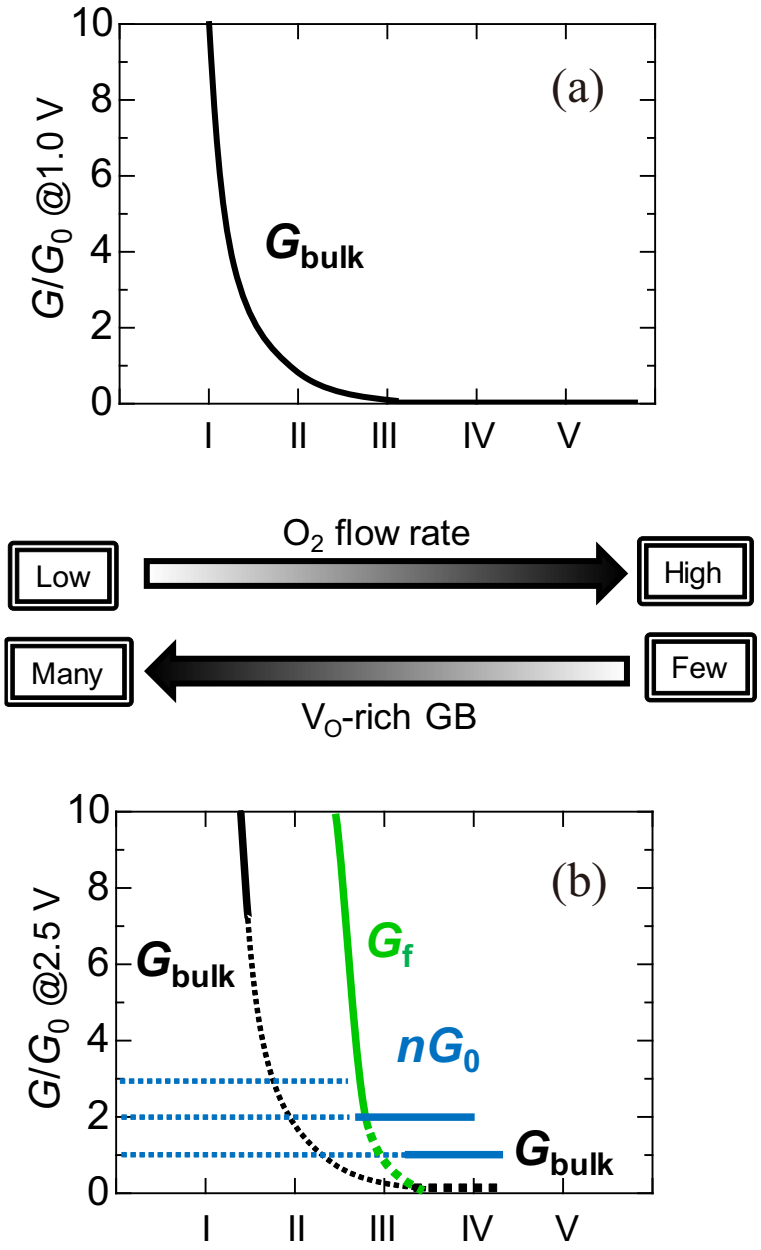

Figure 6.5: Schematic diagrams of dominant cell conductance at (a) 1.0 V and (b) 2.5 V in Fig. 6.4 (solid curves). The horizontal axis schematically represents the O_2 flow rate of sample I to sample V.

apparently differ from each other. As the number of V_Os decreases, G_f decreases, nG_0 begins to appear, and finally nG_0 disappears accompanied by an increase in semi-forming voltage. Note that the schematic diagram of Fig. 6.5(b) is just an example and that the characteristics of G_f and the value of n in nG_0 have large distributions that depend on the number of V_Os at GBs in each cell.

6.2.4 Dependence of dominant cell conductance on cell size

Next, based on the O_2-flow-rate dependence of RT cell conductance as a function of applied voltage to show the forming characteristics of capacitor-type RS cells, the author discusses how RT cell conductance depends on the cell size in terms of the forming characteristics of the crossbar-type RS cells.

Figure 6.6 shows frequency distributions of cell conductance characteristics at RT in crossbar-type RS cells with the sizes of 88×88 μm^2, 20×20 μm^2, and 4×4 μm^2 in three samples (I, II, V). Here, each number of cells in the statistics is more than 15. Conductance fluctuation during conductance quantization before second forming corresponds to characteristic in Fig. 6.4(c). A dominant characteristic of cell conductance in sample II shown in Fig. 6.6(b) shifts from Fig. 6.4(b) to Fig. 6.4(d) as the cell size decreases. All cells exhibit only single forming in sample V with a NiO layer deposited at the higher O_2 flow rate, whereas a dominant characteristic of cell conductance shifts from Fig. 6.4(a) to Fig. 6.4(c) as the cell size decreases in sample I with a NiO layer deposited at lower O_2 flow rate. Therefore, the cell size dependence of RT cell conductance as a function of applied voltage to show the forming characteristics of the crossbar-type RS cells is presented in Fig. 6.7. Here, the transition in the dominant conductance for an 88×88 μm^2 cell is very similar to that of capacitor-type RS cells of the same size, as shown in Fig. 6.4. Figure 6.7(b) shows not only semi-forming and second forming but also the conductance quantization and the conductance fluctuation between semi-forming and second forming for a 20×20 μm^2 cell. As the cell size increases, the conductance fluctuation shown in Fig. 6.7(a) occurs when a voltage above 1 V is applied; this is similar to the change in cell conductance shown in Fig. 6.4(b). Conversely, only single forming occurs as the cell size decreases, as shown in Fig. 6.7(c).

In addition, other samples including crossbar-type Pt/NiO/Pt RS cells with NiO thickness of 30 nm were also prepared. The cell sizes are not only 88×88 μm^2, 20×20 μm^2, and 4×4 μm^2, but also 50×50 μm^2, 30×30 μm^2, and 10×10 μm^2. Figure 6.8 exhibits frequency distributions of conductance characteristics of these cells at RT in three samples (designated as α, β, γ). The O_2 flow rate during NiO deposition gradually increase from sample α to sample γ. A dominant characteristic of cell conductance in sample β shown in Fig. 6.8(b) shifts from Fig. 6.4(a) to Fig. 6.4(d) as the cell size decreases from 88×88 μm^2 to 4×4 μm^2. In comparison with sample II shown in Fig. 6.6(b), distribution of conductance characteristics of cells in sample β is larger within the same cell size. The frequency of occurrence of the characteristics such as Fig. 6.4(b) to (d) tends to decrease in samples with NiO thickness of 30 nm, thinner than that of 80 nm (the conventional sample I–V). Moreover, categorization into the characteristics such as Fig. 6.4 (b) to (d) is more difficult especially in the case of large cell size in the thinner NiO samples than in the

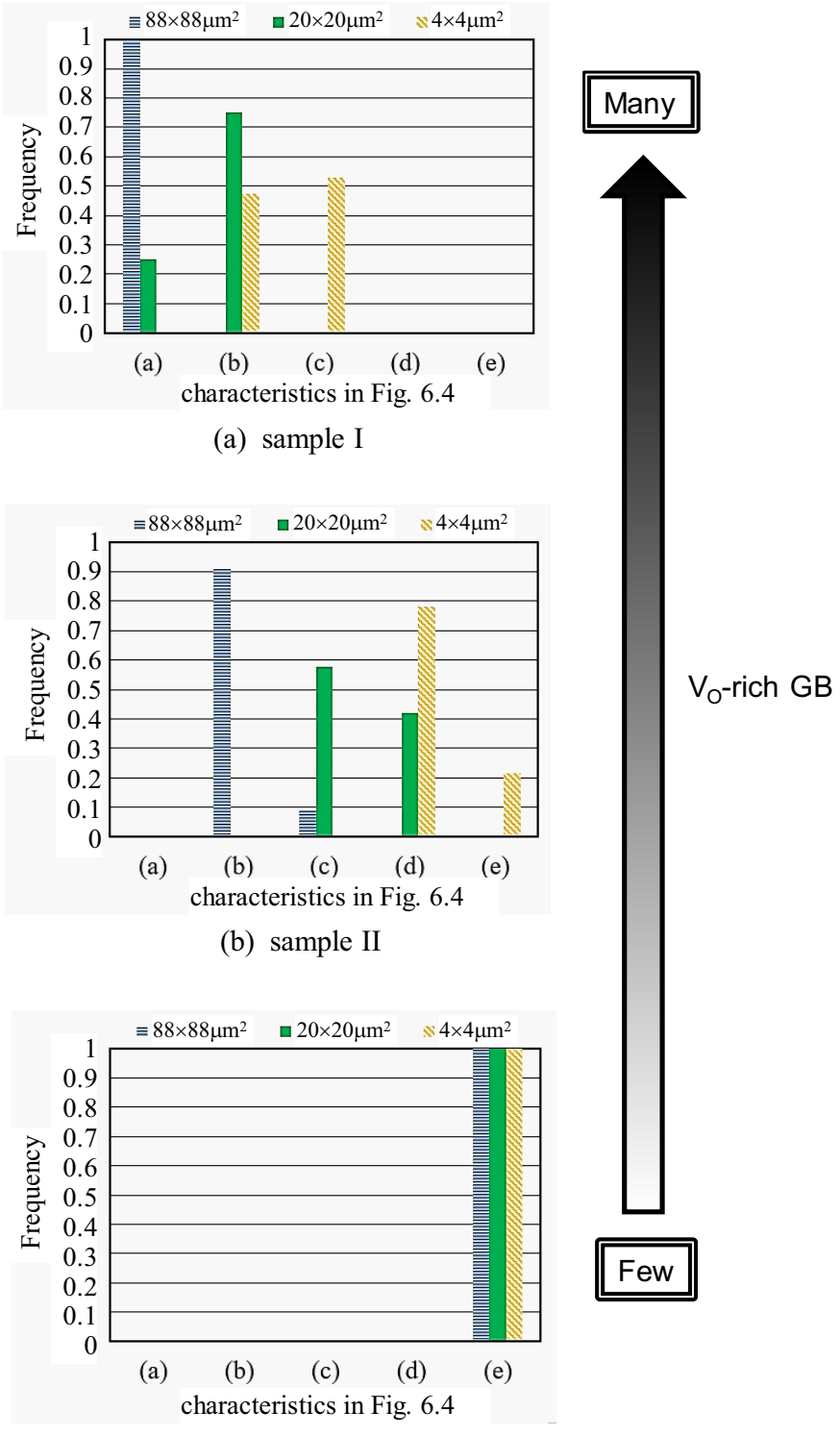

Figure 6.6: Frequency distributions of cell conductance characteristics at RT in crossbar-type RS cells with the sizes of 88×88 μm^2, 20×20 μm^2, and 4×4 μm^2 in three samples. Conductance fluctuation during conductance quantization (semi-forming) before second forming corresponds to a characteristic in Fig. 6.4(c).

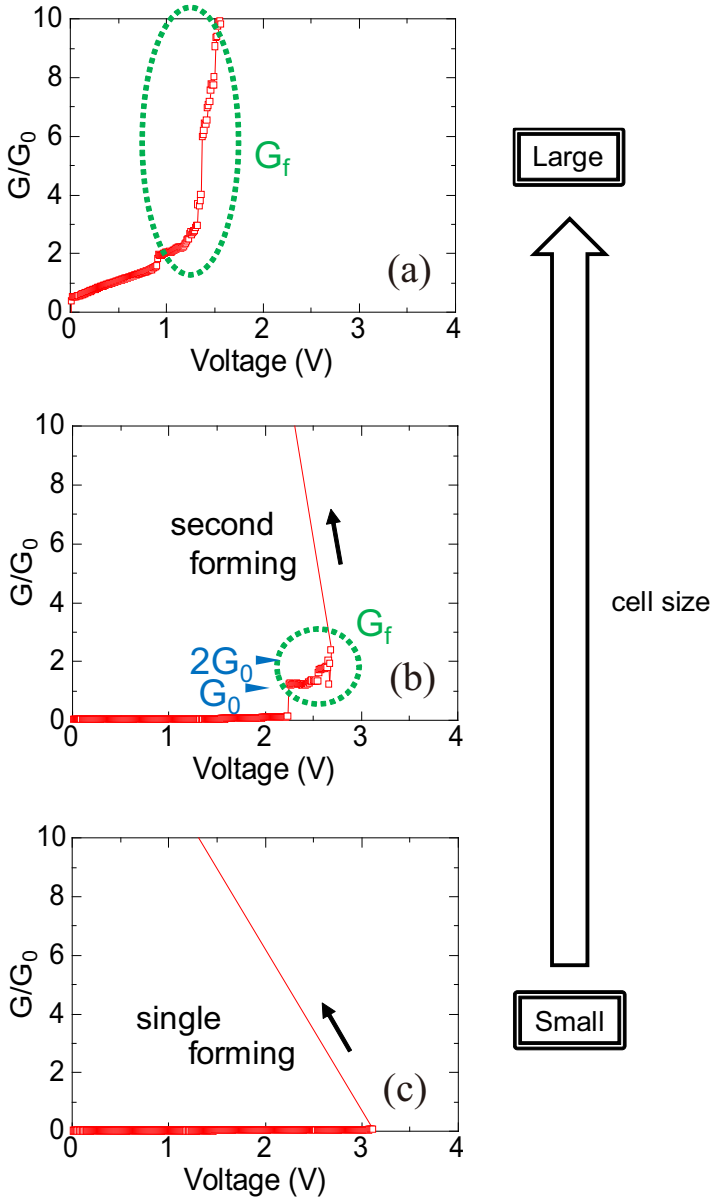

Figure 6.7: Normalized RT cell conductance as a function of applied voltage to show the forming characteristics in crossbar cells. The cell sizes are (a) 88×88 μm^2, (b) 20×20 μm^2, and (c) 4×4 μm^2.

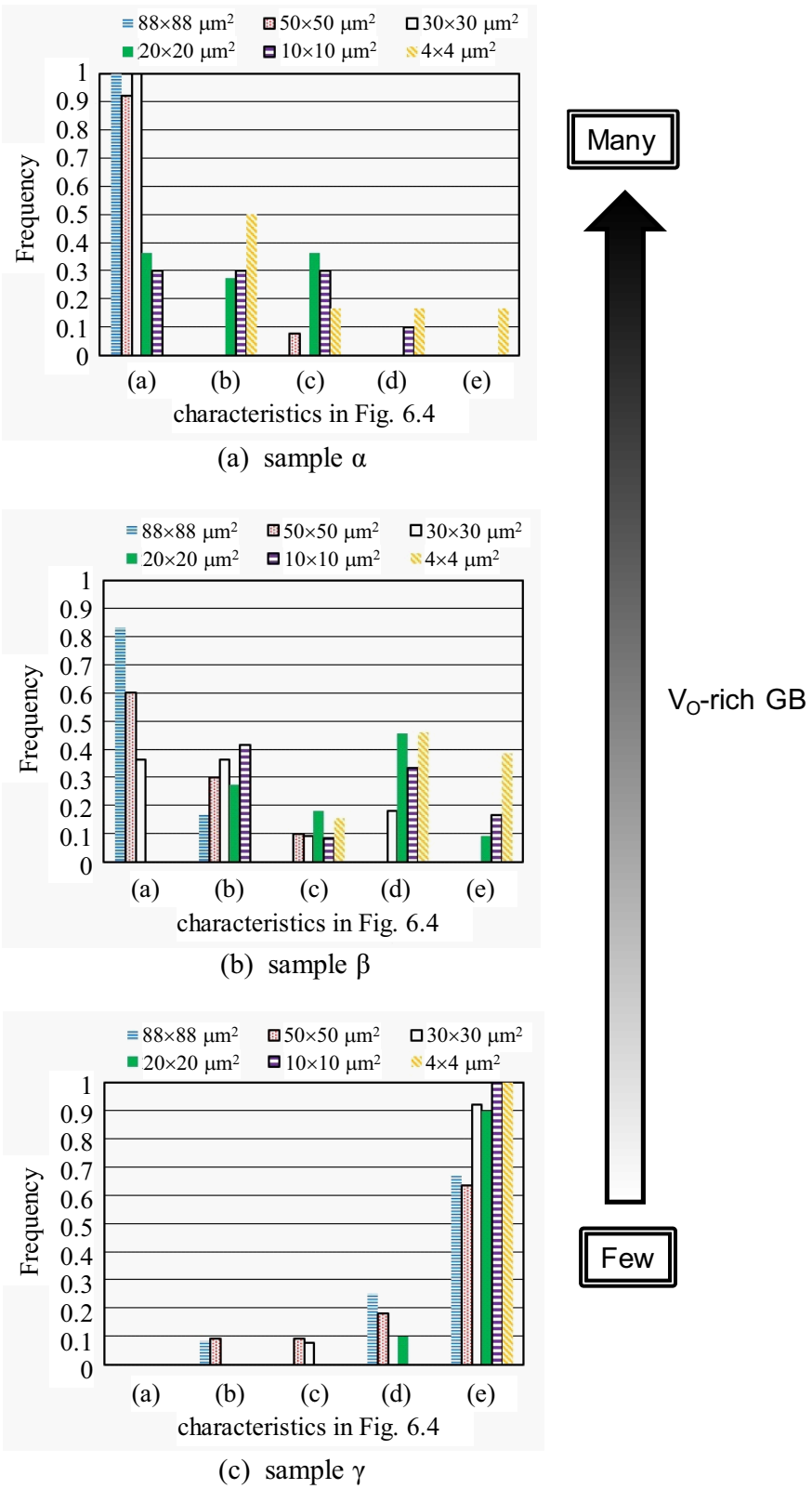

Figure 6.8: Frequency distributions of cell conductance characteristics at RT in crossbar-type RS cells with the sizes of 88×88 μm^2, 50×50 μm^2, 30×30 μm^2, 20×20 μm^2, 10×10 μm^2, and 4×4 μm^2 in three samples.

conventional samples. These results indicate that relatively large cell in the thinner NiO samples easily results in the disappearance of the conductance quantization and conductance fluctuation due to large background conductance, that is to say, components nG_0 and G_f of cell conductance are hindered by increased G_{bulk}. Therefore, G_{bulk} should be decreased by means of an increase in NiO thickness to some extent or a reduction in cell size to observe the conductance quantization and conductance fluctuation.

The dependence of transitions on cell size in dominant cell conductance can be explained in a manner similar to that for the dependence on O_2 flow rate. Although both G_{bulk} and G_f decrease as the cell size reduces, G_f decreases more than G_{bulk} because V_O-rich GB density that contributes to the modification of V_Os upon applying a voltage decreases. A further decrease in G_f leads to the appearance of nG_0 by a reduction in cell size. Moreover, a decreased density of "moderately" V_O-rich GBs or a reduction in cell size results in an increase in semi-forming voltage as discussed in Section 5.4.2, and fewer QPCs as per the relationship described above between the cell size and the number of V_Os at GBs in a NiO layer.

6.3 Effect of Voltage Mode and Heating on Conductance Fluctuation

6.3.1 Step-by-step voltage sweep

In this section, the author considers the properties of conductance fluctuation in detail. A sample in which capacitor-type RS cells exhibit conductance fluctuations without the occurrence of semi-forming was prepared, as shown in Fig. 6.4(b).

The authors swept voltages step by step over the RS cells. The maximum positive voltage gradually increased, for investigation of cell conductance after the modification of V_O concentration in the GBs of a NiO layer. Figure 6.9 shows an example of the results by step-by-step voltage sweeping. In this case, the maximum voltage was set successively to 1.3, 1.7, 2.2, and 2.8 V. If the maximum voltage is below approximately 1 V, the cell conductance tends to remain almost unchanged. Whereas, the cell conductance at a selected voltage below 1 V gradually increases after each applied voltage of 1.3 V or more, which means the appearance of the modification of V_Os by a voltage sweep. Note that the conductance increase was confirmed never to be observe after the voltage sweep even many times as long as the maximum voltage is the same as or less than the prior values. This result suggests that the modification of V_Os is basically caused by the applied voltage and unfortunately does not recover to the state before the modification.

In contrast, several RS cells in the sample exhibit typical conductance fluctuations before and after semi-forming, as shown in Fig. 6.2. Therefore, the number of V_O-rich GBs in the former RS cell is estimated to be more than that in the latter RS cells.

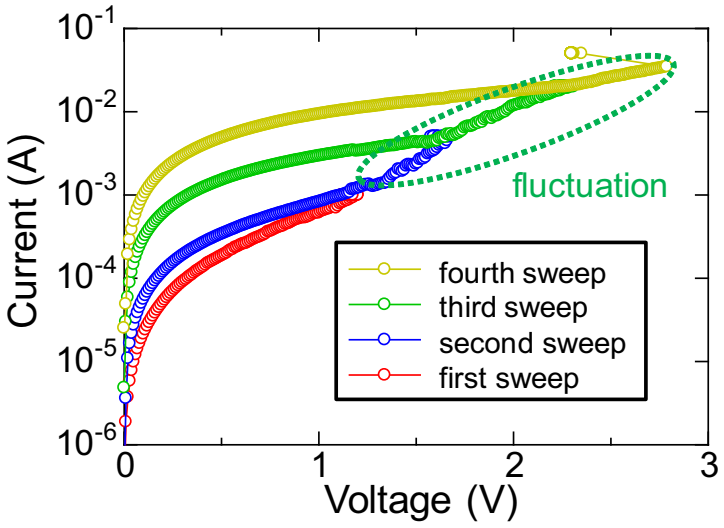

Figure 6.9: Conductance after modification by step-by-step voltage sweeping. The maximum voltage was set successively at 1.3, 1.7, 2.2, and 2.8 V. The cell conductance at less than 1 V gradually increases after each appearance of the modification.

6.3.2 Pulse voltage

For the practical use of the Pt/NiO/Pt RS cell, the electrical characteristics upon applying a pulse voltage to the cell should be investigated.

First, the author investigated the effect of conductance quantization and conductance fluctuation as a function of ramp rate of the applied voltage by using a Keithley 4200-SCS semiconductor parameter analyzer equipped with a source measure unit (SMU) and a pulse measure unit (PMU). The ramp rate R was varied in the range from 10 V/s to 2×10^5 V/s. The measured capacitor-type RS cells were confirmed to exhibit typical conductance fluctuation before and after semi-forming in a conventional voltage sweep, in which R corresponded to 0.2−0.3 V/s. To prevent the cells from the occurrence of semi-forming, I_{comp} was selected as 30 μA. When R was smaller than approximately 10^4 V/s, a conductance fluctuation was clearly observed in the cells. In particular, a few cells exhibited a conductance fluctuation at a voltage below 1 V, which seemed to originate from a relatively larger number of V_O-rich GBs within the cells. Conversely, when R was larger than approximately 10^5 V/s, almost all of cells never exhibited a conductance fluctuation before the cell current reached I_{comp}. Moreover, the author applied these ramped voltages to such cells several times using an R of 2.5×10^3 V/s. Although conductance fluctuation appeared above 1 V during the first ramping of the voltage, the application of the second ramped voltage in several RS cells revealed a disappearance of the conductance fluctuation, as shown in Fig. 6.10. Furthermore, in other RS cells, conductance fluctuation was not observed after the voltage sweep even after many times, as long as the maximum ramped voltage was less than the prior values, which was similar to the result shown in Fig. 6.2. As a consequence, these results indicate that the application of relatively slow ramped voltage to the RS cell in the initial state provokes a conductance fluctuation, whereas conductance fluctuation is insensitive to a relatively fast ramped voltage.

Next, the author attempted to control the conductance quantization by applying a pulse voltage to the capacitor-type RS cells. Tsuruoka *et al.* reported discrete changes of the cell conductance by applying a pulse voltage to silver (Ag)/tantalum pentoxide (Ta_2O_5)/Pt RS cells (results not shown) [18]. The incremental amplitude of the positive pulse voltage with a width of 20 ms at intervals of 2 s resulted in a discrete increase in the cell conductance based on quantized conductance. In like manner, decrease in the quantized conductance was observed by applying a negative pulse voltage according to the typical bipolar RS characteristics in electrochemical metalization memory (ECM), in which the metal ions (Ag) move toward the active electrode (Pt) by application of a negative voltage to the active electrode and the filament is eventually ruptured by application of a negative voltage. However, the control of conductance quantization in TCMs has scarcely been reported. The author prepared two samples (samples A, B) including capacitor-type Pt/NiO/Pt RS cells with TE diameters of 50−200 μm. Several cells in samples A and B were confirmed to exhibit conductance quantization and conductance fluctuation. The thickness of the NiO layers was 50 nm in sample A and 30 nm in sample B. In addition, the typical semi-forming voltage by the conventional voltage sweep was 1.2−1.6 V in sample A and 1.0−1.5 V in sample B, where the values in the smaller cells were likely to be larger than those in the larger cells. Only

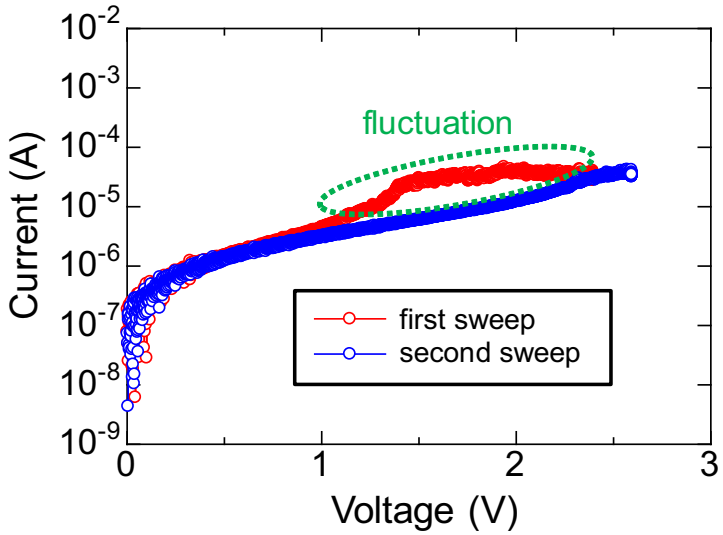

Figure 6.10: Typical $I-V$ characteristics by application of ramped voltage with R of approximately 2.5×10^3 V/s.

one pulse voltage with a rise and fall time of 10 μs and with a width of 500 μs was applied to the cells at each time, to exclude a heating effect from the prior voltage application (sufficiently long interval). Although the adoption of the pulse amplitude at each time was very difficult, the tentative amplitude of the first application was selected as approximately 1.5 times of the typical semi-forming voltage by the conventional voltage sweep in the same sample, and the following amplitude was varied flexibly depending on the prior response at each time.

Figure 6.11 shows an example of the changes of cell conductance in sample A by the application of the pulse voltages for five times. The minimum amplitude of the pulse voltage to induce conductance quantization in the cells with a TE diameter of 50 μm tended to be larger than that in the cells with a TE diameter of 100 μm. In the case shown in Fig. 6.11(a), the second application of 1.8 V amplitude enabled an increase in the conductance by $2\,G_0$, followed by an increase in the conductance by approximately $0.5\,G_0$ upon the fourth application of 1.95 V amplitude, and finally second forming occurred. In the case shown in Fig. 6.11(b), the second application of 1.7 V amplitude enabled an increase in the conductance by approximately $2\,G_0$, followed by a gradual increase in the conductance based on G_0 during the fourth application of 1.9 V amplitude and saturation of approximately $15\,G_0$. Upon the fifth application of 2.0 V, a drastic conductance fluctuation from $9\,G_0$ to $16\,G_0$ was observed. The drastic indiscrete fluctuation was sometimes observed during pulse voltage application under a higher conductance of more than $10\,G_0$. When application of a pulse voltage to the cells in sample A was conducted after semi-forming under I_{comp} of 100 μA followed by reset by applying negative voltage sweep, the cells tended to exhibit conductance quantization more clearly.

However, Fig. 6.12 shows an example of changes of cell conductance in sample B by nine or ten times after application of the pulse voltages. In the case of the cell with a TE diameter of 50 μm shown in Fig. 6.12(a), the second application of 1.8 V amplitude provided a two-step increase in the conductance by G_0, followed by an increase in the conductance by approximately $0.5\,G_0$ upon the fourth application of 2.0 V amplitude, and several times increase by approximately $0.5\,G_0$. Upon the ninth application of 2.4 V, a conductance fluctuation from $5.5\,G_0$ to $6.5\,G_0$, and semi-forming occurred during the tenth application of 2.4 V. In the case of the cell with a TE diameter of 100 μm shown in Fig. 6.12(b), sequential applications of a pulse voltage resulted in an increase in thel conductance by approximately 0.5, 1.0, or $1.5\,G_0$. During the fifth application of 1.6 V to the cell, a periodic conductance fluctuation was observed at a conductance level of approximately $2.5\,G_0$. Most of the cells in sample B exhibited a clear conductance increase by 1.0 or $0.5\,G_0$ until the conductance reached $6-8\,G_0$. The fact that conductance quantization became unstable as the conductance increased agrees with the results in the voltage sweep mode.

These changes in cell conductance based on not only G_0 but also $0.5\,G_0$ have been reported in valence change memories (VCMs) [8, 19–21] and TCMs [4]. Even by the conventional voltage sweep, a quantized plateau at half-integer multiples of G_0 was sometimes observed in the author's Pt/NiO/Pt RS cells, as shown in Fig. 6.13. Therefore, the RS cell can be categorized into a TCM also in terms of the appearance of half-integer multiples of G_0. Nevertheless, the controllability of conductance quantization in the Pt/NiO/Pt RS cells was by no means satisfactory. Although

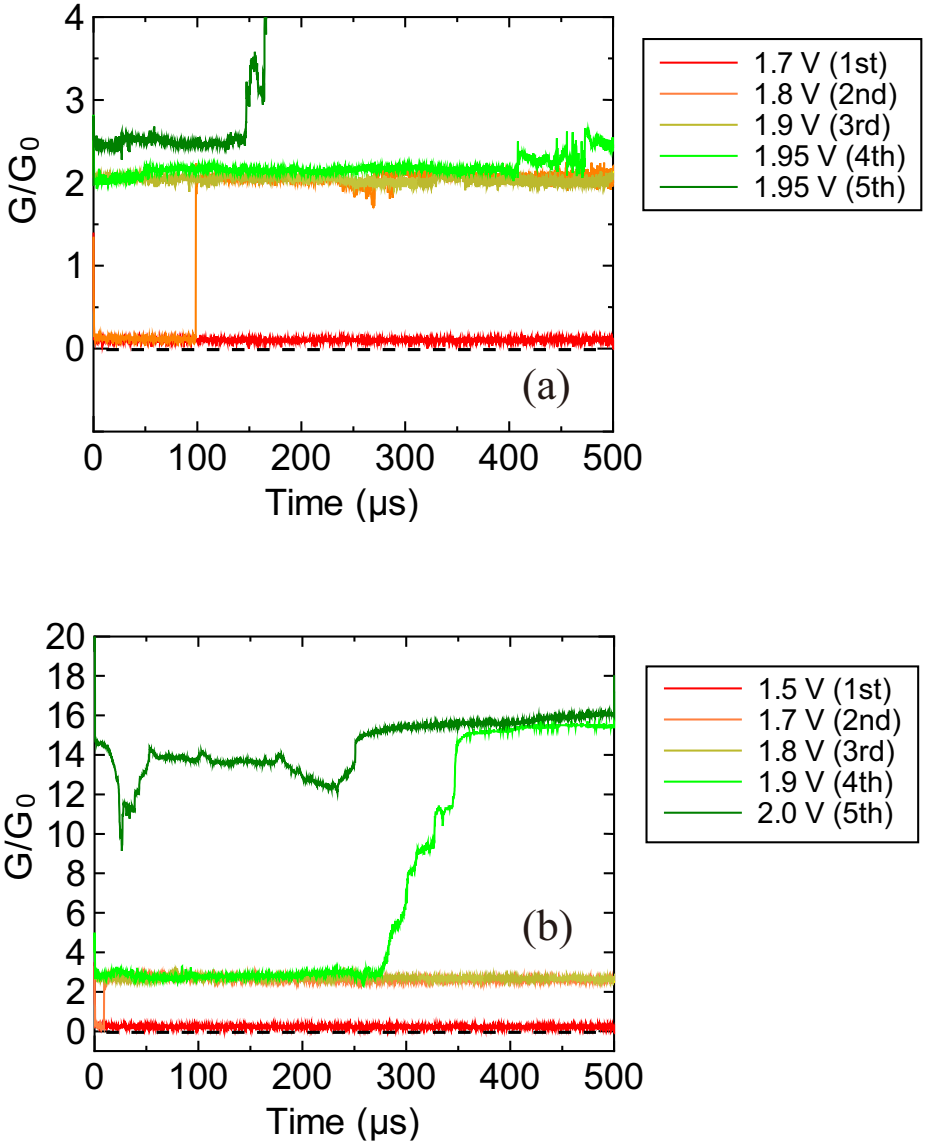

Figure 6.11: An example of changes of cell conductance in sample A by five times application of pulse voltage with a width of 500 μs. The RS cell size of (a) 625π μm^2 and (b) 2500π μm^2.

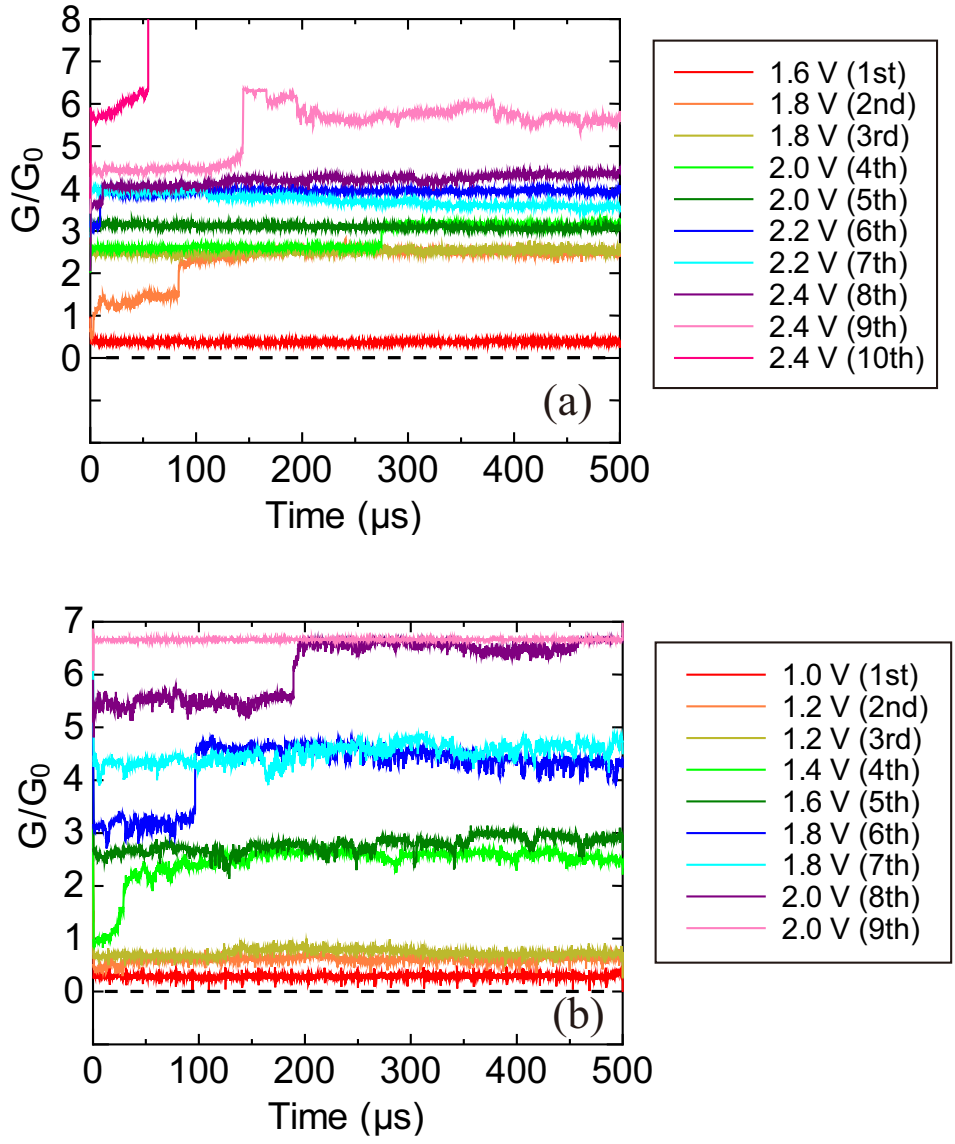

Figure 6.12: An example of changes of cell conductance in sample B by nine or ten times application of pulse voltage with a width of 500 μs. The RS cell size of (a) 625π μm^2 and (b) 2500π μm^2.

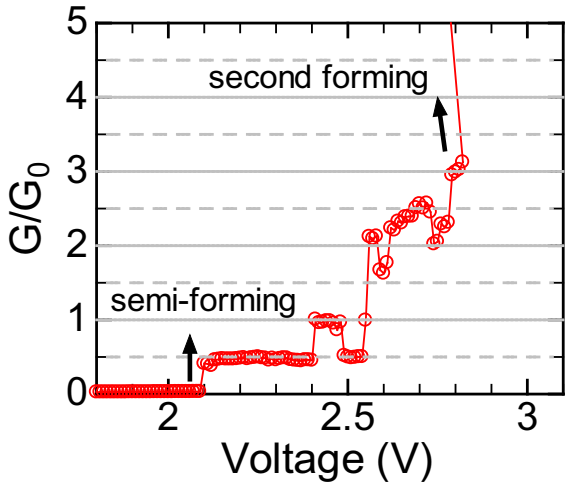

Figure 6.13: $G/G_0 - V$ characteristics by the voltage sweep. Quantized plateau at half-integer multiples of G_0 was observed just after semi-forming.

incremental voltage application to the cells tended to result in a discrete conductance increase by G_0 or $0.5\,G_0$, correlation between the incremental voltage and the incremental conductance exhibited a large distribution, and thus, the author struggled to select the amplitude of the pulse voltage. Moreover, conductance fluctuation was often observed with a pulse width of only 500 μs, especially in relatively large number multiples of G_0.

Finally, the authors attempted to achieve a discrete decrease in the cell conductance in the capacitor-type RS cells by applying a negative pulse voltage as in Ag/Ta_2O_5/Pt RS cells [18]. It has been reported that the opposite polarity of reset voltage to the polarity for set possibly reduces the reset current in TCMs, rather than the same polarity of reset as set [22]. Therefore, reset occurs more easily by the opposite polarity of reset to set rather than by the same polarity of reset as set in TCMs. This seems to originate from an additional drift effect of V_O by the opposite polarity to the Joule heating effect for contributing to the occurrence of reset. Despite the many efforts, however, the application of even a negative pulse voltage to the RS cells provoked only an increase in the cell conductance instead of a decrease. In the voltage sweep, stable nonpolar RS behavior could be obtained in the RS cells, as shown in Fig. 6.1. As a consequence, the enhancement of the controllability should be tried again by an optimization of many parameters in the pulse voltage.

6.3.3 Heat to the cell

The author also investigated how heating affects the fluctuation in conductance. To do this, capacitor-type RS cells in the HRS after semi-forming and subsequent reset were prepared. The TE diameter of the cells was 100 μm, and NiO thickness was 80 nm. By sweeping the voltage to the maximum voltage (the first sweep, see Fig. 6.14) and preventing the set operation, the cell conductance at RT was maintained at $1.48\,G_0$ after the second sweep. Upon heating the sample to 470 K in air, the cell conductance at RT changed to $1.17\,G_0$ after cooling (the third sweep), which is equivalent to the cell conductance before the appearance of the modification. The decrease of $0.31\,G_0$ in conductance ($1.48\,G_0 - 1.17\,G_0$) at RT represents the disappearance of the modification component G_f because of heating to 470 K. In addition, another crossbar-type RS cell with a size of 20×20 μm^2 and 4×4 μm^2 and NiO thickness of 50 nm exhibited similar characteristics. The cells in the same samples were confirmed to cause the conductance quantization and conductance fluctuation. The conductance values of the measured cells at RT were maintained at approximately $1.2-1.9\,G_0$ after semi-forming and stopped voltage. Although several cells with a size of 20×20 μm^2 did not show conductance decrease after heating to 470 K, such cells exhibited the decrease in $0.1-0.6\,G_0$ after heating to 570 K at least. Whereas, conductance at RT of cells with a size of 4×4 μm^2 decreased by $0.2-0.6\,G_0$ after heating to 470 K. As a result, temperature of heating for the disappearance of the modification of V_Os may depend on V_O-rich GB density that contribute to the modification.

Moreover, another capacitor-type RS cell in the LRS was prepared for a similar investigation. The cell conductance G at RT in the HRS and the LRS was $1.48\,G_0$ and $2.47\,G_0$, respectively. Upon heating to 470 K in air, as shown in Fig. 6.15(a), the cell conductance at 470 K suddenly

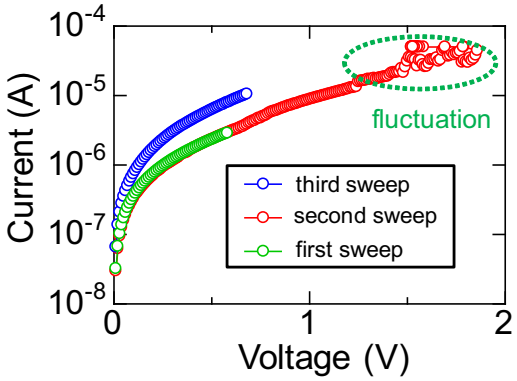

Figure 6.14: Conductance after modification and heating to 470 K. The modification occurs at the first sweep and the cell conductance is confirmed by the second sweep. After heating, the cell conductance decreases by the third sweep.

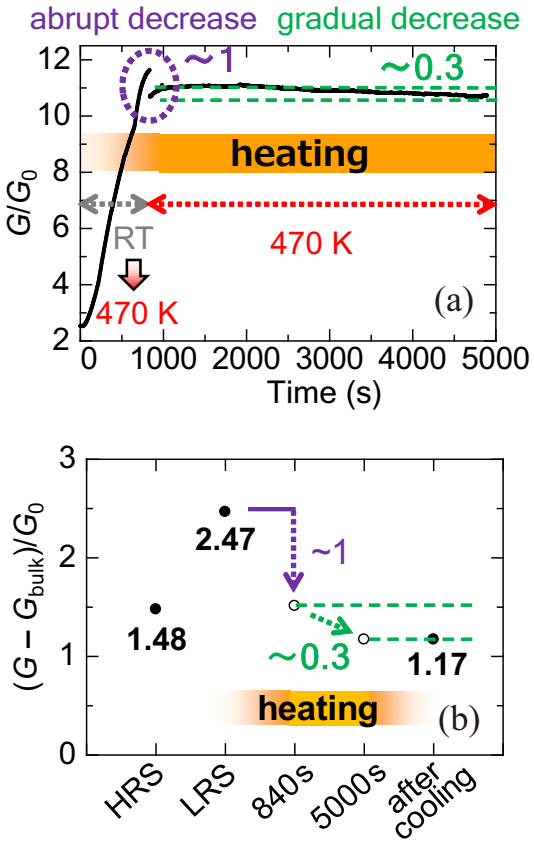

Figure 6.15: Change of (a) G/G_0 during heating to 470 K and (b) $(G - G_{\mathrm{bulk}})/G_0$ at each stage. $(G - G_{\mathrm{bulk}})/G_0$ values at high temperature during heating (open circle) are estimated from the temperature dependence of G in the initial state of other cells in the same sample as that of G_{bulk}.

changed from 11.61 G_0 to 10.66 G_0. Here, a conductance over 10 G_0 originates from the increase in G_{bulk} owing to the high temperature. The difference of approximately G_0 between these values suggests that the QPC has disappeared. Figure 6.15(b) exhibits change of $(G - G_{\mathrm{bulk}})/G_0$ at each stage. $(G - G_{\mathrm{bulk}})/G_0$ values at high temperature during heating are estimated from the temperature dependence of G in the initial state of other cells in the same sample as that of G_{bulk}. The disappearance supports the result involving in the disappearance of QPCs by heating to even 370 K as described in Section 5.2.3. Furthermore, upon heating the cell to 470 K, the cell conductance decreases by approximately 0.3 G_0, as shown in Fig. 6.15(a), which also suggests that the modification has disappeared. As a consequence, the formation of a conductive filament with a QPC and the modification of V_Os at GBs in the NiO layer are possibly destroyed by heating, which means that these phenomena are similar in terms of contributing to the change in cell conductance.

6.4 Driving Force behind Reset

6.4.1 Two types of reset

Based on the proposed model on forming in Fig. 5.14, a further increase in voltage after semi-forming causes second forming by creating a new fat conductive filament instead of transforming a conductive filament with a QPC. The physical basis of the model relies on the fact that the resistance in the HRS is nearly identical to that just after second forming, instead of being the same as the initial resistance of RS, as shown in Fig. 6.1(b). In this section, the author focuses on the reset after second forming in crossbar-type RS cells of varying sizes.

The O_2 flow rate must differ in each cell of different size for both semi-forming and second forming to occur because the semi-forming characteristics depend on the cell size in a given sample, as described in Section 6.2. Two types of reset appear in crossbar-type RS cells with a size of 20×20 $\mu\mathrm{m}^2$, as shown in Fig. 6.16. After second forming, the cell conductance in the HRS is equivalent to either the resistance just after second forming, as described above, or the initial resistance. The former reset after second forming will hereafter be called "reset A," and the latter reset is called "reset B." The probabilities of reset B occurring were 0%, 20%, and 44% in 88×88 $\mu\mathrm{m}^2$, 20×20 $\mu\mathrm{m}^2$, and 4×4 $\mu\mathrm{m}^2$ cells, respectively, which suggests that reset B occurs more frequently as cell size decreases. Moreover, we observed that conductance fluctuations after reset B and before set tended to become unclear in the cells which showed reset B after second forming.

This experimental result and disappearance of QPC upon heating described in Section 6.3.3 clarifies the driving force behind the reset after second forming. The reset B occurs as follows. In the LRS after second forming, a cell conductance of at least 2 mS causes a large current through the fat conductive filament during voltage sweeping. Just before reset occurs at a threshold voltage of approximately 0.5 V, a current of over 1 mA flows, causing local Joule heating around the fat filament created by second forming. If a conductive filament with a QPC exists near the fat filament, Joule heating at second forming would increase the temperature around the filament

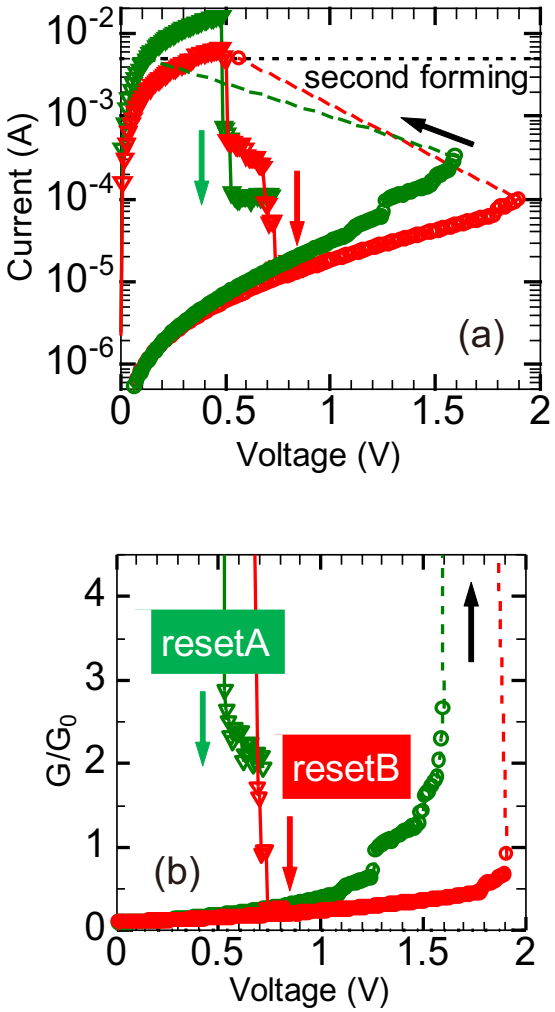

Figure 6.16: Two types of reset after second forming. The vertical axis represents (a) current through the cell and (b) quantized conductance units.

with a QPC. Such heating would dissolve not only the fat filament at reset but also possibly the filament with a QPC such that the cell conductance would finally reach the initial conductance corresponding to reset B. Conversely, if a fat filament were created far from the GBs where the filament with a QPC forms, the cell conductance after reset would result in conductance just after second forming, corresponding to reset A. As a result, the probability of reset B occurring naturally increases as the cell size decreases and the average separation distance between the two types of filaments decreases.

6.4.2 Joule heating by reset

The author demonstrates a rough thermal simulation to validate correlation between Joule heating as a driving force behind reset and experimental results described above. In the thermal simulation using a heat transfer solver in commercial software COMSOL Multiphysics, many assumptions are applied as follows.

Layer structures and parameters are based on single crystal materials, although NiO and Pt layers includes many GBs. The fat conductive filament created by second forming is assumed to be a cylindrical conductor with a diameter of 10 nm, which corresponds to an average apparent size of GB triple points revealed from TEM images. The cross-sectional view of a cylindrical layer structure is shown in Fig. 6.17(a). The fat filament is located at the center of the NiO layer with a width of 44 μm (maximum cell size is 88×88 μm^2). The details of the simulation are described in Section B.1. The physical property values of required parameters for the simulation are shown in Table 6.1. Although particularly the heat capacity C_p of NiO seems to depend on temperature as in Eq. (B.12), the temperature dependence is regarded as negligible. The author adopts the values of physical parameters of Ni as those of the filament region because the filament can be treated as the mixture of NiO and Ni in several simulations [23–25], and V_O concentration seems very high at the filament region. In the cylindrical coordinate system (r, ϕ, z), heat equation of Fourier's law is described as follow:

$$\frac{\partial T}{\partial t} = \alpha \left(\frac{\partial^2 T}{\partial r^2} + \frac{1}{r}\frac{\partial T}{\partial r} + \frac{\partial^2 T}{\partial z^2} \right) + \frac{\dot{Q}}{\rho C_p}, \tag{6.1}$$

where α $(= k/\rho C_p)$ is the thermal diffusivity and $\dot{Q}$ is the internal volumetric heat source originated from Joule heating at the fat filament. The ϕ component can be neglected due to symmetry.

Temperature at the filament region before reset is assumed to be tentatively 600 K, as shown in Fig. 6.17(b), as estimated by reset current of 1 mA [24]. Figure 6.17(c) shows thermal conduction toward the outer region just before reset (tentatively at 1 ms), and after reset the temperature of the outer region gradually falls. One of the thermal simulation results indicates that Joule heating at second forming would elevate the temperature (above 400 K) enough to dissolve the conductive filament with a QPC and to vanish the modification of V_Os especially within approximately 2 μm from the fat filament. As a result, reset after not only second forming but also semi-forming can be thermally induced rather than voltage driven, which results in two types of reset and nonpolar RS operation with different ranges of conductance.

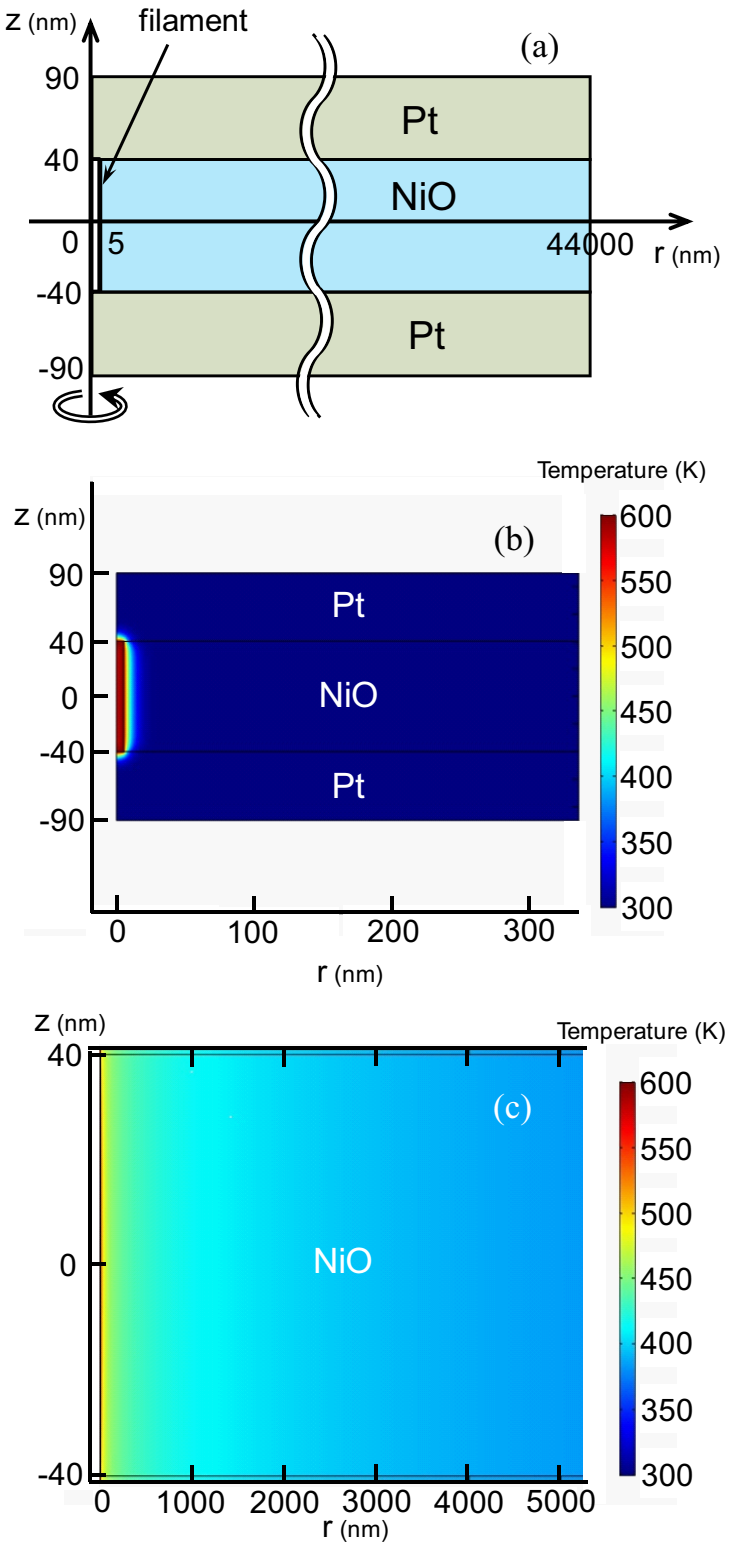

Figure 6.17: Thermal simulation is carried out based on (a) the cross-sectional view of a layer structure. The simulation results of thermal conduction toward outer region are shown (b) at 10 ns after Joule heating at the filament region and (c) just before reset (tentatively at 1 ms).

Table 6.1: Values of parameters used in a thermal simulation.

	Thermal conductivity k (W m^{-1} K^{-1})	Density ρ (kg m^{-3})	Heat capacity C_p (J kg^{-1} K^{-1})
Pt	70	21450	1340
NiO	20	6670	600
Filament	91	8908	4410

6.5 Discussion

The author discusses new and original findings based on the results in the thesis.

Significance of two types of nonpolar resistive switching

Nonpolar RS has been reported much previously in TCMs [26–32]. The driving force behind reset has been considered to be local Joule heating at a conductive filament mainly by using several simulations [24, 25, 33]. However, the estimated temperature required for reset varies widely from 400 K to over 1000 K depending on reports due to possible different assumptions, such as a diameter of the filament [24, 25, 33, 34].

On the contrary, two types of nonpolar RS operation with different conductance range, as shown in Fig. 6.1, have not been reported in any RS cells, and the original phenomena in the specific Pt/NiO/Pt RS cells. Moreover, a conductive filament with a QPC and the modification of V_Os possibly disappear upon heating the RS cells to 370−570 K, which has never reported by other groups. From the viewpoint of a fat filament created by second forming equivalent to the filament reported above by other groups created by the conventional forming, the relatively low temperature required for the disappearance of the conductance quantization and conductance fluctuation in the cells indicates that the estimated temperature to destroy the conventional filament is higher than the temperature to destroy the conductive filament with a QPC and the modification of V_Os.

One of the experimental basis is that the fat filament created by second forming has been never ruptured upon heating the RS samples to 600 K during a few days. Note that the initial resistance of several RS cells in samples decreased and such cells became not to exhibit semi-forming characteristics after the heating temperature to the samples was above 600 K. Other basis is the difference of temperature maps between semi-forming and second forming, as shown in Fig. 5.18. Therefore, the temperature required for reset is thought to exhibit two types depending on the filament properties.

Coupled simulation for reset by voltage sweep

The author demonstrates a rough simulation to validate correlation between Joule heating as a driving force behind reset and experimental results described above. In this simulation using solvers of heat transfer, electric current, and diffusion in commercial software COMSOL Multiphysics, many assumptions are also applied. The conductive filament is assumed to be a cylindrical conductor with a diameter of 10 nm. The cross-sectional view of a cylindrical layer structure is shown in Fig. 6.18. Whereas the thickness of Pt electrodes and NiO is the same as that in thermal simulation in Section 6.4.2, the diameter of the RS cell is 100 μm. The air regions around the cell and heat sink at the bottom of SiO_2 on Si substrate are set for the simulation.

The time-dependent Joule heat conduction equation in these materials are

$$\rho_{\mathrm{Mater.}} C_{\mathrm{pMater.}} \frac{\partial T}{\partial t} = k_{\mathrm{Mater.}} \Delta T + \sigma_{\mathrm{Mater.}} |\nabla V(t)|^2, \tag{6.2}$$

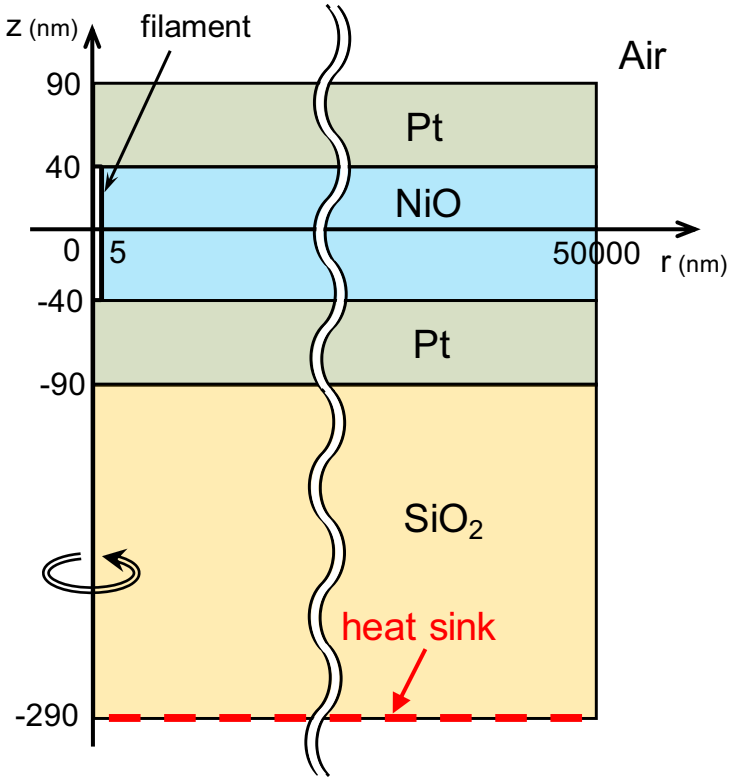

Figure 6.18: Cross-sectional view of a layer structure in a coupled simulation for reset.

under the time-dependent V_O diffusion equation in the NiO layer described by

$$\frac{\partial c_v}{\partial t} = \nabla \cdot (D_v(T)\nabla c_v), \tag{6.3}$$

where D_v is the diffusion coefficient value of V_Os assumed to be isotropic in the NiO layer. The details of the coupled simulation are described in Section B.2. The physical property values of required parameters for the simulation are shown in Table 6.2 [24, 25]. Note that the dependencies of these values of NiO on temperature and the V_O concentration can be reflected in Eqs. (B.10) – (B.12) (described under the table). The values in these equations are shown in Table 6.3. The most difficult assumption is to define the diffusion coefficient of V_Os (D_v) in the NiO. D_v is theoretically described as follow: [35]

$$D_v(T) = D_{v0} \exp\left(-\frac{U_A}{k_B T}\right), \tag{6.4}$$

where D_{v0} is the coefficient and U_A is the energy barrier between the confining potential wells for V_Os. Table 6.4 exhibits the adopted D_{v0} and U_A, as discussed in Section B.2.

The voltage sweep was applied to the cell with a fat filament in the LRS. Figure 6.19 exhibits one of the results of the coupled simulation for reset. The gradual change in the calculated profiles of the filament properties and temperature originated from local Joule heating is caused by the voltage sweep, the rate of which R is 1 V/s. Before the profile of the filament begins to change because of the V_O diffusion at 0.46 V (t = 0.46 s), the maximum temperature in the filament region reaches 600 K at 0.34 V. The V_O diffusion toward outer region is assisted by the Joule heating due to the power dissipation before reset, which extends the depleted gap of V_Os and decreases the electrical conductivity of the cell. At 0.86 V (t = 0.86 s), just before reset, the temperature shows a parabolic profile with a maximum value around 880 K at the middle of the filament. After the reset, the temperature begins to drop drastically because of the sufficient extension of depleted gap and the lack of power dissipation.

It is confirmed that the temperature profiles are parabolic with line symmetry at the center of the filament. This should be because the Pt electrodes work as a sufficient heat sink through the substrate and a probe for the application of voltage to the cell. However, Larentis reported the asymmetric calculated profiles at reset, in which the point of both the V_O depletion and the maximum temperature was above the middle of the filament [36]. The difference of the profiles seems to originate from the drift effect of V_Os. If the drift effect was required, the time-dependent V_O diffusion equation in the NiO layer could be described by Eq. (B.15). The author dared to neglect the drift effect of V_Os because the strict valence number of ionized V_O was not clarified, as discussed in Section B.2. Russo reported that the similar evolution of the depleted gap at increasing voltage, irrespective of the assumed initial diameter of the filament [24]. This can be understood by the independence of the local electric field and temperature on the filament size. Although reset voltage depended on the filament size, it was confirmed by the experimental results that the reset voltage was almost independent of the compliance current at forming and the oxide material composition [37, 38].

Table 6.2: Values of parameters used in a coupled simulation.

	Thermal conductivity k (W m^{-1} K^{-1})	Density ρ (kg m^{-3})	Heat capacity C_p (J kg^{-1} K^{-1})	Electrical conductivity σ (S m^{-1}) $\times 10^6$
Pt	70	21450	1340	9.43
NiO	$k_\mathrm{NiO}(c_\mathrm{v})$	6670	$C_\mathrm{pNiO}(T)$	$\sigma_\mathrm{NiO}(T, c_\mathrm{v})$
SiO_2	1.38	2200	700	10^{-20}

$$k_\mathrm{NiO}(c_\mathrm{v}) = \min\left\{ k_\mathrm{Ni},\ \bar{k}_\mathrm{NiO} + (k_\mathrm{Ni} - \bar{k}_\mathrm{NiO})\frac{c_\mathrm{v}}{c_\mathrm{vth}} \right\}$$

$$C_\mathrm{pNiO}(T) = 506.64\ \mathrm{J/(kg{\cdot}K)} + 10.563\ \mathrm{J/(kg{\cdot}K)} \exp\left(\frac{T}{140.3\ \mathrm{K}}\right)$$

$$\sigma_\mathrm{NiO}(T, c_\mathrm{v}) = \min\left[\sigma_\mathrm{Ni},\ \sigma_\mathrm{Ni}\frac{c_\mathrm{v}}{c_\mathrm{vth}} \exp\left\{ -\frac{E_\mathrm{a}(1 - c_\mathrm{v}/c_\mathrm{vth})}{k_\mathrm{B}T} \right\} \right]$$

Table 6.3: Values used in a coupled simulation.

k_Ni	$\bar{k}_\mathrm{NiO}$	σ_Ni	E_a	c_vth
91 W/(m·K)	20 W/(m·K)	14.4 MS/m	0.3 eV	6.45×10^{27} m^{-3}

Table 6.4: Adopted values used in a coupled simulation.

D_v	U_A
10^{10} m^2/s	1.0 eV

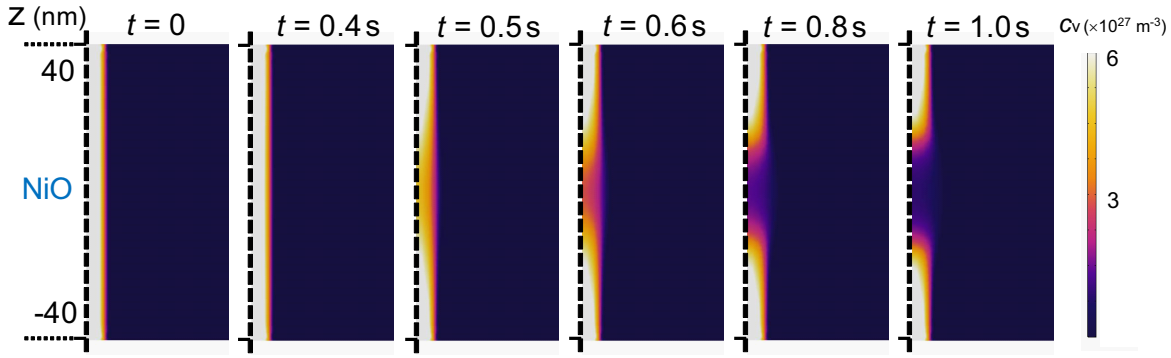

(a) Vo concentration (c_V)

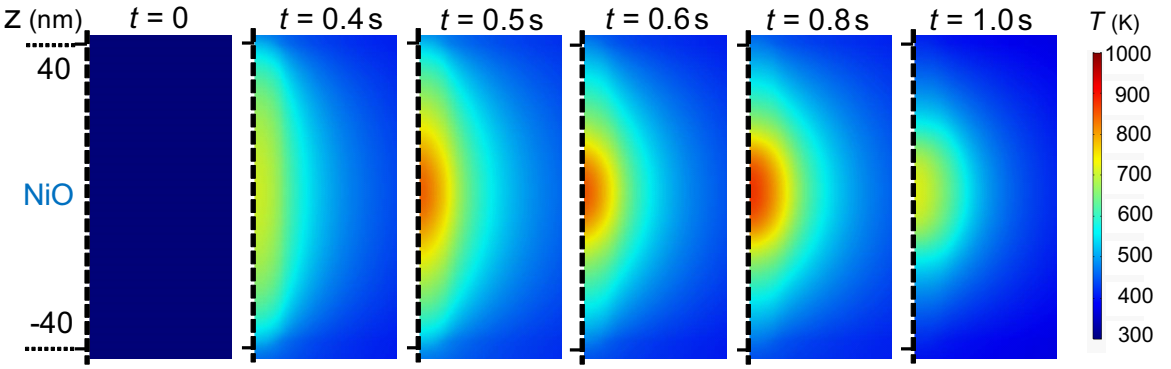

(b) temperature (T)

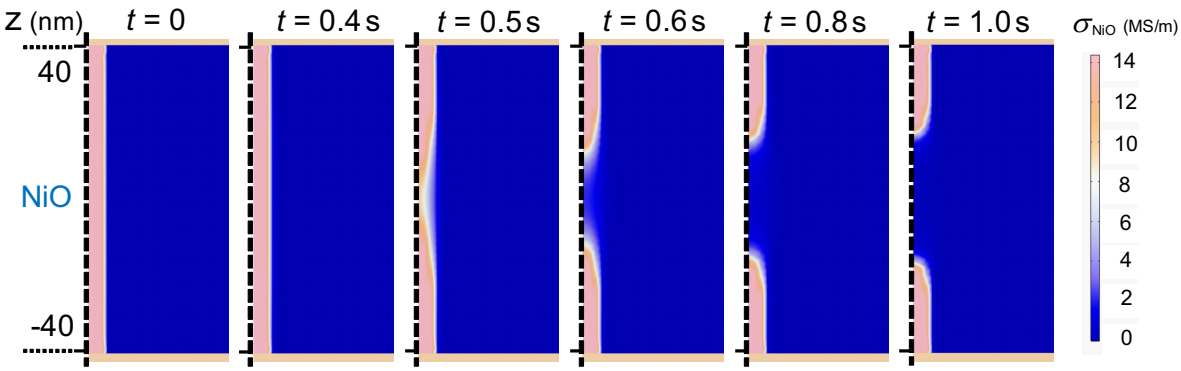

(c) electrical conductivity (σ)

Figure 6.19: Coupled simulation result for reset by the voltage sweep. The time-dependent voltage with a sweep rate R of 1 V/s causes the gradual change in the profiles of (a) V_O concentration, (b) temperature, and (c) electric conductivity in the NiO layer.

The author considers the dependence of the profiles of the filament and temperature on the voltage sweep rate R. Figure 6.20 exhibits the time-dependent temperature profiles both at beginning of the V_O diffusion and just before reset. Note that reset is defined as the beginning of decreasing maximum temperature. The applied voltage required for the trigger of V_O diffusion and reset, as well as the maximum temperature at each event, increases as R increases, because V_O diffusion takes a reasonable time. Figure 6.21 exhibits R dependence of the applied voltage and maximum temperature at each event. Here, the applied voltages required for reaching to the maximum temperature of 350 K and 600 K are also displayed, which reveals the constant value (0.14 V for 350 K, and 0.34 V for 600 K) irrespective of R. These results indicate that the temperature required for the V_Os diffusion is 600 K at least in the R range of $0.01-1000$ V/s. Moreover, when R is more than 1 MV/s in the simulation, the applied voltage can not cause reset or even the V_O diffusion, which may reveal the speed-up limitation of nonpolar reset as long as the conventional D_v is used.

Significance of nonpolar resistive switching based on quantized conductance

The results described above revealed that the temperature for the disappearance of the conventional filament (above 600 K) was higher than that for the conductive filament with a QPC (below 600 K) by heating to the cell during a long time. In the similar manner, the maximum temperature required for V_O diffusion in the fat filament can be estimated to be much higher than that for the filament with a QPC generated by Joule heating during a relatively short time. The experimental and calculated results of two types of the filament with the wide range of conductivity reinforce the validity of Joule heating as the driving force behind reset.

In contrast, forming voltage also tends to increase as the voltage sweep rate increases [39]. Although the contribution degree of Joule heating between forming (set) and reset seems to be different, the tendency of forming voltage is similar to the sweep-rate dependence of reset voltage. The result suggests that electrical accumulated parameter (electric charge, for example) is needed for forming or set, such as the Joule heating for reset.

Two types of reset after second forming revealed that both the conductive filament with a QPC and the modification of V_Os possibly disappeared owing to Joule heating conducted from the fat filament, as discussed in Section 6.4. Considering voltage- and heat-driven conductance fluctuation, the modification of V_O concentration can be seen as a possible precursor of the conductive filament with a QPC created by semi-forming, or even of the fat filament created by second forming. Based on the similarity between possible rupture of the conductive filament with a QPC and the modification by a relatively low heating, conductance quantization seems a special form of the conductance fluctuation.

Although poor retention under the temperature of above 100°C should be solved for applications at high temperatures, the conducted heating from the fat filament does not require any special consideration as long as only the RS based on quantized conductance is used, instead of RS accompanied by large Joule heating after second forming.

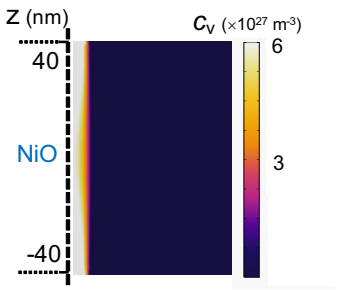

(a) Vo profile at the beginning of the diffusion

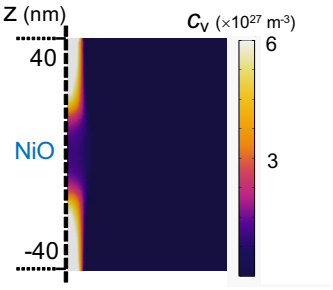

(b) Vo profile just before reset

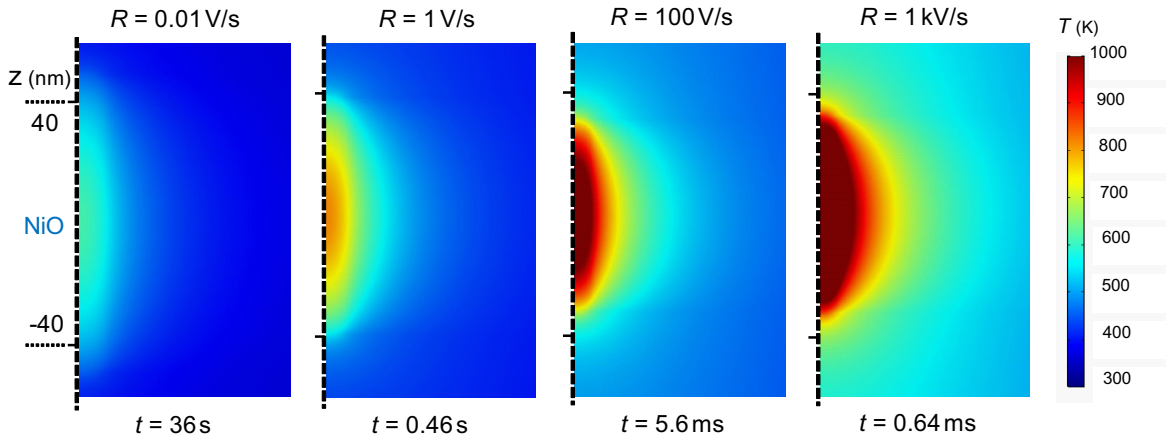

(c) temperature profile at the beginning of Vo diffusion

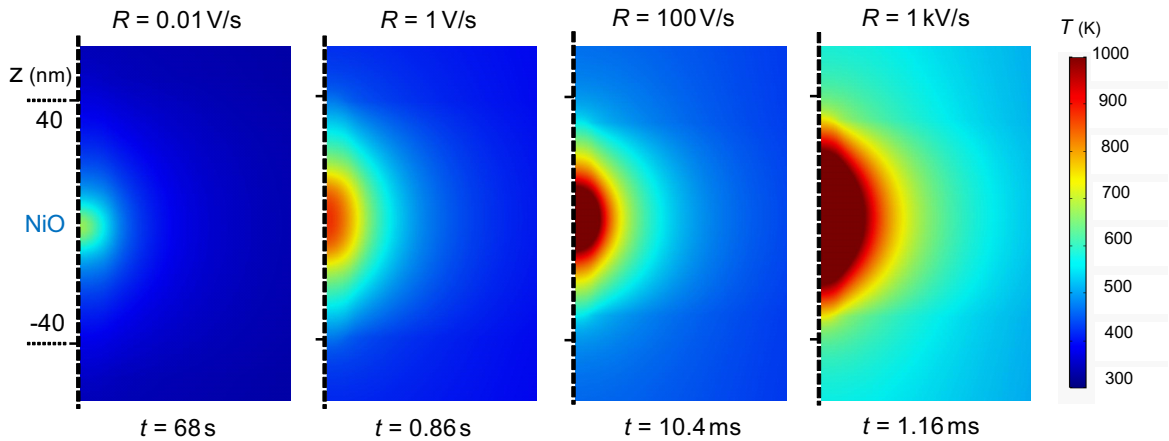

(d) temperature profile just before reset

Figure 6.20: Coupled simulation result for reset by the voltage sweep with the various sweep rates. To result in the V_O profiles at (a) beginning of the diffusion and (b) just before reset, the temperature profiles at (c) beginning of the diffusion and (d) reset are needed, respectively.

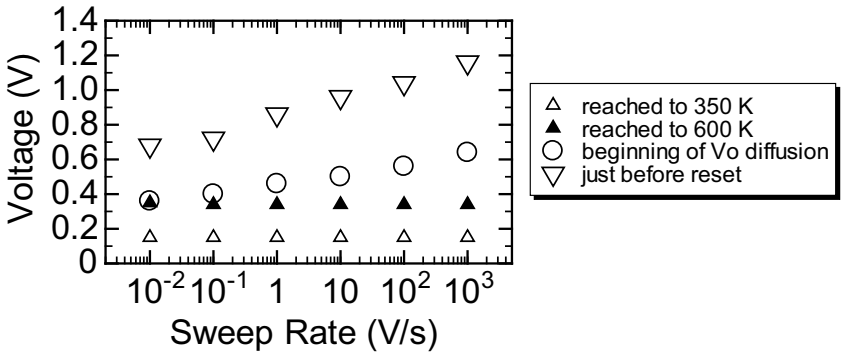

(a) applied voltage

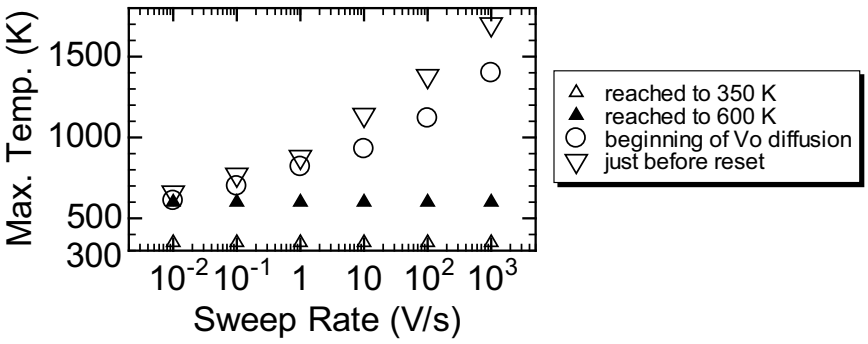

(b) maximum tempeature

Figure 6.21: Voltage-sweep-rate dependence of (a) applied voltage and (b) maximum temperature at the particular events.

Verification of filament model

The location where the conductive filament with a QPC was not directly observed as discussed in Section 5.4.3. However, V_Os as a possible source of the filament at GB triple-points were confirmed owing to the columnar structure in NiO layer deposited by sputtering (in the SP-Pt sample), as described in Section 4.3.2. Nevertheless, the author confirmed conductance quantization in several RS cells in the EB-Pt samples. Although the V_O distribution in the NiO layer in the EB-Pt sample can not be analyzed by EDX due to the granular structure, the appearance condition of QPC seems to be insensitive to the structure of NiO, and just the existence of "moderately" V_O-rich GBs in the NiO layer.

As a consequence, the author has succeeded in verifying the filament model for explanation of RS operation, through the observation of V_O distribution at GBs and nonpolar RS based on quantized conductance.

6.6 Summary

Nonpolar RS operation after semi-forming and second forming in Pt/NiO/Pt stack cells was confirmed, in which the NiO layers were deposited by reactive sputtering at various O_2 flow rates. Upon sweeping the applied voltage, the conductance fluctuates in some cells in the initial state and in the HRS after semi-forming. Conductance fluctuation after semi-forming results in the cell conductance being a non-integer multiple of the quantized conductance G_0. The conductance increase owing to the fluctuations originates from the modification of V_O concentration at grain boundaries in the NiO layer.

Moreover, the modification of V_Os possibly disappears upon heating to 470−570 K through the formation of a conductive filament with a QPC created by semi-forming. Joule heating conducted from another fat filament in the NiO layer created by second forming. Cell size dependence of reset after second forming revealed that both conductive filaments with a QPC and the modification of V_Os possibly disappeared owing to Joule heating conducted from the fat filament. Considering voltage- and heat-driven processes, the modification of V_O concentration can be seen as a possible precursor of the conductive filament with a QPC by semi-forming or even of a fat conductive filament by second forming.

Furthermore, the author considered a driving force at the origin of the reset based on the types of reset that occur after semi-forming in cells of varying size. The large Joule heating caused by the current through the fat filament created by second forming determines whether the cell conductance after reset takes on the value of the conductance just after second forming or whether that depends on the initial conductance. The thermal simulation and coupled simulation with heat and diffusion equation indicated that the maximum temperature required for V_O diffusion in the fat filament was much higher than that for the filament with a QPC generated by Joule heating during a relatively short time. As a result, the dominant driving force behind the reset in Pt/NiO/Pt cells was determined to be Joule heating.

References

[1] R. Waser, R. Dittmann, G. Staikov, and K. Szot, Adv. Mater. **21**, 2632 (2009).

[2] E. Miranda, S. Kano, C. Dou, K. Kakushima, J. Suñé, and H. Iwai, Appl. Phys. Lett. **101**, 012910 (2012).

[3] Y. Y. Chen, L. Goux, S. Clima, B. Govoreanu, R. Degraeve, G. S. Kar, A. Fantini, G. Groeseneken, D. J. Wouters, and M. Jurczak, IEEE Trans. Electron Devices **60**, 1114 (2013).

[4] A. Mehonic, A. Vrajitoarea, S. Cueff, S. Hudziak, H. Howe, C. Labbe, R. Rizk, M. Pepper, and A. J. Kenyon, Sci. Rep. **3**, 2708 (2013).

[5] C. Hu, M. D. McDaniel, J. G. Ekerdt, and E. T. Yu, IEEE Electron Device Lett. **34**, 1385 (2013).

[6] Y.-E. Syu, T.-C. Chang, J.-H. Lou, T.-M. Tsai, K.-C. Chang, M.-J. Tsai, Y.-L. Wang, M. Liu, and S. M. Sze, Appl. Phys. Lett. **102**, 172903 (2013).

[7] D. Ielmini, R. Bruchhaus, and R. Waser, Phase Transitions **84**, 570 (2011).

[8] X. Zhu, W. Su, Y. Liu, B. Hu, L. Pan, W. Lu, J. Zhang, and R.-W. Li, Adv. Mater. **24**, 3941 (2012).

[9] S. Long, X. Lian, C. Cagli, L. Perniola, E. Miranda, M. Liu, and J. Sune, IEEE Electron Device Lett. **34**, 999 (2013).

[10] U. Russo, D. Kamalanathan, D. Ielmini, A. L. Lacaita, and M. N. Kozicki, IEEE Trans. Electron Devices **56**, 1040 (2009).

[11] S. Menzel, U. Böttger, and D. Ielmini, J. Appl. Phys. **111**, 014501 (2012).

[12] J. Brader, W. Senn, and S. Fusi, Neural Comput. **19**, 2881 (2007).

[13] T. Ohno, T. Hasegawa, T. Tsuruoka, K. Terabe, J. K. Gimzewski, and M. Aono, Nat. Mater. **10**, 591 (2011).

[14] Z. Wang, H. Yu, X. A. Tran, Z. Fang, J. Wang, and H. Su, Phys. Rev. B **85**, 195322 (2012).

[15] G. Indiveri, B. Linares-Barranco, R. Legenstein, G. Deligeorgis, and T. Prodromakis, Nanotechnology **24**, 384010 (2013).

[16] A. Flocke and T.G. Noll, *Proceedings of the 33rd European Solid-State Circuits Conference* (2007) p. 328.

[17] E. Linn, R. Rosezin, C. Kügeler, and R. Waser, Nature Materials **9**, 403 (2010).

[18] T. Tsuruoka, H. Hasegawa, K. Terabe, and M. Aono, Nanotechnology **23**, 435705 (2012).

[19] E.-J. Yun, M. F. Becker, and R. M. Walser, Appl. Phys. Lett. **63**, 2493 (1993).

[20] H. Hajto, B. McAuley, A. J. Snell, and A. E. Owen, J. Noncryst. Solids **198**, 825 (1996).

[21] Y. Wang, X. Qian, K. Chen, Z. Fang, W. Li, Appl. Phys. Lett. **102**, 042103 (2013).

[22] Y. F. Chang, P. Y. Chen, Y. T. Chen, F. Xue, Y. Wang, F. Zhou, B. Fowler, and J. C. Lee, Appl. Phys. Lett. **101**, 052111 (2012).

[23] U. Russo, D. Ielmini, C. Cagli, and A. L. Lacaita, IEEE Trans. Electron Devices **56**, 186 (2009).

[24] U. Russo, D. Ielmini, C. Cagli, and A. L. Lacaita, IEEE Trans. Electron Devices **56**, 193 (2009).

[25] K. Kinoshita, S.-H. Koh, T. Moriyama, and S. Kishida, Sci. Rep. **5**, 18442 (2015).

[26] S. Seo, M. J. Lee, D. H. Seo, E. J. Jeoung, D.-S. Suh, Y. S. Joung, I. K. Yoo, I. R. Hwang, S. H. Kim, I. S. Byun, J.-S. Kim, J. S. Choi, and B. H. Park, Appl. Phys. Lett. **85**, 5655 (2004).

[27] B. J. Choi, D. S. Jeong, S. K. Kim, C. Rohde, S. Choi, J. H. Oh, H. J. Kim, C. S. Hwang, K. Szot, R. Waser, B. Reichenberg, and S. Tiedke, J. Appl. Phys. **98**, 033715 (2005).

[28] J.-W. Park, J.-W. Park, K. Jung, M. K. Yang, and J.-K. Lee, J. Vac. Sci. Technol. B **24**, 2205 (2006).

[29] K. Tsunoda, Y. Fukuzumi, J. R. Jameson, Z. Wang, P. B. Griffin, and Y. Nishi, Appl. Phys. Lett. **90**, 113501 (2007).

[30] H. Shima, F. Takano, H. Akinaga, Y. Tamai, I. H. Inoue, and H. Takagi, Appl. Phys. Lett. **91**, 012901 (2007).

[31] W. Wang, S. Fujita, and S. S. Wong, IEEE Electron Device Lett. **30**, 763 (2009).

[32] C. Kügeler, R. Weng, H. Schroeder, R. Symanczyk, P. Majewski, K.-D. Ufert, R. Waser, and M. Kund, Thin Solid Films **518**, 2258 (2010).

[33] D. C. Kim, S. Seo, S. E. Ahn, D.-S. Suh, M. J. Lee, B.-H. Park, I. K. Yoo, I. G. Baek, H.-J. Kim, E. K. Yim, J. E. Lee, S. O. Park, H. S. Kim, U.-I. Chung, J. T. Moon, and B. I. Ryu, Appl. Phys. Lett. **88**, 202102 (2006).

[34] T. Ninomiya, S. Muraoka, Z. Wei, R. Yasuhara, K. Katayama, and T. Takagi, IEEE Electron Dev. Lett. **34**, 762 (2013).

[35] D. B. Strukov, F. Alibart, and R. S. Williams, Appl. Phys. A **107**, 509 (2012).

[36] S. Larentis, F. Nardi, S. Balatti, D. C. Gilmer, and D. Ielmini, IEEE Trans. Electron Devices **59**, 2468 (2012).

[37] D. Ielmini, F. Nardi, and C. Cagli, IEEE Trans. Electron Devices **58**, 3246 (2011).

[38] S. Ambrogio, S. Balatti, A. Cubeta, A. Calderoni, N. Ramaswamy, and D. Ielmini, IEEE Trans. Electron Devices **61**, 2912 (2014).

[39] S. B. Lee, H. K. Yoo, S. H. Chang, L. G. Gao, B. S. Kang, M.-J. Lee, C. J. Kim, and T. W. Noh, Appl. Phys. Lett., **98**, 053503 (2011).

Chapter 7

Conclusions

7.1 Conclusions

In this thesis, the author focused on forming and resistive switching (RS) characteristics in binary transition metal oxide (TMO)-based cells for elucidating the nonpolar RS mechanism of thermochemical memories (TCMs). Distributions of forming voltage and the origin of conductive filaments in TMO-based RS cells created by forming have been investigated. In particular, the formation of conductive filaments with a quantum point contact (QPC) by specific forming in nickel oxide (NiO)-based RS cells has been discussed, as well as the appearance and disappearance of nonpolar RS characteristics based on quantized conductance.

The major conclusions obtained from the results in the present study are summarized as follows.

In Chapter 2, deposition methods of NiO and titanium dioxide (TiO_2) layers as the TMO and platinum (Pt) electrode were explained. The TMO layers were deposited by reactive sputtering using a metallic nickel (Ni) or titanium (Ti) target and a mixture of argon (Ar) and oxygen (O_2), which enabled the control of oxygen composition in the TMO layers by varying the O_2 flow rate. Moreover, the deposition systems for various layers were described, together with their modifications for the severe control of the oxygen composition. The fabrication procedure of the basic Pt/TMO/Pt RS cells was also explained. In addition, dependences of deposition rate and oxygen composition in the NiO layers on O_2 flow rate during reactive sputtering were analyzed based on Berg's model. To obtain appearance of the RS phenomenon, NiO layers were deposited in a metallic mode, while TiO_2 layers were deposited in an oxide mode. The RS condition based on quantized conductance in NiO-based RS cells was given.

In Chapter 3, admittance spectroscopy was performed on NiO layers with various oxygen compositions deposited on *n*-silicon (Si) substrates, whose structures were for characterization of localized defect levels in the NiO layer as a *p*-type semiconductor. The depletion layer width of the *p*-NiO/*n*-Si heterojunction was approximately 10 nm at zero bias, which was much thinner than the thickness of NiO_x layers within x of 1.0−1.2. The localized levels in NiO_x layers strongly depended on the oxygen composition x. For the NiO_x layers with low oxygen compositions ($x \leqq 1.07$), only a single peak was observed in the $(G - G_{dc})/\omega$ curve, while two peaks (or one

peak and a shoulder) existed for the NiO_x layers with higher oxygen compositions ($x \geqq 1.15$). The energy levels of observed defects located above the valence band edge in the NiO_x layers with low oxygen composition ($x \leqq 1.07$) were relatively large, 120−170 meV, whereas those with higher oxygen composition ($x \geqq 1.10$) were smaller than 100 meV. In addition, current-voltage (I–V) measurement of Pt/NiO/Pt structures on p-Si substrates was also conducted. The structures with lower oxygen composition ($x \leqq 1.07$) only exhibited RS operations because of the deposition of NiO_x layers by reactive sputtering in a metallic mode. The NiO-based resistive random access memory (ReRAM) cells exhibited potential for high-temperature applications in the future, because the Pt/$NiO_{1.07}$/Pt RS cells showed repeatable RS operation even at temperature as high as 550 K.

In Chapter 4, effects of crystallinity of the TMO layers and deposition condition on RS characteristics, especially forming characteristics, in TMO-based RS cells were investigated. At first, the thermal annealing condition dependence of crystallinity and oxygen composition in the NiO layers was examined. The annealing contributing to oxygen diffusion toward the NiO surface brought about changes in the crystalline orientation, strain, and oxygen composition in the NiO layer, which could obtain multiple resistance states of the RS cells. Next, crystallinity and time-dependent forming (TDF) characteristics in as-deposited Pt/NiO/Pt and Pt/TiO_2/Pt RS cells were investigated. While the NiO layers exhibited a granular structure on Pt bottom electrodes (BEs) deposited by electron beam (EB) evaporation, NiO columns preferentially exhibited <111> orientation on the Pt BE deposited by sputtering. Conversely, whereas both the TiO_2 layers exhibited a granular structure in the two types of samples, the concentration of oxygen vacancies (V_Os) differs between these samples. These results revealed that the crystalline structure and oxygen composition of the TMO layers reflected the crystalline structure of Pt BEs. In addition, Weibull distributions of time to forming under constant voltage stress (CVS) in various cells were also investigated. The results indicated that the formation of conductive filaments at forming followed a weakest-link theory, and that the weakest spots such as V_Os were distributed in the TMO layers according to Poisson statistics. The Weibull slope depended on the crystallinity of Pt BEs in NiO and TiO_2-based RS cells, independent of constant voltage and oxide thickness. As a result, the difference of Weibull distributions between the TMO-based RS cells reflected differences in both grain boundary (GB) density (crystallinity) and the V_O concentration (oxygen composition) in NiO and TiO_2-based RS cells. Furthermore, the difference of correlation between variations of initial resistance and distributions of time to forming was explained based on the crystallinity and the oxygen composition in the TMO layers. The author concluded that GBs in the TMO layers were where conductive filaments were created by forming.

In Chapter 5, the appearance condition of conductance quantization in the Pt/NiO/Pt cells was discussed. When a NiO layer was deposited by reactive sputtering at a selected O_2 flow rate, the specific characteristics of two types of forming were observed. The first abrupt current increase was referred to as “semi-forming,” and the second one as “second forming,” Dependence of forming characteristics on oxygen composition in the NiO layer revealed that the forming characteristics strongly depended on the number of V_Os at GB triple points in the NiO layers confirmed by

transmission electron microscopy (TEM)-energy-dispersive X-ray spectrometry (EDX) mapping, and that the O_2 flow rate during sputtering for the appearance of two types of forming should increase as the cell size reduced. Moreover, cell size dependence of semi-forming characteristics was explained by the area scaling law, which indicated an analogy of semi-forming with second forming (corresponding to the conventional forming). In addition, an RS model based on quantized conductance was proposed as follows. A voltage sweep resulted in a conductive filament with a QPC created by semi-forming at the weakest V_O-rich GB. Upon the voltage sweep after semi-forming, the conductive filament with a QPC gradually began to be fat according to conductance quantization. Further voltage application caused second forming by creating a new fat conductive filament at one of the other weak V_O-rich GBs. After both semi-forming and second forming, RS behavior occurred due to the rupture and formation of both the conductive filament with a QPC and the other fat filament, respectively. As a result, the appearance condition of a QPC turned out to be the existence of "moderate" V_O-rich GBs as long as the V_O-rich GBs were identical to the weakest V_O-rich GB in the NiO layer.

In Chapter 6, nonpolar RS operations after both semi-forming and second forming were focused on in terms of the Pt/NiO/Pt RS cells as TCMs. The O_2 flow rate during sputtering for the appearance of dominant conductance fluctuation was confirmed to be a bit smaller than that for the appearance of conductance quantization in RS cells of the same size. The physical origin of conductance fluctuation accompanied by conductance quantization was estimated to be the modification of V_Os at GBs in the NiO layers. The conductance fluctuation before and after semi-forming resulted in the cell conductance being a non-integer multiple of the quantized conductance G_0. In addition, the voltage-driven conductance fluctuation as well as conductance quantization probably disappeared upon heating the RS cells to 470−570 K. Moreover, cell size dependence of the appearance of two types of nonpolar RS operations indicated that conductance quantization and conductance fluctuation also disappeared by Joule heating conducted from another fat filament in the NiO layer created by second forming. From the viewpoint of voltage- and heat-driven disappearance of the conductive filament with a QPC and the modification of V_Os, conductance quantization seemed to be a special form of the conductance fluctuation. As a result, the driving force behind reset after semi-forming was considered to be Joule heating.

7.2 Future Outlook

The author offers several challenges and suggestions for detailed understanding of RS phenomena.

Other resistance change materials

In this thesis, the author focused on forming and RS characteristics in binary TMO (NiO and TiO_2)-based RS cells. To generalize the proposed conclusion that the correlation between variations of initial resistance and distributions of time to forming was explained based on the crystallinity and the oxygen composition in the TMO layers, the statistical analyses of forming

characteristics in RS cells using other resistance change materials should be investigated for the comparison with the results for NiO and TiO_2-based RS cells.

Tantalum pentoxide (Ta_2O_5) is suitable as a candidate for such the other materials. The basic crystalline structure of Ta_2O_5 is an orthorhombic crystal system in the stoichiometric Ta_2O_5 instead of cubic and tetragonal crystal systems such as Pt, NiO, and TiO_2. The difference of the basic crystalline structure in Ta_2O_5 from that in Pt may be of importance for the generalization of the correlation between variations of initial resistance and distributions of time to forming. Moreover, the difference seems to affect the crystalline orientation of Ta_2O_5 on Pt BE, which results in poor crystallinity and a reduction in grain size, and therefore an extremely low density of GBs in Ta_2O_5. As a result, various electric characterizations of GB-free resistance change material can be obtained, without hindering the intrinsic physical property of the bulk by GBs.

Control of number of V_Os at grain boundaries in NiO layers

As discussed in Chapter 5, V_Os are distributed at GBs in as-deposited NiO layers according to Poisson statistics. The variation of forming characteristics and dominant cell conductance seems to originate from the almost random distribution of V_Os. As long as NiO layers are deposited by reactive sputtering, the distribution is unavoidable because of the intrinsically physical deposition method in spite of a reactive (chemical) element. To suppress the variation, therefore, the NiO deposition method should be changed to a more chemical one, or be performed by post treatment. As the latter approach, post thermal annealing of as-deposited NiO may be effective.

Quantized plateau in conductance quantization

As discussed in Chapter 6, Pt/NiO/Pt TCMs with a QPC will face the possible problem of very-fast reset operation, because of an insufficiently high diffusion coefficient of V_Os. To avoid the problem, potentiality for NiO-based ECMs with a QPC as one of the solutions should be considered. Although the author succeeded in acquiring RS based on almost quantized conductance by using silver (Ag) or gold (Au) as top electrodes (TEs), the quantized plateau was less clear than that in the Pt/NiO/Pt cells. The quantized plateau in conductance quantization has been considered to be integer of G_0 in electrochemical metalization memories (ECMs) and half-integer of G_0 in valence change memories (VCMs) [1, 2]. However, the physical reason remains unclear, and correlation between the plateau and types of ReRAM should be investigated to clarify RS mechanism based on quantized conductance.

References

[1] A. Mehonic, A. Vrajitoarea, S. Cueff, S. Hudziak, H. Howe, C. Labbe, R. Rizk, M. Pepper, and A. J. Kenyon, Sci. Rep. **3**, 2708 (2013).

[2] F. Pan, S. Gao, C. Chen, C. Song, and F. Zeng, Mater. Sci. Eng. R **83**, 1 (2014).

Appendix A

Reactive Sputtering Model

Berg's model is well known as one of models which explains reactive sputtering quantitatively. The model assumes the steady-state values, instead of time-variations during reactive sputtering [1, 2].

A.1 Equations in Berg's model

A flux of reactive gas F molecules to the surfaces of the target and collector is caused by introducing partial pressure of the reactive gas P in the chamber. The relationship between F and P is described by

$$F = \frac{P}{\sqrt{2k_{\mathrm{B}}T\pi m}} \tag{A.1}$$

where k_{B} is the Boltzmann constant, T the temperature, and m the mass of the reactive gas molecule. The total supply Q_{tot} is the sum of all sources for reactive gas consumption, such as the consumption at the target Q_{t}, the consumption at the collector (including the substrate) Q_{c}, and the evacuation by a pump Q_{p}:

$$Q_{\mathrm{tot}} = Q_{\mathrm{t}} + Q_{\mathrm{c}} + Q_{\mathrm{p}} = \alpha_{\mathrm{t}}F(1-\theta_{\mathrm{t}})A_{\mathrm{t}} + \alpha_{\mathrm{c}}F(1-\theta_{\mathrm{c}})A_{\mathrm{c}} + SP, \tag{A.2}$$

where θ_{t} and θ_{c} are the sticking coefficient for unreacted fraction at the target and at the collector, respectively, θ_{t} and θ_{c} the compound fraction at the target with a size of A_{t} and at the collector with a size of A_{c}, respectively, and S pumping speed. Here, the total number of sputtered compound molecules F_{c} and metal atoms F_{m} per unit time from the target can be described by

$$F_{\mathrm{c}} = \frac{J}{e}Y_{\mathrm{c}}\theta_{\mathrm{t}}A_{\mathrm{t}}, \tag{A.3}$$

$$F_{\mathrm{m}} = \frac{J}{e}Y_{\mathrm{m}}(1-\theta_{\mathrm{t}})A_{\mathrm{t}}, \tag{A.4}$$

where J is the ion current density to the target, e the elementary charge, and Y_{c} and Y_{m} the sputtering yield of compound molecules and metal molecules, respectively.

The author assumes reactive atom composition n in the compound MX_n (M: metal, X: reactive gas). Therefore, a steady-state equation of X atoms for the target is described as follow:

$$nF_{\mathrm{c}} = 2Q_{\mathrm{t}}. \tag{A.5}$$

Here, a factor of 2 means normal number of atoms per the reactive gas molecule. In the similar manner, a steady-state equation for the collecting area is described as follow:

$$2Q_c + nF_c(1 - \theta_c) = F_m\theta_c. \tag{A.6}$$

Note that the terms on the left and right hand correspond the contributions supporting an increase and decrease in θ_t, respectively.

A.2 O_2 Flow Rate Dependence

The author calculated the dependences of characteristic parameters on oxygen (O_2) flow rate Q_{tot} during the nickel oxide (NiO) deposition.

Partial pressure

θ_t and θ_t can be derived from Eqs. (A.3)−(A.6). Q_{tot} can be easily described as a function of the O_2 partial pressure P by using Eqs. (A.1) and (A.2).

Deposition rate

When the compound fraction θ_c at A_c are calculated, the deposition rate D is expressed as

$$D = \frac{F_m + F_c}{A_c}\{c_1(1 - \theta_c) + c_2\theta_c\}, \tag{A.7}$$

where c_1 and c_2 are constants accounting for unit conversions. The first term represents the contribution by elemental metal atoms, while the second term represents the contribution by compound material. In the NiO deposition, c_1 and c_2 are 1.10×10^{-29} m^3 and 1.82×10^{-29} m^3, respectively.

Oxygen composition

The oxygen composition x in the NiO_x layer is equivalent to $n\theta_c$. Note that the author assumed n as 1.2 because experimental oxygen composition deposited in an oxide mode were approximately 1.2.

References

[1] S. Berg, J. Vac. Sci. Technol. A **5**, 202 (1987).

[2] S. Berg and T. Nyberg, Thin Solid Films **476**, 215 (2005).

Appendix B

Coupled Simulation

COMSOL Multiphysics provides lots of solvers of various scientific and engineering phenomena, which enables a coupled simulation based on multiple physics phenomena simultaneously. The author has utilized the coupled simulation with heat transfer, electric currents, and transport of diluted species.

B.1 Heat Conduction Simulation

Thermal simulation involving Joule heat conduction in oxide-based resistive switching (RS) cells can be simply performed by using the heat transfer solver. The heat source relates to electric heating through conductive filaments by applied voltage to the cell. The Joule heat conduction takes place in the oxide mainly by molecular motion which take the form of lattice vibrations (phonons) in the matrix.

Heat equation in solids is described as follow:

$$\rho C_{\mathrm{p}} \frac{\partial T}{\partial t} + \nabla \cdot \boldsymbol{q} = \dot{Q}, \tag{B.1}$$

where ρ is the density, C_{p} the heat capacity, $\boldsymbol{q}$ the heat flux by conduction, and $\dot{Q}$ the internal volumetric heat quantity. Here, heat convection and heat transfer by radiation in the heat transfer solver are not considered. The dependent variable is temperature T. Fourier's law indicates that conductive heat flux is proportional to the temperature, according to which the heat equation in the oxide, nickel oxide (NiO) in this thesis, is described by

$$\boldsymbol{q} = -\boldsymbol{k} \nabla T, \tag{B.2}$$

where $\boldsymbol{k}$ is the thermal conductivity, which is normally anisotropic. Although the thermal conductivity of the NiO layers with a crystalline structure of columnar along to the thickness direction is obviously anisotropic, it is assumed that $\boldsymbol{k}$ is isotropic and regarded as not a tensor but the specific value k. Therefore, the adopted heat equation becomes

$$\rho C_{\mathrm{p}} \frac{\partial T}{\partial t} = k \boldsymbol{\Delta} T + \dot{Q}. \tag{B.3}$$

The author applied the heat equation to platinum (Pt)/NiO/Pt RS cells in which a fat conductive filament created by second forming was located at the center in the cylindrical coordinate system, as described in Section 6.4.2. Figure 6.17(a) shows the cross-sectional view of a cylindrical layer structure. The thickness is 50 nm in Pt top and bottom electrode, and 80 nm in NiO. The diameters of the fat filament and the RS cell is 10 nm and 88 μm, respectively. For simplicity, heat source was supplied as the specific temperature T_0 in the filament area instead of the correct change of Joule heat (product of current density and electric field), because the specific change of heat quantity by Joule heating is not important in the rough thermal simulation. As discussed in Section 6.4.2, T_0 was set tentatively as 600 K. Table 6.1 shows the values of k, ρ, and C_p of the materials for the simulation.

The setting of thermal insulation affects the thermal simulation result. In Section 6.4.2, no material around the cell region were set and the outer portion of the cell was thermally insulated. Therefore, the heat transfer simulation result under the above condition tend to enhance the temperature in the cell. The actual temperature can be lower than the simulation result value for the air region around the cell or heat sink below the Pt BE (strictly the bottom of the Si substrate under the Pt BE).

B.2 Coupled Simulation for Reset

The coupled simulation for reset can be performed by using three solvers of heat transfer, electric currents, and transport of diluted species. The heat transfer solver was already explained in Section B.1.

In the electric current solver, stationary electric current density $\boldsymbol{J}$ is described by Ohm's law as follow:

$$\boldsymbol{J} = \sigma \boldsymbol{E} = -\sigma \nabla V, \tag{B.4}$$

where $\boldsymbol{E}$ is the electric field and σ is the electrical conductivity. Here, the externally generated current density is neglected. The static form of the equation of current continuity for electrical conduction is

$$\nabla \cdot \boldsymbol{J} = -\nabla \cdot (\sigma \nabla V) = 0. \tag{B.5}$$

The dependent variable is voltage V.

Joule heat conduction can be simulated to combine all features from the electric currents solver with the heat transfer solver. In the electromagnetic heat interface, the internal volumetric heat source $\dot{Q}$ is replaced as Joule heat $\boldsymbol{J} \cdot \boldsymbol{E}$. Therefore, the heat equation in Eq. (B.3) becomes

$$\rho C_\mathrm{p} \frac{\partial T}{\partial t} = k \Delta T + \sigma |\nabla V|^2. \tag{B.6}$$

The dependent variables T and V are linked by this equation. In the simulation involving Joule heat conduction, the definition of the electrical conductivity σ of the material related to heat conduction is very crucial for the simulation results.

Next, in the transport of diluted species solver, mass balance equation in transport of the species through diffusion and convection is as follow:

$$\frac{\partial c}{\partial t} = \nabla \cdot (D_{ij} \nabla c) - \boldsymbol{u} \cdot \nabla c \tag{B.7}$$

where D_{ij} is ij component of the normally anisotropic diffusion coefficient $\boldsymbol{D}$, and $\boldsymbol{u}$ is the velocity vector. The first term on the right hand expresses the diffusive flux according to Fick's law, whereas the second term accounts for the convective transport due to the velocity $\boldsymbol{u}$. Here, a kind of reaction rate expression for the species is neglected. The dependent variable is the concentration of the species c.

The author conducted the coupled simulation in Pt/NiO/Pt RS cells in low-resistance state (LRS) (with a conductive filament) during voltage sweep for reset. Let the physical origin of the filament be oxygen vacancies (V_Os). The usual reset mechanism by Joule heating is qualitatively explained as follows. As Joule heat raises temperature (T) by voltage (V) sweep at the filament with high concentration of the V_Os (c_v) and thus low electrical conductivity and its surrounding region, more V_Os diffuse outward due to rapid increase in the diffusion coefficient. Consequently, the concentration at the filament gradually decreases, and thus a reduction in the electrical conductivity brings about the dissolution of V_Os at the part of the filament, that is, occurrence of reset. Therefore, correlation between the concentration and temperature is a key for the simulation. Moreover, the diffusion by Soret effect can be introduced by $S_{ij}\nabla T$ as $\boldsymbol{u}\cdot$, where S_{ij} is coefficient of thermophoresis to temperature gradient [1]. Kinoshita reported the coupled simulation for reset in the RS cells by combination of Fick and Soret diffusions [2].

The dependent variables T, V, and c_v are directly linked each other through Eqs. (B.3), (B.7), and other dependent parameters. One of the effective characteristics is temperature and the concentration dependence of the electrical conductivity. As a result, the time-dependent equations from the viewpoint of the dependences in the NiO layer are

$$\rho_{\mathrm{NiO}} C_{\mathrm{pNiO}}(T) \frac{\partial T}{\partial t} = k_{\mathrm{NiO}}(c_v) \Delta T + \sigma_{\mathrm{NiO}}(T, c_v) |\nabla V(t)|^2, \tag{B.8}$$

$$\frac{\partial c_v}{\partial t} = \nabla \cdot (D_v(T) \nabla c_v), \tag{B.9}$$

where parameters with a subscript of NiO are the physical property values of NiO, and D_v is the diffusion coefficient value of V_Os assumed to be isotropic in the NiO layer.

Figure 6.18 shows the cross-sectional view of a cylindrical layer structure. The thickness of Pt electrodes and NiO is the same as that in the thermal simulation in Section B.1. The diameter of the filament composed of V_Os is 10 nm, whereas the diameter of the RS cell is tentatively 100 μm, which does not affect the simulation results as long as the diameter is more than approximately 10 μm. In contrast, the setting of thermal insulation possibly affects the results. Therefore, the air region around the cell and heat sink below the Pt BE (strictly the bottom of the SiO_2 on a Si substrate and a sample stage for measurements) are set.

The simulation results were confirmed to be very sensitive to the initial concentration of V_Os at the filament, the concentration dependence of electrical conductivity of NiO, and the diffusion coefficient of V_O in the NiO.

The author considers the initial concentration of V_Os (c_{vini}) in the filament region in the LRS. The concentration of V_Os in the NiO layer varies from the minimum (c_{vmin}= 0) as a stoichiometric NiO to the maximum (c_{vmax}= 5.38×10^{28} m^{-3}) as almost metallic nickel (Ni). Taking into account of sufficiently high conductivity of the filament equivalent to a metal, c_{vini} is assumed to be approximately 1.2 c_{vth}, where the specific value c_{vth} (= 0.1 c_{vmax}) means the threshold between Ni and V_O-depleted NiO. That is to say, the filament with the concentration (c_v) of larger than c_{vini} can be regarded as a row of metallic Ni atoms. Based on the above assumptions, the concentration dependence of the thermal conductivity of NiO is described by

$$k_{NiO}(c_v) = \min\left\{ k_{Ni},\ \bar{k}_{NiO} + (k_{Ni} - \bar{k}_{NiO})\frac{c_v}{c_{vth}} \right\}, \tag{B.10}$$

where k_{Ni} and $\bar{k}_{NiO}$ are the thermal conductivity of Ni [91 W/(m·K)] and the stoichiometric NiO [20 W/(m·K)] [3], respectively. In the same manner, the concentration and temperature dependence of the electrical conductivity of NiO shown in Fig. B.1 is described by

$$\sigma_{NiO}(T, c_v) = \min\left[\sigma_{Ni},\ \sigma_{Ni}\frac{c_v}{c_{vth}} \exp\left\{ -\frac{E_a(1 - c_v/c_{vth})}{k_B T} \right\} \right], \tag{B.11}$$

where σ_{Ni} is the electrical conductivity of Ni [14.4 MS/m], E_a the activation energy for electrical conduction in NiO [0.3 eV] (0.17–0.45 eV from the authors' results), and k_B the Boltzmann constant. In this case of c_{vini}= 6.45×10^{27} m^{-3}, resistance of the RS cell in the LRS at room temperature (RT) equals with approximately 70 Ω. Furthermore, c_v in initial state or high-resistance state (HRS) at RT is estimated to be approximately 6×10^{21} m^{-3}, because experimental resistance of the RS cell in the HRS equals with 100 kΩ.

Table 6.2 shows the values of k, ρ, C_p, and σ of Pt, NiO, and SiO_2 for the simulation. The heat capacity can be expressed as follow: [2, 4]

$$C_{pNiO}(T) = 506.64\ \text{J/(kg·K)} + 10.563\ \text{J/(kg·K)} \exp\left(\frac{T}{140.3\ \text{K}} \right). \tag{B.12}$$

Anyway, $C_{pNiO}(T)$ was confirmed not to affect the simulation results as well as $k_{NiO}(c_v)$.

The most difficult assumption is to define the diffusion coefficient of V_Os (D_v) in the NiO. D_v is theoretically described as follow: [1]

$$D_v(T) = f_{esc} a^2 \exp\left(-\frac{U_A}{k_B T} \right) = D_{v0} \exp\left(-\frac{U_A}{k_B T} \right), \tag{B.13}$$

where f_{esc} is the effective vibrational frequency of V_Os within their confining potential wells, and a and U_A are the distance and the energy barrier between the wells, respectively. The author adopted D_{v0} as 10^{10} m^2/s, because f_{esc} and a were roughly estimated to be 10^8 Hz and 10^{-9} m, respectively. Moreover, U_A was selected as 1.0 eV [2].

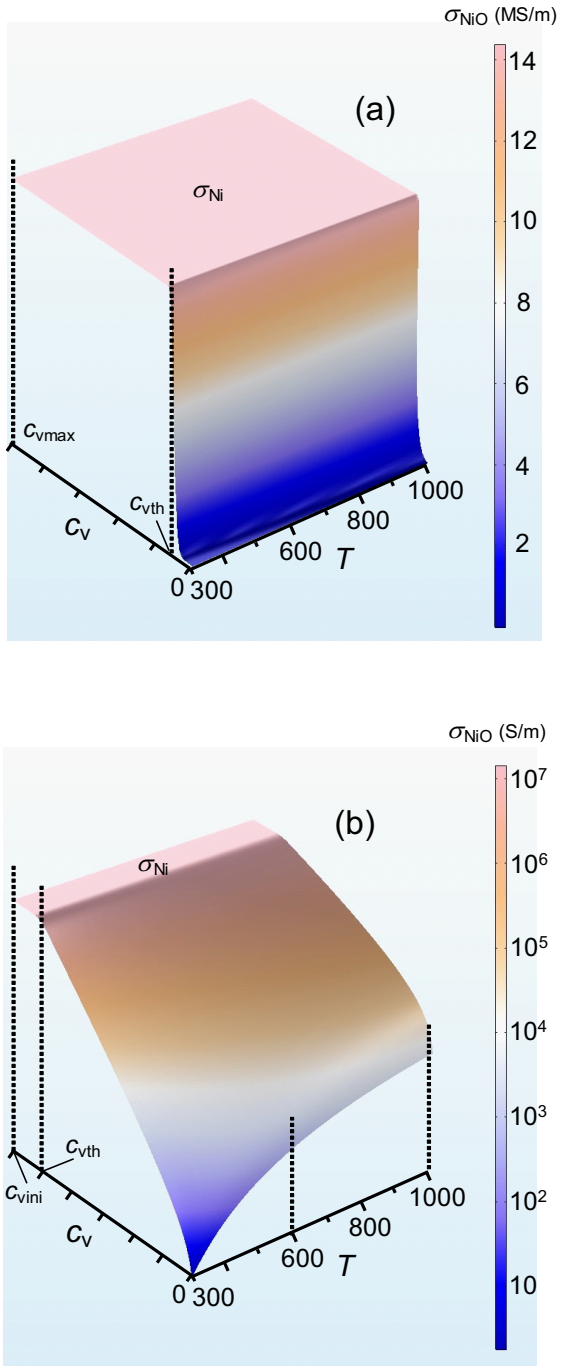

Figure B.1: Temperature and the concentration of V_Os dependence of electrical conductivity of NiO in (a) linear and (b) log scale.

When the Soret diffusion is considered as in Refs. [1] and [2], the diffusion equation should be transformed to the below:

$$\frac{\partial c_{\mathrm{v}}}{\partial t} = \nabla \cdot (D_{\mathrm{v}} \nabla c_{\mathrm{v}}) - D_{\mathrm{v}} S_{\mathrm{v}} \nabla \cdot (c_{\mathrm{v}} \nabla T), \tag{B.14}$$

where $S_{\mathrm{v}} = U_{\mathrm{A}}/(k_{\mathrm{B}} T^2)$ is the Soret coefficient value of $\mathrm{V_O}$s. The Soret diffusion tends to help prevent the reset resulting in even the increase in the cell resistance by voltage sweep, which was also experimentally confirmed as the voltage sweep rate increases [2]. The results indicate that the Fick and Soret diffusions are competing during voltage sweep, and that the Soret diffusion can enhance the maximum temperature just before reset.

In the meantime, when the drift effect is considered as in Refs. [3] and [1], the diffusion equation should be transformed to the below:

$$\frac{\partial c_{\mathrm{v}}}{\partial t} = \nabla \cdot (D_{\mathrm{v}}(T) \nabla c_{\mathrm{v}}) - \frac{Ze}{k_{\mathrm{B}} T} \nabla \cdot (D_{\mathrm{v}}(T) c_{\mathrm{v}} \nabla V), \tag{B.15}$$

where Z is the valence number of $\mathrm{V_O}$s and e is the elementary charge. Here, it should be assumed that the diffusion coefficient value D_{v} is isotropic in the NiO layer. Russo reported the asymmetric calculated profiles at reset, in which the point of both the $\mathrm{V_O}$ depletion and the maximum temperature was below the middle of the filament [3]. The author dared to assume Z as zero in the simulation because the strict Z and the expression of ionization energy of $\mathrm{V_O}$s during applied voltage were not clarified, although the valence number of ionized $\mathrm{V_O}$s may be naturally considered to be 2 ($\mathrm{V_O}^{+2}$).

References

[1] D. B. Strukov, F. Alibart, and R. S. Williams, Appl. Phys. A **107**, 509 (2012).

[2] K. Kinoshita, S.-H. Koh, T. Moriyama, and S. Kishida, Sci. Rep. **5**, 18442 (2015).

[3] U. Russo, D. Ielmini, C. Cagli, and A. L. Lacaita, IEEE Trans. Electron Devices **56**, 193 (2009).

[4] *Thermochemcal Data of Pure Substrates* edited by I. Barin (VCH, 1989).

List of Publications

A. Full Length Papers and Letters

1. Y. Nishi, T. Iwata, and T. Kimoto
   "Correlation between oxygen composition and electrical properties in NiO thin films for resistive random access memory,"
   Jpn. J. Appl. Phys. **50**, 015802 (2011).

2. T. Iwata, Y. Nishi, and T. Kimoto
   "Effect of heat treatment on the resistive switching characteristics of Pt/NiO/Pt stack structures,"
   Jpn. J. Appl. Phys. **50**, 081102 (2011).

3. T. Iwata, Y. Nishi, and T. Kimoto
   "Microscopic investigation of the electrical and structural properties of conductive filaments formed in Pt/NiO/Pt resistive switching cells,"
   Jpn. J. Appl. Phys. **52**, 041801 (2013).

4. T. Iwata, Y. Nishi, and T. Kimoto
   "Dominant conduction mechanism in NiO-based resistive memories,"
   J. Appl. Phys. **117**, 225701 (2015).

5. H. Sasakura, Y. Nishi, and T. Kimoto
   "Temperature dependence of conductance in NiO-based resistive switching memories showing two modes in the forming process,"
   Appl. Phys. Lett. **107**, 223510 (2015).

6. Y. Nishi and T. Kimoto
   "Effect of NiO crystallinity on forming characteristics in Pt/NiO/Pt cells as resistive switching memories,"
   J. Appl. Phys. **120**, 115308 (2016).

7. Y. Nishi, H. Sasakura, and T. Kimoto
   "Appearance of quantum point contact in Pt/NiO/Pt resistive switching cells,"
   J. Mater. Res. **32**, 2631 (2017), invited feature paper.

8. Y. Nishi, H. Sasakura, and T. Kimoto
"Conductance fluctuation in NiO-based resistive switching memory,"
J. Appl. Phys. **124**, 152134 (2018), invited to special topic.

9. M. Arahata, Y. Nishi, and T. Kimoto
"Effect of TiO_2 crystallinity and oxygen composition on forming characteristics in Pt/TiO_2/Pt resistive switching cells,"
AIP Adv. **8**, 125010 (2018).

10. T. Iwata, Y. Nishi, and T. Kimoto
"Grain boundary structures and their impact on electrical properties of NiO films deposited by reactive sputtering,"
in preparation.

11. T. Miyatani, Y. Nishi, and T. Kimoto
"Dominant conduction mechanism in TaO_x-based resistive switching memory,"
in preparation.

12. Y. Nishi, Y. Kuriyama, and T. Kimoto
"Appearance of semi-high resistance state in the forming process in Pt/TiO_2/Pt cells,"
in preparation.

13. Y. Nishi and T. Kimoto
"Constant and ramped voltage stress application to Pt/NiO/Pt stack structures,"
in preparation.

14. Y. Nishi, T. Miyatani, Y. Kuriyama, and T. Kimoto
"Reactive sputtering condition for transition metal oxide-based resistive switching cells,"
in preparation.

B. Proceedings of International Conference

1. Y. Nishi, T. Iwata, and T. Kimoto
"Correlation between oxygen composition and electrical properties in NiO thin films for resistive random access memory,"
Mater. Res. Soc. Symp. Proc. **1250**, 209 (2010).
(*MRS Spring Meeting*, San Francisco, CA, USA, 2010.)

2. Y. Nishi, T. Iwata, and T. Kimoto
"Time-dependent forming characteristics in Pt/NiO/Pt stack structures for resistive random access memory,"
Mater. Res. Soc. Symp. Proc. **1430**, 141 (2012).
(*MRS Spring Meeting*, San Francisco, CA, USA, 2012.)

3. T. Iwata, Y. Nishi, and T. Kimoto
   "Identification of the location of conductive filaments formed in Pt/NiO/Pt resistive switching cells and investigation on their properties,"
   Mater. Res. Soc. Symp. Proc. **1430**, 159 (2012).
   (*MRS Spring Meeting*, San Francisco, CA, USA, 2012.)

4. T. Iwata, Y. Nishi, and T. Kimoto
   "Impact of the oxygen amount of an oxide layer and post annealing on forming voltage and initial resistance of NiO-based resistive switching cells,"
   Mater. Res. Soc. Symp. Proc. **1562**, dd14-11 (2013).
   (*MRS Spring Meeting*, San Francisco, CA, USA, 2013.)

C. International Conferences

1. T. Iwata, Y. Nishi, and T. Kimoto
   "The effect of annealing under vacuum on the electrical characteristics of Pt/NiO/Pt stack structures,"
   17th Int. Workshop on Oxide Electronics, 20-P-18, Awaji, Japan, 2010.

2. Y. Nishi, T. Iwata, and T. Kimoto
   "Weibull distributions of forming characteristics in Pt/NiO/Pt stack structures for resistive random access memory,"
   MRS Spring Meeting, DD11.04, San Francisco, CA, USA, 2013.

3. Y. Nishi, H. Sasakura, T. Iwata and T. Kimoto
   "Forming characteristics of NiO-based resistance change random access memory,"
   61st JSAP Spring Meeting Int. Symposium, 18p-E1-10, Tokyo, Japan, 2014.

4. Y. Nishi, T. Iwata, and T. Kimoto
   "DC and AC conduction mechanism in different resistance states of Pt/NiO/Pt stack structures,"
   MRS Fall Meeting, M4.05, Boston, MA, USA, 2014.

5. H. Sasakura, Y. Nishi, and T. Kimoto
   "Quantized conductance in Pt/NiO/Pt cells showing two modes in forming process and resistive switching,"
   MRS Fall Meeting, KK9.08, Boston, MA, USA, 2015.

6. Y. Nishi, Y. Kuriyama, and T. Kimoto
   "Different resistance switching characteristics in NiO-based ReRAM cells between Pt and Ag as top electrodes,"
   MRS Fall Meeting, KK10.15, Boston, MA, USA, 2015.

7. Y. Nishi, H. Sasakura, Y. Kuriyama, and T. Kimoto
"Conductance quantization in binary-oxide-based ReRAM cells," (invited)
29th Int. Microprocesses and Nanotechnology Conference, 11C-8-1, Kyoto, Japan, 2016.

8. Y. Nishi, H. Sasakura, and T. Kimoto
"The appearance condition of quantized conductance in NiO-based resistive switching cells,"
MRS Fall Meeting, EM10.2.01, Boston, MA, USA, 2016.

9. Y. Nishi and T. Kimoto
"Distribution of forming characteristics in NiO-based resistive switching cells with two kinds of NiO crystallinity,"
MRS Spring Meeting, EP01.7.03, Phoenix, AZ, USA, 2018.

10. R. Matsui, Y. Kuriyama, Y. Nishi, and T. Kimoto
"Resistance increase by overcurrent suppression in forming process in Pt/TiO_2/Pt cells,"
MRS Spring Meeting, EP01.7.05, Phoenix, AZ, USA, 2018.

11. Y. Nishi, H. Sasakura, and T. Kimoto
"Driving force behind reset process in Pt/NiO/Pt stack cells,"
14th Int. Conference on Atomically Controlled Surfaces, Interfaces and Nanostructures, 22E24, Sendai, Japan, 2018.

12. T. Miyatani, Y. Nishi, and T. Kimoto
"DC and AC electrical characteristics of Ta_2O_5-based ReRAM cells,"
31th Int. Microprocesses and Nanotechnology Conference, 16P-11-24, Sapporo, Japan, 2018.